A geochemical characterization of the lower part of the Miocene shield-building lavas on Gran Canaria

Romina Peetz

Masters thesis in Geology at Lund University - Lithosphere and Biogeosphere Sciences, no. 252 (45 hskp/ECTS)

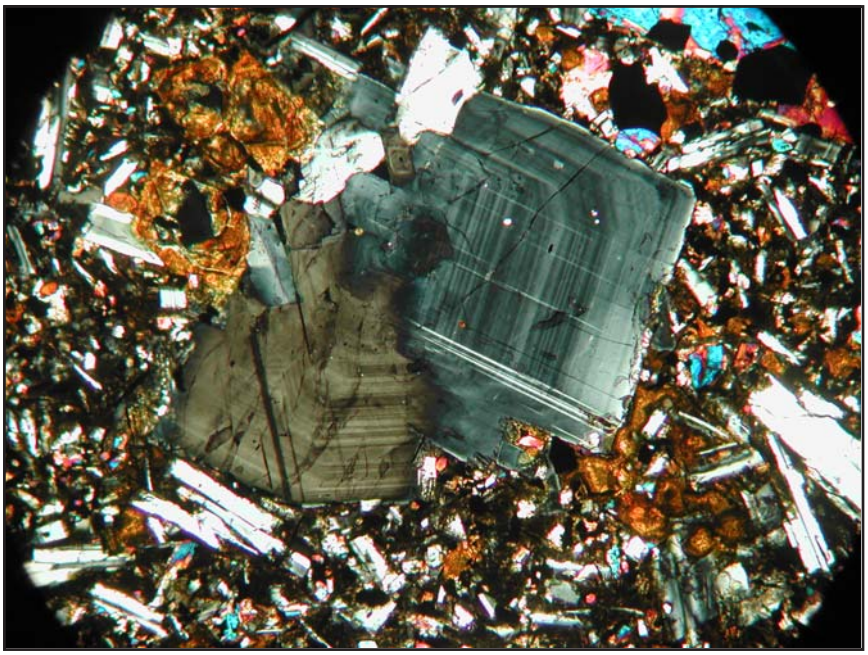

Geologiska institutionen
Centrum för GeoBiosfärsvetenskap
Lunds universitet
2009

A geochemical characterization of the lower part of the Miocene shield-building lavas on Gran Canaria

Master Thesis

Romina Peetz

Department of Geology
Lund University
2009

Contents

1 Introduction 6
2 Geological Setting 6
2.1 The Canary Islands 6
2.1.1 The origin of the Canary Islands 6
2.1.2 Magma types on the Canary Islands 9
2.2 Gran Canaria 9
2.2.1 Shield-building mafic rocks 9
2.2.2 Mogán and Fataga Groups 9
2.2.2.1 Mogán Group 10
2.2.2.2 Montaña Horno Formation 10
2.2.2.3 Fataga Group 10
2.2.3 Las Palmas Formation 10
2.2.4 Roque Nublo Group 10
2.2.5 Post Roque Nublo Group 11
2.3 Güigüi and Hogarzales Formation 11
3 Sample description 12
4 Methods 15
4.1 Sample preparation 15
4.2 Thin sections 15
4.3 Major and trace elements 15
4.4 Scanning electron microscope (SEM) 15
4.5 Illustration 15
5 Results 15
5.1 Description of the thin sections 15
5.2 Major elements 19
5.2.1 Total alkali versus silica diagrams 19
5.2.2 Bivariate plots 20
5.2.3 Normative minerals 27
5.2.3.1 The forsterite-anorthite-olivine diagram 27
5.2.4 Discrimination diagram based upon minor elements 28
5.3 Trace elements 28
5.3.1 Large ion lithophile elements (LILE) 28
5.3.2 High field strenght elements (HFSE) 30
5.3.3 Transition metals 30
5.3.4 Rare earth elements (REE) 32
5.3.5 Normalized multi-element diagram 33
5.4 Phenocryst phases 33
5.4.1 Clinopyroxene 34
5.4.2 Olivine 37
5.4.3 Plagioclase 37
5.4.4 Summary 40
5.5 Opaque phases 40
5.5.1 Ilmenite 40
5.5.2 Spinel 42

Contents, continuation

5.6 Alteration products 44
5.6.1 Iddingsite 44
5.6.2 Altered olivine 44
6 Discussion 45
6.1 Source components involved in the shield magmatism 45
6.2 Parental magma 47
6.3 Primary magma and fractional crystallization 50
7 Conclusion 51
8 Acknowledgments 52
9 References 52
Appendix 1 - Geological map of Gran Canaria 57
Appendix 2 - Map of the sampled localities at Barranco de Tasártico 58
Appendix 3 - Table of the whole rock chemistry 59
Appendix 4 - Table of the normative minerals 65
Appendix 5 - Table of the chemical composition of the clinopyroxene phenocrysts 66
Appendix 6 - Table of the calculated aegirine component and Tschermak's substitution 75
Appendix 7 - Table of the chemical composition of the olivine phenocrysts 84
Appendix 8 - Table with the calculated olivine crystallization temperatures 89
Appendix 9 - Table of the chemical composition of the plagioclase phenocrysts 95
Appendix 10 - Table of the chemical composition of ilmenite 98
Appendix 11 - Table with the chemical composition of the spinel phase 100
Appendix 12 - Table of the calculated spinel components 106
Appendix 13 - Table of the chemical composition of iddingsite 112
Appendix 14 - Table of the chemical composition of altered olivine 114

A geochemical characterization of the lower part of the Miocene shield-building lavas on Gran Canaria

ROMINA PEETZ

Peetz, R., 2009: A geochemical characterization of the lower part of the Miocene shield-building lavas on Gran Canaria. *Examensarbeten i geologi vid Lunds universitet*, Nr. 252, 118 pp. 45 ECTS.

Abstract:: Gran Canaria is a classical example of Atlantic plume-related magmatism. Its magmatic history is rather long, 15 Ma. Therefore, it is well suited for a study. A comprehensive study of the lower Miocene shield-building lavas is performed for this thesis. The samples come from Barranco de Tasártico. The shield-building lavas range from picro-basalt to basalt and basanite (SiO_2=44.5-49.7 wt%; Na_2O+K_2O=2.3-4.6 wt%). MgO contents vary significantly (5.1-16.0 wt%). The studied lavas are generally enriched in LILE and HFSE (e.g. Sr=358-664 ppm, Ba=114-251, Zr=199-377 ppm, Nb=29-57 ppm, Ta=1.8-3.5 ppm). The sampled rocks have a high abundance of clinopyroxene, olivine and plagioclase phenocrysts. Clinopyroxene phenocrysts range between augitic and diopsidic compositions. End-member calculations suggest Tschermak substitution and aegirine in all analysed crystals. No jadeite component could be identified. Olivine ranges between Fo_{79} and Fo_{88}. Labradorite (An_{50} to An_{70}) is the most common plagioclase in the studied thin sections. The identified opaque phases are ilmenite and chromium-spinel. Bivariate plots of the major elements versus MgO indicate two different fractionation trends. At MgO contents >8 wt%, clinopyroxene and olivine control the variation trends. After the onset of plagioclase fractionation at 8 wt% MgO, the trends are controlled by clinopyroxene, olivine and plagioclase fractionation. The strong enrichment in Nb and Ta ($[Nb/La]_n$=1.1-1.4; $[Ta/La]_n$=1.2-1.5) as well as the depletion in K and Pb ($[K/La]_n$=0.6-0.9; $[Pb/La]_n$=0.1-0.5) are characteristic for mafic HIMU-type magmas. The ratio La/Nb (0.72-0.88) plotted versus Ba/Nb (3.4-5.3) suggests that the shield-building lavas from Gran Canaria could be generated by mixing of three mantle components: HIMU, DMM and EM. A relatively moderate enrichment in light over heavy REEs ($[La/Lu]_n$=8.9-12.1) suggests the exclusion of garnet as a significant residual phase in the source. Since no negative Eu anomalies are disclosed, the effect of plagioclase fractionation is small. Obtained Zr/Y ratios (9.7-11.8) argue against peridotite as the only source for the lavas. High Zr/Y ratios are most easily explained by significant garnet among the residual phases, which is inconsistent with the REE results. Garnet peridotite or eclogite as source rocks would result in garnet among the residual phases. The high Zr/Y ratios are thus ambiguous. One possible explanation is fractionation of Zr and Y at the time of, or prior to, formation of the source material. The impact of clinopyroxene on the Zr/Y ratio could not be determined. This ratio increases slowly with fractionation. There are no data allowing the most primitive ratio to be determined. This together with low Ba/Nb (3.4-5.3) and high K/La (217-292) ratios suggests that the derivation from a single source, containing varying proportions of garnet is not possible. The general depletion in K, Rb and Ba displayed in the normalized multi-element diagram suggests a derivation from recycled oceanic crust. Since earlier published εNd values (3.9-5.8) are higher than expected for undepleted OIB, a significant impact of depleted lithosphere on the source material composition is proposed. Thus, the results imply the derivation from a heterogeneous source. This source probably resembles recycled subducted eclogitic oceanic crust (<2 Ga), which has been stirred into or reacted with ambient peridotitic mantle. Primary magmas formed within the garnet stability field. Previous investigators have suggested that they are picritic and have formed at temperatures between 1500 and 1600°C at 3 GPa. After migration into magma reservoirs, fractional crystallization of clinopyroxene, olivine and small amounts of plagioclase affected the magma composition. The crystallization of the phenocryst phases occurred at high temperatures and low pressures. Calculated temperatures, associated with large errors, indicate that olivine phenocrysts crystallized at temperatures between 1172 and 1218° C.

Keywords: Gran Canaria, shield-building lavas, Güigüi Formation

Romina Peetz, Department of Geology, GeoBiosphere Science Centre, Lund University, Sölvegatan 12, SE-223 62 Lund, Sweden. E-mail: romina.peetz@student.uni-halle.de

A geochemical characterization of the lower part of the Miocene shield-building lavas on Gran Canaria

ROMINA PEETZ

Peetz, R., 2009: A geochemical characterization of the lower part of the Miocene shield-building lavas on Gran Canaria. *Examensarbeten i geologi vid Lunds universitet*, Nr.252, 118 pp. 45 högskolepoäng.

Sammanfattning: Gran Canaria är ett klassiskt exempel på atlantisk plymrelaterad magmatism Den magmatiska historien är ganska lång, ungefär 15 miljoner år. Ön utgör därför ett lämpligt studieobjekt. Detta masterarbete omfattar en undersökning av de undermiocena sköldbyggande basalterna. Provtagningen är gjord i Barranco de Tasártico. De sköldbyggande lavorna har sammansättningar från pikritbasalt till basalt och basanit. (SiO_2=44,5-49,7 vikts%; Na_2O+K_2O=2,3-4,6 vikts%). MgO-halten varierar kraftigt (5,1-16,0 vikts%). De undersökta lavorna är i allmänhet anrikade på LILE och HFSE (t.ex. Sr=358-664 ppm, Ba=114-251, Zr=199-377 ppm, Nb=29-57 ppm, Ta=1,8-3,5 ppm). Rikligt med fenokrister av klinopyroxen, olivin och plagioklas finns i de provtagna bergarterna. Sammansättningen på klinopyroxenfenokristerna varierar mellan augit och diopsid. Ändledsberäkningar visar på Tschermakssubstitution och ägerin i alla analyserade kristaller; något jadeitled kunde inte identifieras. Olivin varierar mellan Fo_{79} och Fo_{88}. Labradorit (An_{50} till An_{70}) är den vanligaste plagioklasen i de undersökta tunnslipen. De identifierade opaka faserna utgörs av ilmenit och kromspinell. Tvåelementdiagram med huvudelementen plottade mot MgO ger två olika fraktioneringstrender: klinopyroxen och olivin kontrollerar bergartsvariationen vid MgO-halter >8 vikts%,. Efter det att plagioklasfraktioneringen börjat vid 8 vikts% MgO, kontrolleras variationen av klinopyroxen, olivin och plagioklas. Den starka anrikningen på Nb och Ta ($[Nb/La]_n$=1,1-1,4; $[Ta/La]_n$=1,2-1,5) liksom utarmningen på K och Pb ($[K/La]_n$=0,6-0,9; $[Pb/La]_n$=0,1-0,5) är karakteristisk för mafiska HIMU- magmor. Förhållandet La/Nb (0,72-0,88) mot Ba/Nb (3,4-5,3) indikerar att de sköldbyggande lavorna från Gran Canaria kan ha bildats från en källbergart, som består av en blandning av tre mantelkomponenter: HIMU, DMM och EM. En måttlig anrikning av lätta jämfört med tunga REE ($[La/Lu]_n$=8,9-12,1) innebär att granat inte utgör någon väsentlig fas i restiten efter magmabildningen. Eftersom bergarterna inte uppvisar några negativa Eu-anomalier är effekten från plagioklasfraktioneringen liten. De erhållna Zr/Y-förhållandena (9,7-11,8) utgör ett argument mot peridotit som den enda magmakällan. Höga Zr/Y förhållanden förklaras enklast med en signifikant granathalt bland residualfaserna. Detta står i motsatsförhållande till REE resultaten. Granatperidotit eller eklogit som källbergart skulle ge upphov till granat bland residualfaserna; de höga Zr/Y-förhållandena är således tvetydiga. En möjlig förklaring skulle kunna vara fraktionering av Zr och Y vid eller före bildningen av källbergarten. Hur klinopyroxen på verkar Zr/Y-förhållandet kunde inte fastställas. Förhållandet ökar långsamt med fraktioneringen. Tillgängliga data tillåter inte en bestämning av det mest primitiva förhållandet. De diskuterade förhållandena tillsammans med låga Ba/Nb- (3,4-5,3) och höga K/La- (217-292) förhållanden indikerar att en enda källbergart, som innehåller varierande mängder granat inte är tänkbar. Den allmänna utarmningen av K, Rb och Ba, som framgår av det normaliserade multielement diagrammet, tyder på att återförd oceanskorpa är involverad i genesen. Eftersom tidigare publicerade εNd värden (3,9-5,8) är högre än förväntat för en icke utarmad OIB, föreslås att källmaterialet har påverkats markant av utarmad litosfär. Resultaten implicerar att basalterna kommer från en heterogen källbergart. Denna bergart liknar förmodligen återförd, subducerad eklogitisk oceankrusta (<2 Ga), som har blandats in i eller reagerat med den omgivande peridotitiska manteln. Den primära magman bildades i granatens stabilitetsfält. Man har tidigare föreslagit att den var pikritisk och bildats vid temperaturer mellan 1500 och 1600°C och 3GPa. Efter det att magman förflyttats till reservoirer, påverkade fraktionering av klinopyroxen, olivin och små mängder plagioklas dess sammansättning. Kristallisationen av fenokristfaserna skedde vid hög temperatur och lågt tryck. Beräknade temperaturer, dock associerade med stora fel, indikerar att olivinfenokristerna kristalliserade vid temperaturer mellan 1172 och 1218°C.

Nyckelord: Gran Canaria, shield-building lavas, Güigüi Formation

Romina Peetz, Department of Geology, GeoBiosphere Science Centre, Lund University, Sölvegatan 12, SE-223 62 Lund, Sweden. E-mail: romina.peetz@student.uni-halle.de

1 Introduction

Ocean islands and the connected intraplate volcanism play an important role in understanding the dynamics of mantle magnetism. This magnetism is also important for understanding the contributions from the various mantle components of ocean islands. It is generally believed that ocean island basalt (OIB) is derived from mantle plumes, whose roots can be traced to the lower mantle and even to the D″ layer at the core/mantle boundary. This was shown for example by Williams and Garnero, 1996; Revenough and Meyer, 1997; van der Hilst et al., 1997; Williams et al.,1998; Albarède and van der Hilst, 1999; Kellog et al., 1999; Montelli et al. 2004 and Gurenko et al., 2006.

The volcanism of the Canary Archipelago is derived from a mantle plume (Geldmacher et al., 2001, 2005). According to geophysical observations the Canary Islands are underlain by a low velocity anomaly consistent with the presence of a mantle plume (Hoernle et al., 1995; Goes et al., 1999; Montelli et al., 2004; Gurenko et al., 2006). The Canary plume is one of the few that has been traced to the core-mantle boundary (Montelli et al., 2004). Hence, the Canary Islands are well qualified for a study encompassing mantle magmatism and its corresponding geochemistry.

Since Gran Canaria is a classical example of Atlantic plume-related magmatism and has a rather long magmatic history of 15 Ma (Morgan, 1981; Gurenko et al. 1996), it is well suited for a study. Furthermore, Gran Canaria encompasses almost the whole spectrum of rocks that are found on ocean islands. The shield-building rocks include tholeiitic through transitional to alkaline basalt as well as picrite and basanite. At the shield stage, most of the magma forming the island is produced. In addition, it is suggested that these magmas originate from the central parts of the mantle plume and thus provide direct information of deep-seated mantle processes (Gurenko et al., 1996). Hence, in this thesis particular attention is paid to the lower Miocene shield-building lavas. The studied rocks come from a well exposed section in Barranco de Tasártico.

Geochemical signatures of shield-building lavas on Gran Canaria indicate that the mafic magmas require a HIMU-type mantle source, which is generally attributed to recycled <2 Ga old oceanic crust (e.g. Sun, 1980; Hoernle et al., 1991; Hoernle and Tilton, 1991; Marcantonio et al., 1995; Thirlwall, 1997; Hoernle, 1998, Widom et al., 1999; Simonsen et al., 2000; Geldmacher et al., 2001, 2005; Gurenko et al., 2006).

Primary magmas are believed to be picritic. They formed within the garnet stability field between 1500 and 1600°C at pressures of 3 GPa (Schmincke, 1982; Hoernle and Schmincke, 1993a; Heuschkel, 1996; Gurenko et al., 1996, 1998). The whole rock composition of magmas erupted during the shield-building stage is characterized by fractional crystallization of clinopyroxene, olivine, spinel group minerals and minor fractionation of plagioclase. Thus, the shield-building rocks feature a geochemical signature that is different from that of the primary magma.

The present master thesis comprises a comprehensive set of data that includes whole rock major and trace element compositions and mineral chemistry of phenocryst, opaque and alteration phases. The focus of the thesis is to characterise the shield-building lavas from Barranco de Tasártico. The following items will be especially considered:

- The characterization includes a petrographic description, chemical composition, classification and variation of the lavas.
- The phenocryst phases will be defined. Differentiation trends will be discussed in terms of phenocryst compositions.
- The discussion will also include possible source rocks for the magma.
- The results of this investigation will include a comparison of earlier published compositions of rocks from the sampled group with the new data obtained here.

2 Geological setting

2.1 The Canary Islands

The Canary Islands are a group of 7 major volcanic islands which extend for almost 500 kilometres roughly east west 100 kilometres off Northwest Africa (Schmincke, 1982).

According to Carracedo et al. (2002) the archipelago to which the Canary Islands belong to can be found on the oceanic Jurassic lithosphere in the central eastern Atlantic Ocean. Therefore, the archipelago lies close to the African continental margin (Mitchell et al., 2002). Due to the fact that the islands show a general east to west age progression of the main island shield-building phases, ranging from 20 Ma in Fuerteventura in the east to 1-2 Ma in El Hierro in the west, an origin related to hotspot volcanism has been suggested by Carracedo et al. (1998). This however has been a long-standing discussion which resulted in a large number of theories about how the islands may have formed.

2.1.1 The origin of the Canary Islands

Among these theories is the already mentioned mantle plume hypothesis which was developed by Morgan in 1971 on Wilson's hotspot concept (Anguita & Hernán, 2000). In accordance with this theory the Canary Islands were proposed to represent the surface expression of a column of fertile material which had risen through the mantle (Anguita and Hernán, 2000). However, several features of the Canary Islands can not be explained using this hypothesis. These feature include (1) the long volcanic history of the Canary

chain and of individual islands in the chain, (2) low melt productivity for individual islands and the whole island chain, (3) large chemical diversity of volcanics and plutonics, (4) the temporal and spatial variation in geochemistry and (5) multiple cycles of volcanism on the islands (Hoernle and Schmincke, 1993). Some of these peculiarities can of course be explained, as pointed out by Hoernle and Schmincke (1993), by the extreme tectonic setting of the islands. The Canaries are underlain by a very old ocean crust formed in the Jurassic and thus, the mechanical boundary layer will have a maximum thickness for oceanic lithosphere. This thick mechanical boundary layer is one possible explanation for the low Canarian melt production (Hoernle and Schmincke, 1993). According to Anguita and Hernán (2000) an ad hoc hotspot model that would for instance include a plume with low melting rates under a quasi-stationary African plate would produce islands with long volcanic histories, low productivity and complex geochemistry. Nevertheless, there are features that cannot be explained by using the plume model. Therefore other hypotheses were developed including a new plume model of the "blob type", which has been introduced by Hoernle and Schmincke in 1993. In conformity with that model (Fig. 1) the plume beneath the Canary Islands consists of upwelling blobs of deeper mantle separated by entrained asthenosphere (Hoernle and Schmincke, 1993). This blob model would feature a dipping conduit which would underlie the whole Canaries archipelago and would dip to the west due to the African plate viscous drag (Anguita and Hernán, 2000). Even though, this theory would offer solutions to several problems such as (1) higher melt production and growth rates during the submarine evolution of the volcano than during the later subaerial history (Hoernle and Schmincke, 1993), (2) multiple cycles of volcanism on the islands and (3) the geochemical diversity, it also implies several drawbacks. These are mainly based on the geometry of the model. In reference to Anguita and Hernán (2000) these drawbacks include the fact that it is not clear whether the African plate could produce an effective viscous drag since it could be altogether stationary or moving

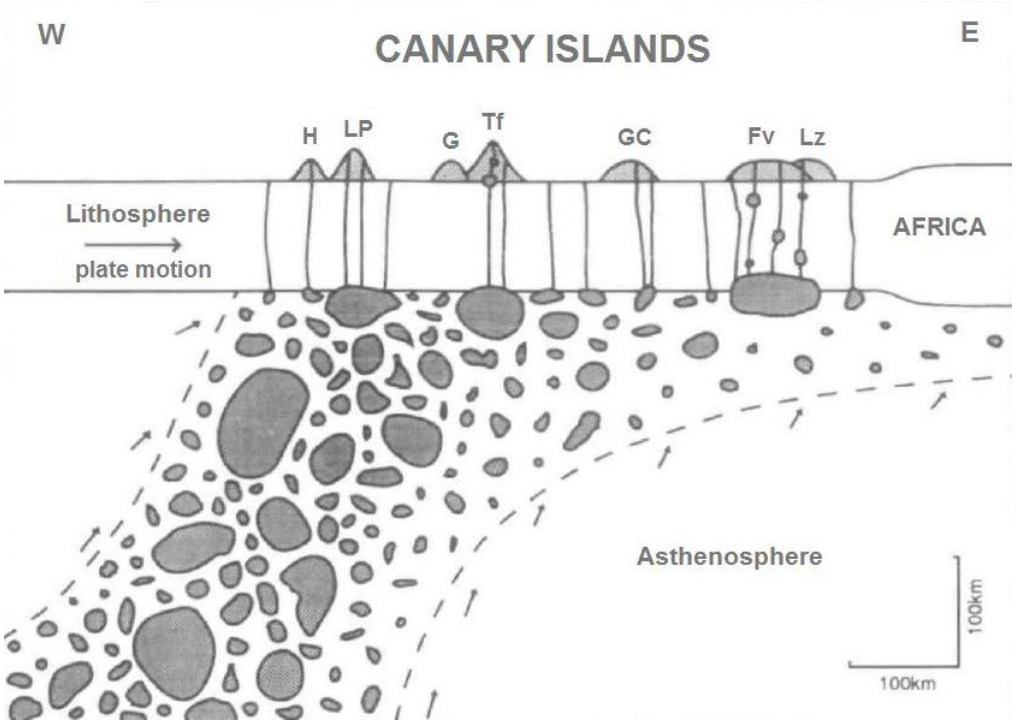

Fig. 1: A 'blob-type' model after Hoernle and Schmincke (1993) to explain volcanism in the Canary Islands. The plume beneath the Canary Islands consists of upwelling blobs (HIMU-like) of deeper mantle separated by entrained asthenosphere (DM). At depth (> 200 km), the plume consists of a cylindrical conduit; in the upper asthenosphere, it spreads out along the base of the lithosphere, preferentially in the direction of mantle flow. As is indicated by the arrows, entrainment of asthenosphere can occur at the margins of the plume, primarily along the downstream margin. The largest concentration of material from depth will be above the centre of the upwelling conduit, at present between the islands of La Palma and Tenerife. A volcano's highest growth rate (shield stage) will occur while it is over the centre of the conduit. Movement of the lithosphere over the center of the conduit is responsible for the age progression of the chain. A cycle of volcanism on an island reflects melting of a blob. If the blob is sufficiently large, tholeiitic melts can be formed in its interior even if it is at the downstream end of the plume head. Volcanic hiatuses reflect intervals when cooler, entrained shallow asthenosphere is in the melting zone beneath an island. As the lithosphere moves the volcano away from the centre of the conduit, fewer hot blobs will reach the melting zone beneath the volcano and thus volcanic hiatuses will become more frequent and also possibly longer in duration. Abbreviations: H—Hierro, LP—La Palma, G—La Gomera, Tf—Tenerife, GC—Gran Canaria, F—Fuerteventura, Lz—Lanzarote. Hoernle and Schmincke (1993).

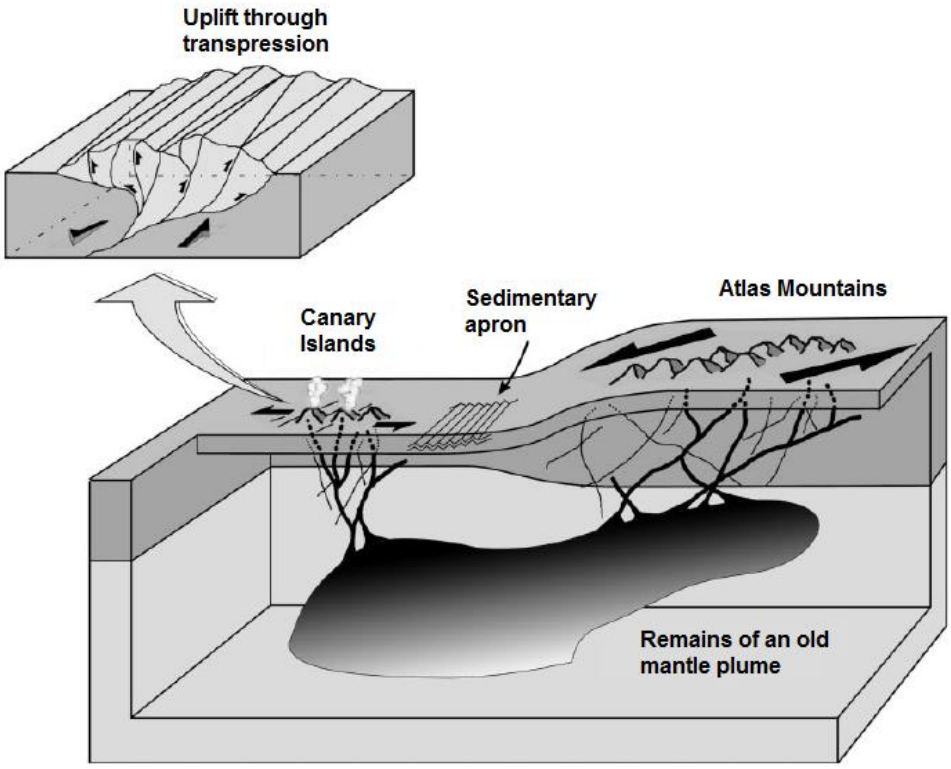

Fig. 2: Cartoon illustrating the unifying hypothesis on the origin of the Canary Islands. The inset represents a transpressive phase, when the islands would emerge as flower structures (modified after Anguita and Hernán, 2000).

too slow to do so. Furthermore, the blobs should reach the western-most islands first, and thus these should be the oldest ones (Anguita and Hernán, 2000).

The fact that the origin of the Canary Islands could not completely been explained by the hotspot models gave rise to other hypotheses introduced by other authors. Anguita and Hernán (1975) for instance tried to explain the origin of the islands using a propagating fracture model, which was also supported by Robertson and Stillman (1979). This hypothesis tries to explain the origin of the Canaries on the basis of a geological connection with the Atlas Mountains. Based on Anguita and Hernán (1975, 2000) a leaky megashear connects both areas with each other. The volcanism in the Canary Islands would thus be a result of decompression melting during a tensional phase. In contrast to that quiescent periods would ensue during compression phases (Anguita and Hernán, 2000). Though this hypothesis offers a solution to the problems of the cyclic structure of the Canaries, it could not explain the uplift of the insular blocks (Anguita and Hernán, 2000). Furthermore, it is rather implausible that stretching of the lithosphere without an underlying thermal source could generate as much magma as it took to build the Canary Islands chain (Anguita and Hernán, 2000).

Given that the propagating fracture model was causing new problems in the explanation of the origin of the Canary Islands Anguita and Hernán modified their hypothesis and introduced a unifying model in 2000 (Fig. 2). However, this model still includes the geological connection between the Canaries and the Atlas Mountains but introduces a thermal anomaly that underlies North Africa, the Canary Islands, and western and central Europe as a possible thermal source that could be able to produce enough magma.

According to Anguita and Hernán (2000) this anomaly has the shape of a sheet and is the remnant of a "fossil" plume that does not enter the lower mantle. This putative plume was designated by Oyarzun et al. (1997) as the Central Atlantic Plume. It is also known as the Central Atlantic Magmatic Province (Marzoli et al., 1999). Oyarzun et al. (1997) and Moreira et al. (1999) suggested that the remnants of the plume head, which is now detected under the African margin and Europe, migrated eastward and that magmatism occurred whenever an efficient fracture system provided a pathway (Anguita and Hernán, 2000). In conjunction with that the magmatism on the Canaries could be explained through the tapping of the thermal anomaly by the fractures inherited from the Mesozoic failed arm rift (Anguita and Hernán, 2000). Even though, this hypothesis gathers solutions for many problems concerning the origin of the Canary Islands such as (1) long magmatic history of the Canary Islands chain, (2) geochemical diversity, (3) multi-Ma gaps in magmatic activity, (4) diminishing volume of magmas erupted in each successive cycle and (5) the uplift of the islands it cannot explain all peculiarities.

Further models use compressive tectonics (Araña and Ortiz, 1986, 1991) or Cenozoic extensional structures (Fúster, 1975) to explain the magmatism

and the uplift of the islands but none of the mentioned models could offer solutions to all issues concerning the origin of the Canary Islands. It is therefore easily conceivable that more models relating to that matter will be introduced and that the already existing models will be modified in future.

2.1.2. Magma types on the Canary Islands

Based on the fact that the islands show a multiphase episodic magmatic evolution the magma types that appear on the islands show a large variety.

In general the shield-building magma type is a saturated to moderately saturated alkali basalt with local tholeiites (Schmincke, 1982). The development of highly differentiated magma columns resulted in (quartz)-trachyte in the eastern and phonolitic plugs in the central and western islands. This primarily happened during the waning stages (Schmincke, 1982). On Gran Canaria and Tenerife major differentiated magma reservoirs culminated in large caldera-forming ash eruptions. Furthermore, inhibit the evolution and partial emptying of such large differentiated zoned magma columns the surface eruption of basaltic magmas (Schmincke, 1982). Since the magmatic evolution on the Canary Islands is generally divided into multiphase cycles, the first phase of volcanism is separated from the second volcanic phase by a volcanic hiatus that can last for several million years. The second volcanic cycle is broadly characterised by more alkaline and silica undersaturated volcanic rocks. According to Schmincke (1982) late stage basanites and nephelinites occur and are locally nodule bearing, of small volume and only slightly fractionated. Furthermore, haüyne phonolites and tephrites appear.

During the second volcanic cycle the rate of magma generation generally declines and the degree of partial melting decreases. This is probably a result of the thicker lithospheric crust which depresses the magma-generating zones into deeper parts of the mantle.

2.2 Gran Canaria

Gran Canaria is the third largest of the Canarian Islands and is located in the centre of the archipelago. The subaerial evolution of Gran Canaria can be divided into three main magmatic cycles: Cycle I or the Old Cycle (Miocene, 14.5 Ma-8.5 Ma), Cycle II or the Roque Nublo Cycle (Pliocene 5.5 Ma-2.7 Ma) and Cycle III or the Recent Cycle (Plio-Quarternary, 2.9 Ma-Present) (Schmincke, 1976; McDougall and Schmincke, 1976; Araña and Carracedo, 1978; ITGE, 1992; Pérez-Torrado et al., 1995).

The first of these cycles comprises the shield-building phase including the formation of the mainly basaltic shield volcano with several eruptive centres. According to Schmincke (1976) it was subsequently covered with numerous trachytic, rhyolitic and phonolitic lava flows, as well as ignimbrites. The emission of these was accompanied by the collapse of the island which led to the formation of a caldera which was later filled by volcanics of similar composition (Schmincke, 1976) and intruded by a trachyte cone sheet swarm, syenite bodies and phonolite dikes (McDougall and Schmincke, 1976).
After that an erosional hiatus that lasted more than three million years occurred. During that period the formation of thick clastic debris fans interbedded with marine sedimentary rocks ensued.

The second magmatic cycle which is better known as the Roque Nublo Cycle is mainly characterised by the occurrence of alkalic silica-undersaturated basanites, ankaramites, tephrites, haüyne phonolites, essexites and breccia sheets composed of rocks of similar compositions (McDougall and Schmincke, 1976). The lavas of this cycle mainly filled the deep valleys that were built during the previous erosional interval.

A second erosional interval separates the Roque Nublo Cycle from the following Recent Cycle which is also known as the Post Roque Nublo Cycle. During that cycle mainly olivine nephelinite, melilite nephelinite and basanite flows erupted from many local centres (McDougall and Schmincke, 1976). Rothe mentions in his Geological guide (2008) that due to new age determinations an independency of the Post Roque Nublo Cycle is rather questionable. This thesis is based on a paper by Guillou et al. (2004) that presents new ages for both the Roque Nublo and the Post Roque Nublo Cycle which clearly indicates coactivity between 3.7 Ma and 2.9 Ma.

2.2.1 Shield-building mafic rocks

The oldest rocks on Gran Canaria are characterised by the mafic volcanic rocks of the Güigüi and Hogarzales Formations. Due to the fact that those rocks were the main subject of this thesis there will be a closer look upon these in chapter 2.3, so they will only be mentioned shortly here. In general the oldest volcanics are made up of basaltic flows which mainly occur in the Güigüi Formation. By contrast the rocks of the younger Hogarzales Formation are of trachybasaltic composition.

2.2.2 Mogán and Fataga Groups

The basaltic rocks of the shield-building phase are followed by more felsic Miocene rocks belonging to the Mogán and Fataga Groups. In general the older rocks of these felsic volcanics are dominated by ignimbrites, whereas the younger ones are characterised by lava flows. According to Rothe (2008) their eruption can be associated with the Tejeda Caldera. Furthermore these two groups are subdivided by the Montaña Horno Formation, which can be interpreted as an interstratified unit.
In conformity with McDougall and Schmincke (1976) the rocks of the Mogán Group overlie the shield-

building basaltic lavas of the Güigüi and Hogarzales Formations conformably and are made up of silica-undersaturated to saturated trachytic to rhyolitic lavas and ignimbrites. They occur mainly in the south and south-west of the island but can also be found in the north of San Lorenzo.

2.2.2.1 Mogán Group

Formerly the Mogán Group was described as a formation which can be divided into two parts. According to Schmincke (1976) the lower part of the formation is made up of about seven soda rhyolite lava flows and ignimbrites, whereas the upper parts are composed of about nine comenditic and pantelleritic ignimbrite units. Nowadays the Mogán Group is subdivided into three formations: Lower, Middle and Upper Mogán Formation (Schmincke, 1990; v. d. Bogaard and Schmincke, 1998, Rothe, 2008). According to Rothe (2008) they are composed of ignimbrites and several lava flows. Their composition ranges between rhyolitic, peralkaline, comenditic and pantelleritic. The main phenocrysts are clinopyroxene, aegirin and anorthoclase. Locally amphibole can occur as a phenocryst phase. Rothe (2008) furthermore mentions that many of the ignimbrites show a zoning with vitreous welded basis areas which pass into unwelded pumice tuffs. Furthermore, laminar flow-structures indicate an eruption centre west of the recent geometric island centre (Schmincke and Swanson, 1967a).

2.2.2.2 Montaña Horno Formation

As already mentioned earlier, the Mogán and the Fataga Group are separated by the Montaña Horno Formation. According to McDougall and Schmincke (1976) this formation comprises rhyolitic, trachytic and trachyphonolitic tuffs, flows, ignimbrites and intrusions which filled the collapse structure of the Tejeda volcano. Therefore, the main features of this formation are the colourful tuffs that mark the caldera rim. The tuffs are mainly green, red and yellow coloured and unconsolidated pumices. The colourful appearance of the rocks is a result of hydrothermal processes and oxidation. At the locality Fuente de los Azulejos several xenolithes of basalt can be found within the tuffs. In connection to that ignimbrites and smaller intrusions can be found as well. Rothe (2008) furthermore states that the pantelleritic and comenditic composition of the rocks can be parallelised with the Upper Mogán Formation.

2.2.2.3 Fataga Group

The silica undersaturated trachytic to phonolitic ignimbrites and lavas of the Fataga Group generally lie conformably on the silica oversaturated volcanics of the Mogán Group (McDougall and Schmincke, 1976). These rocks occur not only in the southeastern and southern parts of Gran Canaria, they also appear in the north and northwest, where they locally underlie the marine sediments of the Las Palmas Formation. According to Rothe (2008) the magmatic activity of the Fataga Group is rather long in comparison to the Mogán Group. It therefore lasted from 12.43 Ma to 9.85 Ma. The proposed main eruptive centre of the phonolites is the highly diked area between Cruz Grande, Chira and Ayacata. This area also contains the most abundant phonolite tuffs (Schmincke, 1976).

In general the rocks of the Fataga Group comprise ignimbrites, which can reach a thickness of about 500 metres and several phonolitic lava flows. According to Schmincke (1976) and Rothe (2008) these rocks are very thick columnar, platy and partly brecciated. The main phenocryst phases that occur are anorthoclase, amphibole or phlogopite and Fe-/Ti-oxide phenocrysts in the ignimbrites and anorthoclases and Na-rich clinopyroxene in the lava flows (Schmincke, 1976). Just like the Mogán Group the Fataga Group is subdivided into three formations: the Lower, Middle and Upper Fataga Formation.

2.2.3 Las Palmas Formation

After the formation of the Fataga Group, a period of intensive erosion that lasted from 9 Ma till 5 Ma set in. This period marks the time interval between the formation of the mainly phonolitic Fataga Group and the initiation of the following volcanism of the Roque Nublo Group. During that time clastic material was deposited foremost in the northeast and south of Gran Canaria. In accordance with Rothe (2008), the sediments of the Las Palmas Formation can be interpreted as alluvial cones. The material forming these alluvial cones comes mostly from the centre of the island. The cones are not only made up of material coming from the Fataga Group, such as phonolitic conglomerates and fanglomerates, but also consists of debris flows and marine carbonates.

The marine sand-layers occasionally show cross-bedding, ripple marks or bioturbated structures. Furthermore Rothe (2008) states that the deposits can be divided into an upper and a lower part. Whereas the lower parts mainly consist of phonolitic boulders the upper parts predominantly contain basalt, tephrite and even material that belongs to the Roque Nublo Group. There is a controversial discussion on how these alluvial cones may have formed. Whereas Klug (1968) proposed a formation during high sea levels, Lietz (1973) suggested a formation mainly controlled by climate during times of low sea levels.

In accordance with Rothe (2008) the main difference between the southern and the northern parts of the Las Palmas Formation is the occurrence of marine carbonates. Whereas they commonly occur in the northern parts they do not occur at all in the southern parts of the formation.

2.2.4 Roque Nublo Group

The rocks originated during the second magmatic cycle form the Roque Nublo Group. According to

Pérez-Torrado et al. (1995) the first eruptive episodes of the Roque Nublo volcanism is characterised by the eruption of basanitic and nephelinitic magmas. These furthermore gave rise to the formation of strombolian cones and associated lavas located in the meridional zones of Gran Canaria following a NW-SE-directed tectonic lineation (Pérez-Torrado et al., 1995). Due to the fact that the rocks of the Roque Nublo Group can also be found in the centre of the island, it can be suggested that the volcanic activity later moved towards the centre of the island where it stayed until the end of the Roque Nublo Cycle. Whereas the rocks of the first eruptive period were basanitic and nephelinitic, the eruptive rocks of the later period were mainly basanite, alkali basalt and trachyt-phonolite. In addition to that breccia-type pyroclastic flows erupted. The eruption of these took place at the same time as the intrusion of endogenous domes of phonolitic composition (Pérez-Torrado et al., 1995).

Even though, both Rothe (2008) and Pérez-Torrado et al. (1995) state that the breccia-type pyroclastic flows are the most outstanding feature of the Roque Nublo Group, they also both mention that the eruptive mechanisms have been disputed. Fuster et al. (1968) therefore proposed that these eruptions originated from Saint Vincent-type plinian eruptions, whereas Anguita (1972, 1973) stated that the eruptions must have been high-intensity vulcanian eruptions (Pérez-Torrado et al., 1995). Furthermore, Pérez-Torrado (1990, 1992) interpreted these pyroclastic flows as unwelded lithic-rich ignimbrites and suggested a vulcanian phreatomagmatic eruption as the origin.

The main feature of the Roque Nublo ignimbrites is, as pointed out by Pérez-Torrado et al. (1995), that they are highly indurated. Brey and Schmincke (1980) attributed this fact to postemplacement diagenetic alteration processes caused by the percolation of meteoric water through these deposits, producing the dissolution of the original vitric fragments to be subsequently replaced by zeolites (Pérez-Torrado et al., 1995).

The Roque Nublo Group comprises 6 formations: the El Tablero Formation, the Riscos de Chapín Formation, the Tirajana Formation, the Rincón de Tejeda Formation, the Ayacata Formation and the Tenteniguada Formation. The intrusion of the phonolites of the Tenteniguada Formation occurred contemporary with the first episodes of the third cycle.

2.2.5 Post Roque-Nublo Group

The third cycle of volcanic activity is represented by the Post Roque Nublo Group. The rocks of this group cover most of the northeastern parts of Gran Canaria. According to McDougall and Schmincke (1976) they comprise strongly alkaline and silica-undersaturated lavas and pyroclastics whose composition range from olivine nephelinite and melilite nephelinite to basanite. It is suggested that the Post Roque Nublo Group shows a subdivision into three formations which can be distinguished by the state of erosion, alteration of rocks, erosional unconformities and petrographic and chemical criteria (Schmincke, 1976).

The oldest of these rocks, belonging to the Llanos de la Pez Formation, are characterised by an approximately 200 metre thick series of olivine-nephelinite lavas. Schmincke (1976) points out that these lavas have generally only olivine phenocrysts. Phenocrysts of clinopyroxene and nepheline are rather scarce. An erosional unconformity, as well as several metres of tuffaceous sandstone separates the Llanos de la Pez lavas from those of the Roque Nublo Group. The duration of this volcanic activity is estimated to have lasted from 3.0 Ma to 2.2 Ma (v. d. Bogaard and Schmincke, 1998).

The nephelinite rocks of the Llanos de la Pez Formation are unconformably overlain by the pegmatoid and lherzolite nodule bearing haüyne melilite nephelinite flows and dikes of the Los Pechos Formation (Schmincke, 1976). Rothe (2008) furthermore states that the younger volcanic constructions of Montaña Arucas and Montaña Cardones in the northwest of Gran Canaria also belong to the Los Pechos Formation. They are mainly made up of tephrites that contain rather large haüyne crystals. The cinders and lavas that occur in the northwest of Gran Canaria can also be linked to this formation. The rocks of the Los Pechos formation are 1.8 Ma to 1.5 Ma old (Rothe, 2008).

The youngest volcanoes on Gran Canaria which are generally very well preserved belong to the La Calderilla Formation. Rothe (2008) suggests that they are maars because their construction is the result of a phreatomagmatic activity in connection with ground- or surface water. In regards of petrography these rocks can be described as basanites (Schmincke, 1990). Further features of this formation include pyroclastics which contain xenolithes of the bedrock of the volcanoes, cross bedding and concentric bands of tuffs with lapilli (Rothe, 2008).

2.3 Güigüi and Hogarzales Formations

Due to the fact that the samples which were analysed within the framework of this thesis belong to the Güigüi and Hogarzales Formations there should be a closer look upon these.

In general, as it was already pointed out, the rocks of the Güigüi and Hogarzales Formations represent the oldest shield-building rocks on Gran Canaria. These oldest rocks are a series of basalt flows of 1000 meter total thickness above sea level which crop out mainly in the west and southwestern parts of the island (Schmincke, 1976). According to Schmincke (1976) their formation is the result of a complex shield volcano which was fed from several eruptive centres. There are three main eruptive centres proposed by Schmincke (1976): one near Agaëte in the northwest, one south of San Nicolás in the Güigüi Grande area and the third one in the southeastern part of the island near Ãgüimes. The position of these eruptive centres

were mainly pointed out from the interpretation of positive gravity anomalies (Bosshard and MacFarlane, 1970), concentration of dyke swarms, abundance of pyroclastics and primary dips of the flows (Schmincke, 1976). Due to the fact that at least two of these three volcanoes collapsed, the eruption centres can nowadays be found offshore.

According to McDougall and Schmincke (1976) the Güigüi Formation is characterised by thin basaltic flows of mildly alkaline to transitional composition which are locally cut by dykes. They generally range from aphyric to porphyric lavas. The main phenocryst phases occurring in the lavas are olivine and clinopyroxene. Plagioclase phenocrysts can be found as well but their appearance is scarcer compared to that of olivine and clinopyroxene. Whereas the occurring pyroxenes are generally fresh and without any signs of alteration, the olivine phenocrysts are usually highly altered.

The basalts can also contain vesicles and amygdules that are filled with chalcedon, zeolith or calcite.

The basalts of the Güigüi Formation can be differentiated from these of the younger Hogarzales Formation by four main features. First of all the petrographic composition is slightly different: picrites and ankaramites commonly occur in the Güigüi Formation. Furthermore the rocks of the Güigüi Formation are highly altered and show a higher abundance of dykes (Rothe, 2008). In addition to that the Güigüi lavas show a more mafic composition than the Hogarzales lavas. Due to that the lava beds in the Güigüi Formation are generally thicker than in the Hogarzales Formation.

Even though, McDougall and Schmincke (1976) stated that the erosional interval between the two formations is rather short and probably did not last longer than 0.5 Ma the basalts of the Hogarzales Formation overlie the basalts of the Güigüi Formation with a strong unconformity. This conformity is made up of several metres of palagonite tuffs and fanglomerates in the southwest of Gran Canaria followed by a trachybasaltic series (Schmincke, 1968a and 1976). From Montaña Tirma in the west to Barranco de Mogán these trachybasaltic flows increase in thickness from 100 metres to several 100 metres in the Barranco de Güigüi. According to McDougall and Schmincke (1976) the Hogarzales lavas dip gently in the same direction as the underlying lavas and consist of hawaiite and mugearite. In accordance to that Schmincke (1976) stated that these lavas are in general fine-grained, thick and brecciated. Locally olivine phyric and plagioclase phyric basalts appear. Thereby the plagioclase phyric basalts make up the lower parts of the Hogarzales Formation which are underlain by the olivine phyric basalts (Schmincke, 1976).

The ages proposed for the Güigüi Formation range from 14.3 Ma to 13.9 Ma while these for the Hogarzales vary between 14.1 Ma and 14.04 Ma (Boogard and Schmincke, 1998).

The K-Ar ages provided by McDougall and Schmincke (1976) for lavas from the two formations collectively indicate that the shield-building dominantly basaltic rocks of Gran Canaria were erupted over a rather short interval of time. The duration of the subaerial main shield-building volcanism is unlikely to have exceeded about 0,5 m.y. (McDougall and Schmincke, 1976).

3 Sample description

The samples were collected along the road GC 204 (Appendix A) in March 2009. The sampling was carried from the stratigraphical lower parts and then progressed towards the stratigraphical higher parts of the formation. The original plan envisioned a sampling every 5 metres in altitude but could not be accomplished due to the strong alteration and oxidation of the rocks. Therefore, it was necessary to pay attention that only rocks with little or no signs of alteration or oxidation were sampled because the processes of alteration and oxidation could have changed the original chemical composition of the rocks. Thus, the intervals between the sample locations can vary between 5 and 20 metres in altitude. Furthermore, dykes that occur frequently along the road were not included in the sampling process.

In general, the sampled areas showed the same main features. For the most parts the sampled areas had a more massif appearance than the strongly altered and oxidised adjoining rocks surrounding them. The massif layers had an average thickness of one to five metres and were characterized by a strongly altered and oxidized top part (Fig. 3). The thickness of the altered top part varied between one to five metres.

The sampled rocks were mainly medium to dark grey basalts, which are characterised by a fine grained and homogeneous matrix. The main phenocryst phases are olivine, pyroxene and plagioclase. Whereas olivine and pyroxene could be found in all samples, plagioclase occurs rather scarce and could only be identified as phenocrysts in the samples RH 3-6, RH 8-9, RH 11, RH 13 and RH 20. Nevertheless, plagioclase probably makes up a huge part of the matrix although it is too small in size to be identified macroscopically.

In general, it could be observed that even though the olivine phenocrysts appear to be slightly smaller than the pyroxene, they occur more frequently (Fig. 4). Thus, they represent the main phenocryst phase in the rocks. Simply in the samples RH 4-6 and RH 9 the main phenocryst phase is represented by pyroxene whilst olivine appears only scarce in these samples. The size of the olivine and of the pyroxene can vary between one millimetre and one centimetre.

The main feature of olivine is a general strong or complete alteration. When strongly altered it usually gets a reddish brown reaction rim made up of iddingsite. Iddingsite also occurs along cracks and fractures within the minerals. In the state of complete

Fig. 3: Sampled area in location RH 14. The picture displays two magma layers that are separated by a strongly altered area that is oxidised at the boundary to the upper magma layer. Furthermore, the picture shows that the sampled areas were more massif than the altered areas due to the higher abundance of vesicles and amygdules in the altered areas.

alteration the olivine is entirely transformed into reddish brown iddingsite. Fresh olivine could not be identified in any of the samples. Compared to the strongly altered olivine, pyroxene and plagioclase were mainly fresh and showed no signs of alteration. Since the pyroxene features a dark green colour the discussed pyroxene could be diopside or augite. This, however, can only be ascertained by the microscopic examination of the thin sections and the EDS analysis of the phenocrysts.

The plagioclase phenocrysts usually have a columnar appearance and can reach a maximum size of about seven millimetres. Whereas the plagioclase commonly shows a glomeroporphyritic structure, the aggregation of olivine and pyroxene is rather uncommon. All phenocryst phases occur as euhedral to subhedral crystals and their fragments.

The rocks of the sampled areas contain vesicles and amygdules. It is quite obvious that vesicles and amygdules appear more often in the alterated surrounding rocks than in the fresher parts. In addition, the abundance and the size of the vesicles and amygdules increase upwards in the stratigraphy. Therefore, a lot more vesicles and amygdules could be found in the higher parts than in the lower parts. Both structures imply that bubbles of gas expanded during the solidification of the rock. The amygdules are analogues of chalcedony, calcite or zeolite. Chalcedony and calcite are the secondary minerals that occurr most often. Calcite can easily be distinguished from chalcedony by its typical cleavage planes (Fig. 5). Zeolites appeared rather scarce and were characterised by their low hardness.

Another striking feature is the red colour of some parts of the rocks, which is the result of oxidation. These oxidised areas commonly occurred at the boundary between two magma layers. Therefore, the top of the lower layer was oxidised due to the high temperatures that appeared in connection with the eruption of the new magma layer. Similar to the increasing abundance of vesicles and amygdules upwards in the stratigraphy, it could also be observed

Fig. 4: Basalt at location RH 17. The basalt is characterised by a medium grey matrix and contains phenocrysts of olivine and pyroxene. The olivine phenocrysts are smaller than the pyroxene ones and are almost completely altered to iddingsite. Due to the fact that location RH 17 is rather high in stratigraphy, the basalt contains a high abundance of vesicles.

Fig. 5: Secondary calcite minerals close to location RH 13. The mineral can easily be distinguished due to the typical cleavage planes that do not occur in chalcedony. Furthermore, the hardness of chalcedony compared to calcite is higher.

that the amount of the oxidised areas increased in the same direction. As already mentioned these parts were not considered during sampling because oxidation might have changed the chemical composition.

Furthermore, it could be observed that the sampled rocks are magnetic. Thus, it can be assumed that the rocks contain magnetite as an opaque phase. Whether this is true can only be ascertained by the microscopic

examination of the thin sections and the EDS analysis.

4 Methods

4.1 Sample preparation

The samples were prepared for chemical analysis and the production of thin sections at the Geological Department in Lund.

To make sure that neither oxidation nor alteration affects the chemical analyses the altered and oxidised areas of the samples were removed. At the same time ten chosen samples were prepared for the production of thin sections. After removing the oxidised and altered parts of the samples, the rocks were crushed using a jaw breaker. The crushed samples were milled in a disk mill (Type T 100 from Siebtechnik GmbH Mülheim-Ruhr).

4.2 Thin sections

For the microscopic and chemical analysis of the phenocryst phases, ten polished thin sections were prepared at the Martin-Luther University Halle-Wittenberg. The thin sections come from the samples RH 2, RH 3, RH 6, RH 8, RH 10, RH 11, RH 13, RH 16, RH 18 and RH 20. Since the thin sections were also used to study the phenocryst phases, the samples with the highest abundances and the freshest phenocryst phases were selected.

For the microscopic analysis in reflected and transmitted light a Nikon Eclipse E400 POL microscope was used. In addition, pictures of the thin sections were taken using a Nikon Alphaphot YS 2 and a Nikon digital camera.

4.3 Major and trace elements

For the chemical analysis of the major elements the samples were analysed by Elisabeth Thun in Hamburg using fluorescent X-ray analysis. The trace elements were analysed at AcmeLab in Vancouver, Canada with inductively-coupled plasma mass-spectrometry (ICP-MS) following a Lithium metaborate/ tetraborate fusion and nitric acid dissolution.

4.4 Scanning electron microscope (SEM)

As already mentioned, the phenocryst phases were analysed in a scanning electron microscope (SEM) at Geological Department in Lund. The SEM is a Hitachi S-3400 N. An Oxford INCA energy dispersive X-ray system (EDS) is fitted to the SEM. The thin sections were coated with carbon to ensure electrical conductivity. For this purpose the Cressington Carbon Coater 108 Carbon/A from Cressington Scientific Instruments Limited was used. Since the sampled rocks are basaltic volcanics with a relatively high porosity, a rather thick carbon coating was necessary. A too thin carbon coating causes electric charging and thus influences the measurements. The phenocryst phases were meassured at 15 kV and a working distance of ten millimeters. The chemical analyses and data correction were performed by the computer program INCA Suite Version 4.06 from Oxford Instruments Analytical Limited.

4.5 Illustration

The obtained data was digitalized by using several programs. Bivariate diagrams were plotted using Microsoft Office Excel, whereas ternary diagrams were plotted using GCDkit for Win 2.3. In addition, Corel Draw 12 was used to digitalize several diagrams.

5 Results

5.1 Description of the thin sections

As already mentioned in chapter 4, ten thin sections were prepared for the microscopic analysis. In general, the matrix of all samples is similar. It is extremely fine grained and thus its exact mineral composition could not be conclusively determined even under biggest magnification. However, since the fact that the analysed rock is basalt, it can be assumed that the minerals that define the matrix are mainly olivine, pyroxene and plagioclase. From these three minerals only plagioclase was large enough to be explicitly identified in the thin sections RH 8, RH 13, RH 16, RH 18 and RH 20. Additionally, pyroxene crystals can be distinguished from plagioclase. Thus, the pyroxene crystals are coloured. In contrast, the plagioclase crystals feature a first-order grey as interference colour. In addition, small apatite needles could be identified in the matrix.

Furthermore, the matrix features a partially vitreous appearance but no flow structures could be identified within it. The vitreous appearance of the matrix is the result of a small amount of fine grained glass in the matrix. The glass features a green or murky brown colour.

All thin sections have a high abundance of phenocryst phases in common. Of these olivine, pyroxene and plagioclase are the three major ones. Whereas pyroxene phenocrysts can be found in all analysed thin sections, the occurrence of plagioclase is rather scarce. Thus, plagioclase phenocrysts only appeared in the thin sections RH3, RH6, RH 8, RH 11, RH 13 and RH 20. Additionally, it must be mentioned that plagioclase represents the dominant phenocryst phase in the thin sections RH 6 and RH 8. For the rest of the thin sections the main phenocryst phase is olivine, which is found in all thin sections except RH 6.

For the most part all phenocrysts are euhedral or at least represent fragments of euhedral phenocrysts. In contrast the occurrence of subhedral phenocrysts is rather scarce. Furthermore, the phenocrysts tend to form glomerocrysts. Whereas the plagioclase phenocrysts commonly form agglomerates, the

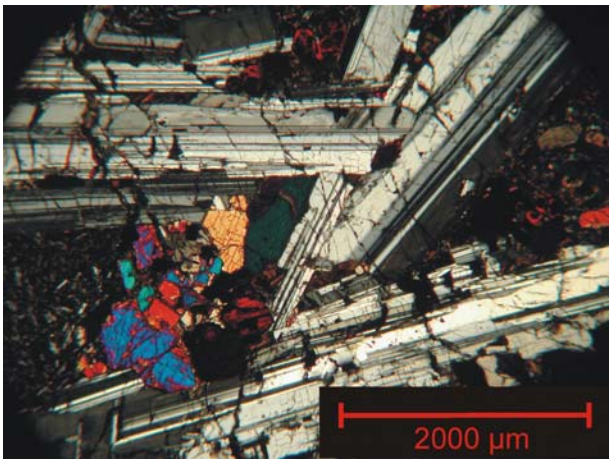

Fig. 6: Glomerocryst in the thin section RH 8 containing all three phenocryst phases: plagioclase as the biggest of the phases, pyroxene and completely altered olivine. The pyroxene shows typical second order interference colours, whereas the olivine and plagioclase crystals show low interference colours.

pyroxene and olivine phenocrysts rarely do so. Nevertheless, in the thin sections RH 8 and RH 20 glomerocrysts made up of all three phenocryst phases could be identified (Fig. 6).

The olivine phenocrysts occur in two different varieties. It is possible to distinguish strongly altered from completely altered olivine (Fig. 7). The strongly altered olivine crystals are mainly colourless in plane polarized light but show a reddish brown reaction rim of iddingsite. In addition to the iddingsite rim, iddingsite occurs along the cracks within the minerals. According to Phillips and Griffen (1981), lack of colour in plane polarized light indicates magnesium-rich olivines. This, however, can only be confirmed by a chemical analysis, which will be performed in the SEM (chapter 5.4). Completely altered olivine has a reddish brown colour in plane polarized light and mostly also features a reaction rim in a lighter red colour. None of the varieties are pleochroitic. In addition, it must be mentioned that only the larger phenocrysts can be separated into completely and strongly altered olivine; smaller phenocrysts are always completely altered to iddingsite in all thin sections. According to Phillips and Griffen (1981), the alteration of olivine to iddingsite is most characteristic for oxidation and weathering in volcanic rocks. Even though, iddingsite appears optically homogenous, with high refractive index and extreme birefringence, it is a fine-grained aggregate containing goethite and some combination of smectite (montmorillonite), chlorite, silica, calcite, talc and periclase (Phillips and Griffen, 1981).

Under crossed polarized light the olivine phenocrysts show common interference colours of second order. In contrast to that lower interference colours occur as well, for instance in thin section RH 16.

Furthermore, MacKenzie and Guilford (1981) also state that second-order interference colours in olivine indicate that the present olivine is magnesium-rich, because iron-rich olivine usually shows third-order interference colours. Conclusive evidence of the olivine composition comes from the presented chemical data (chapter. 5.4.2).

In addition, it should be mentioned that the interference colour of completely altered olivines is masked by the dark-red to brown colour of iddingsite.

The phenocrysts do not show a cleavage but it is stated that the relatively poor cleavage of olivine can usually not be seen in thin section. (Nesse, 1991). In contrast, the olivine grains in the thin sections display a distinctive irregular fracture pattern.

Even though, Phillips and Griffen (1981), state that olivine in volcanic rocks commonly shows a normal zoning this cannot be confirmed for the present olivine phenocrysts. However, the lack of zoning is a result of the strong alteration of the minerals. Furthermore, no twinning could be identified.

Whereas the olivine phenocrysts could be split into two varieties due to their grade of alteration, the pyroxene phenocrysts occur only as relatively fresh

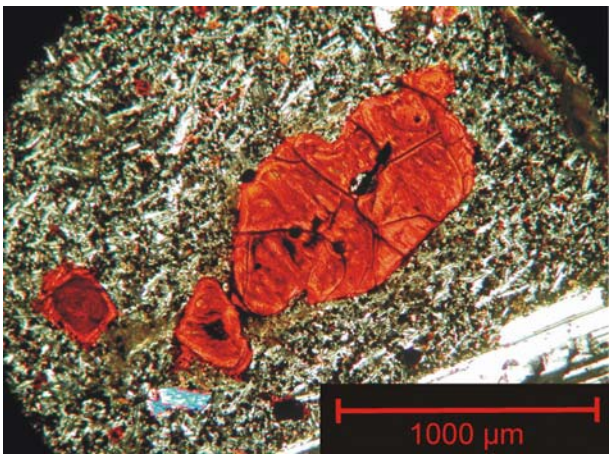

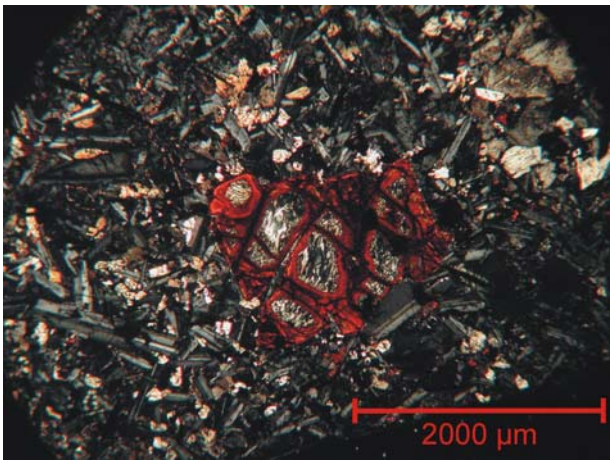

Fig. 7: The two variations of olivine: the left side shows a completely altered olivine in thin section RH 8 and the picture on the right side shows a strongly altered olivine glomerocrysts in thin section RH 3. The reddish iddingsite rim around the olivine crystaly is easily seen.

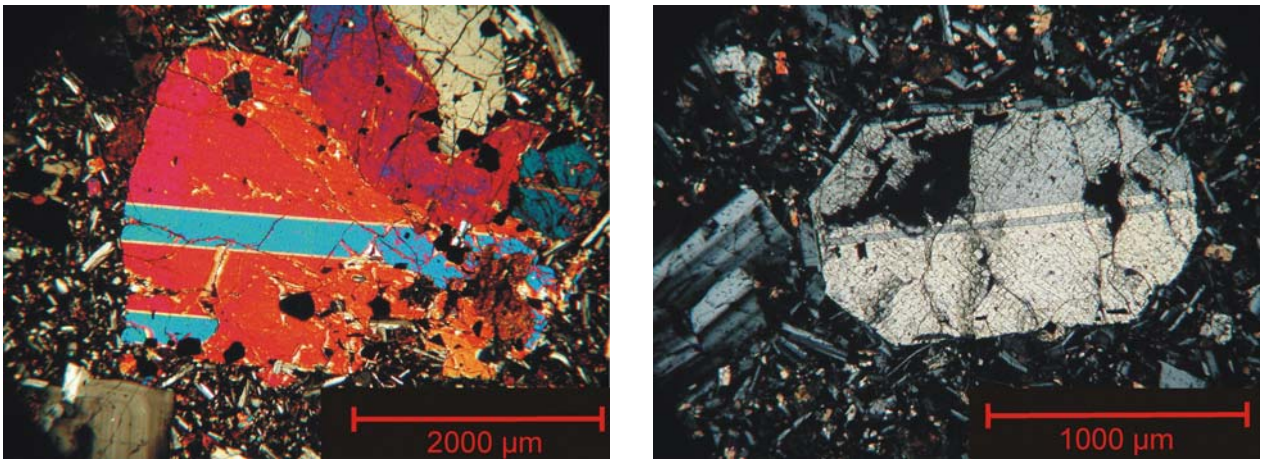

Fig. 8: Example of pyroxene crystals showing different interference colours. The pyroxene on the left features a bright second-order interference colour. The pyroxene on the right side shows an interference colour of lower order. Both phenocrysts are found in thin section RH 6 and show simple twinning.

crystals that show no sign of alteration. They generally represent a colourless to neutral pale grey colour in plane polarized light and are not pleochroitic. The pyroxene phenocrysts show a rather high relief similar to olivine. Another common feature for olivine and the pyroxene is the appearance of the interference colours. Therefore, pyroxene generally shows an interference colour of second order. Interference colours of a lower order could also be found but occurred scarcer (Fig. 8).

The main feature that distinguishes pyroxene from olivine apart from alteration is cleavage, which could be identified in all thin sections. The measured angles between the cleavage directions are characteristic for pyroxene. Furthermore, in contrast to olivine the pyroxene tends to be zoned. The main zoning is a oscillatory zoning but sector zoning ("hour glass zoning") could also be found in the thin sections RH 10 and RH 13 (Fig. 9). It can be assumed that the zoning displays different chemical compositions. According to MacKenzie, Donaldson and Guilford (1982) the opposite sectors have an identical chemical composition, whereas adjacent ones differ in composition. However, the exact compositions are obtained in combination with the analysis of the phenocrysts using the EDS and will be discussed later (chapter 5.4.1).

Another striking feature about the zoning of pyroxene is that zoned phenocrysts generally feature an interference colour of lower order. Furthermore, the pyroxene commonly shows a simple twinning (Fig. 8).

The third phenocryst phase that occurs in the thin sections is, as already mentioned, plagioclase. In plane polarised light the phenocrysts are generally colourless. The relief of the plagioclase is low in comparison to those of pyroxene and olivine. Furthermore, their lath-shaped appearance is striking. In crossed polarised light, the plagioclase phenocrysts show typical interference colours of low order. First-order grey is characteristic for plagioclase according to Phillips and Griffen (1981). Furthermore, the polysynthetic normal twinning according to the albite law could be observed in all phenocrysts. The only exceptions to this are the small plagioclase grains that belong to the matrix. Furthermore, simple parallel

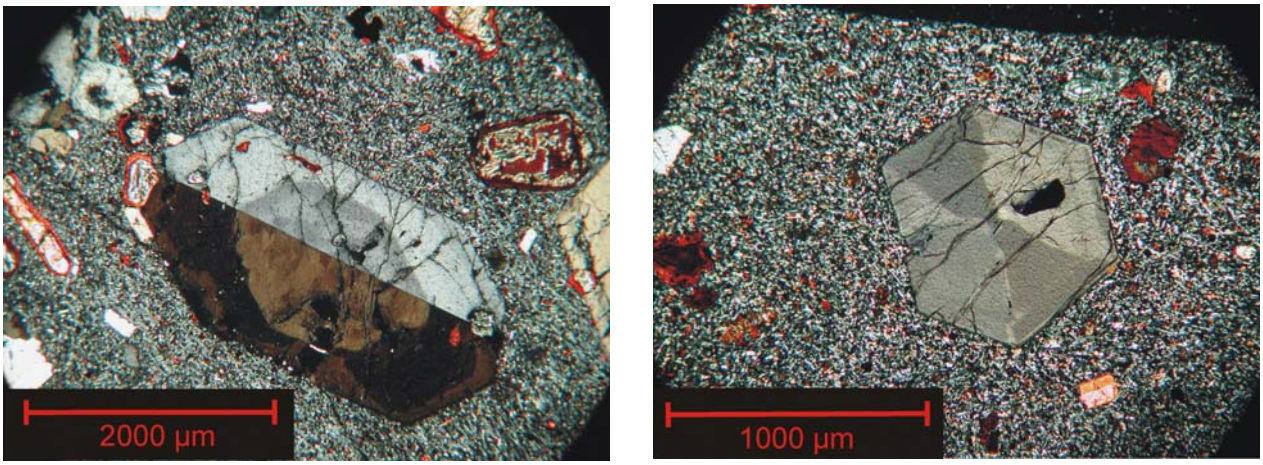

Fig. 9: Different kinds of zoning in pyroxene phenocrysts. The left pyroxene is featuring an oscillatory zoning (thin section RH 16) and the right pyroxene is showing a sector or "hour glass zoning" (thin section RH 10). Both phenocrysts also show low-order interference colours.

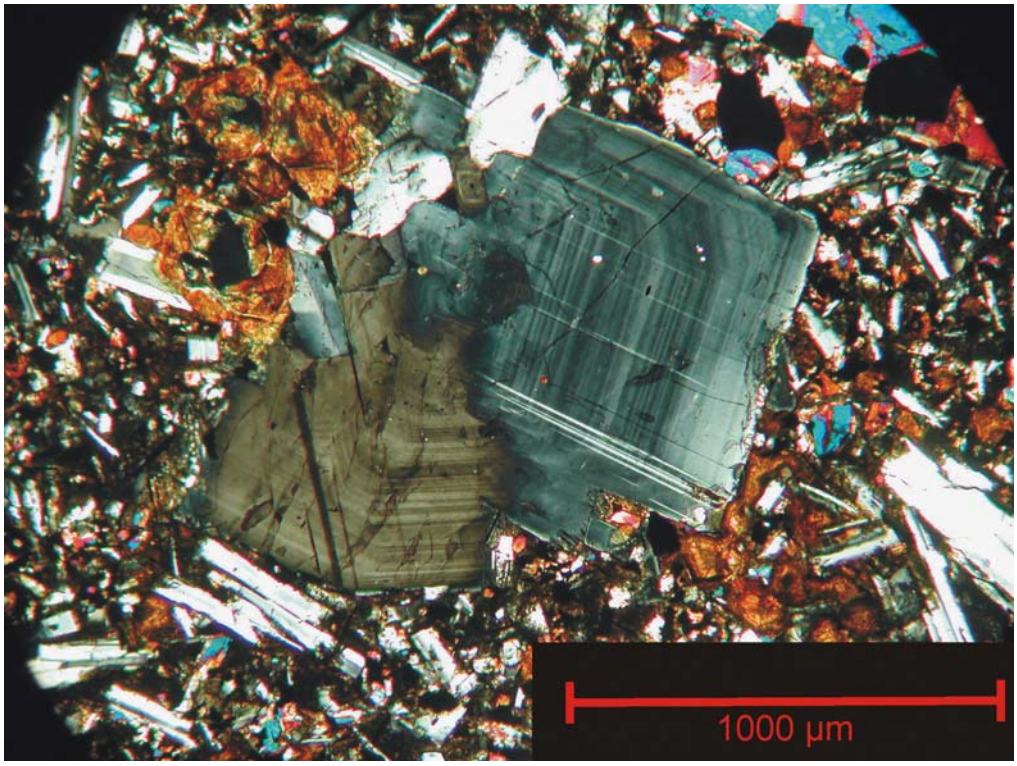

Fig. 10: Oscillatory zoned plagioclase phenocryst in crossed polarised light in thin section RH 6. The zoning indicates disequilibrium conditions during crystallization history of the phenocryst.

Carlsbad twinning is common, even though simple twinning occurs rarer than in the pyroxene phenocrysts. Similar to the pyroxene the plagioclase tends to show an oscillatory zoning (Fig. 10) which according to Phillips and Griffen (1981) suggests a considerable disequilibrium during crystallization. These oscillatory zonings can best be seen in the thin sections RH 6 and RH 8. In addition, the plagioclase phenocrysts are generally fresh and do not show any signs of alteration.

Other special features that could be observed during the microscopic observations of the thin sections were the occurrence of vesicles and pseudomorphs after olivine. Whereas the vesicles only appeared in the thin sections RH 8 and RH 16, the pseudomorphs occur commonly in almost all thin sections except RH 3 and RH 8. In general, the pseudomorphs occur as two different varieties (Fig. 11). Both varieties have a rim with a radial structure but only one of them contains spherulitic structures in the core of the mineral. Due to the appearance of the minerals, it can be assumed that both minerals are hydrothermal alteration products of olivine. Hence, the discussed minerals could be serpentine. Whether this assumption is right or not can only be confirmed after the chemical analysis using the EDS.

Furthermore, opaque phases occur in all the observed thin sections. These minerals commonly

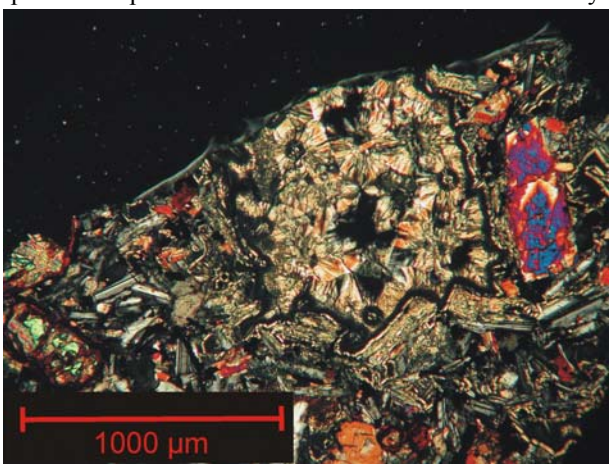

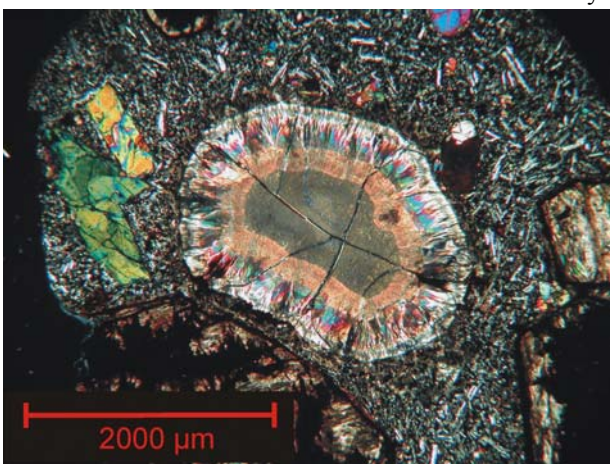

Fig.11: The different variations of pseudomorphs after olivine that appear in the thin sections. The left image represents an pseudomorph with a spherulitic structure (thin section RH 2) and the right picture shows a pseudomorph without the spherulitic structure (thin section RH 18).

appear as small grains in the matrix, but also as bigger crystals. Moreover, the opaque minerals are commonly attached to the borders of the pyroxene and plagioclase phenocrysts.

Due to the fact that all the sampled rocks are magnetic, it can be presumed that the opaque phases contain iron and might therefore be magnetite. Since chemical analyses of older samples from Gran Canaria where reviewed for this thesis it can also be assumed that the opaque phases could be titanium-iron oxides like ilmenite or ulvöspinel. Again the chemical analysis of the minerals performed by EDS will give more exact results for this.

5.2 Major elements

5.2.1 Total alkali versus silica diagrams

The total alkali versus silica diagram was chosen because it is one of the most used and useful classification schemes for volcanic rocks (Rollinson, 1993). Figure 12 shows clearly that all the samples plot in the alkalic field of the diagram. Furthermore, it can be observed that four samples differ significantly from the rest. These samples, RH 3 to RH 6, range between 48.7 wt% and 49.7 wt% SiO_2, whereas the other samples vary between 44.5 wt% and 47.1 wt%. It is suggested that they are more evolved than the others (Table App.3).

In general, fractional crystallization enriches magmas in SiO_2 and depletes them in MgO. Thus, it can be assumed that the degree of fractional crystallization is higher in the magmas with > 48 wt% SiO_2.

In addition, it should be noted that the concentration of the alkalis increases with decreasing degree of partial melting and increasing degree of crystal fractionation. The SiO_2 concentration increases with increasing fractional crystallization and decreasing degree of partial melting.

The normative minerals (chapter 5.2.3) confirm that the discussed four samples are silica-oversaturated; they have normative quartz. This will be discussed in more detail in chapter 5.2.3.

Including the earlier published data (Cousen et al., 1990; Gurenko et al., 2006; Schmincke, 1976 and 1982; Thirlwall et al., 1997), it becomes apparent that the samples from Barranco de Tasártico fit the general trend for the shield-building lavas on Gran Canaria.

If the samples are plotted in the TAS diagram (Le Bas et al., 1986), all the samples plot in the basalt field. Since almost all samples plot between 45 and 52 wt% SiO_2 the samples are classified as basic (Fig. 13). Only three samples have SiO_2 contents less than 45 wt% and are classified as ultrabasic picrobasalt and basanite.

Figure 13 also compares the present data with literature data (Cousen et al., 1990; Gurenko et al., 2006; Schmincke, 1976 and 1982; Thirlwall et al., 1997) clearly demonstrating the similarities. Only a few rocks have so far been classified as picrobasalt, trachybasalt or basaltic andesite among the shield-

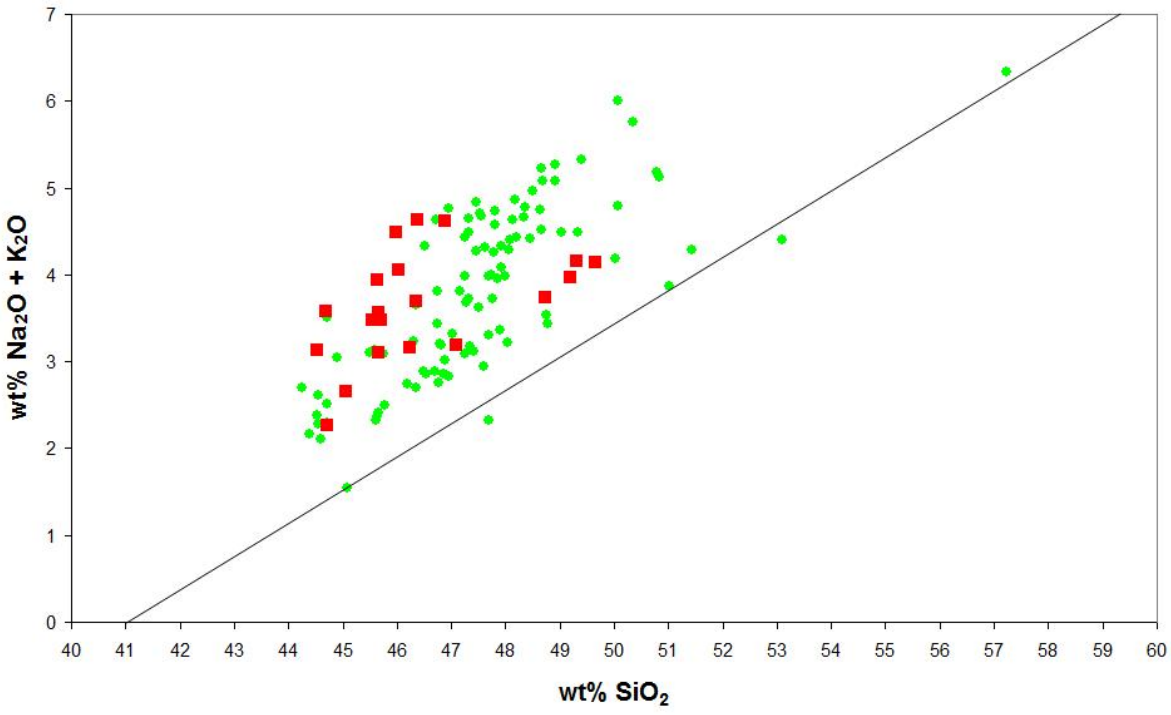

Fig.12: Total alkali versus SiO2 concentration for the shield-building lavas on Gran Canaria. Red squares: Tasartico samples. Green circles: earlier published data (Cousen et al., 1990; Gurenko et al., 2006; Schmincke, 1976 and 1982; Thirlwall et al., 1997). The dividing line between the alkalic and tholeiitic basalt fields is from MacDonald and Katsura (1964).

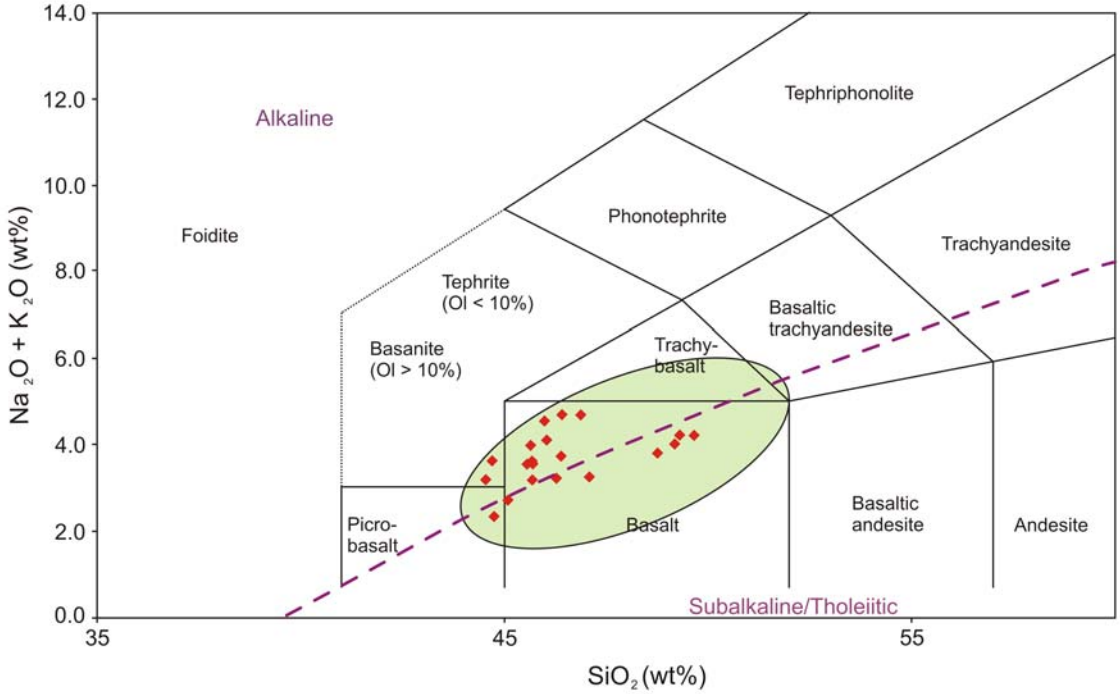

Fig.13: Total alkali versus silica diagram of Le Bas et al. (1986) for the studied samples from Barranco de Tasártico in comparison with earlier published data (Cousen et al., 1990; Gurenko et al., 2006; Schmincke, 1976 and 1982; Thirlwall et al., 1997). Red squares: Tasártico samples. Green ellipse: Plotting area of the earlier published samples. The dashed line separates the alkaline from the subalkaline rocks (Le Bas et al. 1986).

building lavas. Hence, the new data are consistent with the general trend for the shield-building lavas on Gran Canaria.

The purple line in the diagram divides the subalkaline/tholeiitic field from the alkaline field. The studied rocks plot within both fields and can be described as transitional in composition.

According to Rollinson (1993) the TAS diagram is intended for normal, fresh volcanic rocks (suspected cumulate rocks) as well as for altered rocks or rocks that show obvious signs of crystal fractionation. The MgO content is not very high and the rocks are not very differentiated. Thus, the TAS diagram can be used for the studied samples.

5.2.2 Bivariate plots

In general, bivariate plots are used to show variations between samples and to identify trends. In igneous rocks, trends might be the result of either mixing of two different magmas, addition and/or subtraction of a solid phase during contamination or fractional crystallization or addition of melt increments during partial melting (Rollinson, 1993). Given that fractional crystallization is a major process in the evolution of ocean island basalt, it might be assumed to be the main cause for the trends in the variation diagrams.

Again the samples were plotted together with earlier published data (Cousen et al., 1990; Gurenko et al., 2006; Schmincke, 1976 and 1982; Thirlwall et al., 1997) from shield-building lavas from Gran Canaria to find out, whether the present results fit a general trend or to be able to demonstrate appearing variation trends better.

In general, the major elements correlate well with MgO. In addition, MgO represents a more significant evolution parameter in basaltic lavas than SiO_2. Thus, all diagrams for the major elements are plots versus MgO (Table App.3).

Especially the diagrams for Na_2O and Al_2O_3 demonstrate a good correlation between the major elements and MgO. The correlation coefficient can be seen in figure 14.

The rocks show a higher concentration of Al_2O_3 (8.3 wt%-14.6 wt%) than of Na_2O (1.6 wt%-3.3 wt%), but the trend is similar in both diagrams (Fig. 15). Thus, the concentrations of both increase with decreasing MgO contents. According to Rollinson (1993) this could be the result of fractional crystallization. However, different degrees of partial melting could result in the same trend. The comparison with earlier published data (Cousen et al., 1990; Gurenko et al., 2006; Schmincke, 1976 and 1982; Thirlwall et al., 1997) for Gran Canaria displays that the Barranco de Tasártico samples follow the general trend.

Although the trends for both elements suggest a steeper increase for lavas below 8 wt% MgO this cannot clearly be seen due to increasing scatter in these lavas. Even the diagrams that include the earlier published data (Cousen et al., 1990; Gurenko et al.,

	MgO/Al_2O_3	MgO/Na_2O	MgO/K_2O	MgO/P_2O_5
r	-0.941	-0.931	-0.889	-0.924

	MgO	**Al_2O_3**	**Na_2O**	**K_2O**	**P_2O_5**
s	2.791	1.593	0.436	0.2	0.0755
s^2	7.791	2.538	0.19	0.04	0.0057

Fig.14: The upper table displays correlation coefficients (r). The lower Table displays covariance s and variance s^2 for several oxides.

2006; Schmincke, 1976 and 1982; Thirlwall et al., 1997) present only a slight indication of a change in trend.

Figure 15 also shows the bulk compositions plotted together with the average composition of the phenocryst phases. The purple line displays the general trend given by the whole rock composition. The diagrams can be used to display which phenocryst phases might have caused the major element trends when they fractionate. First of all, both diagrams suggest a huge effect of clinopyroxene fractionation. In the case of Na_2O versus MgO the diagram suggests 70% clinopyroxene and 30% olivine. The diagram Al_2O_3 versus MgO suggests almost the same ratio between the fractionating phases (64% clinopyroxene and 36% olivine). Since the scatter and extrapolation are moderate, these result should be reliable. Whether this ratio is consistent with the other diagrams will be shown in this chapter.

In addition, both diagrams indicate that magnesium-rich samples plot on the right side of the line connecting clinopyroxene and plagioclase. Thus, a plagioclase fractionation for those samples can be excluded. After the intersection between the fractionation trend line and the join clinopyroxene-plagioclase fractionation of plagioclase would be possible. However, this should have caused a change in the direction of the fractionation-line. Since this is not the case an effect of plagioclase fractionation on the trends displayed in the two diagrams is insignificant.

The P_2O_5 concentration varies between 0.28 wt% and 0.57 wt%. These values are consistent with earlier published data (Cousen et al., 1990; Gurenko et al., 2006; Schmincke, 1976 and 1982; Thirlwall et al., 1997). The samples from Barranco de Tasártico simply show a general trend, where the P_2O_5 concentration increases with decreasing MgO contents (Fig. 16). Figure 16 also indicates a slightly steeper increase in P_2O_5 for lavas with MgO contents below 7

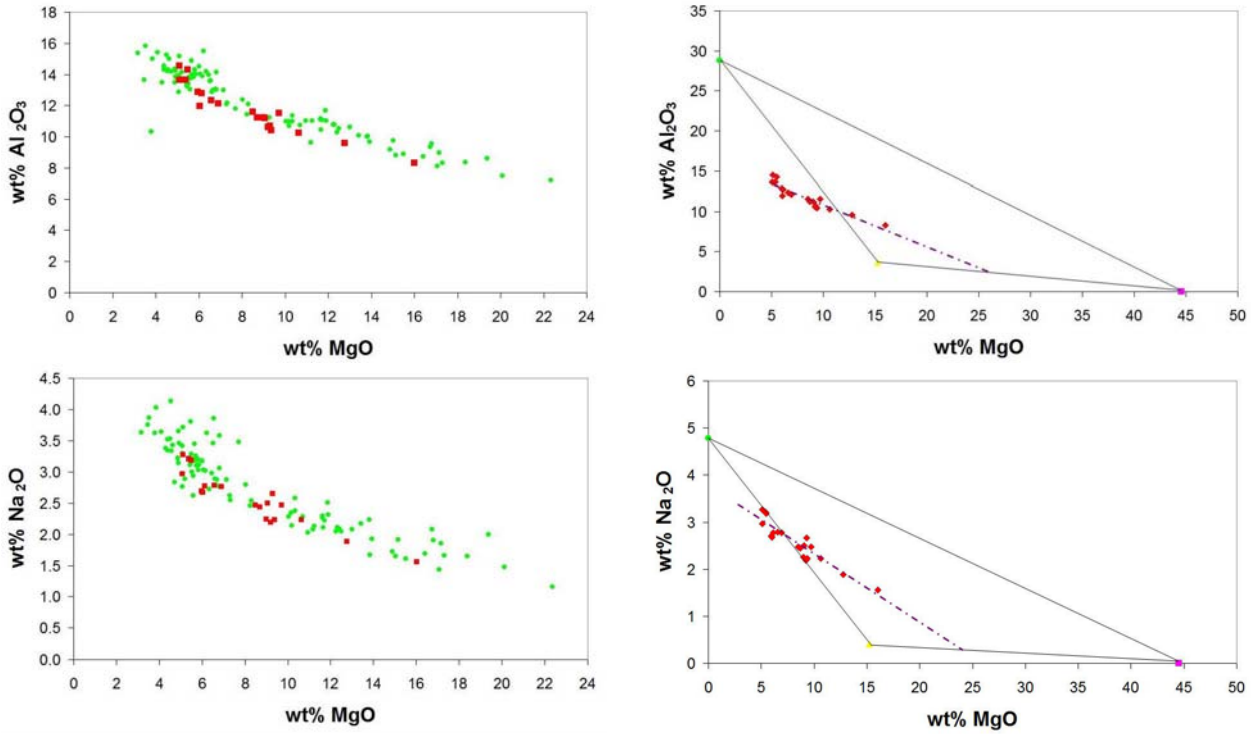

Fig.15: On the left side plots for Al_2O_3 and Na_2O versus MgO are displayed. Red squares: Barranco de Tasártico samples. Green circles: earlier published data (Cousen et al., 1990; Gurenko et al., 2006; Schmincke, 1976 and 1982; Thirlwall et al., 1997). The diagrams on the right side display the whole rock composition as well as the average phenocryst composition for the Tasártico samples. Red squares: Whole rock composition. Pink square: Olivine composition. Yellow triangle: Clinopyroxene composition. Green circle: Plagioclase composition. The purple line displays the general trend given by whole rock composition.

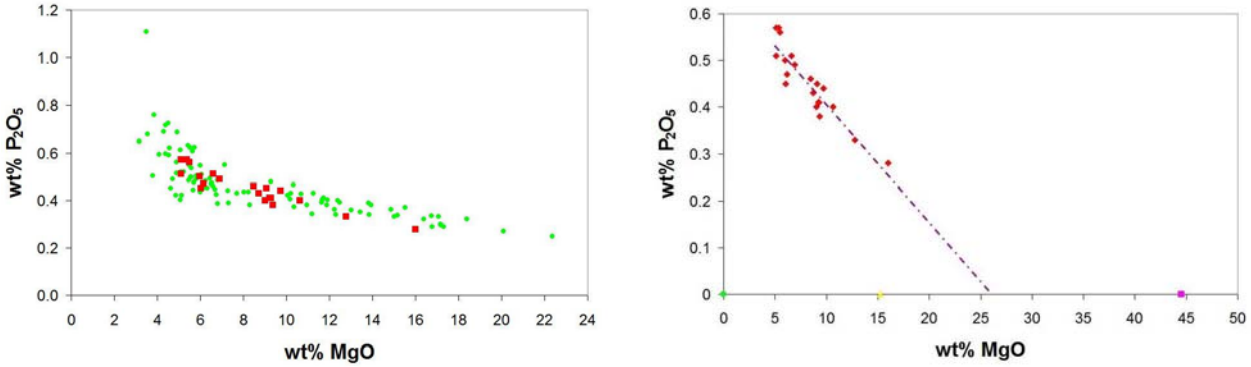

Fig.16: On the left side the plot for P_2O_5 versus MgO is displayed. Red squares: Barranco de Tasártico samples. Green circles: earlier published data (Cousen et al., 1990; Gurenko et al., 2006; Schmincke, 1976 and 1982; Thirlwall et al., 1997). The diagram on the right side displays the whole rock composition as well as the average phenocryst composition for the Barranco de Tasártico samples. Red squares: Whole rock composition. Pink square: Olivine composition. Yellow triangle: Clinopyroxene composition. Green circle: Plagioclase composition. The purple line displays the general trend given by whole rock composition.

wt%. This behaviour of P_2O_5 at MgO contents below 7 wt% MgO becomes even more apparent when the earlier published data (Cousen et al., 1990; Gurenko et al., 2006; Schmincke, 1976 and 1982; Thirlwall et al., 1997) are included in the plots. Hence, the Barranco de Tasártico samples reflect a general trend for P_2O_5 in the shield-building lavas on Gran Canaria.

The steeper increase displayed in the diagram cannot be a result of fractional crystallization of apatite. An explanation for the trend displayed in the diagram could be the onset of plagioclase fractionation, which would result in a slower decrease of the MgO content. The slowed-down change in MgO would not affect the increase in phosphorous and results in the steeper trend for lavas with a MgO content below 7 wt%. Apatite is identified as small needles within the thin sections and thus stayed in the rocks, apatite does not affect the whole rock trend.

Mullen (1983) is of the opinion that the abundance of P_2O_5 is rather related to the degree of partial melting than to fractional crystallization. Thus, the typical high concentration of P_2O_5 in alkalic ocean island rocks is the result of a small amount of partial melting. In addition, it must be noted that apatite starts to crystallize earlier in alkali basalt than in tholeiite.

Figure 16 indicates that the ratio of clinopyroxene and olivine fractionation is 63% to 37%. This ratio is consistent with the ratio calculated for the Al_2O_3 and Na_2O versus MgO diagrams.

The concentrations of K_2O range between 0.7 wt% and 1.4 wt%. In general, K_2O follows the same trend that is displayed by most of the major elements. Hence, the concentration of K_2O increases with decreasing MgO contents due to fractional crystallization (Fig. 17). In addition, the diagram displays a change in trend for lavas with more than 8 wt% MgO.

Figure 17 also displays that the Barranco de Tasártico samples fit into the general trend obtained from earlier published data (Cousen et al., 1990; Gurenko et al., 2006; Schmincke, 1976 and 1982; Thirlwall et al., 1997) for the shield-building lavas on Gran Canaria.

In figure 17 a diagram plotted for the whole rock composition and the average composition of the phenocryst phases is shown. The two purple lines display the two different trends. Thus, the diagram indicates a huge effect not only of olivine and

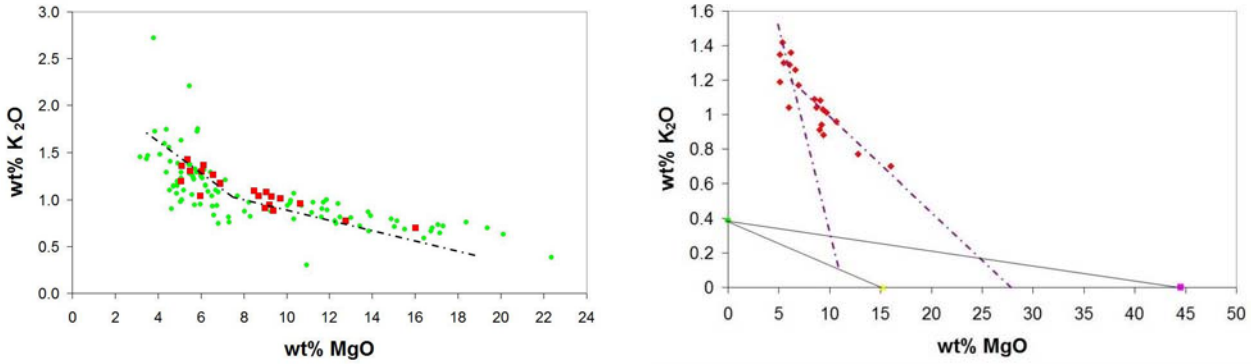

Fig.17: On the left side the plot for K_2O versus MgO is displayed. Red squares: Barranco de Tasártico samples. Green circles: earlier published data (Cousen et al., 1990; Gurenko et al., 2006; Schmincke, 1976 and 1982; Thirlwall et al., 1997). The diagram on the right side displays the whole rock composition as well as the average phenocryst composition for the Barranco de Tasártico samples. Red squares: Whole rock composition. Pink square: Olivine composition. Yellow triangle: Clinopyroxene composition. Green circle: Plagioclase composition. The purple line displays the two trends given by whole rock composition.

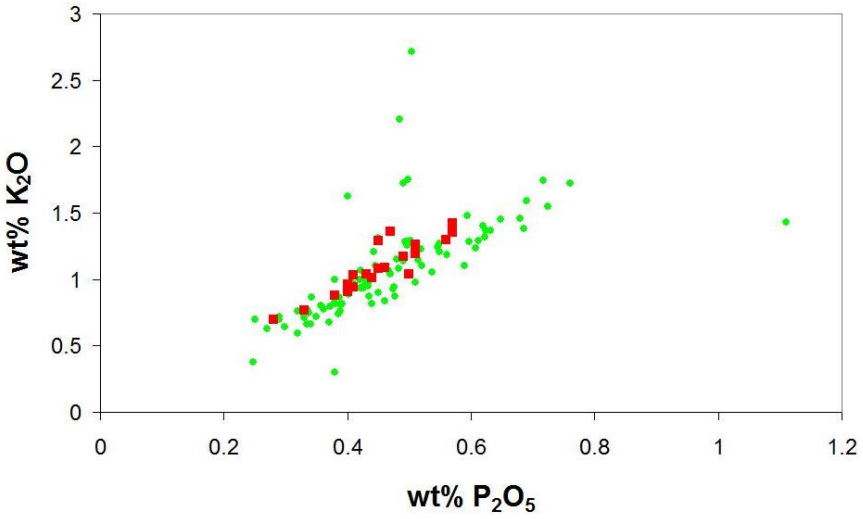

Fig.18: The diagram displays the plot for K_2O versus P_2O_5. Red squares: Barranco de Tasártico samples. Green circles: earlier published data (Cousen et al., 1990; Gurenko et al., 2006; Schmincke, 1976 and 1982; Thirlwall et al., 1997).

clinopyroxene crystallization but at later stages also of plagioclase fractionation. The magma is enriched in potassium during the fractionation of the non-K bearing fractionation minerals olivine, clinopyroxene and later plagioclase.

It is likely that the onset of plagioclase crystallization has an effect on the K_2O trend. Hence, MgO should be fractionated at a lower rate after the onset of plagioclase fractionation. To demonstrate that this conclusion is correct, the diagram K_2O versus P_2O_5 was plotted. Since phosphorium does not occur in olivine, clinopyroxene and plagioclase the trend should not show a change in direction. As can be seen in figure 18 this is the case. Thus, the trend displayed by K_2O is the effect of the crystallization of the three fractionating minerals.

Again the ratio between clinopyroxene and olivine fractionation was calculated. This time the ratio is 57% clinopyroxene and 43% olivine. Since the involved extrapolation is longer than for Al_2O_3 and Na_2O (Fig. 15) and the samples scatter more than in the mentioned diagrams, the error is larger than in the Al_2O_3 and Na_2O versus MgO diagrams. Still the calculated ratio fits into the general trend displayed so far.

An element oxide that correlates well with MgO but does not show any change of trend in TiO_2 (Fig. 19). The concentration of TiO_2 varies between 2.8 wt% and 4.3 wt%. These concentrations are rather high, which is consistent with the normal enrichment in TiO_2 in ocean island basalt (tholeiitic and alkalic) (Wilson, 1991). Like the other trends, the almost linear trend (correlation coefficient can be seen in Fig. 14) displays an increase in the concentration of TiO_2 with decreasing MgO contents, which is also consistent with the general trend for the shield-building lavas on Gran Canaria (Fig. 19). This trend must be largely controlled by the fractional crystallization of clinopyroxene. Since titanium is excluded from olivine fractionation and only gets accommodated in clinopyroxene and titanomagnetite. In addition,

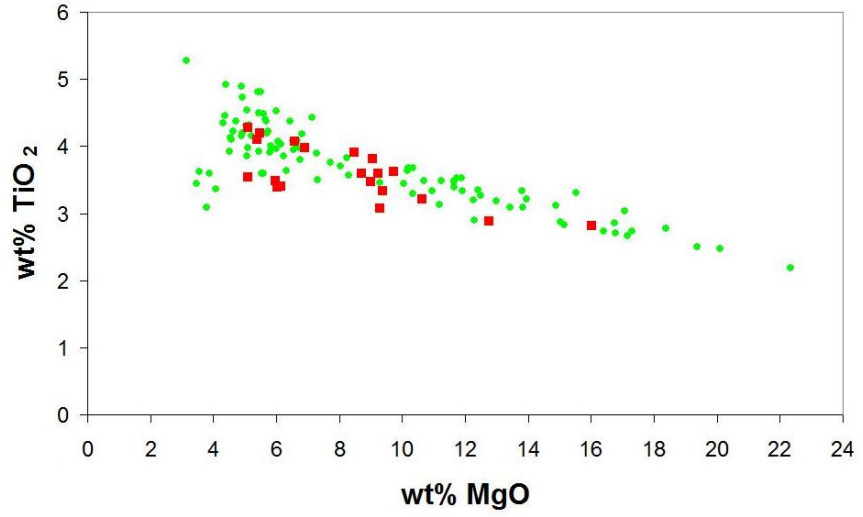

Fig.19: The diagram displays the plot for TiO_2 versus MgO. Red squares: Barranco de Tasártico samples. Green circles: earlier published data (Cousen et al., 1990; Gurenko et al., 2006; Schmincke, 1976 and 1982; Thirlwall et al., 1997).

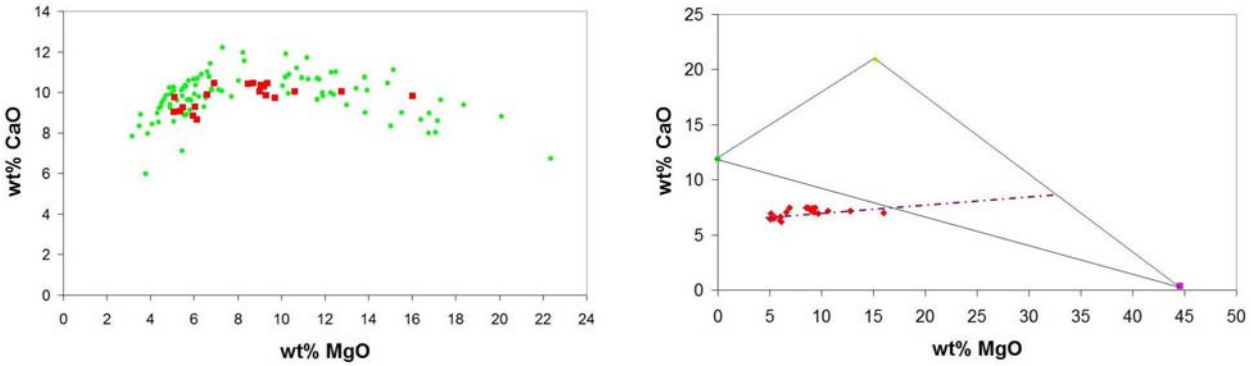

Fig.20: On the left side the plot for CaO versus MgO is displayed. Red squares: Barranco de Tasártico samples. Green circles: earlier published data (Cousen et al., 1990; Gurenko et al., 2006; Schmincke, 1976 and 1982; Thirlwall et al., 1997). The diagram on the right side displays the whole rock composition as well as the average phenocryst composition for the Barranco de Tasártico samples. Red squares: Whole rock composition. Pink square: Olivine composition. Yellow triangle: Clinopyroxene composition. Green circle: Plagioclase composition. The purple line displays the general trend given by whole rock composition.

titanomagnetite does not belong to the phases that crystallize and get removed from the lava. The result is the constant increase in the titanium content displayed in Figure 19.

The trend for CaO versus MgO is different compared to the others (Fig. 20). The concentrations for CaO in the studied samples range between 8.8 wt% and 10.5 wt%. The diagram clearly shows that to the point, where the MgO content has decreased to 8 wt% the CaO concentrations increase with increasing MgO contents. For lavas with MgO content below 8 wt% the trend is almost linear. The earlier published data (Cousen et al., 1990; Gurenko et al., 2006; Schmincke, 1976 and 1982; Thirlwall et al., 1997) from Gran Canaria makes this even more evident. Hence, it becomes apparent that CaO correlates negatively for lavas below 8 wt% MgO (Fig. 20). This can be explained as a result of fractional crystallization. The part of the trend that correlates positively and thus indicates a removal of CaO and MgO from the lava is largely controlled by clinopyroxene and olivine fractionation. Since plagioclase starts to crystallize at 8 wt% MgO, the part of the trend that correlates negatively is controlled by the fractionation of olivine, clinopyroxene and plagioclase.

In addition, a diagram (CaO versus MgO) that includes not only the whole rock compositions but also the average compositions of the phenocryst phases was plotted (Fig. 20). This diagram also suggests a fractionation of all three phases. The ratio between clinopyroxene and olivine fractionation was calculated again. This time the diagram indicates a ratio of 62% clinopyroxene and 38% olivine. Again this ratio (62% clinopyroxene and 38% olivine) is consistent with the ones that were already calculated.

The last diagrams that were plotted are the diagrams for Fe_2O_3 (total iron) and MnO versus MgO. The concentrations of Fe_2O_3 range between 11.6 wt% and 13.5 wt%, whereas the concentrations for MnO vary between 0.14 wt% and 0.24 wt%.

Even though the concentrations for both differ much from each other the plots display similar trends (Fig. 21). It is apparent that the abundance of both increases for lavas below 8 wt% MgO. According to Mullen (1983) MnO is partitioned into olivine as well as into clinopyroxene. In addition, olivine that is removed by fractionation, removes more MnO from the magma the more fayalitic it becomes (Mullen, 1983). Even though Mullen (1983) mentions that the main portion of MnO is removed by clinopyroxene, it must be noted that this depends on the ratio of olivine and clinopyroxene fractionation. Although manganese

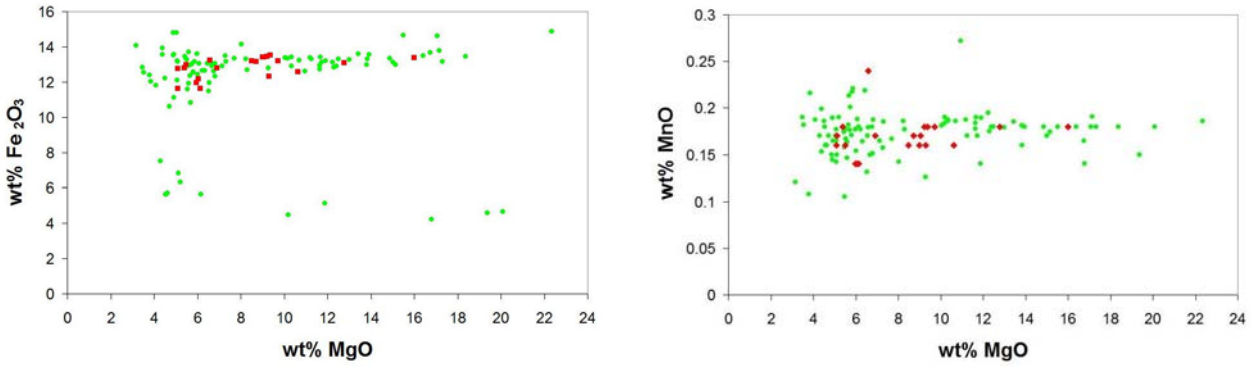

Fig.21: On the left side the plot for Fe_2O_3 versus MgO is displayed. On the right side the plot for MnO versus MgO is shown. Red squares: Barranco de Tasártico samples. Green circles: earlier published data (Cousen et al., 1990; Gurenko et al., 2006; Schmincke, 1976 and 1982; Thirlwall et al., 1997). whole rock composition.

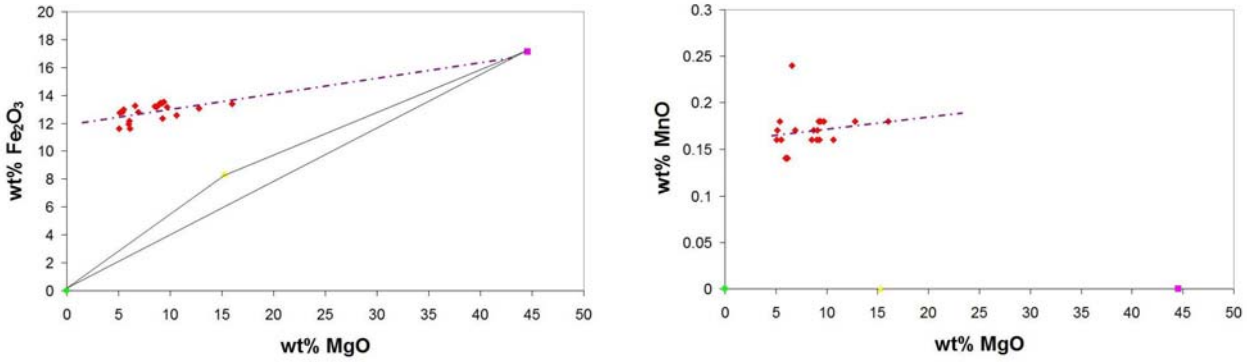

Fig.22: On the left side the plot for Fe2O3 versus MgO is displayed. The diagram on the right side shows the plot for MnO versus MgO. The diagrams display the whole rock composition as well as the average phenocryst composition for the Barranco de Tasártico samples. Red squares: Whole rock composition. Pink square: Olivine composition. Yellow triangle: Clinopyroxene composition. Green circle: Plagioclase composition. The purple line displays the general trend given by whole rock composition.

preferentially enters the M2 position of clinopyroxene, it also enters the smaller M1-M2 position in olivine but to a lesser degree. Thus, olivine can be the major controlling factor of manganese fractionation only if much more olivine fractionates than clinopyroxene. However, this can be excluded since the calculated clinopyroxene:olivine ratios clearly demonstrate that more clinopyroxene than olivine fractionates.

In addition, manganese behaves more incompatible than magnesium due to its larger ionic radius. Thus, the contents of manganese increase with decreasing MgO contents.

Since the trend for total iron is similar to the trend for MnO, it can be assumed that the controlling factors are the same i.e. olivine and clinopyroxene fractionation.

To demonstrate that this assumption is correct, the whole rock composition and the composition of the average phenocryst compositions were plotted into one diagram (Fig. 22). The diagram plotted for total iron versus MgO seems to indicate that olivine should be more abundant in the fractionating assemblage than clinopyroxene (Fig. 22). The calculated ratio for clinopyroxene and olivine fractionation is 6% clinopyroxene and 94% olivine. Since the samples scatter significantly, the extrapolation-line is rather long and the angle between the crossing lines is small, this diagram is not very reliable. This results in a ratio that is contradictory to the ratios displayed by the other diagrams.

The diagram plotted for MnO versus MgO (Fig. 22) cannot be used to determine which phase mostly controls the trend. Since manganese could not be identified in the phenocryst phases, the compositions plot on the MgO axis of the diagram.

The plot for Fe_2O_3 versus MgO for the earlier published data from Gran Canaria (Cousen et al., 1990; Gurenko et al., 2006; Schmincke, 1976 and 1982; Thirlwall et al., 1997) displays two linear trends. The lower plot that includes samples with a Fe_2O_3 concentration of about 4 to 8 wt% Fe_2O_3 all belong to samples from Barranco de Güigüi.

In summary, the trends displayed in the variation diagrams indicate two different fractionation patterns. From the start, the trends are largely controlled by olivine and clinopyroxene fractionation. It must be noted that the ratio between olivine and clinopyroxene fractionation is almost constant and does not vary significantly. At an MgO content of 8 wt% plagioclase starts to fractionate. Then, the trend is controlled by olivine, clinopyroxene and plagioclase fractionation.

Since the minerals that control the trends are known it is possible to calculate the ratio in which the minerals are responsible for the differentiation. This was done by transforming three-phase triangles into an equilateral form as proposed by Cox et al. (1979). The basis for this are the diagrams plotted for Al_2O_3 versus Na_2O, Al_2O_3 versus MgO and Na_2O versus MgO (Fig. 23). Each triangle with its bulk compositional trend is transformed into an equilateral triangle (Fig. 23), which are then superimposed (Fig. 24). The bulk compositional trends should intersect in a point that gives the mineral composition satisfying all the data (Cox et al., 1979). As can be seen in figure 24 the three compositional trends do not intersect in one point but form a triangle of error. The best fit values of mineral proportions for the ratio clinopyroxene:olivine:plagioclase can than be determined using this superimposition. The ratio determined is approximately 66:22:12. According to Cox et al. (1979) the calculations confirm that the removal of phenocrysts actually present in the lavas is capable of driving compositions along the observed bulk compositional trend, at least as far as the relative behaviour of MgO, Al_2O_3 and Na_2O is concerned. This confirms that clinopyroxene and olivine fractionation largely control the trends given by whole rock composition, whereas plagioclase fractionation is less significant.

It must be emphasized that this calculation only represents an average ratio for the studied samples. As was already shown in this chapter, two different fractionation patterns could be identified. First olivine and clinopyroxene dominate the trends displayed in the diagrams. Later plagioclase fractionation occurs in addition to olivine and clinopyroxene fractionation.

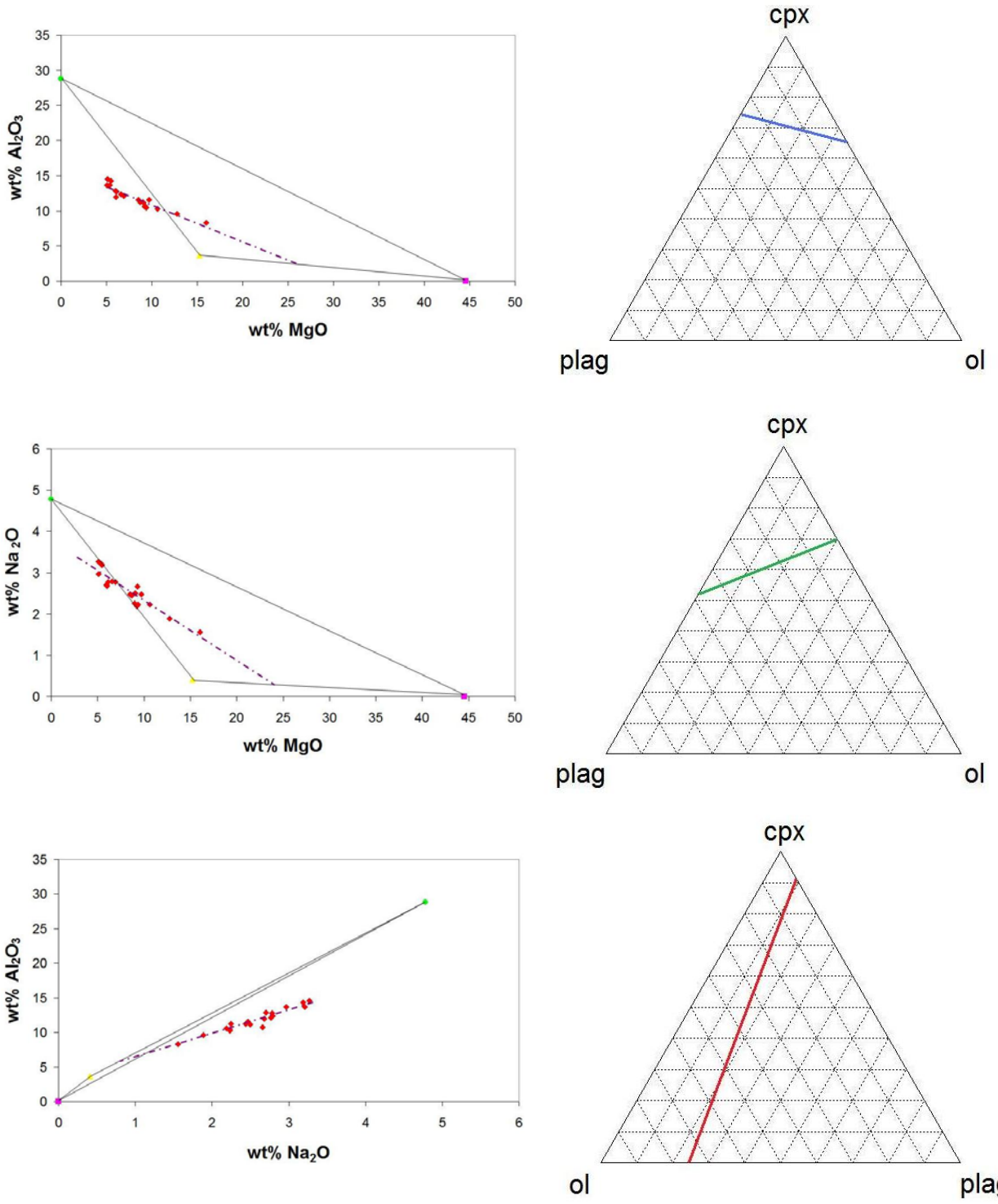

Fig.23: On the left side the diagram plotted for the whole rock and phenocryst compositions are plotted. Red squares: Whole rock composition. Pink square: Olivine composition. Yellow triangle: Clinopyroxene composition. Green circle: Plagioclase composition. The purple line displays the trend given by whole rock composition. On the right side the transformed triangle systems are displayed. The lines display the trend given by whole rock composition.

The trend of different mineral fractionation cannot be displayed with the method used by Cox et al. (1979). In addition, the ratio calculated using the diagrams displaying the whole rock composition compared to the average composition of the phenocryst phases clearly indicate a clinopyroxene:olivine ratio of approximately 2:1. The ratio calculated using the method according to Cox et al. (1979) displays a clinopyroxene:olivine ratio of approximately 3:1.

Compared to the other Canarian Islands the lavas of Gran Canaria show a general enrichment in SiO_2 and TiO_2 (Gurenko et al., 2006). They also state that the

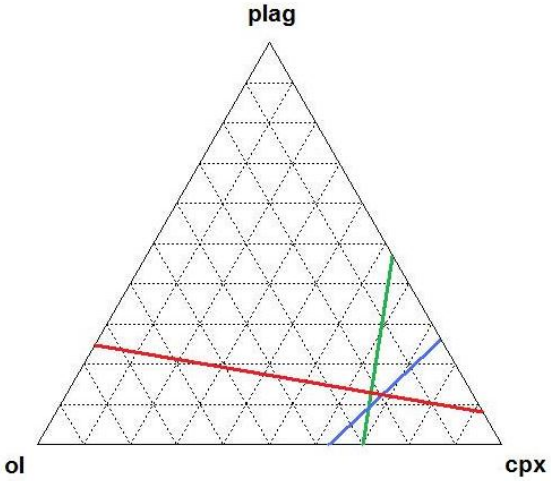

Fig.24: Superimposition of the three equilateral three-phase triangles to determine the mineral proportions. The lines display he trends from figure 23.

lavas from Gran Canaria have lower CaO and Al_2O_3 contents compared to the other shield basalts on the other islands.

5.2.3 Normative minerals

The normative minerals display different silica saturations (Table App.4). According to Yoder and Tilley (1962) silica-undersaturated basalt (alkali basalt) is characterized by normative olivine and nepheline, silica-saturated basalt (olivine tholeiite) is characterized by normative hypersthene and olivine, and silica-oversaturated basalt (quartz tholeiite) is characterized by normative quartz and hypersthene. The studied samples represent all types of silica-saturation. Thus, sample RH 13 can be described as alkali basalt, whereas the other samples range between olivine and quartz tholeiite. The already mentioned four high-SiO_2 samples can also be classified as quartz tholeiite. The normative quartz content of these four samples is significantly higher than that of the other quartz normative samples (RH 9, RH 11 and RH 15).

5.2.3.1 The forsterite-anorthite-diopside diagram

In the normative-mineral diagram (Fig. 25) most samples plot within the fields of diopside+liquid and olivine+liquid, whereas only one sample plots in the field of anorthite+liquid. This indicates that the ratio of the fractionating phases clinopyroxene and olivine is consistent with the general appearance of the forsterite-anorthite-diopside diagram.

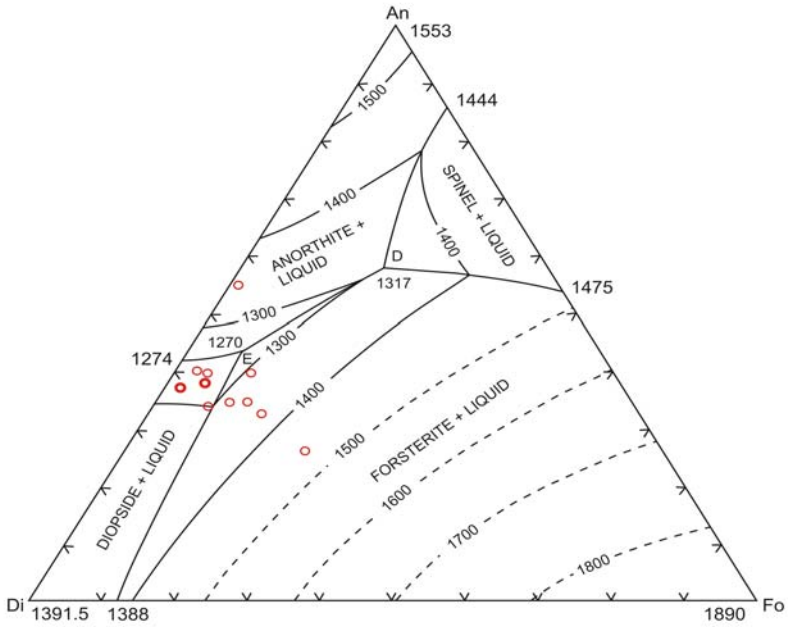

Fig.25: The forsterite-diopside-anothite system after Morse (1980). Plotted are the samples from Barranco de Tasártico, which are displayed by red circles.

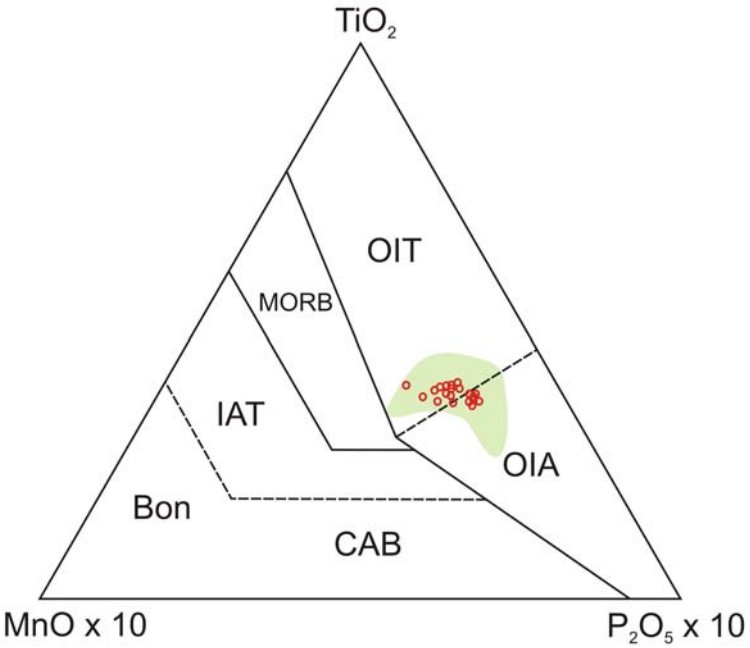

Fig.26: The MnO-TiO_2-P_2O_5 discrimination diagram for basalts and basaltic andesites after Mullen et al. (1983). The fields are: MORB; OIT- ocean island tholeiite; OIA- ocean island alkali basalt; CAB- island-arc calc- alkaline basalt; IAT- island-arc tholeiite; BON- boninite. The samples from Barranco de Tasártico are displayed by red circles whereas the earlier published data (Cousen et al., 1990; Gurenko et al., 2006; Schmincke, 1976 and 1982; Thirlwall et al., 1997) is displayed by the green area.

5.2.4. Discrimination diagram based on minor elements

Discrimination between ocean island basalt and ocean island tholeiite is made with the MnO-TiO_2-P_2O_5 diagram of Mullen (1983) (Fig. 26). According to Rollinson (1993) the advantage of the used elements Ti, Mn and P as discriminants between basalt types is that these elements are more accurately determined than the trace elements. The diagram is especially useful for basalt in the range of 45 to 54 wt% SiO_2. Figure 26 demonstrates the plot for the samples from Barranco de Tasártico together with the earlier published data (Cousen et al., 1990; Gurenko et al., 2006; Schmincke, 1976 and 1982; Thirlwall et al., 1997).

The Barranco de Tasártico samples plot close to the boundary between ocean island tholeiite (OIT) and ocean island alkali basalt (OIA). Hence, their composition can be described as transitional. The earlier published data (Cousen et al., 1990; Gurenko et al., 2006; Schmincke, 1976 and 1982; Thirlwall et al., 1997) suggest that this is a general feature of the shield-building lavas on Gran Canaria.

5.3 Trace elements

5.3.1 Large ion lithophile elements

The first group of elements that is going to be discussed in this chapter includes Cs, Rb, K, Ba, Pb and Sr. These elements belong to the low field strength elements which are also known as large ion lithophile elements (LILE).

In general, the concentrations of these cations are high in the ocean island basalts that were studied for this thesis (Table App. 3).

According to Wilson (1991) the abundances of these elements are mainly controlled by several factors such as source composition, residual mineralogy, degree of partial melting and extent of subsequent fractional crystallization.

The plots for Pb, Rb and Cs versus MgO do not represent a trend since the results scatter significantly (Fig. 27). Thus, the plots of Pb, Rb and Cs against MgO show a significant variation for samples with an MgO content between 5 wt% and 16 wt%. These diagrams simply display that the concentrations of these elements is generally high in the samples from Barranco de Tasártico compared to MORB. In addition, figure 27 also displays that in the plot for Pb versus MgO, four samples differ significantly from the rest. These four samples are the four more evolved samples RH 3 to RH 6 that were already discussed in chapter 5.2.1. Thus, the more evolved samples have a higher Pb content than the less evolved samples.

In contrast, K clearly demonstrates that the contents of this element increase with decreasing MgO contents (Fig. 27). As was already mentioned in chapter 5.2.2 the trend displayed in the diagram shows

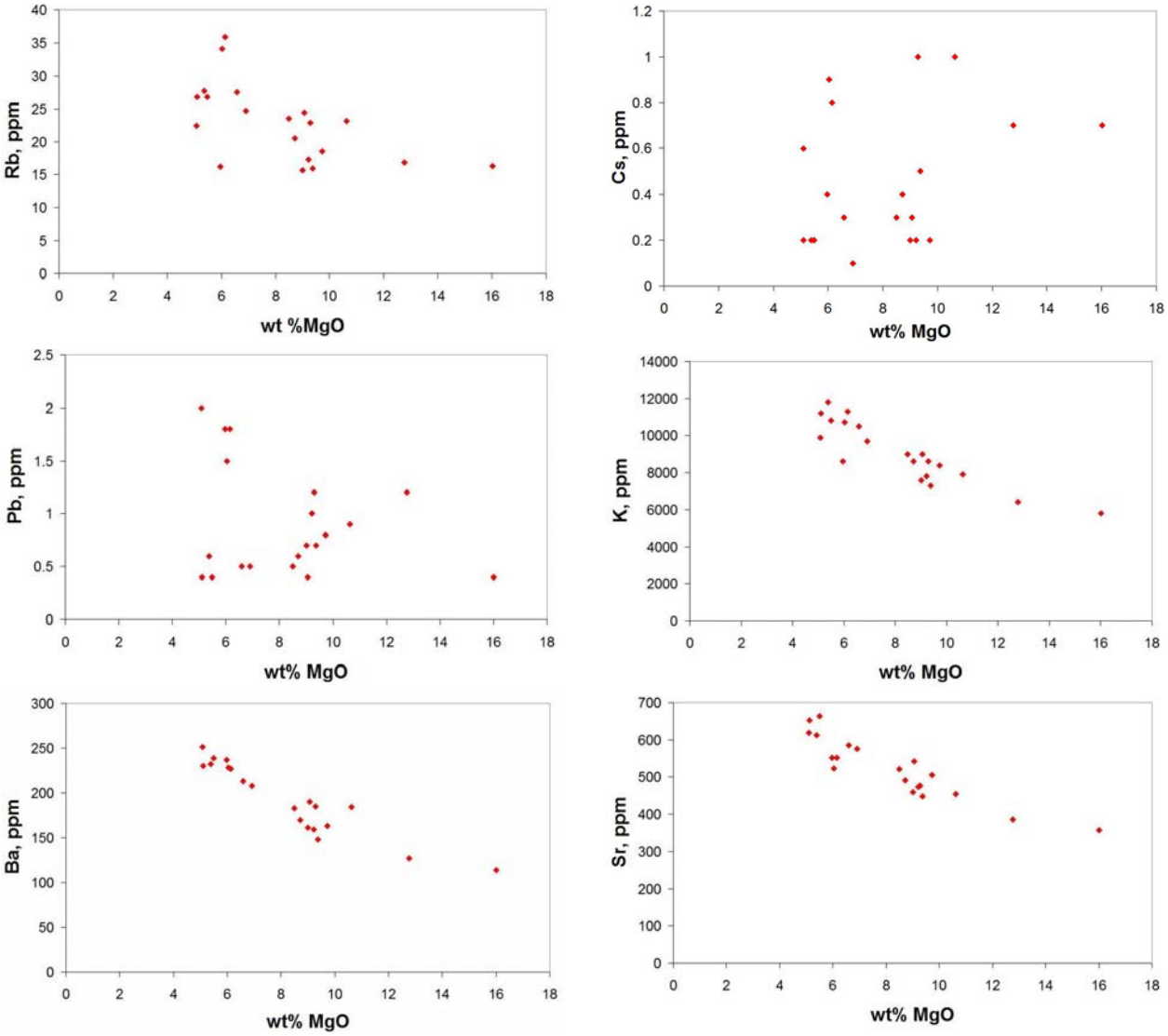

Fig.27: Large ion lithophile elements versus MgO variation diagrams plotted for the shield-building lavas from Barranco de Tasártico.

a steeper increase for samples with an MgO content below 8 wt%. The first part of the trend is mainly controlled by clinopyroxene and olivine fractionation, whereas the trend from 8 wt% MgO on is controlled not only by olivine and clinopyroxene fractionation but also by plagioclase fractionation. In addition, the magma gets enriched in potassium during the fractional crystallization of olivine and clinopyroxene plus plagioclase from 8 wt% MgO on.

Thus, the K behaviour is largely controlled by fractional crystallization of all three phenocryst phases. In addition, it behaves incompatibly and is therefore enriched in the lava.

Similarly to K, Ba and Sr both increase with decreasing MgO contents. According to Wilson (1991) Ba and Sr are preferentially incorporated into early-crystallizing minerals like plagioclase and therefore behave compatibly after the onset of plagioclase fractionation (Wilson, 1991). This cannot only be displayed by plotting Ba and Sr against MgO but also by plotting the two elements against SiO_2.

Figure 28 displays that the contents of Ba and Sr increase with increasing SiO_2 until a SiO_2 content of about 49 wt% and then are almost steady at 230 ppm for Ba and 550 ppm for Sr (Fig. 28). As stated before, Ba and Sr are preferentially incorporated in early plagioclase crystallization. Therefore, it is possible to assume that plagioclase starts to fractionate at a SiO_2 content of 49 wt%. Until the onset of the plagioclase fractionation Ba and Sr behave incompatibly and are enriched in the lava. After the onset of the plagioclase fractionation these elements are incorporated into plagioclase, whereupon the abundances of Ba and Sr in the lava decrease. If the fractionation of olivine and clinopyroxene predominates the increase of Ba and Sr in the melt, it can diminish or end completely. If more plagioclase fractionates the contents of Ba and Sr can decrease.
Therefore, the steady contents of both elements mark the onset of the plagioclase fractionation.

To test this assumption the studied 20 samples from Barranco de Tasártico were compared to the 105

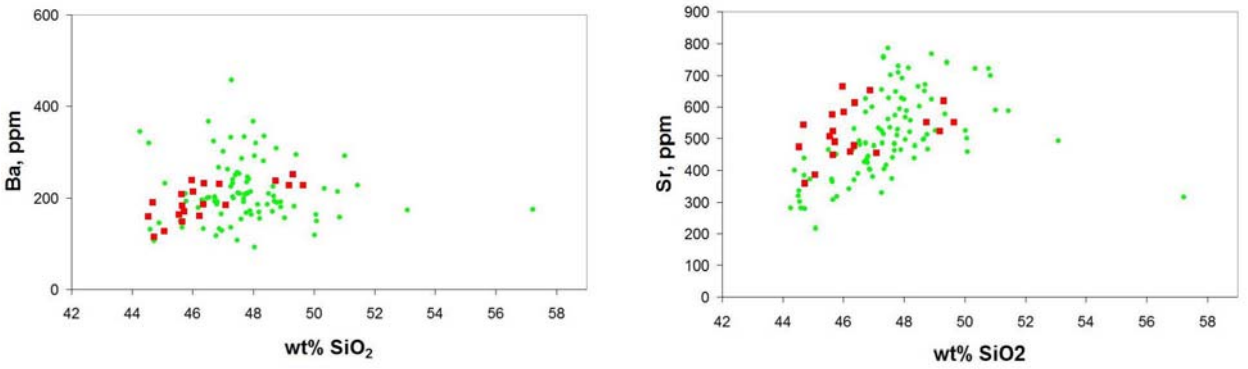

Fig.28: Ba and Sr plotted versus SiO_2 for the shield-building lavas from Barranco de Tasártico. The diagram displays the comparison between the Barranco de Tasártico samples and earlier published data (Cousen et al., 1990; Gurenko et al., 2006; Schmincke, 1976 and 1982; Thirlwall et al., 1997). Red squares: Barranco de Tasártico samples. Green circles: earlier published data (Cousen et al., 1990; Gurenko et al., 2006; Schmincke, 1976 and 1982; Thirlwall et al., 1997).

earlier published samples (Cousen et al., 1990; Gurenko et al., 2006; Schmincke, 1976 and 1982; Thirlwall et al., 1997). In comparison with these samples, it becomes apparent that the Barranco de Tasártico samples fit well into the general trend since the contents of both elements increase with increasing SiO_2 contents until a SiO_2 content of 49 wt%. This demonstrates that plagioclase begins to fractionate from the lava at 49 wt% SiO_2 and incorporates Ba and Sr. After that their abundances start to decrease. This conclusion is consistent with those made in chapter 5.2.2. Thus, the Ba and Sr diagrams reflect the onset of plagioclase fractionation at 49 wt% SiO_2 whereas the diagrams plotted for the major elements display the onset of plagioclase fractionation at 8 wt% MgO.

Furthermore, the LILE can be used as indicators of source heterogeneity. According to Wilson (1991) especially the K/Ba ratio is useful. In appendix 3 it can be seen that the K/Ba ratios vary between 36.3 and 51.5. Compared to the K/Ba ratio of a MORB that usually varies between 20 and 160 (Wilson, 1991) the ratio in the studied basalts are relatively low. According to Wilson (1991) variations in K/Ba ratio are sensitive indicators of source heterogeneity. The low ratios in ocean island basalts relative to MORB suggest their derivation from a mantle source that is different from the MORB source.

5.3.2 High field strength elements

The high field strength elements (HFSE) include the Lanthanides Sc and Y, as well as Th, U, Pb, Zr, Hf, Ti, Nb and Ta. Compared to the LILE the HFSE are small ions that are considered immobile compared to the mobile LILE.

In the studied basalts, both have an incompatible behaviour in common and are therefore preferentially enriched in the liquid phase. Hence, all of the mentioned elements show similar trends when plotted against MgO (Fig. 29).

The only difference is a varying degree of scatter. Thus, the behaviour of the HFSE is preferentially controlled by fractional crystallization of clinopyroxene, olivine and plagioclase. Especially the diagrams plotted for Zr and Y display a change in trend for samples with an MgO content below 8 wt%. Again, this displays that the steeper part of the trend (lavas below 8 wt% MgO) is dominated by clinopyroxene and olivine fractionation, whereas the other part of the trend is the result of the fractional crystallization of all the three phenocryst phases. This is consistent with the conclusions drawn by the major element diagrams in chapter 5.2.2.

According to Gurenko et al. (2006) the rocks on Gran Canaria show higher concentrations of Zr and Y at a given MgO content compared to the lavas from the other Canarian Islands.

5.3.3 Transition metals

The two transition metals taken into consideration here are Ni and Cr. In general, Ni and Cr concentrations decrease with decreasing MgO from 514 ppm to 19 ppm for Ni and from 1059 ppm to 24 ppm for Cr (Fig. 30).

According to Wilson (1991) Ni is a sensitive indicator for olivine fractionation from basaltic magmas because of its large mineral/melt partition coefficient. But not only olivine incorporates Ni. Clinopyroxene and magnetite also feature high partition coefficients. Therefore, oceanic island volcanic suites display good correlations between Ni and MgO as can be seen in figure 30. The fractional crystallization of olivine, clinopyroxene and magnetite are thus the main processes controlling the behaviour of Ni in ocean-island basalts.

Gurenko et al. (2006) stated that Ni scatters significantly in the lavas with MgO > 10 wt% which

Fig.29: High field strength elements versus MgO content for the shield-building lavas from the Güigüi Formation. The plotted diagrams display that the studied elements all behave incompatible and that their behaviour is controlled by crystal fractionation of olivine and clinopyroxene.

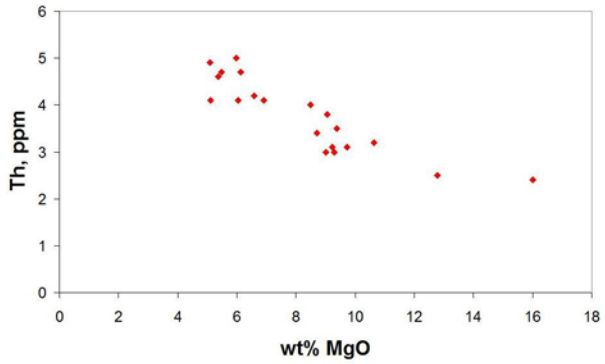
Th, ppm
wt% MgO

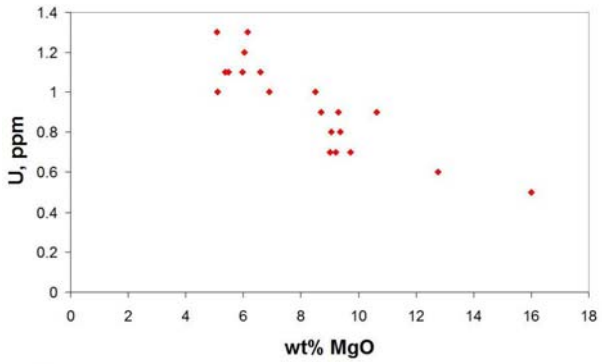
U, ppm
wt% MgO

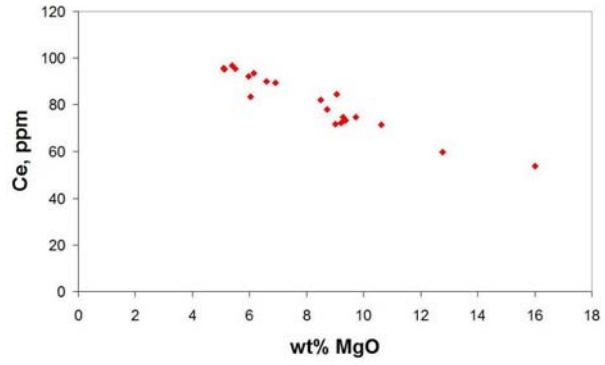
Ce, ppm
wt% MgO

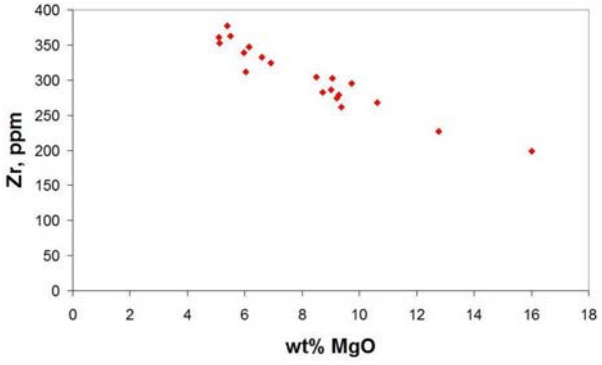
Zr, ppm
wt% MgO

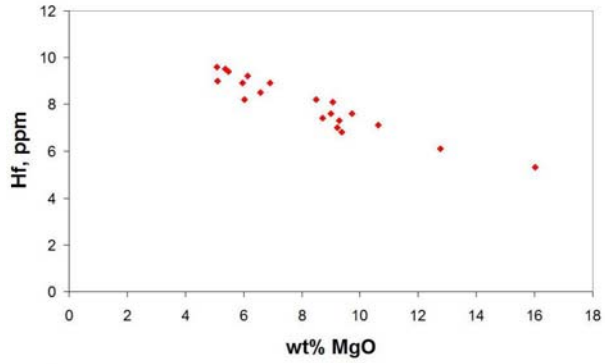
Hf, ppm
wt% MgO

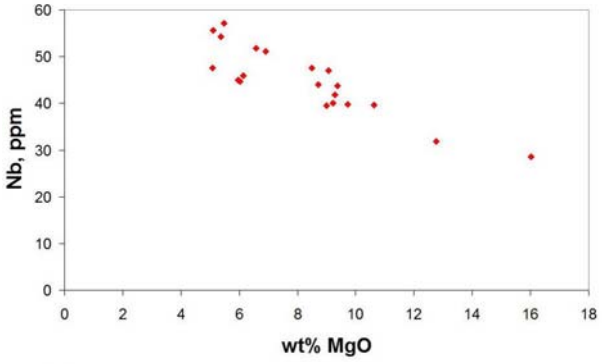
Nb, ppm
wt% MgO

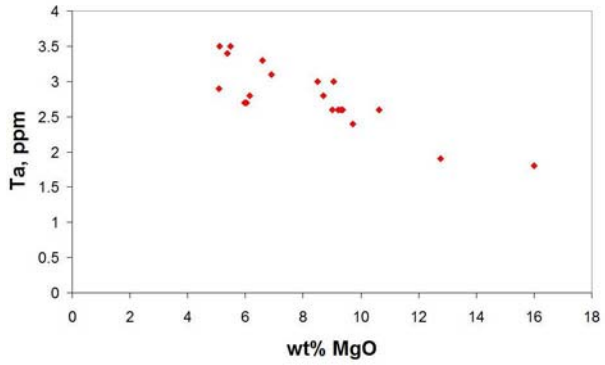
Ta, ppm
wt% MgO

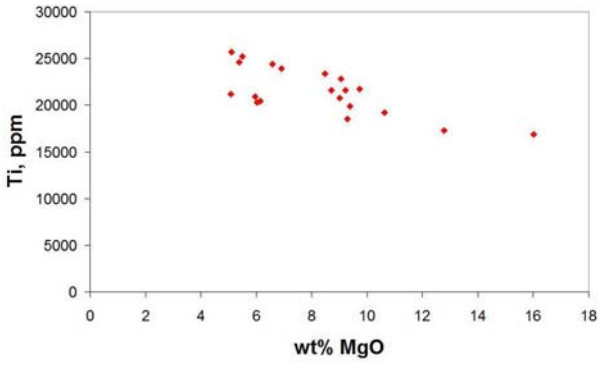
Ti, ppm
wt% MgO

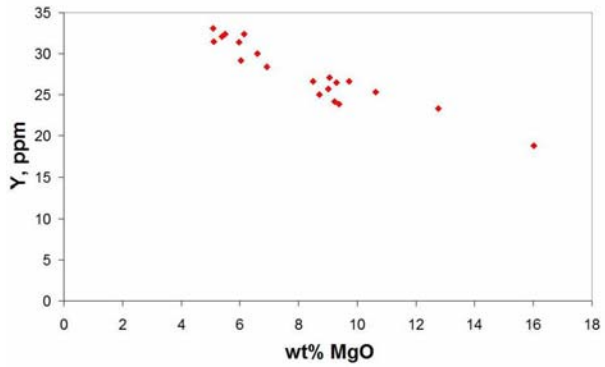
Y, ppm
wt% MgO

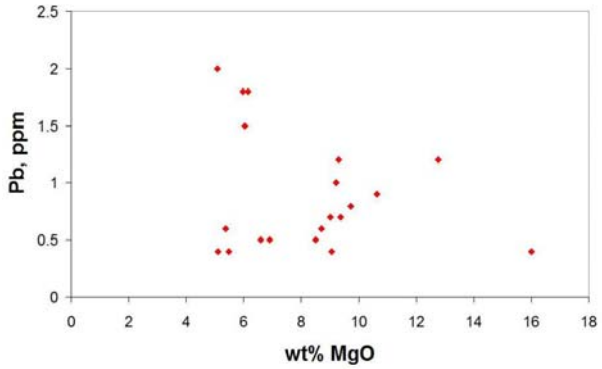
Pb, ppm
wt% MgO

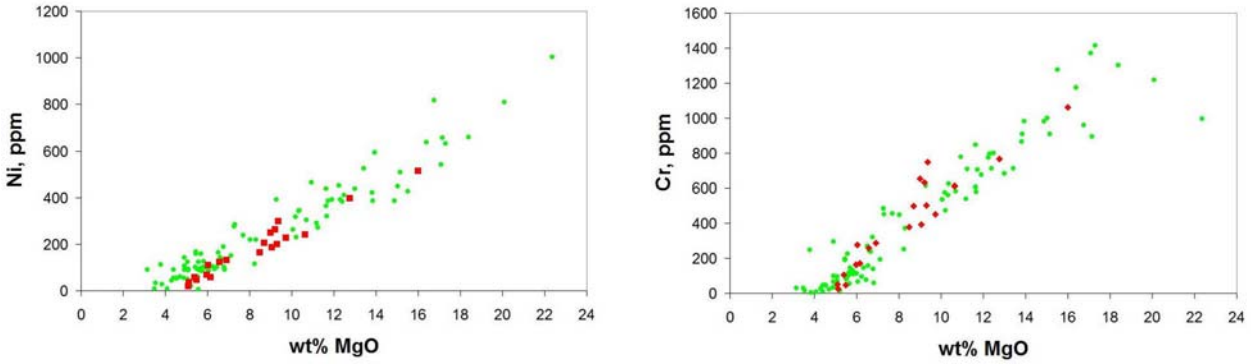

Fig.30: Variation for Ni and Cr content (ppm) versus wt% MgO. The diagrams display the variation for the Barranco de Tasártico samples in comparison to the earlier published data (Cousen et al., 1990; Gurenko et al., 2006; Schmincke, 1976 and 1982; Thirlwall et al., 1997). Red squares: Barranco de Tasártico samples. Green circles: earlier published data (Cousen et al., 1990; Gurenko et al., 2006; Schmincke, 1976 and 1982; Thirlwall et al., 1997).

according to him could not be related to various degrees of olivine accumulation in the rock samples. The offered conclusion is that the scatter represents true variations in the melt. For the samples that were studied in this thesis this can not be confirmed, since only three samples have an MgO content above 10 wt% MgO. Compared with the samples from the literature (Cousen et al., 1990; Gurenko et al., 2006; Schmincke, 1976 and 1982; Thirlwall et al., 1997) the Ni contents scatter in the lavas with MgO contents > 10 wt%. Hence, it can be assumed that the primary Canarian rocks generally show variations in the melt even though this cannot be confirmed for the present basalt samples. As is the case for Zr and Y the Gran Canarian rocks show a higher Ni concentration at a given MgO content compared to the other Canarian Islands (Gurenko et al., 2006).

Cr tends to correlate with MgO as seen in figure 30, but in contrast to Ni the trend for Cr is not only controlled by olivine crystallization. Wilson (1991) states the trend for Cr is a result of the concurrent crystallization of olivine and a Cr-rich spinel phase. In addition, clinopyroxene fractionation can also play a significant role. Due to the fact that clinopyroxene, olivine and a Cr-rich spinel with up to 17.4 atomic percent Cr could be found in the thin sections of the basalts (chapter 5.5.2) this statement can be taken for granted.

5.3.4 Rare earth elements (REE)

To fascilitate the interpretations of the rare earth elements (REE) a chondrite-normalized diagram was plotted. This diagram compares the present samples with earlier published ones (Cousen et al., 1990; Gurenko et al., 2006; Schmincke, 1976 and 1982; Thirlwall et al., 1997). Figure 31 displays a REE pattern for ocean island basalts. It becomes apparent that the rocks are enriched in light rare earth elements (LREE) relative to the heavy rare earth elements (HREE). According to Wilson (1991) the high LREE abundances relative to those of the HREE suggest a derivation from a relatively undepleted mantle sources. Even though the LREEs are enriched relative to the HREEs, the enrichment is not large enough to indicate a derivation by small degrees of partial melting of a source that contains garnet as a residual phase. If that was the case the enrichment in LREE would have been greater. Therefore, a source that contains garnet as a residual phase can be excluded.

To prove this, it was tried to develop a model representing the partial melting. Since we talk about a magma chamber batch melting was used to do so. However, it was not possible to develop a model using the batch melting and the given rare earth composition. Thus, it can be assumed that late differentiation occurred in a high degree. This changed the original composition of the magma too much to allow a modelling using the batch model.

Furthermore, the fractionation of the HREE relative to the LREE can also be caused by the presence of olivine and clinopyroxene due to the fact that the partition coefficients increase by an order of magnitude from La to Lu in these minerals (Rollinson, 1993). Thus, it must be noted that the crystallization of olivine is not the main controlling process in this case due to its small partition coefficient. Furthermore, the partition coefficient of clinopyroxene is not high enough to explain the fractionation of the HREE relative to the LREE. Garnet has a higher partition coefficient for the LREE than for the HREE. This could explain an enrichment of the LREEs compared to the HREEs. However, the presence of garnet as a residual phase in the source was excluded earlier.

In addition, the plotted diagram does not show any Eu anomaly, which would indicate a significant plagioclase fractionation. This suggests that the plagioclase fractionation that was indicated by the behaviour of Ba and Sr (chapter 5.3.2) is not sufficient to leave a significant mark in the REE patterns.

Compared to the earlier published data (Cousen et al., 1990; Gurenko et al., 2006; Schmincke, 1976 and 1982; Thirlwall et al., 1997) it is apparent that the studied samples follow the same trend even though the abundances of REEs in the studied samples are higher than in those of the earlier published ones (Cousen et

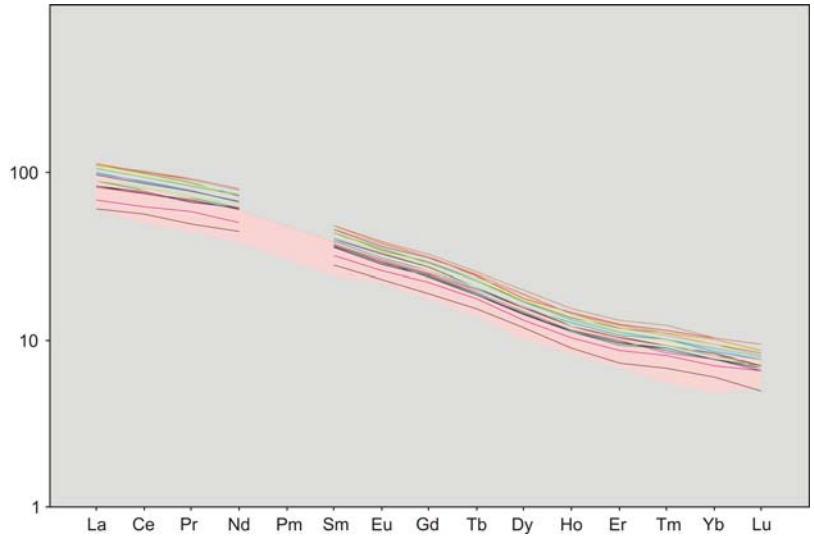

Fig.31: Chondrite-normalized REE pattern for the studied samples from Barranco de Tasártico in comparison to earlier published data (Cousen et al., 1990; Gurenko et al., 2006; Schmincke, 1976 and 1982; Thirlwall et al., 1997). The earlier published samples (Cousen et al., 1990; Gurenko et al., 2006; Schmincke, 1976 and 1982; Thirlwall et al., 1997) are represented by the pink area. The normalizing values are those of Taylor and McLennan (1985).

al., 1990; Gurenko et al., 2006; Schmincke, 1976 and 1982; Thirlwall et al., 1997). One reason for this might be that the studied samples from Barranco de Tasártico in average come from more evolved rocks than the earlier published samples.

5.3.5 Normalized multi-element diagram

The last diagram that was plotted using the trace elements is a normalized multi-element diagram (Fig. 32). For this purpose the trace element concentrations were normalized to the composition of the primordial mantle. The normalizing values are those of McDonough et al. (1991).

Like the chondrite-normalized REE pattern this diagram also shows a general enrichment in light rare earth elements. Furthermore, it is showing a distinctive enrichment in Nb and Ta. According to Rollinson (1993) a negative Nb anomaly would indicate a contamination with crustal material, since negative Nb anomalies are characteristic for the continental crust. Hence, a contamination with crustal material can be excluded.

In addition, the diagram displays a general depletion in K and Pb that according to Gurenko et al. (2006) is common for high U/Pb mantle-type (HIMU) mafic rocks.

5.4 Phenocryst phases

As already described in chapter 5.1 three phenocryst

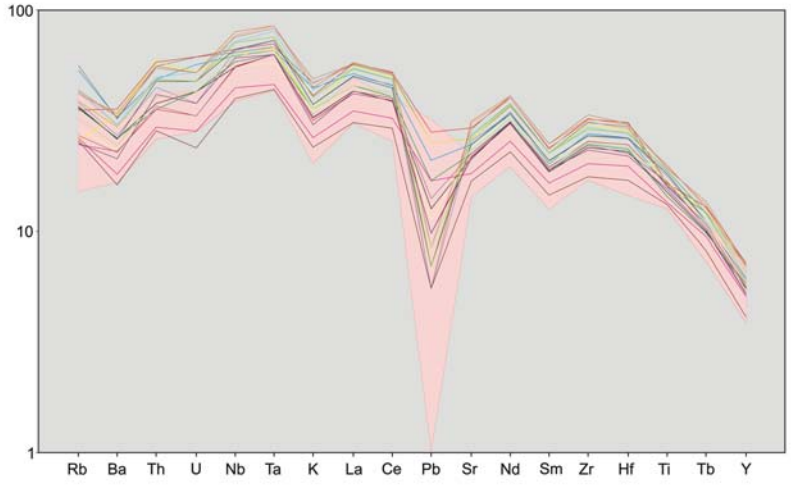

Fig.32: Trace element concentrations normalized to the composition of the primordial mantle in comparison to earlier published data (Cousen et al., 1990; Gurenko et al., 2006; Schmincke, 1976 and 1982; Thirlwall et al., 1997). The earlier published data (Cousen et al., 1990; Gurenko et al., 2006; Schmincke, 1976 and 1982; Thirlwall et al., 1997) is represented by the pink area. The normalizing values are those of McDonough et al. (1991).

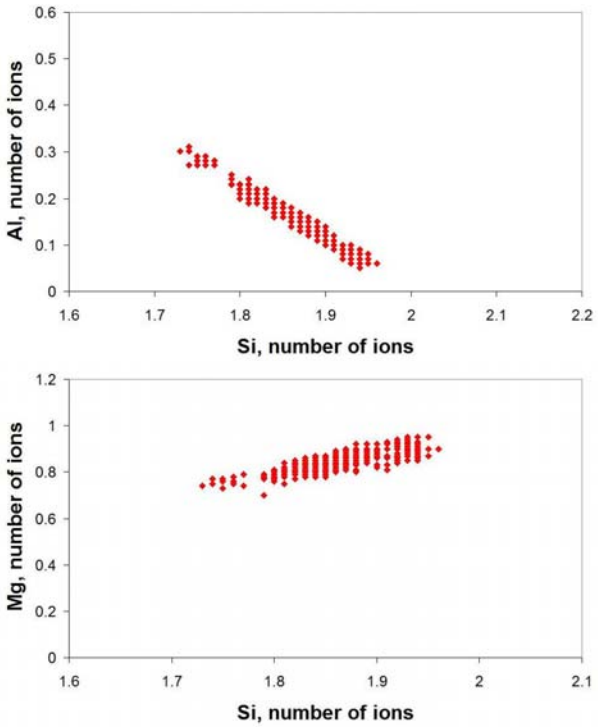

Fig.33: Diagrams plotted for Al, Ti and Mg versus Si (number of ions calculated for six oxygen ions). All diagrams display almost linear trends.

phases, olivine, clinopyroxene and plagioclase, occur in the observed basaltic rocks. After studying the phenocrysts phases in transmitted light (chapter 5.1) these phases were also analysed in the SEM and with EDS techniques.

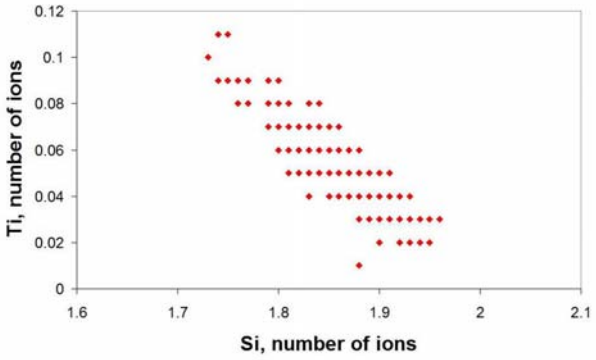

5.4.1 Clinopyroxene

Clinopyroxene is the most common phenocryst phase. Even though the phenocrysts of clinopyroxene tend to be larger than those of olivine, they occur more frequently and are found in all of the observed thin sections. In the SEM, the clinopyroxene appears as medium grey crystals that tend to be zoned especially at their rims. This zoning was studied together with the general chemical composition. Altogether 471 EDS spectra were obtained and the results can be found in appendix 5. The results clearly show that the Ca and Mg contents of the observed clinopyroxene are almost identical irrespective of the mineral composition ranging between 0.69 and 0.95 ions when calculated for six oxygen ions. The number of ions of Si varies between 1.73 and 1.96 (Table App. 5).

In addition to Ca, Mg and Si, Na, Fe, Al, Ti and Cr occur in amounts above the detection limit. All of these are normal elements in clinopyroxene. They occur in concentrations less than 0.39 ions per six oxygen ions. Aluminium and iron show the highest

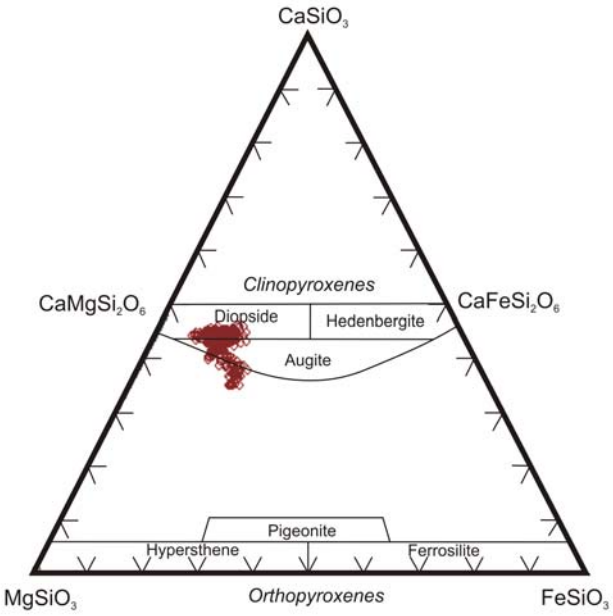

Fig.34: Ternary system plotted for the pyroxene modified after Mattes (1990). The system clearly shows that the studied pyroxenes plot within the field of clinopyroxene that have a composition of diopside and augite. Samples plotting in the miscibility gap are common for volcanic rocks.

concentrations of these elements.

Several relations between the elements can be observed. Thus, the abundances of Al and Ti decrease with increasing Si contents. In contrast, concentrations of Mg increase with increasing Si contents (Fig. 33).

The results for the pyroxene phases were plotted in an $MgSiO_3$-$CaSiO_3$-$FeSiO_3$ diagram to demonstrate the composition of the clinopyroxene (Fig. 34). The more precise classification is a composition varying between diopside and augite. According to Mattes (1990) diopside and augite form a complete solid solution series. In addition, augite incorporates some Na instead of Ca and some Al instead of Mg and Si (Mattes, 1990). It can therefore be assumed that the relatively high concentrations of Al (up to 0.39 numbers of ions) are a result of these substitutions. The diagram also demonstrates that several samples plot within the miscibility gap that exists between augite and pigeonite. According to Mattes (1990) volcanic rocks commonly contain clinopyroxene that features a composition that lies within this miscibility gap. The miscibility gap is temperature dependent. Thus, the clinopyroxene can have crystallized within its field of stability.

Since the increase in the Fe content also results in a decrease of Ca and an increase in Al and Na it can be assumed that aegirine component could be present. In addition, the decreasing Ca und increasing Al contents could indicate Tschermak substitution.

To see whether aegirine ($NaFeSi_2O_6$) or Tschermak's substitution ($CaAl_2SiO_6$) occurs in the studied clinopyroxene the following calculation was made. First the amount of octahedral and tetrahedral Al was estimated. Since Tschermak's substitution means that tetrahedral Al is balanced with octahedral Al, an octahedral Al content in excess of tetrahedral Al could indicate the presence of jadeite ($NaAlSi_2O_6$). To identify the amount of Al in the different positions it was assumed that the amount of tetrahedral Al equals the difference between 2 and the number of Si ions calculated for 6 oxygens. Appendix 6 displays that the amount of tetrahedral Al is lower than the whole Al content. This means that octahedral Al is present in the clinopyroxene phenocrysts. Thus, a Tschermak's substitution can be verified. In addition, the presence of jadeite can be excluded since the amount of octahedral Al is lower than the amount of tetrahedral Al. Thus, no Al is left to calculate jadeite. This leads to the conclusion that the studied samples formed at reasonably low pressure. Since jadeite can be excluded, sodium is calculated as aegirine. However, the amount of aegirine is rather low.

As already mentioned the crystals are zoned especially at their rims. To be able to explain the chemical differences between the different zones line maps of the concerned areas were performed using the EDS line mapping facilities. The results are demonstrated by using the map of a pyroxene crystal in the thin section RH 2. As can be seen in figure 35 the clinopyroxene crystal is zoned displayed as a darker grey zone within a slightly lighter grey areal. The mapping line is displayed by the yellow line in

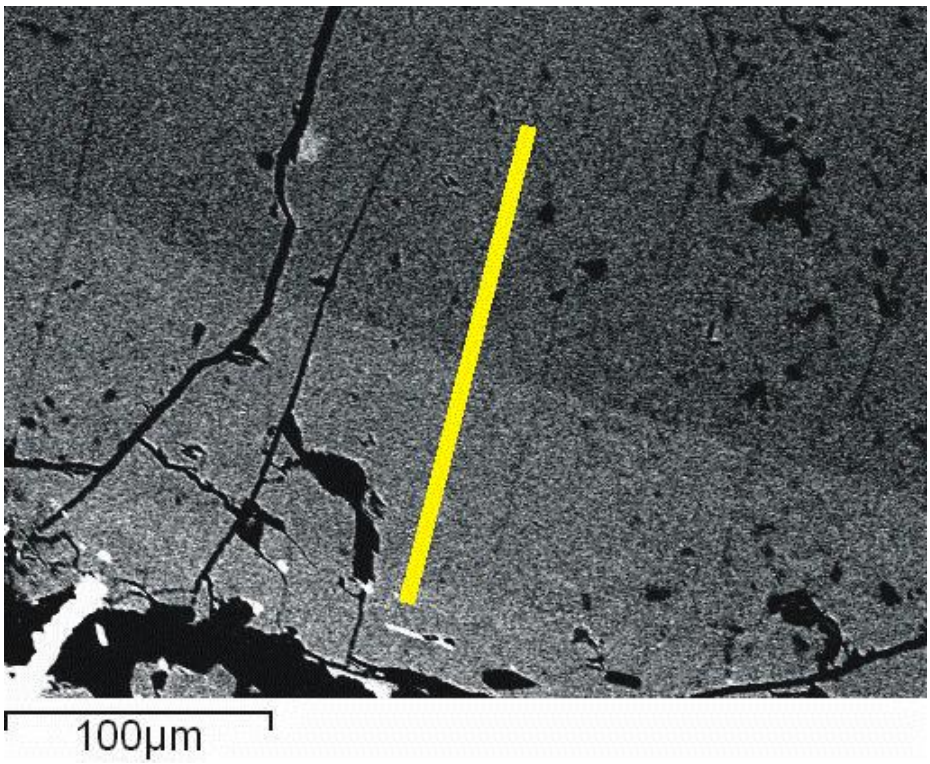

Fig.35: Zoned clinopyroxene in thin section RH 2. The picture shows that the clinopyroxene crystal is zoned displayed as a darker grey zone within a slightly lighter grey areal. The lighter area is the result of enrichment in Al, Ti and Fe, whereas enrichment of Mg and Si results in the darker area. The yellow line is the mapping line.

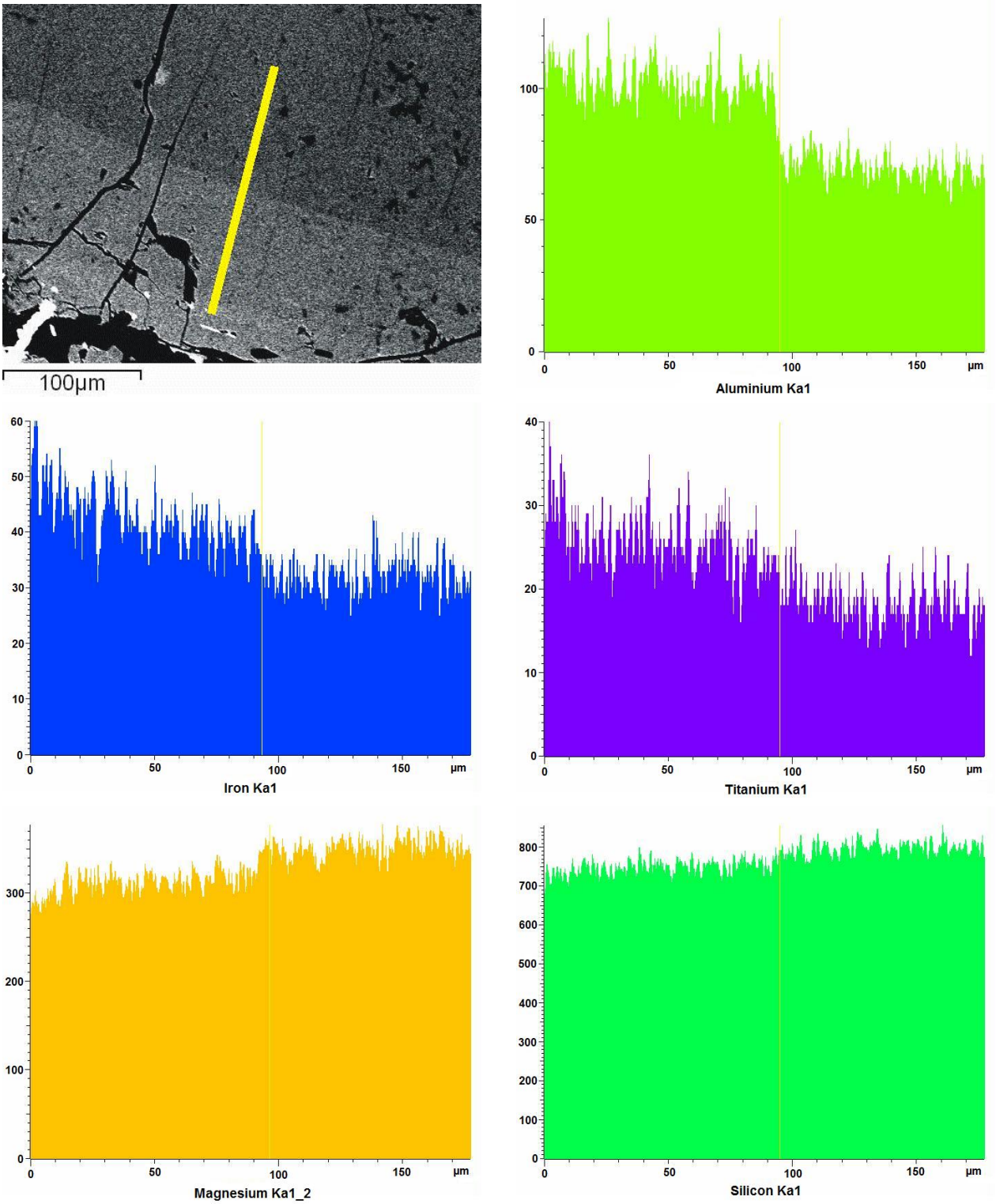

Fig.36: Line spectra analysed for a clinopyroxene in thin section RH 2. The spectra are shown for aluminium (light green), iron (dark blue), titanium (purple), magnesium (orange) and dark green (silicon).

figure 35 and covers the darker grey zone as well as the lighter grey part of the crystal. It can be assumed that the darker areas of the crystal are significantly depleted in heavy elements like Ti and Fe, whereas the lighter areas are enriched in these elements. The associated spectra shows the variations for the elements Al, Fe, Mg, Si and Ti (Fig. 36). These elements were chosen because they demonstrate the difference in the chemical composition most clearly. The line spectra for Al, Fe and Ti clearly show that the darker area is significantly depleted in these elements relative to the lighter parts of the crystal. In contrast, the darker areas show a higher concentration not only of Mg but also of Si.

5.4.2 Olivine

Olivine is a common phenocryst phase in the observed samples. Although no completely fresh olivine phenocrysts could be found, it was possible to examine the olivine composition in the thin sections RH 2, RH 10, RH 16 and RH 20 since parts of the olivine crystals were still preserved in these sections. Olivine always has a reaction rim of iddingsite. Iddingsite is an iron-rich alteration product of olivine and therefore contains a high concentration of a heavy element. It has a light colour in the SEM. The unaltered parts of the olivine crystals have a grey colour and show no signs of significant heterogeneity or zoning as the clinopyroxene does. Altogether 266 spectra of olivine are obtained. The results can be seen in Appendix 7. This table shows that the analysed olivine crystals have between 1.6 and 1.8 Mg-ions per four oxygen ions. Consequently the iron content is rather low and varies between 0.23 and 0.4 ions per four oxygen atoms. The Si content is constant and varies only between 0.99 and 1.02 ions. This range corresponds approximately to the analytical error.

The two olivine end-members forsterite and fayalite form a complete solid solution series. The observed olivine contains a composition that ranges between Fo_{79} and Fo_{88}.

The only relationship between the elements observed for the olivine is the relationship between Fe and Mg. Hence, the Fe content decreases with increasing Mg content (Fig. 37). This is consistent with the fact that the two end-members form a complete solid solution series.

In addition, it was tried to calculate the temperature at which olivine starts to crystallize. To do so the following equation according to Roeder and Emslie (1970) was used:

$$\log \frac{X_{MgO}^{Ol}}{X_{MgO}^{Liq}} = \frac{3740}{T} - 1.87$$

The temperatures calculated range between 1172 and 1218°C (Table App. 8). It becomes apparent that even though the temperatures between the thin sections vary, the temperatures in the same crystals are almost constant and only show differences of 1 to 5°C. The calculated temperatures are a bit too low but since all the observed olivines were altered, the explanation for the too low temperatures could be alteration.

It should be mentioned that an effort to calculate the temperatures using the iron equation by Roeder and Emslie (1970) was also made. These calculated temperatures show a larger variation (1140-1273°C) than these calculated with the magnesium equation. Since the proportion Fe^{2+}/Fe^{3+} cannot be determined, a possible explanation could be that this ratio is not constant and thus provides more varying results. The fact that the temperatures calculated from one single crystal do not vary significantly is consistent with this assumption but cannot be considered as evidence in favour of it.

5.4.3 Plagioclase

The least common phenocryst phase is plagioclase. As already mentioned in chapter 5.1, plagioclase phenocrysts appear only in the thin sections RH 3, RH 6, RH 8, RH 11, RH 13 and RH 20. Similar to the clinopyroxene phenocrysts, the plagioclase

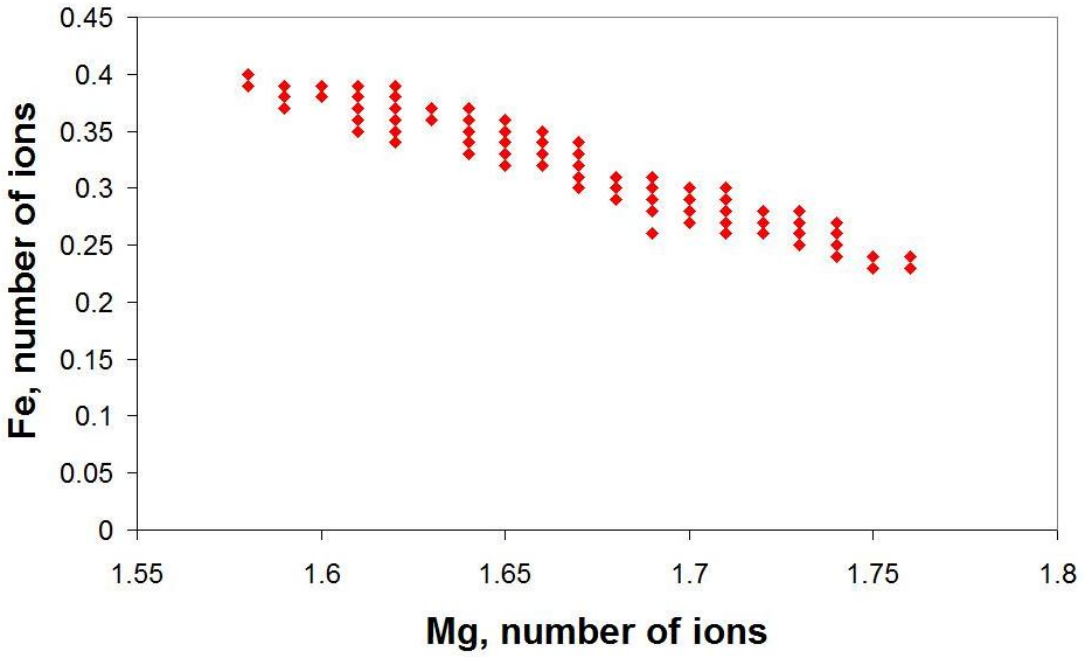

Fig.37: Diagram showing a plot for magnesium versus iron for the studied olivine phenocrysts. It becomes apparent that iron contents decrease with increasing magnesium contents.

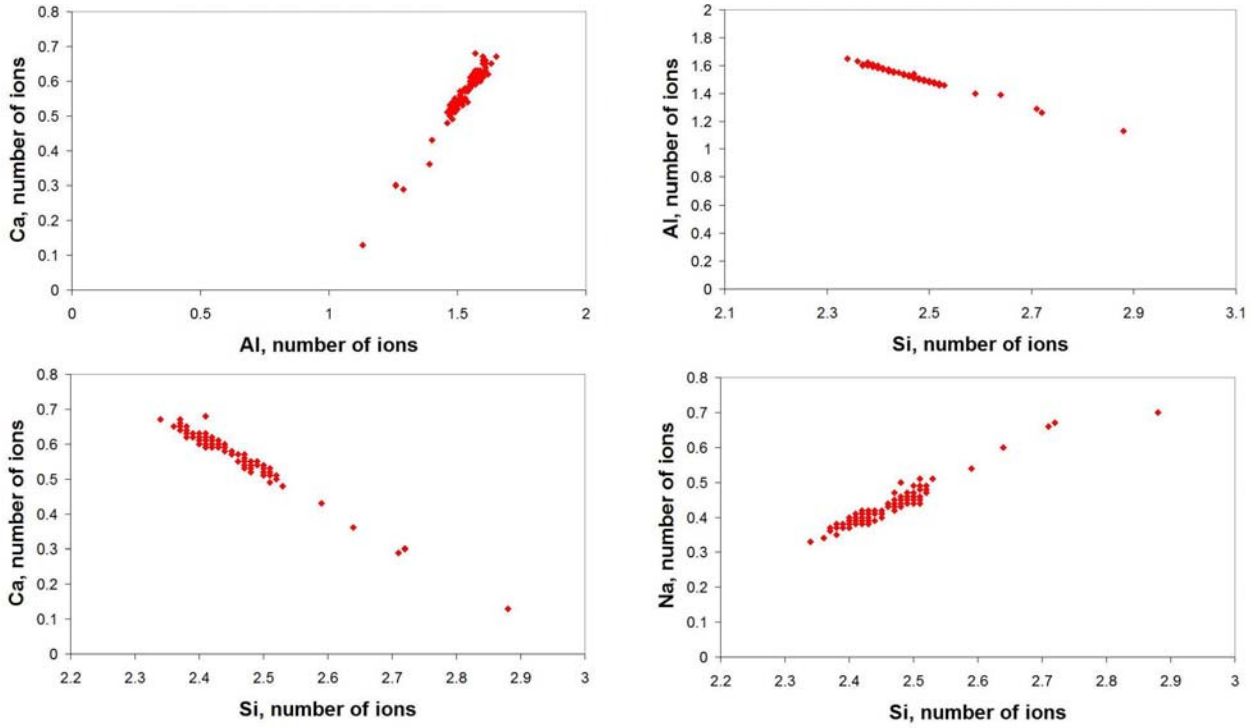

Fig.38: Variation diagrams for the studied plagioclase phenocrysts from Barranco de Tasártico. The plots indicate the expected relations between Na, Al, Ca and Si.

phenocrysts are euhedral and feature a grey colour in the SEM. However, it was easy to distinguish the two due to the darker grey appearance of the plagioclase. In addition, zoning occurs more seldom in the plagioclase phenocrysts compared to the clinopyroxene ones. However, the zoning was mapped in the same way as the zoning in the clinopyroxene crystals.

The results of the chemical analyses are displayed in appendix 9. Potassium could be identified in trace amounts. In general, Al and Si show the highest abundances. They range between 1.1 and 1.7 ions for Al and 2.3 and 2.9 ions of Si (eight oxygen atoms). The abundances of Na vary between 0.71 and 0.25 and that of Ca between 0.13 and 0.76.

As was the case for olivine and clinopyroxene several diagrams were plotted to demonstrate existing relationships between the elements. These plots (Fig.

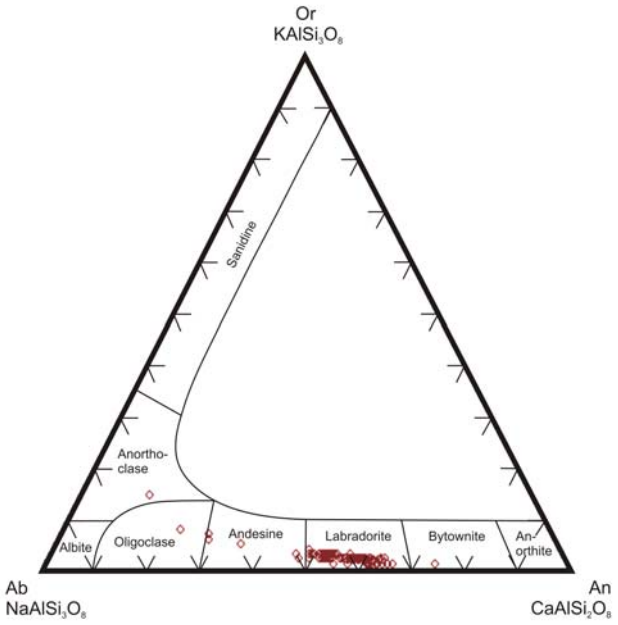

Fig.39: Ternary system Ab-Or-An modified after Mattes (1990) for the plagioclase phenocrysts from Barranco de Tasártico.

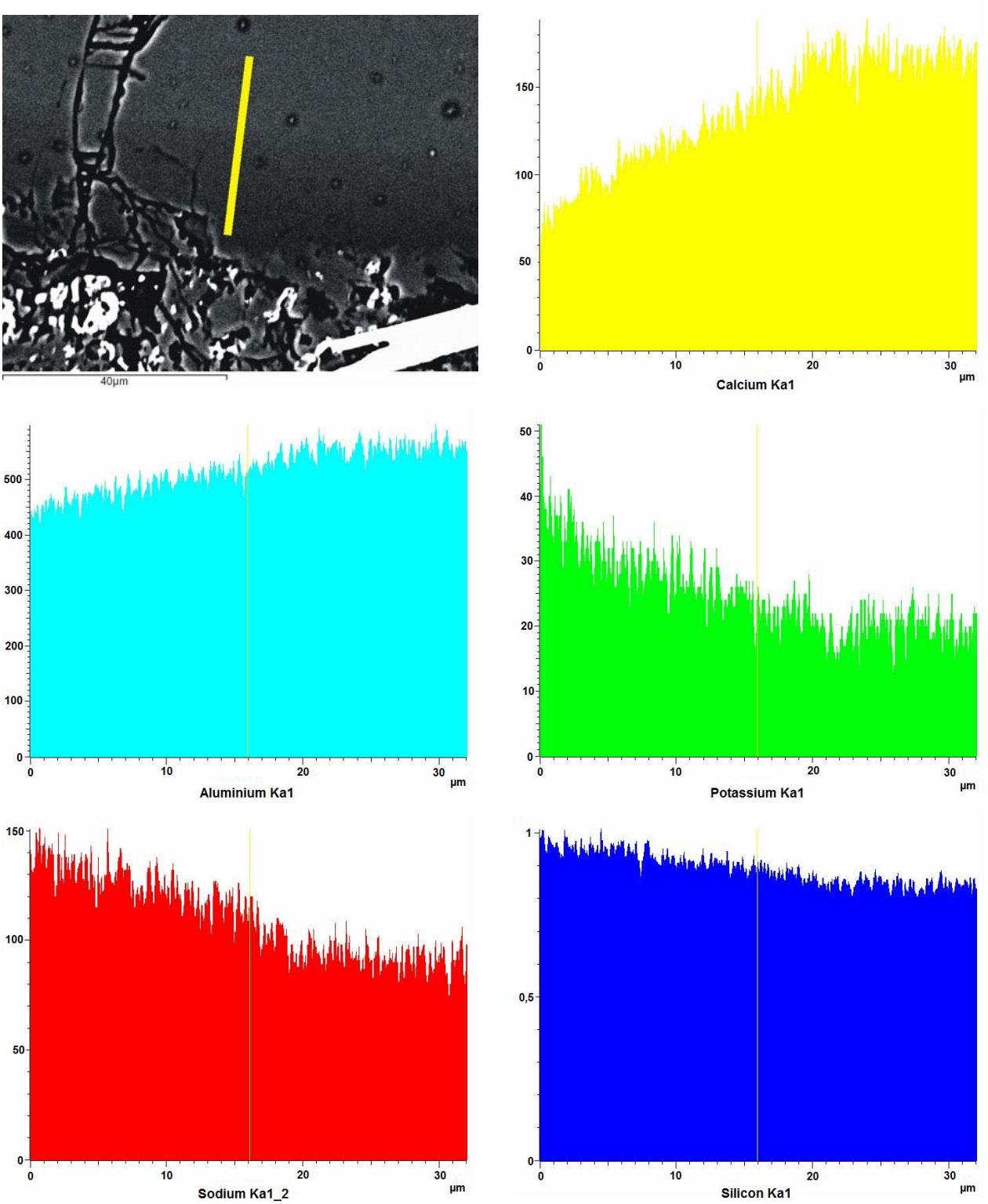

Fig.40: Line spectra analysed for a plagioclase in thin section RH 3. The spectra are shown for calcium (yellow), aluminium (light blue), potassium (green), sodium (red) and silicon (dark blue). The picture in the right top displays the crystal.

38) indicate the expected relations between Na, Al, Ca and Si expressed as compositions between albite and anorthite. In some crystals some Na is replaced by K.

Most samples plot within a range of An_{50} and An_{70} (labradorite). To be able to classify the plagioclase more precisely the results for the observed plagioclase phenocrysts were plotted in the albite–orthoclase-anorthite system after Deer, Howie and Zussmann (1963) and Mattes (1990). This ternary system can be seen in figure 39. According to the diagram the plagioclase occurring as phenocrysts is mainly labradorite. Only few plagioclase crystals plot in the fields of bytownite, andesine and oligoclase. Furthermore, one sample plots within the field of

anorthoclase. This spectrum belongs to a more potassium rich exsolution lamellae within a plagioclase crystal.

As already mentioned the plagioclase phenocrysts show a zoning mainly at the crystal rims. To display the zoning, a plagioclase from thin section RH 3 is used. As can be seen in figure 40 the crystal displays a rim that is slightly darker than the rest of the crystal. The line spectrum for the plagioclase shows that this darker rim has lower abundances of Ca and Al and higher abundances of K, Na and Si than the rest of the crystal. This is consistent with the line spectra for other plagioclase phenocrysts. According to Phillips and Griffen (1981) the zoning within the plagioclase phenocrysts can be interpreted as the result of disequilibrium during crystallization.

5.4.4 Summary

As a summary it can be noted that the most common phenocryst phase in the observed samples is a magnesium- and calcium-rich clinopyroxene whose composition ranges between diopside and augite. The zoning that occurs frequently in the crystals is the result of a substitution among the elements Fe, Ti, Al and Mg.

In contrast, magnesium-rich olivine phenocrysts show no visible signs of zoning. In composition, they range between Fo_{79} and Fo_{88} and therefore plot close to the forsterite end-member.

Plagioclase represents the least frequent phenocryst phase. The plagioclase crystals display a zoning that is caused by a depletion of calcium and aluminium and an enrichment of potassium, sodium and silicon. The plagioclase phenocrysts can be classified as labradorite. More potassium-rich feldspar occurs only scarcely and can be interpreted as potassium-rich exsolution lamellae within the plagioclase.

5.5 Opaque phases

The ten thin sections, which were prepared for the work with the SEM, were also used to examine the opaque phases in reflected light and the SEM. Two different opaque phases could be identified: ilmenite and a spinel phase with varying Ti and Cr contents. During the examination of the thin sections it became obvious that the opaque phases show a distinct distribution within the studied stratigraphy. The ilmenite phase is the dominant opaque phase in the lower parts of the studied stratigraphy. The spinel phase represents the dominant opaque phase in the upper parts of the studied stratigraphy, where ilmenite still occurs as small crystals within the matrix but does not form any large crystals.

5.5.1 Ilmenite

Ilmenite represents the dominant opaque phase in the lower stratigraphic parts. It could be identified in the thin sections up to RH 8.

In general, the ilmenite crystals feature a light colour and a homogenous appearance in the SEM (Fig. 41). In reflective light the crystals show a strong anisotropy. No exsolution lamellae of hematite could be observed within the crystals and no signs of zoning were found in the ilmenite crystals. Compared to the

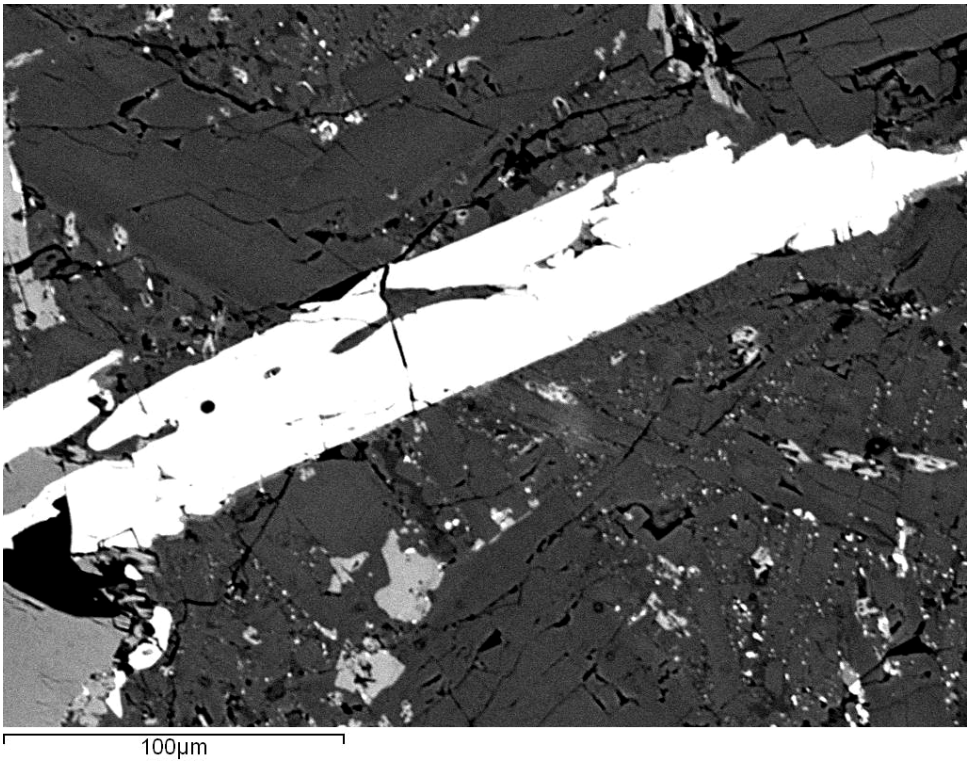

Fig.41: Back-scatter image of columnar ilmenite in thin section RH 3. The opaque phase is euhedral and shows no signs of zonation.

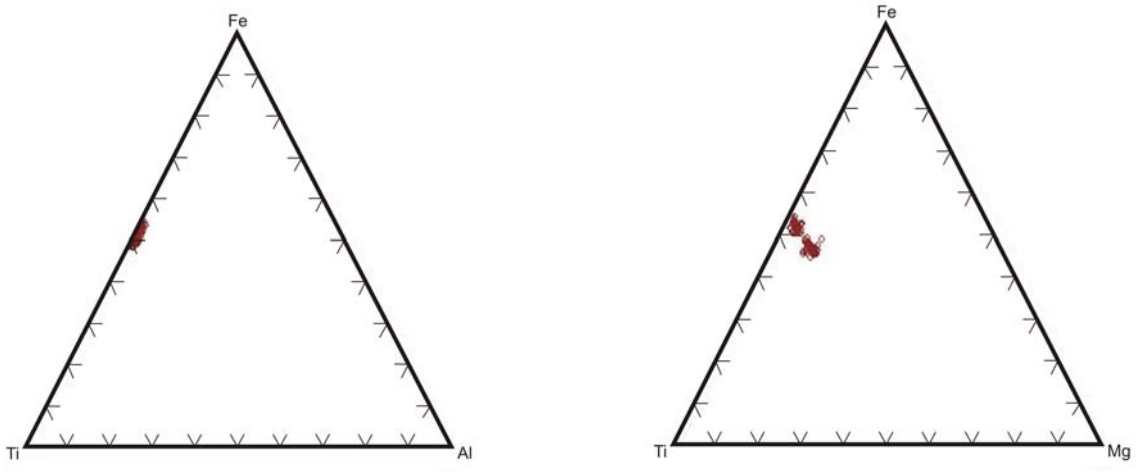

Fig.42: Ti-Fe-Al diagram (left side) and Ti-Fe-Mg diagram (right side) plotted for the ilmenite phase. The two clusters in the Ti-Fe-Mg diagram are the result of varying Mg contents in the different parts of stratigraphy.

spinel phases the appearance of the ilmenite phase mostly is columnar, whereas non-columnar crystals occur but with a lower frequency.

As can be seen in appendix 10 the Ti as well as the Fe contents in the ilmenite is high and ranges between 0.88 and 0.97 numbers of ions for Ti and 0.87 and 1.06 numbers of ions for Fe calculated for three oxygens. Furthermore elements like Al, Mg, V, Mn and Co occur as minors.

For the ilmenite two ternary diagrams were plotted: Ti-Fe-Al and Ti-Fe-Mg. The system Ti-Fe-Al (Fig. 42) clearly displays that the chemical composition of ilmenite plots within a relatively small range with a ratio between Ti and Fe close to one.

The second ternary diagram (Fig. 42) displays basically the same: a relatively small variation in chemical composition of the ilmenite. In addition, it is apparent that the samples plot within two clusters with slightly different Mg contents. In general, the Mg-richer cluster displays ilmenite samples coming from higher parts of the stratigraphy. They usually occur in the thin sections RH 6 and RH 8. The average number of Mg ions varies between 0.12 and 0.2 numbers calculated for three oxygens. Lower Mg contents are

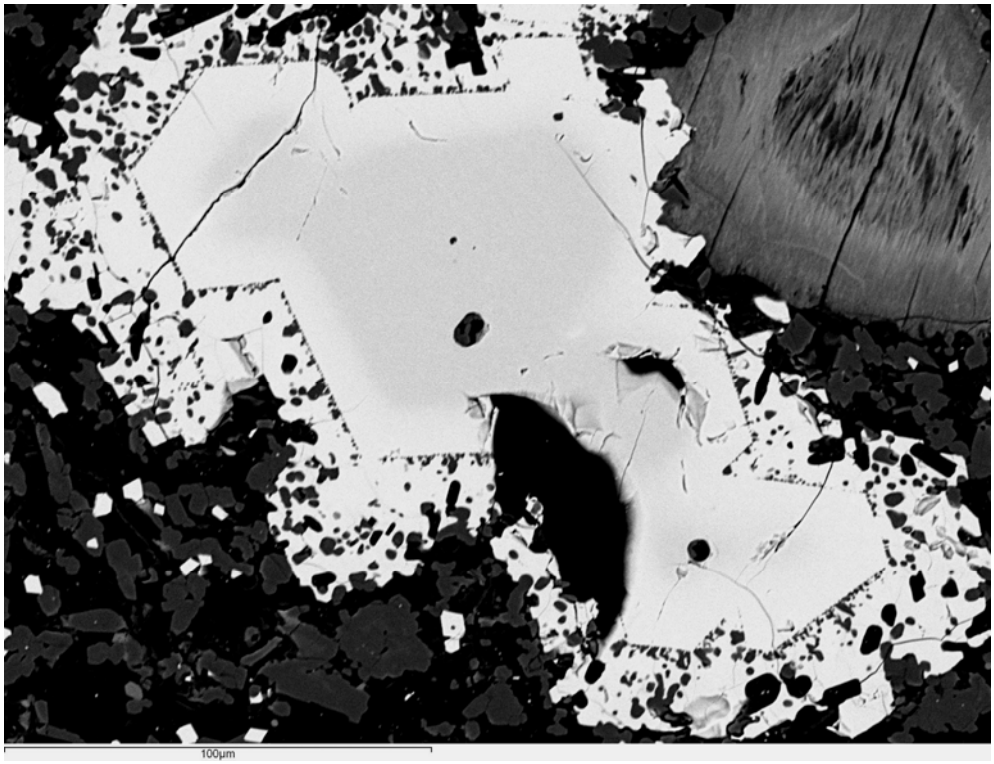

Fig.43: Backscatter image of a zoned spinel phase in thin section RH 10. The crystal is euhedral and has a ″frayed″ rim. The core is enriched in chromium relative to the rest of the crystal.

scarce in these thin sections. In contrast, ilmenite occurring in the lower parts shows number of Mg ions varying between 0.02 and 0.07 calculated for three oxygens.

5.5.2 Spinel

The second opaque phase that could be identified is a spinel. The spinel phase appears first in the thin section RH 2 and is the dominating opaque phase from thin section RH 11 on. In thin section RH 2 till RH 10 the spinel phase occurs in a lower frequency than ilmenite and is generally Cr-poor. The main striking feature of the spinel is an occasional zoning. The zoning (Fig. 43) is simple and usually features a darker grey core that is enriched in Cr relative to the rest of the crystal and a rim that features a lighter colour due to its higher Fe content. Thus, the Cr content decreases from the core to the edge whereas the concentrations of Ti and Fe increase from the core to the edges. Another feature that could be observed for the spinel phase is that the edges of the crystals can look ″frayed″ (Fig. 43).

The spinel crystal shown in figure 43 is a zoned spinel with a ″frayed″ edge from the thin section RH 10. The crystal has a Cr-rich core that can be seen due to its darker appearance in the image. The Cr-rich core is surrounded by an area with a higher Ti and Fe content. The boundary between the crystal and the ″frayed″ area is relatively sharp and characterized by an assemblage of small crystals. The ″frayed″ area has slightly higher Ti and Fe contents than the Ti- and Fe-rich area close to the core. The inclusions in the mineral were not studied in the electron microscope. Thus, their composition is unknown.

In addition, spinels with almost constant Cr, Ti and Fe contents occur as well. Up to thin section RH 8 the Ti and Fe contents are generally high whereas the Cr content is relatively low. Zoned spinels do not occur in the thin sections RH 2 till RH 8. In contrast, they appear commonly in the thin section RH 10, RH 11, RH 16 and RH 18.

In addition, the spinel phases were observed in reflected light. Here the spinel phases could easily be differentiated from ilmenite since spinel is isotropic under reflected light whereas ilmenite is anisotropic.
The Cr, Ti and Fe contents vary significantly within the spinel. Appendix 11 displays this. The concentration of Cr ranges between 0.12 and 17.45 atomic percents. The concentrations of Fe vary between 13.5 and 33.38 atomic percents and the concentration of Ti between 0.25 and 13.22 atomic percents.

In addition to the elements that occur in a higher concentration, there are a couple of elements that only occur as minor elements like Mg, Al, V and Mn.
Of these Al and Mg show the highest abundances (Table App. 11). Aluminium and magnesium increase in concentration from the core to the edges.

Four diagrams, Ti-Fe-Cr, Ti-Fe-Al, Ti-Fe-Mg and Al-Cr-Fe, are plotted. The diagrams for Ti-Fe-Al and Ti-Fe-Mg (Fig. 44) basically display the same things. The samples plot within two clusters that are close to the Fe corner of the diagram. The two clusters are a result of the zoning of the spinel phase and the associated significant variation in abundance of the elements. In addition, the clusters display either enrichment in Ti or in Al and Mg respectively.

The third diagram Al-Cr-Fe features an almost linear trend with two main clusters (Fig. 45). One cluster representing the cores plots close to a composition of Cr_{50}. Thus the Cr and Fe contents in these are almost similar. The samples of the second cluster representing the rims plot close to Fe_{90}. The samples plotting between the two clusters represent areas with rapidly decreasing Cr contents in between core and rim. The content of Al is essentially constant. The Ti-Fe-Cr diagram displays all of the already mentioned features for the other diagrams (Fig. 45).

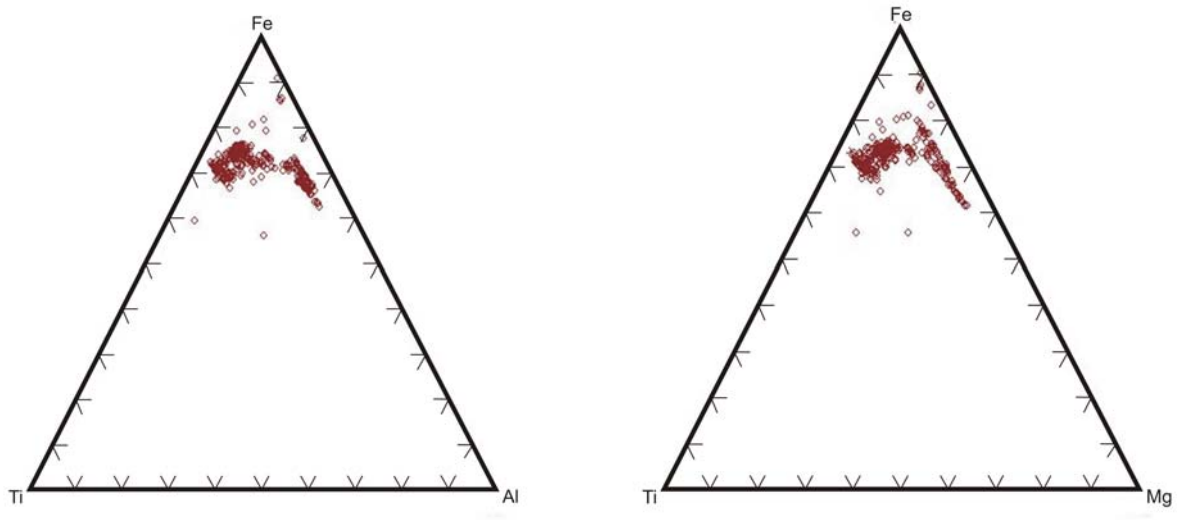

Fig.44: Ti-Fe-Al diagram (left side) and Ti-Fe-Mg diagram (right side) plotted for the spinel phase. The diagrams show two clusters representing the Cr-rich core and the Ti- and Fe-rich rims.

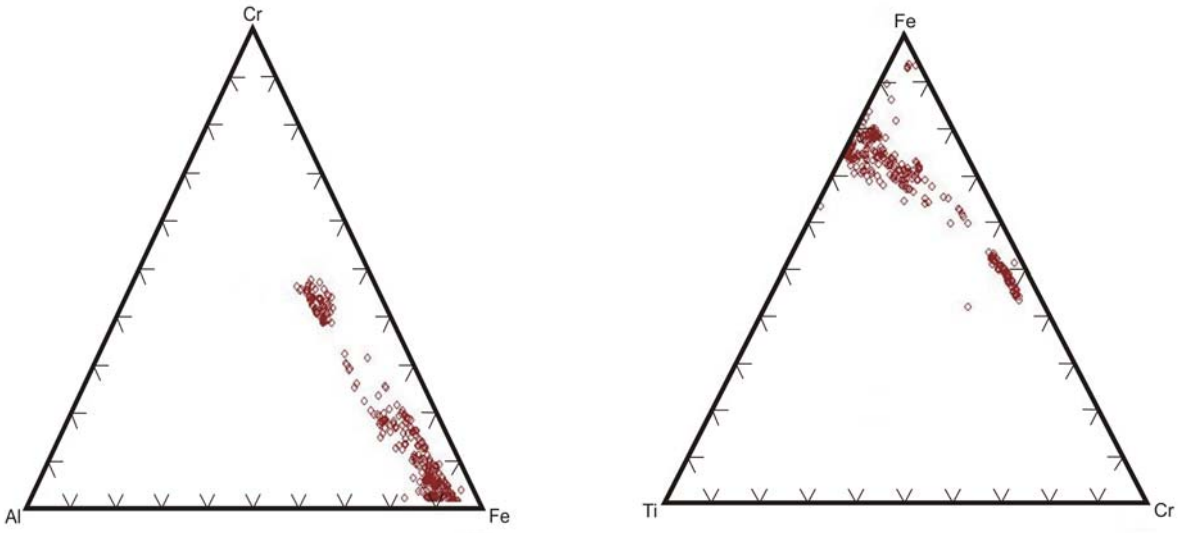

Fig.45: Al-Cr-Fe diagram (left side) and Ti-Fe-Cr diagram (right side) plotted for the spinel phase. The diagrams show two clusters representing the Cr-rich core and the Ti- and Fe-rich rims.

One of the spinel components in the studied samples from Tasartico is magnetite. This is consistent with the observation that the rocks are magnetic. In addition, it must be noted that the observed spinels are not pure magnetites due to high concentrations of Ti, Cr, Mg and Al in the spinel.

Hence, the spinel phases also have ulvöspinel, chromite, magnesium-aluminium-spinel and magnesioferrite components. The contents of the various spinel components were calculated. Titanium was calculated as ulvöspinel, chromium as chromite and magnesium and aluminium as magnesium-aluminium-spinel. The rest of the magnesium calculated as magnesioferrite. The remaining iron goes into magnetite. Hercyanite could not be identified among the spinel components.

In addition, appendix 12 also displays how the ratio of the components varies in the spinel. This variation can be linked to the clusters in the ternary diagrams. Thus, the major component in the Cr-rich

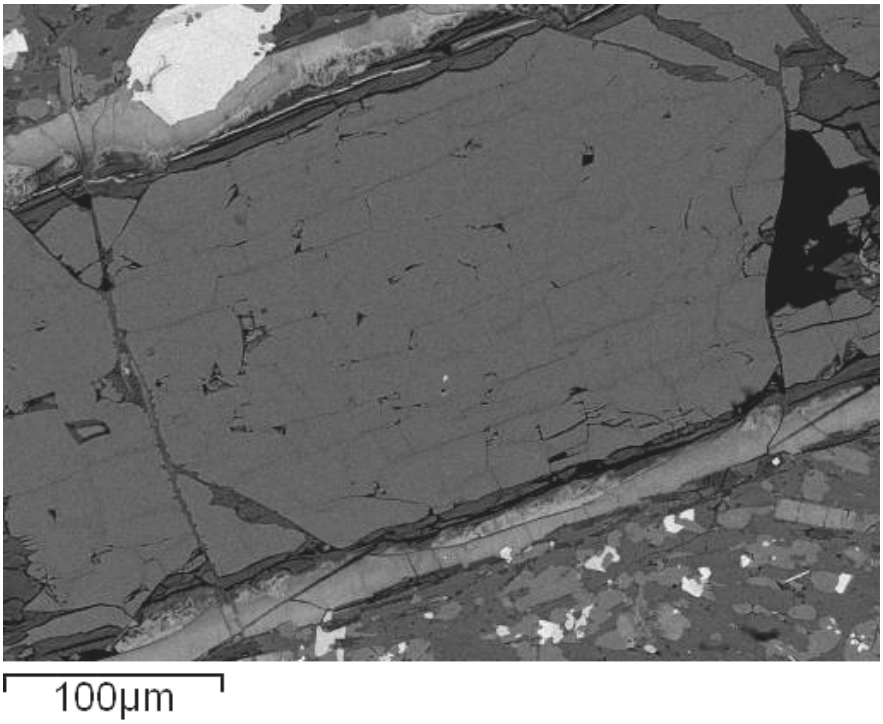

Fig. 46: Altered olivine phenocryst in thin section RH 16. The crystal features a light grey iddingsite rim. The core of the phenocryst consists of an olivine with a preserved olivine composition of Fo_{82}. The olivine already shows signs of alteration at the edges (dark grey).

core is chromite. The other components are lower. In some cases, no magnetite could be identified within the cores. The Ti- and Fe-rich edges of the crystals are made up of ulvöspinel and magnetite. In some cases, chromite could not be identified in the crystal rims.

In general, the trend displayed is that chromite decreases from the core to the rims whereas ulvöspinel and magnetite increase in the same direction. Magnesium-aluminium-spinel follows chromite. Appendix 12 confirms these trends.

5.6 Alteration products

The last minerals that were studied in the SEM are the alteration products. The only mineral that shows signs of alteration in the observed rocks is olivine. The following description is separated into iddingsite alteration and other types of alteration of olivine.

5.6.1 Iddingsite ($MgO•Fe_2O_3•3SiO_2•4H_2O$)

Iddingsite is a common alteration product of olivine and could be observed in all thin sections that contain olivine as a phenocryst phase. As already mentioned in chapter 5.1, it essentially occurs at the rims and along fractures in the crystals. Iddingsite is a pseudomorph after olivine, the external form of the phenocrysts is preserved, whereas the chemical composition has changed (Fig. 46).

According to appendix 13, Fe, Mg and Si are the major elements in iddingsite. In addition, small amounts of Ca and Na could also be identified. Titanium occurs as a minor element.

Compared to olivine, iddingsite is lower in Mg and Si, whereas the abundances of Al and Fe are higher. Thus, the chemical process that is associated with the alteration of olivine involves the addition of Fe and the removal of Mg. Calcium appears in the chemical analysis because it can substitute for Mg to some extent. According to Gay and Le Maitre (1961) Na enters iddingsite as the alteration process progresses.

Considering the formula of iddingsite the relatively low totals that range between 70 and 90 percent can easily be explained with the varying but rather large amounts of water incorporated into the mineral.

5.6.2 Altered olivine

The second alteration product that could be identified in the thin sections is also a pseudomorph after olivine. In contrast to iddingsite, this alteration product does not only occur at the edges of the former olivine minerals but affects the whole phenocryst. Thus, the phenocrysts maintain their general appearance but the chemical composition changes significantly. Furthermore, the altered olivine in most cases has an iddingsite reaction rim. Although the altered olivine crystals might look differently, they all have a similar chemical composition. Appendix 14 shows that the main elements detected are again Mg, Si and Fe. In addition, Al, Ca, K and Na occur. It is apparent that compared to olivine the contents of Mg and Fe are lower in the altered olivine, whereas the contents of Si and Ca are higher.

As was already mentioned in chapter 5.1., the altered olivine phenocrysts seem to be zoned. This observation is confirmed. Thus, the altered olivine can

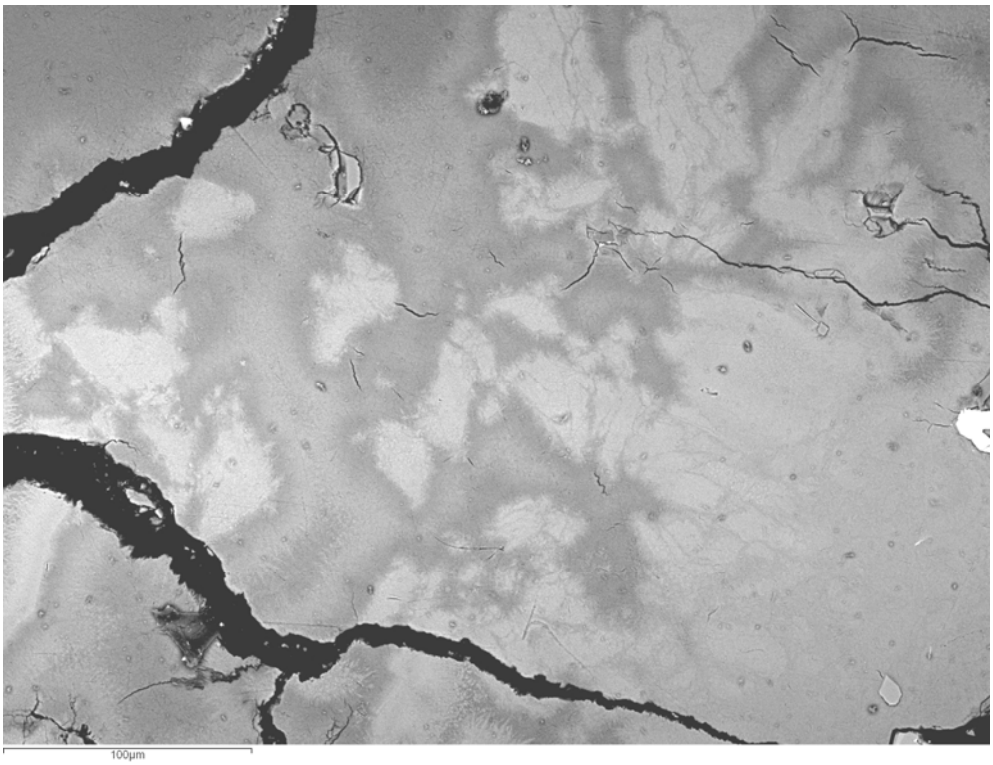

Fig.47: Altered olivine in thin section RH 2. The alteration product is relatively inhomogeneous featuring a higher iron content at the edges of the crystal.

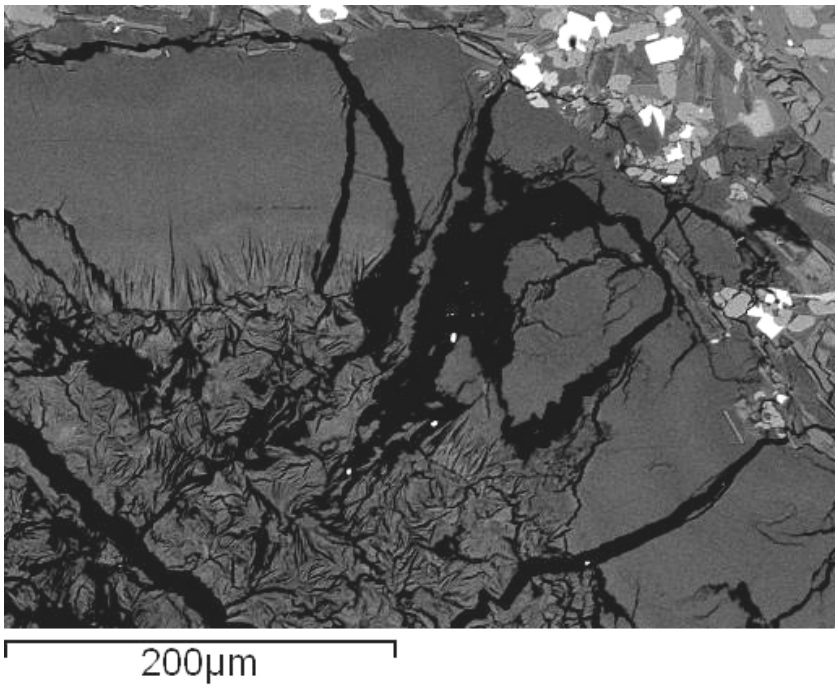

Fig.48: Altered olivine in thin section RH 13. The chemical composition of the concerned alteration product does not vary significantly. The structure that seems to be spherulitic under the polarizing microscope does not have an effect of the chemical composition.

be relatively inhomogeneous as seen in figure 47. The chemical analysis indicates that the lighter parts of the mineral are higher in Fe, Al and K, whereas the other elements occur in lower concentrations. All altered olivine crystals are not zoned although they have a spherulitic structure. An olivine crystal altered in this way is shown as an example in figure 11 in chapter 5.1. It is approximately homogenous in chemical composition and appearance in the SEM (Fig. 48).

The olivine crystal is obviously altered to a serpentine. The low sum of the analysis is consistent with the high hydroxide content in serpentine. Due to its high Fe content it is probably antigorite.

However, it should be mentioned that the chemical composition of the observed alteration products does not precisely match that of serpentine. The cation sums are too high due to too high magnesium content. This indicates that the alteration process to antigorite is not completed and some unaltered olivine might remain.

6 Discussion

6.1 Source components involved in the shield magmatism

Since no isotope analyses are included in this study earlier published isotope data (Gurenko et al., 2006; Thirlwall et al., 1997; Hoernle et al. 1991) are used to help constrain the source components involved in the shield-building magmatism on Gran Canaria. This is justified by the chemical similarities between the studied Barranco de Tasártico samples and earlier published data (Cousen et al., 1990; Gurenko et al., 2006; Schmincke, 1976 and 1982; Thirlwall et al., 1997). These results are used to test whether the Barranco de Tasártico samples can be modelled from the same source components as the rocks used in earlier published studies (Gurenko et al., 2006; Thirlwall et al., 1997; Hoernle et al. 1991).

Five diagrams were plotted using earlier published isotope data (Gurenko et al., 2006; Thirlwall et al., 1997; Hoernle et al. 1991): $^{207}Pb/^{204}Pb$, $^{208}Pb/^{204}Pb$, $^{86}Sr/^{87}Sr$ and $^{143}Nd/^{144}Nd$ were plotted versus $^{206}Pb/^{204}Pb$ (Fig. 49) and $^{143}Nd/^{144}Nd$ was plotted versus $^{86}Sr/^{87}Sr$ (Fig. 50). The four diagrams plotted versus $^{206}Pb/^{204}Pb$ display basically the same: the samples plot between the HIMU component (or low velocity component (LVC), Hoernle et al., 1995) and the depleted MORB mantle (DMM) component, diverging slightly towards the composition of the pelagic sediments or the enriched mantle (EM2) component. The HIMU-like component was called LVC by Hoernle et al. (1995) because it is associated with a sublithospheric low seismic velocity anomaly extending to depth (Gurenko et al., 2009). Gurenko et al. (2009) also interpret this component as a common plume type component found beneath the Canary and Madeira Islands, the western Mediterranean and Western Europe.

The samples plot within a restricted field to the right of the HIMU component in the $^{143}Nd/^{144}Nd$ versus $^{86}Sr/^{87}Sr$ diagram.

No isotopic data are available for the studied samples from Barranco de Tasártico. Thus, trace elements are employed to test whether these samples indicate the same mantle source components as discussed above. The diagram (Fig. 51) used is the Ba/Nb versus La/Nb diagram modified after Weaver et al. (1986). The diagram shows that the studied

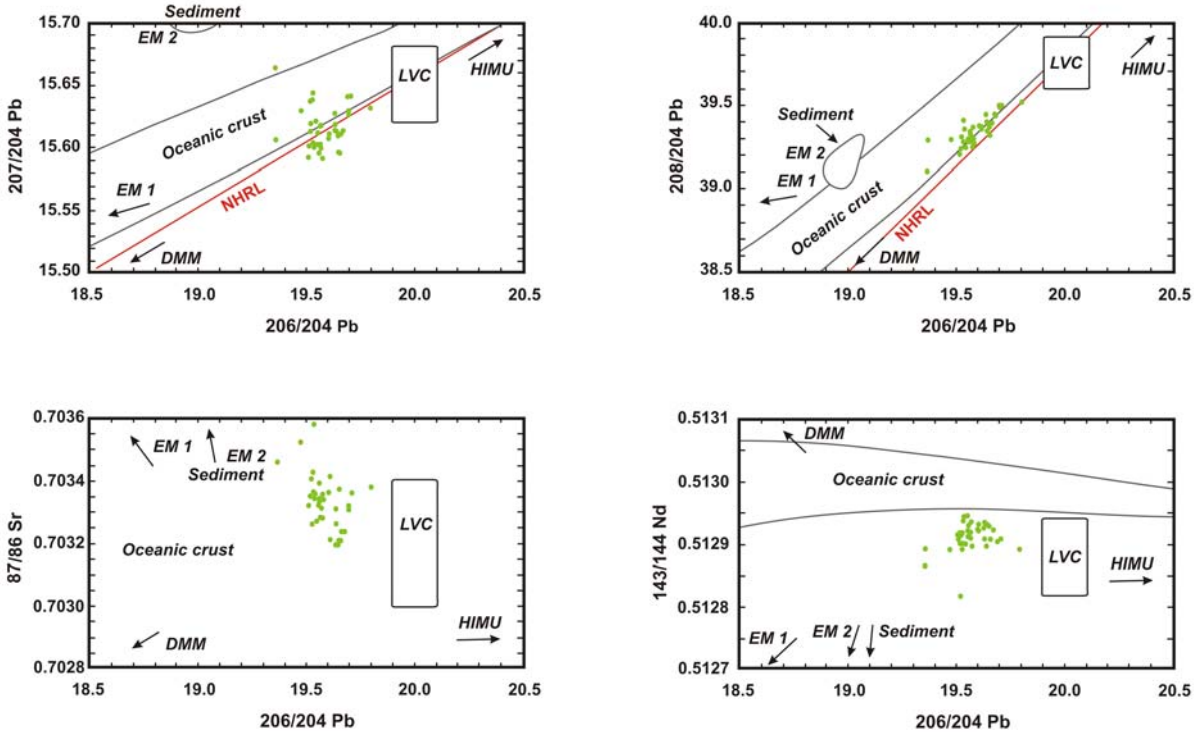

Fig.49: Plots for $^{207}Pb/^{204}Pb$, $^{208}Pb/^{204}Pb$, $^{86}Sr/^{87}Sr$ and $^{143}Nd/^{144}Nd$ versus $^{206}Pb/^{204}Pb$ for earlier published data (Gurenko et al., 2006; Thirlwall et al., 1997; Hoernle et al. 1991). HIMU- high U/Pb mantle, DMM- depleted MORB mantle, EM 1 and EM2- enriched mantle, LVC- low velocity component, NHRL- Northern Hemisphere Reference Line. The compositions of DMM, HIMU, EM1 and EM2 are taken from Zindler and Hart (1986). The composition of LVC is taken from Hoernle et al. (1995). NHRL from Hart (1984). The fields of local sediments (*Sediment)* and Layer 2 and Layer 3 pillow lava, sheet flows, dikes and gabbros (Oceanic Crust) are based on the data from Hoernle et al. (1991) and Hoernle (1998). Diagrams were modified after Gurenko et al. (2006).

Tasártico samples follow the general trend for shield-building lavas on Gran Canaria and that the samples all plot within the field of Miocene saturated mafic volcanics (SMV; Hoernle and Schmincke, 1993).

It is apparent that all samples plot between the HIMU-type component and the N-MORB depleted mantle (N-MORB DM) component diverging slightly towards the enriched mantle (EM) component. However, the divergence towards EM is more evident in the earlier published data (Cousen et al., 1990; Gurenko et al., 2006; Schmincke, 1976 and 1982; Thirlwall et al., 1997) than for the samples studied here.

Evidences indicating a HIMU–type component were already mentioned in chapter 5.3.5: the pronounced Nb and Ta enrichment ($[Nb/La]_n$=1.1-1.4, $[Ta/La]_n$=1.2-1.5) when normalized to primitive mantle and K and Pb depletion ($[K/La]_n$=0.6-0.9, $[Pb/La]_n$=0.1-0.5). Both are characteristic for HIMU-type mafic rocks. Thus, the trace elements for the rocks from Barranco de Tasártico indicate the same source components as the isotope data for the earlier pulished rocks (Gurenko et al., 2006; Thirlwall et al., 1997; Hoernle et al. 1991) from Gran Canaria.

The mixing of three mantle components is consistent with the general trend for the older, more evolved magmas from the eastern Canary Islands (Lanzarote, Fuerteventura, Gran Canaria and the Anaga Massif on Tenerife). In contrast, the younger magmas from the western Canary Islands show no divergence towards the composition of pelagic sediments or EM2 (Hoernle et al., 1991; Gurenko et al., 2006, 2009). According to Gurenko et al. (2009) the EM-type component of the shield basalts on the eastern Canary Islands is related to/derived from continental lithosphere. This could either be in the form of crustal splinters beneath the islands/seamounts or recycled subcontinental lithospheric mantle incorporated in the upper mantle (Gerlach et al., 1988; Hoernle and Tilton, 1991; Hoernle et al., 1991, 1995; Widom et al., 1999; Geldmacher and Hoernle, 2000; Hoernle et al., 2002; Lundstrom et al., 2003; Doucelance et al., 2003; Escrig et al., 2005; Geldmacher et al., 2005; Gurenko et al., 2009). Since Geldmacher et al. (2008) have confirmed an origin of the EM-type mantle through recycling of subcontinental lithosphere globally, most studies favour an origin of the EM component through plume-upper mantle interaction (Gurenko et al., 2009).

The HIMU-type signature in the ocean island basalt is the result of the recycling of deeply subducted <2 Ga old oceanic crust (Sun, 1980; Hoernle et al.,

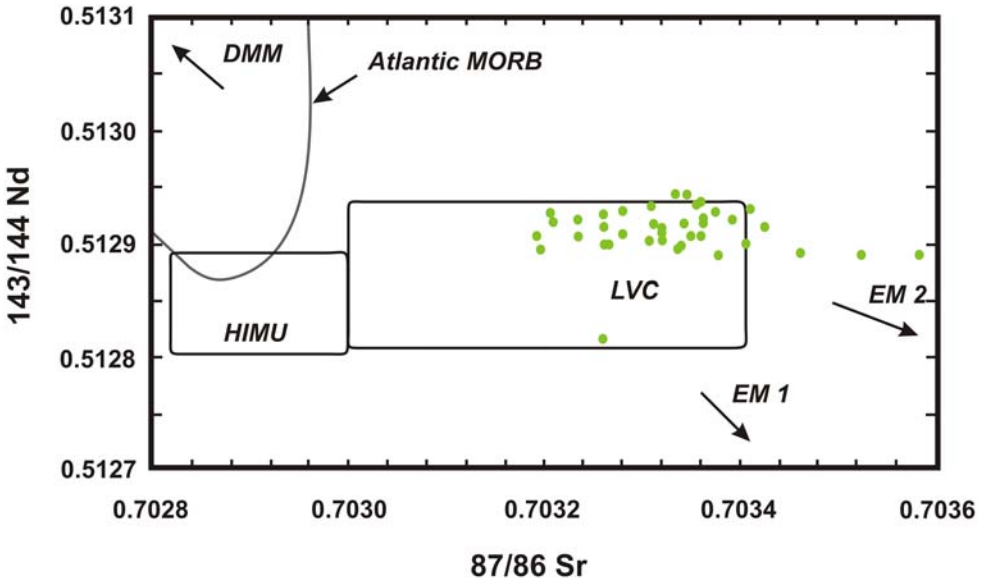

Fig. 50: Plot for $^{143}Nd/^{144}Nd$ versus $^{86}Sr/^{87}Sr$ for earlier published data (Gurenko et al., 2006; Thirlwall et al., 1997; Hoernle et al. 1991). HIMU- high U/Pb mantle, DMM- depleted MORB mantle, EM 1 and EM2- enriched mantle, LVC- low velocity component. The compositions of DMM, HIMU, EM1 and EM2 are taken from Zindler and Hart (1986). The composition of LVC is taken from Hoernle et al. (1995). Diagrams were modified after Gurenko et al. (2006).

1991; Hoernle and Tilton, 1991; Marcantonio et al., 1995; Thirlwall, 1997; Hoernle, 1998; Widom et al., 1999; Simonsen et al., 2000; Geldmacher et al., 2001 and 2005; Gurenko et al., 2006) in the form of eclogite. Since the roots of the Canary plume can be traced to the core-mantle boundary (Goes et al., 1999; Montelli et al., 2004, 2006) a generation at the core-mantle boundary is plausible. Hoernle et al. (1991) suggested that the HIMU-type component is located within the plume and reflects mixing of recycled altered oceanic crust in the plume and N-MORB from the asthenosphere.

Isotope data are not the only data suggesting that the sources of the older eastern Canary Islands and the younger western Canary Islands are distinct from each other. Several trace element ratios can also be employed to show the same thing. Thus, the studied samples from Barranco de Tasártico show relatively low Ba/Nb (3.4-5.3) and Ba/Th ratios (42-58), whereas the ratios for K/La (217-292) and Zr/Nb (6.0-7.6) are relatively high compared to the ratios for the western Canary Islands (Ba/Nb=3.6-7.7, Ba/Th=51-108, K/La=65-239 and Zr/Nb=3.6-6.6, Gurenko et al., 2006). Hoernle and Tilton (1991), Hoernle et al. (1991), Abratis et al. (2002), Lundstrom et al. (2003) and Gurenko et al. (2006) suggest that this general difference between the western and eastern Canary Islands is a result of a temporal change in the composition of the plume or reflects a difference in the lithosphere beneath the eastern and western Canary Islands.

6.2 Parental magma

The source rock that has melted to give a magma similar to the studied lavas from Barranco de Tasártico must either have a peridotitic or eclogitic composition. Characteristics of both materials that qualifying them as possible candidates for the generation of basaltic magmas are:

1) their occurrence is appropriate for deep-seated environments
2) their mineral assemblages are stable at high pressures and temperatures and
3) they have the appropriate densities and seismic velocities since they are mainly made up of garnet+omphacite (eclogite) and clinopyroxene +olivine+garnet (garnet peridotite).

These two materials have been discussed earlier and several models have been developed favouring either peridotite or eclogite as the possible source material. However, also a combination of both materials has recently been discussed by Gurenko et al. (2006, 2009).

As was already mentioned in chapter 6.1 it is generally accepted that the source material for the Gran Canarian shield-building lavas has a HIMU-type signature. The HIMU signature is associated with the subduction of <2 Ga old eclogitic oceanic crust (Morgan, 1971; Hofmann and White, 1982; Kellogg et al., 1999; Albarède and van der Hilst, 1999).

However, Gurenko et al. (2009) suggest that the HIMU-type rock component in the Canaries is not limited to eclogite but could also be peridotite. They

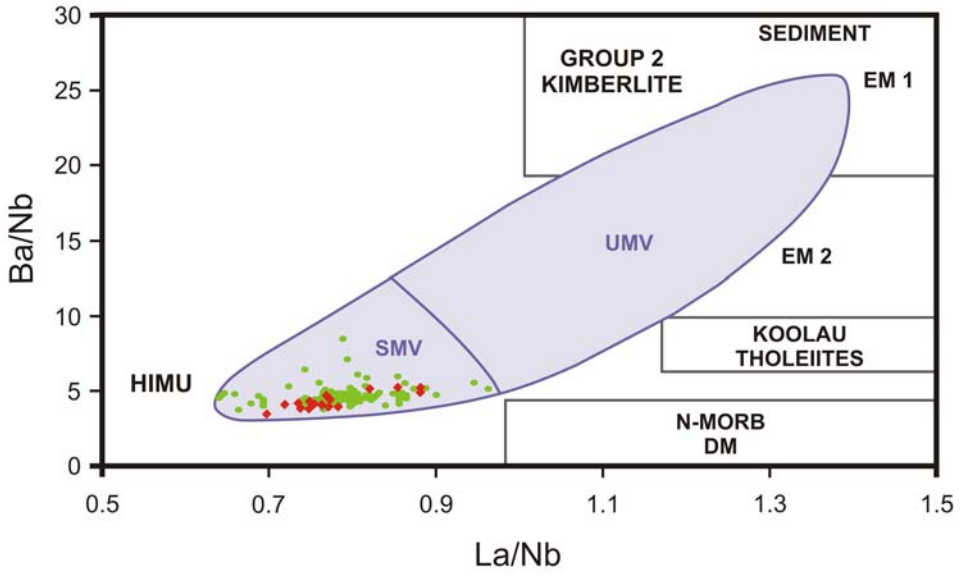

Fig.51: Ba/Nb versus La/Nb for the studied samples from Barranco de Tasártico (red squares) in comparison with earlier published data (Cousen et al., 1990; Gurenko et al., 2006; Schmincke, 1976 and 1982; Thirlwall et al., 1997). The samples follow the general trend and plot within the field of Miocene saturated mafic volcanics (SMV; Hoernle et al., 1993). The diagram is modified after Weaver et al. (1986).

based their suggestion on olivine chemistry. Since melts derived from peridotite have high Ni and low Ca contents, olivine crystallized from such magma would also have high Ni and low Ca contents. The studied olivine phenocrysts from Barranco de Tasártico show low Ca contents. Ni was not noted in the olivine phenocrysts from Barranco de Tasártico. There are suggestions of Ni contents close to the detection boundary (0.2% at the used analytical conditions) in some olivine spectra. Since olivine fractionation has taken place, it can be assumed that the earliest Ni-rich olivine phenocrysts are not present in the rocks from Barranco de Tasártico anymore. The absence of these early Ni-rich olivine phenocrysts could result in the observed low Ni contents. Thus, an explicit conclusion concerning the Ni content for the olivine phenocrysts cannot be given. The suggestion of Gurenko et al. (2009) that the HIMU component could be derived from 1.2 Ga old (Widom et al., 1999) recycled oceanic crust in the form of eclogite that has been stirred into or reacted with ambient peridotitic mantle in the Canary source cannot be tested with the present data from Barranco de Tasártico.

A "peridotite-based" model to explain the origin of the HIMU component was proposed by Halliday et al. (1995). This model suggests that the HIMU component could be derived through metasomatism of the oceanic lithospheric mantle. This occurs at the time of formation of the lithosphere by small degree partial melts produced in equilibrium with a combination of residual upper mantle major silicate phases together with minor accessory phases such as amphibole, sulphide and phlogopite (Gurenko et al., 2009). Thus, the HIMU signature could be explained with the recycling of lithospheric mantle (Gurenko et al., 2009).

One of the factors arguing against a single source for the shield-building lavas is the Zr/Y ratio. In the studied samples from Barranco de Tasártico this ratio ranges between 9.7-11.8 (Table App. 3). According to Gurenko et al. (2006) a Zr/Y ratio ranging between 6.7 and 10.3 can be explained by low degrees of partial melting (1-10%) of a peridotite source containing 2-20% garnet. This is based on a batch model of partial melting. For their calculation, they used a primitive mantle composition with initial Zr and Y concentrations as proposed by Hofmann (1988). Gurenko et al. (2006) state that higher Zr/Y ratios can only be explained by low degree partial melting of peridotite that contains more than 30% garnet. This is higher than expected in garnet peridotite. If the studied samples from Barranco de Tasártico are plotted in the diagram: Zr/Y ratio versus $(La/Sm)_n$ modified after Gurenko et al. (2006) it is apparent that the high Zr/Y ratios also require unrealistic high garnet contents (Fig.52). In this connection it must be mentioned that it was not possible to calculate the degree of partial melting for the studied samples from Barranco de Tasártico due to a significant differentiation (chapter 5.3.4). Since the studied lavas from Barranco de Tasártico plot in the same area as the earlier published data (Gurenko et al., 2006) a low degree partial melting (5-10%) can be assumed.

Thus, it can be concluded that peridotite cannot be the only source for the studied shield-building lavas from Barranco de Tasártico. This however, is

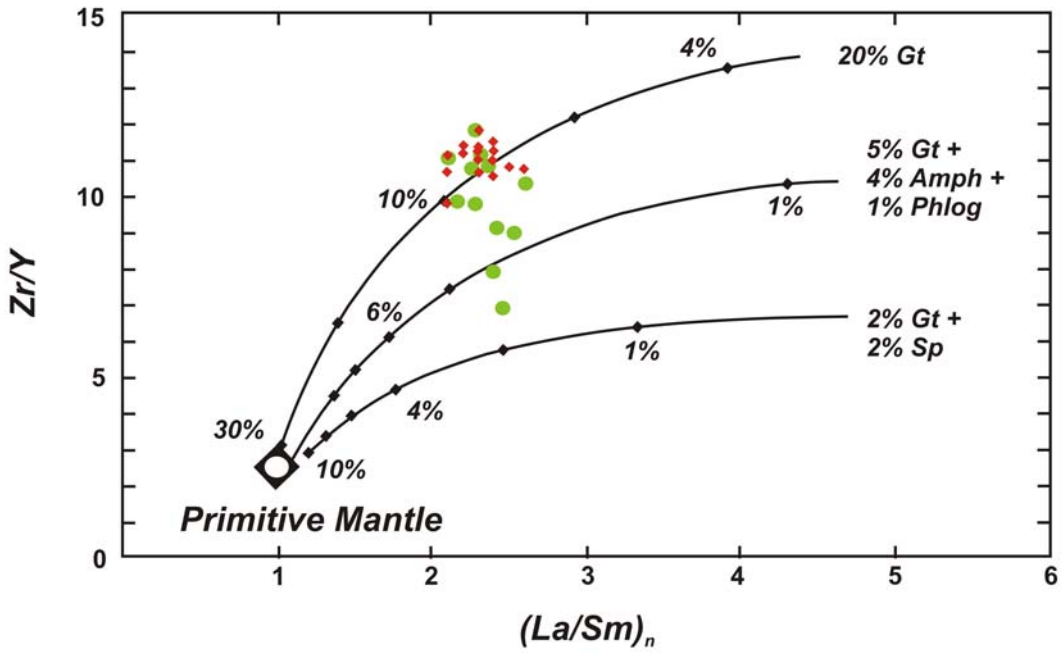

Fig.52: Zr/Y ratio plotted versus $(La/Sm)_n$ for the shield-building lavas from Barranco de Tasártico (red squares) in comparison to earlier published data (Gurenko et al., 2006) in green circles. This demonstrates the effect of partial melting of a peridotite source with varying amounts of garnet as suggested by Gurenko et al. (2006). Solid lines represent melt compositions resulting from batch melting (Shaw, 1970) of a peridotite with a composition corresponding to primitive mantle (Hofmann, 1988). Diagram modified after Gurenko et al. (2006).

dependent on how primitive the mantle beneath the Canary Islands is. Since this cannot be estimated due to the fact that the studied samples do not resemble the original composition of the mantle source because of fractional crystallization of clinopyroxene, olivine and plagioclase. Thus, it can only be assumed that peridotite cannot be the only source.

Eclogite contains more garnet than peridotite. Since Y is compatible in garnet, whereas Zr is not, high Zr/Y ratios could be produced if garnet resides in the restite. This however, requires that garnet is a residual phase in the melt which is contradicted by the gentle slope of the REE diagram (Fig. 31).

There are several possible explanations for the high Zr/Y ratios. One possibility is that Zr and Y could have been fractionated before the formation of the source took place. However, the obtained data from Barranco de Tasártico do not provide proof for this hypothesis.

Another explanation could be that clinopyroxene affects the Zr/Y ratios. To test whether this is the case the Zr/Y ratio was plotted versus the Mg/Fe ratio (Fig. 53). This diagram suggests that Zr/Y increases with decreasing Mg/Fe. However, the increase is rather low. Since it is not possible to calculate the amount of early fractionated clinopyroxene it is not possible to estimate the total effect of clinopyroxene fractionation on the Zr/Y ratios.

Hence, no unambiguous explanation for the high Zr/Y ratios can be given with the obtained data from Barranco de Tasártico.

The depletion of K and Ba as displayed in the normalized multi-element diagram (chapter 5.3.5) can provide indications for the source material too. According to Gurenko et al. (2006) amphibole and/or phlogopite in association with garnet and ilmenite could fractionate Ba, Nb and K from other incompatible elements due to relatively high amphibole-melt and phlogopite-melt partition coefficients (e.g. LaTourrette et al., 1995; Halliday et al., 1995; White, 1997). This is consistent with previously reported data from Schmincke and Flower (1974), Hoernle and Schmincke (1993b), Neumann et al. (1999), Wulff-Pedersen et al. (1999) and Lundstrom et al. (2003). Since amphibole and phlogopite are not stable at high temperatures and pressures they break down during the subduction of the oceanic crust. Elements like K, Ba and Rb that are compatible in these minerals would be lost to the subarc mantle (Gurenko et al., 2006). This results in the depletion of the mentioned elements as apparent in the normalized multi-element diagram plotted for the studied Barranco de Tasártico samples (chapter 5.3.5). Thus, the explanation for the observed depletion in K, Ba and Rb is the recycling of oceanic crust into peridotitic mantle in the Canary source.

In addition, it must be mentioned that oceanic crust is generally depleted in K, Rb and Ba. Thus, the observed pattern in the normalized multi-element diagram (Fig. 32) could resemble the general pattern in the oceanic crust instead of being the result of amphibole and phlogopite breakdown during subduction. The observed pattern in the normalized multi-element diagram reflects the involvement of

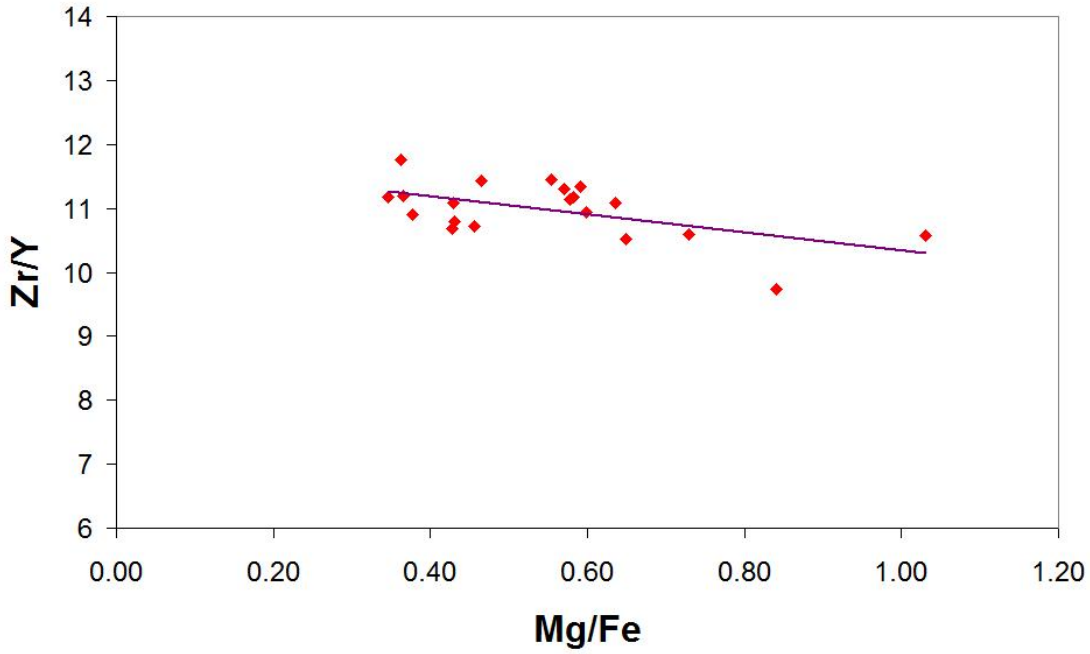

Fig.53: Plot for Zr/Y versus Mg/Fe for the studied samples from Barranco de Tasártico. The purple line represents the general trend line.

recycled oceanic crust (eclogite). The ƐNd for earlier published data (Hoernle et al., 1991; Thirlwall et al., 1997) ranges between 3.9 and 5.8. This is rather high for an ocean island. This also suggests that the source material contains appreciable amounts of depleted material in the form of subducted oceanic crust (eclogite).

However, it was not possible to provide unambiguous evidence for the parental source of the shield-building lavas from Barranco de Tasártico with the obtained data. The involvement of subducted oceanic crust is probable from the depletion in K, Rb and Ba in the normalized multi-element diagram. Evidences for the involvement of peridotite suggested by Gurenko et al. (2006) could not unambiguously be transferred to the shield-building lavas from Barranco de Tasártico. This is mostly due to fractional crystallization. Thus, high Ni and low Ca contents in olivine phenocrysts could not be used without limitation since Ni contents are rather low due to fractionation of Ni-rich early olivines. Variations in Zr/Y ratios cannot be explained by low degree partial melting of garnet peridotite or melting of eclogite, since the resulting significant content of garnet among the residual phases is inconsistent with the weak differentiation of the REEs (Fig. 31). The effect of clinopyroxene on the Zr/Y ratio cannot be conclusively determined and the fractionation of Zr and Y before the formation of the source material is uncertain. Consequently, Zr/Y ratios cannot be ascribed to one particular source material.

In addition, low Ba/Nb (3.4-5.3) and high K/La (217-292) ratios cannot be explained by a single source containing varying proportions of garnet. Hence, a mixture of two parental sources seems inevitable.

Thus, the present data do not contradict earlier suggestions of the source rock components. Earlier published rather high values of ƐNd indicate a high content of a depleted component. This is consistent with the suggestion by Gurenko et al. (2006). They state that compared to the western Canary Islands the reported lower CaO contents and CaO/Al_2O_3 ratios as well as the higher SiO_2 contents (chapter 5.2.2) indicate a higher eclogite versus peridotite ratio for Gran Canaria.

6.3 Primary magma and fractional crystallization

As was already mentioned, the primary magmas for the shield-building lavas from Gran Canaria are believed to be picritic. They formed within the garnet stability field at temperatures between 1500°C and 1600°C and pressures of 3 GPa (Schmincke, 1982; Hoernle and Schmincke, 1993a; Heuschkel, 1996; Gurenko et al., 1996, 1998).

Major and trace element plots (chapter 5.2.2) suggest that the main process affecting the primary magma composition was fractional crystallization of clinopyroxene and olivine, joined at a later stage by plagioclase. The effect of plagioclase fractionation is small compared to that of clinopyroxene and olivine. This conclusion is based on the missing negative Eu anomaly in the REE patterns (chapter 5.3.4) and the trends of the bivariate plots for the major and trace elements presented in chapters 5.2.2 and 5.3.1. No apatite crystallization could be observed even in the

most evolved samples studied.

Crystal fractionation of olivine, clinopyroxene and plagioclase slowly increases the SiO_2 content in the melt. This changes the composition of the primary picritic magma in the direction of a basaltic composition. The composition becomes more basaltic the more advanced the fractional crystallization is.
Thus, the samples RH 3 to RH 6 display:

1) a highest degree of evolution observed for the Tasártico samples and
2) the highest degree of fractional crystallization.

The compositions of these samples differ most from that of the primary picritic magma. The samples with the lowest SiO_2 contents plot within the picro-basalt and basanite field of the TAS-diagram (chapter 5.2.1) and have a composition that is most similar to that of the primary magma. Particular attention should be paid to sample RH 19. This sample features the highest MgO content (16.0 wt%) and the highest abundances of Ni (514 ppm) and Cr (1059 ppm). The sample RH 19 is the least differentiated one.

The more evolved the samples are the lower they are in Mg, Fe and Ca. This is explained with fractional crystallization of olivine and pyroxene leaving the residual melt enriched in silica and depleted in Mg, Fe, and Ca.

RH 19 is the least modified sample and resembles the primary magma most, but nevertheless it also has experienced differentiation. This makes it plausible that the parental magma is picritic. Picritic magmas have $SiO_2 < 47\%$, Na2O+K2O < 2% and MgO > 18%. This is not too different to the composition of RH 19 (SiO_2= 44.7, MgO=16.0 and Na_2O+K_2O= 2.3). Thus, the mentioned effects of fractional crystallization (SiO_2 enrichment, depletion in Mg, Ca and Fe) change the picritic composition in the direction of the obtained whole rock compositions from the Barranco de Tasártico samples. Fractional crystallization also results in enrichment in incompatible phases.
However, crystallization of the phenocryst phases occurred at high temperatures and low pressures as indicated by olivine and clinopyroxene phenocrysts. Hence, the olivine crystallization temperatures calculated according to the magnesium equation of Roeder and Emslie (1970) range between 1172 and 1218°C (chapter 5.4.2). Clinopyroxene phenocrysts indicate that the crystallization occurred at low pressures since no jadeite component could be identified within the samples. End-component calculations suggest aegirine in all analysed clinopyroxene crystals as already mentioned in chapter 5.4.1.

It is suggested that disequilibrium during cooling resulted in zoned clinopyroxene and plagioclase phenocrysts. The zoning studied in the clinopyroxene is the result of higher Al, Fe and Ti contents at the rims of the crystals. Plagioclase minerals have rims that are moderately enriched in K, Na and Si compared to the rest of the crystals.

7 Conclusions

- The studied shield-building lavas from Barranco de Tasártico range from picrobasalt to basalt and basanite. Phenocryst phases are clinopyroxene, olivine and plagioclase.
- Clinopyroxene phenocrysts range between augite and diopside. Calculations suggest that Tschermak substitution and aegirine occur in all samples. Zoning of the clinopyroxene crystals is the result of higher Al, Fe and Ti contents at the rims of the crystals. A jadeite component could not be identified within the samples, suggesting phenocryst crystallization at low pressures.
- Olivine phenocrysts are generally altered and range between Fo_{79} and Fo_{88}. Crystallization temperatures calculated range between 1172 and 1218°C.
- Plagioclase phenocrysts are mainly labradorite. Disequilibrium during crystallization results in higher K, Na and Si contents at the rims.
- The early fractionation pattern is controlled by clinopyroxene and olivine. At a MgO content of 8 wt% they are joined by plagioclase.
- The shield-building lavas are generally enriched in incompatible trace elements. The enrichment can be linked to fractional crystallization.
- Transition metal like Ni and Cr are controlled by fractional crystallization of olivine and clinopyroxene.
- The opaque phases are ilmenite and chromium spinel. Ilmenite represents the dominant opaque phase in the lower parts of the studied stratigraphy whereas chromium spinel is dominant mainly in the upper parts.
- Magnetite, ulvöspinel, chromite, magnesium-aluminium-spinel and magnesioferrite are the components of the chromium spinel.
- Chromium spinel is zoned: Cr, Mg and Al decrease from the core to the rim. Fe and Ti increase in the same direction.
- Iddingsite occurs mainly at the rims of the crystals and along cracks. Serpentinization affects the whole crystal. The serpentine is classified as antigorite.
- Trace element data suggests derivation from a mantle source different from the MORB source. A relatively moderate enrichment of LREE compared to HREE indicates that garnet as a residual phase can be excluded. The strong enrichment in Nb and Ta as well as depletion in K and Pb is characteristic for mafic HIMU-type magmas. The plot for Ba/Nb versus La/Nb resembles a mixture of three source components: HIMU-type, DMM-type and EM-type components.
- An unambiguous explanation for high Zr/Y ratios cannot be offered since the total effect of clinopyroxene on the Zr/Y ratio cannot be estimated and it cannot be determined whether Zr/Y ratios were high already in the source

material.

- Depletion of K, Ba and Rb in the normalized multi-element diagram can only be associated with subducted oceanic crust. The impact of depleted lithospheric crust is also suggested by published high ℇNd values.
- Low Ba/Nb (3.4-5.3) and high K/La (217-292) ratios cannot be explained by a single source containing varying proportions of garnet. Thus, a mixture of two parental sources seems inevitable.
- The source components probably are recycled subducted oceanic crust (<2 Ga) and ambient peridotitic mantle (Gurenko et al., 2006).

8 Acknowledgments

This thesis gave me the opportunity to discover new aspects of igneous geology as well as new analysis methods. Special thanks go to Anders Lindh, my supervisor at Lund University, for making this thesis possible and for discussing and reviewing it. Your guidance during the sample preparation and the work with the scanning electron microscope is greatly appreciated. I want to thank Thomas Degen, my supervisor at the Martin-Luther University Halle-Wittenberg, for supporting this thesis. I also want to thank Ulf Söderlund and Johan Olsson for their support during the collection of the samples on Gran Canaria.

9 References

Abratis, M., Schmincke, H.U. and Hansteen, T.H. (2002): Composition and evolution of submarine volcanic rocks from the central and western Canary Islands. International Journal of Earth Science. 91. pp. 562-582.

Albarède, F. and Hilst, R.D.v.d (1999): New mantle convection model may reconcile conflicting evidence. EOS. 80. pp. 537-539.

Anguita, F. (1972): La evolucion magmatica en el ciclo Roque Nublo (Gran Canaria). Estud. Geol. 28. pp. 377-482.

Anguita, F. (1973): Genesis of Roque Nublo Formation: a special kind of ignimbrite eruption in Gran Canaria. Bulletin of Volcanology. 37. pp. 111-121.

Anguita, F. and Hernán, F. (1975): A propagating fracture model versus a hotspot origin for the Canary Islands. Earth and Planetary Science Letters. 27. pp. 11-19

Anguita, F. and Hernán, F. (2000): The Canary Islands origin: a unifying model. Journal of Volcanology and Geothermal Research. 103. pp. 1-26.

Araña, V. and Carracedo, J.C. (1978): Los Volcanos de las Islas Canarias. III Gran Canaria. Rueda. Madrid. 175 pp.

Araña, V. and Ortiz, R. (1986): Marco geodina Âmico del volcanismo canario. An. Física. Vol. Esp. 82. pp. 202-231.

Brey, G. and Schmincke, H.U. (1980): Origin and diagenesis of the Roque Nublo breccia, Gran Canaria (Canary Islands). Petrology of Roque Nublo Volcanics II. Bulletin of Volcanology. 43. pp. 15-33.

Bogaard, P.v.d. and Schmincke, H.U. (1998): Chronostratigraphy of Gran Canaria. In: Weaver, P.P.E., Schmincke, H.U., Firth, J.V. and Duffield, W. (Eds.): Proceeding Ocean Drilling Program. Scientific Results. 157. pp. 127-140.

Bosshard, E. and MacFarlane, D.J. (1970): Crustal structure in the western Canary Islands from seismic refraction and gravity data. Journal of Geophysical Research. 75. pp. 4901-4918.

Araña, V. and Ortiz, R. (1991): The Canary Islands: Tectonics, magmatism and geodynamic framework. In: Kampunzu, A.B. and Lubala, R.T. (Eds.), Magmatism in Extensional Structural Settings: the Phanerozoic African Plate. Springer. New York. pp. 209-249.

Carracedo, J.C., Day, S., Guillou, H., Rodriguez Badiola, E., Canas, J.A. and Perez-Torrado, F.J. (1998): Hotspot volcanism close to a passive continental margin. The Canary Islands. Geological Magazine. 135. Issue 5. pp. 591-604.

Carracedo, J.C., Pérez-Torrado, F.J., Ancochea, E., Meco, J., Hernán, F., Cubas, C.R., Casillas, R., Rodríguez-Badiola, E. and Ahijado, A. (2002): Cenozoic Volcanism II, The Canary Islands. In: Gibsson, W. and Moreno, T. (Eds.), The Geology of Spain. The Geological Society. London. pp. 439–472.

Cousen, B.L., Spera, F.J. and Tilton, G.R. (1990): Isotopic patterns in silicic ignimbrites and lava flows of the Mogan and lower Fataga Formations, Gran Canaria, Canary Islands: temporal changes in mantle source composition. Earth and Planetary Science Letters. 96. pp. 319-335.

Cox, K.G., Bell, J.D. and Pankhurst, R.J. (1979): The interpretation of igneous rocks. Unwin Hyman. London.

Deer, J., Howie, R.A. and Zussman, J. (1963): Rock-forming minerals. Volume 4 Framwork silicates. Longman. London.

Doucelance, R., Escrig, R., Moreira, M., Gariepy, C. And Kurz, M.D. (2003): Pb-Sr-He isotope and trace element geochemistry of the Cape Verde Archipelago. Geochimica et cosmochimica Acta. 67. pp. 3717-3733.

Escrig, S, Doucelance, R., Moreira, M. and Allegre, C.J. (2005): Os isotope systematics in Fogo Island: evidence for lower continental crust fragments under the Cape Verde Southern Islands. Chemical Geology. 219. pp. 93-113.

Fuster, J.M. (1975): Las Islas Canarias: un ejemplo de evolución temporal y espacial del vulcanismo oceánico. Est. Geol. 31. pp. 439-463.

Fuster, J.M., Hernández-Pacheco, A., Muñoz, M., Rodriguez, E. and García, L. (1968): Geología y Vulcanología de las Islas Canarias. Gran Canaria. Intitut Lucas Mallada. 243 pp.

Gay, P. and Le Maitre, R.W. (1961): Some observations on iddingsite. American Mineralogist. 46. pp. 92-111.

Geldmacher, J. and Hoernle, K. (2000): The 72 Ma geochemical evolution of the Madeira hotspot (eastern North Atlantic): recycling of Paleozoic (≤500 Ma) basaltic and gabbroic crust. Earth and Planetary Science Letters. 183. pp. 73-92.

Geldmacher, J, Hoernle, K., Bogaard, P.v.d., Zankl, G. and Garbe-Schönberg, D. (2001): Earlier history of the 70 Ma-old Canary hotspot based on the temporal and geochemical evolution of the Selvagen Archipelago and neighboring seamounts in the eastern North Atlantic. Journal of Volcanology and Geothermal Research. 111. pp. 55-87.

Geldmacher, J., Hoernle, K., Bogaard, P.v.d., Duggen, S. and Werner, R. (2005): New 40Ar/39Ar age and geochemical data from seamounts in the Canary and Madeira volcanic province: support fort he mantle plume hypothesis. Earth and Planetary Science Letters. 237. pp. 85-101.

Geldmacher, J., Hoernle, K., Bogaard, P.v.d. and Bindemann, I. (2008): Geochemistry of a new eniched mantle type locality in the northern hemisphere: implications for the origin of the EM-I source. Earth and Planetary Science Letters. 265. pp.167-182.

Gerlach, D.C., Cliff, R.A., Davies, G.R., Norry, M.J. and Hodgson, N.R. (1988): Magma sources of the Cape Verde archipelago: isotopic and trace element constraints. Geochimica et cosmochimica Acta. 52. pp. 2979-2993

Goes, S., Spakman, W. and Bijwaard, H. (1999): A lower mantle source for Central European volcanism. Science. 268. pp. 1928-1931.

Guillou, H., Pérez-Torrado, F.J., Machin, A.R.H., Carracedo, J.C. and Gimeno, D. (2004): The Plio-Quarternary volcanic evolution of Gran Canaria based on new K-Ar ages and magnetostratigraphy. Journal of Volcanology and Geothermal Research. 135. pp. 221-246.

Gurenko, A.A., Hansteen, T.H. and Schmincke, H.U. (1996): Evolution of parental magmas of Miocene shield basalts of Gran Canaria (Canary Islands): constraints from crystal, melt and fluid inclusions in minerals. Contributions to Mineralogy and Petrology. 124. pp. 422-435.

Gurenko, A.A., Hansteen, T.H. and Schmincke, H.-U., (1998): Melt, crystal, and fluid inclusions in olivine and clinopyroxene phenocrysts from the submarine shield stage hyaloclastites of Gran Canaria, Sites 953 and 956. In: Weaver, P.P.E., Schmincke, H.-U., Firth, J.V., Duffield, W. (Eds.): Proceedings of the Ocean Drilling Program. Scientific Results. 157. Ocean Drilling Program, College Station, TX. pp. 375–401.

Gurenko, A.A., Hoernle, K.A., Hauff, F., Schmincke, H.-U., Han, D., Miura, Y.N. and Kaneoka, I. (2006): Major, trace element and Nd-Sr-Pb-O-He-Ar isotope signatures of shield stage lavas from the central and western Canary Islands: Insights into mantle and crustal processes. Chemical Geology. 233. pp. 75-112.

Gurenko, A.A., Sobolev, A.V., Hoernle, K.A., Hauff, F. and Schmincke, H.U. (2009): Enriched, HIMU-type peridotite and depleted recycled pyroxenite in the Canary plume: A mixed-up mantle. Earth and Planetary Science Letters. 277. pp. 514-524.

Halliday, A.N., Lee, D.C., Tommasini, S., Davies, G.R., Paslick, C.R., Fitton, J.G. and James, D.E. (1995): Incompatible trace elements in OIB and MORB and source enrichment in the sub-oceanic mantle. Earth and Planetary Science Letters. 133. pp. 379-395.

Hart, S.R. (1984): A large-scale isotope anomaly in the Southern Hemisphere mantle. Nature. 309. pp. 753–757.

Heuschkel, S. (1996): Die miozänen Schildbasalte von Gran Canaria: Stratigraphische and geochemische Untersuchungen zum Aufbau and zur Entwicklung der Schildphase einer ozeanischen Vulkaninsel im Atlantic. Ph. D. thesis, University Kiel.

Hilst, R.v.d., Widiyantoro, R.S. and Engdahl, R. (1997): Evidence for deep mantle circulation from global tomography. Nature. 386. pp. 578–584.

Hoernle, K. (1998): Geochemistry of Jurassic oceanic crust beneath Gran Canaria (Canary Islands): implications for crustal recycling and assimilation. Journal of Petrology. 39. pp. 859-880.

Hoernle, K. and Schmicke, H.U. (1993): The role of partial melting in the 15-Ma geochemical evolution of Gran Canaria: A blob model for the Canary Hotspot. Journal of Petrology. Volume 34. Part 3. pp. 599-626.

Hoernle, K. and Tilton, G.R. (1991): Sr-Nd-Pb isotope data for Fuerteventura (Canary Islands) basal complex and subaerial volcanics: application to magma genesis and evolution. Schweizer Mineralogisch Petrologische MItteilungen. 71. pp. 5-21.

Hoernle, K., Tilton, G., Le Bas, M.J., Duggen, S. and Garbe-Schönbeg, D. (2002): Geochemistry of oceanic carbonatites compared with continental carbonatites: mantle recycling of oceanic crustal carbonate. Contributions to Mineralogy and Petrology. 142. pp. 520-542.

Hoernle, K., Tilton, G. and Schmincke, H.U. (1991): Sr-Nd-Pb isotopic evolution of Gran Canaria: evidence for shallow enriched mantle beneath the Canary Islands. Earth and Planetary Science

Letters. 106. pp. 44-63.
Hoernle, K., Zhang, Y.S. and Graham, D. (1995): Seismic and geochemical evidence for large-scale mantle upwelling beneath the eastern Atlantic and western and central Europe. Nature. 374. pp. 34-39.
Hofmann, A.W. and White, W.M. (1982): Mantle plumes from ancient oceanic crust. Earth and Planetary Science Letters. 57. pp. 421-436.
Hofmann, A.W. (1988): Chemical differentiation of the Earth: the relationship between mantle, continental crust and oceanic crust. Earth and Planetary Letters. 90. pp. 297-314.
ITGE (1992): Mapa geologico de españa escala 1:25000. Gran Canaria San Nicolas de Tolentino (81-84/82-84).
ITGE (1992): Memoria y mapa geologico de EspaIia a escala 1:100000. Gran Canaria (21-21/21-22).
Kellog, L.H., Hager, B.H. and van der Hilst, R.D. (1999): Compositional stratification in the deep mantle. Science. 283. pp. 1881-1884.
Klug, H. (1968): Morphologische Studien auf den Kanarischen Inseln. Beiträge zur Küstenentwicklung und Talbildung auf einem vulkanischen Archipel. Schriften des Geographischen Instituts der Universität Kiel. 24. 184 pp.
LaTourrette, T., Hervig, R.L. and Holloway, J.R. (1995): Trace element partitioning between amphibole, phlogopite, and basanite melt. Earth and Planetary Science Letters. 135. pp. 13–30.
Le Bas, M.J., Le Maitre, R.W., Streckeisen, A. and Zanettin, B. (1986) : A chemical classification of volcanic rocks based on the total alkali-silica diagram. Journal of Petrology. 27. pp. 745-750.
Lietz, J. (1973): Fossile Piemont-Schwemmfächer auf der Kanaren-Insel Gran Canaria und ihre Beziehungen zur Lage des Meeresspiegels. Zeitschriften für Geomorphologie, N.F. 18. pp. 105-120.
Lundstrom, C.C., Hoernle, K. and Gill, J. (2003): U-series disequilibria in volcanic rocks from the Canary Islands: plume versus lithopheric melting. Geochimica et cosmochimica Acta. 67. pp. 4135-4177.
Mattes, S. (1990): Mineralogie: Eine Einführung in die spezielle Mineralogie, Petrologie und Lagerstättenkunde. Springer. Berlin.
MacDonald, G.A. and Katsura, T. (1964): Chemical Composition of Hawaiian Lavas. Journal of Petrology. 5. pp. 82-133.
MacKenzie, W.S. and Guilford, C. (1981): Atlas of rock-forming minerals in thin section. Longman. London.
MacKenzie, W.S., Donaldson, C.H. and Guilford, C. (1982): Atlas of igneous rocks and their textures. Longman. London.
Marcantonio, F., Zindler, A., Elliott, T. and Staudigel, H. (1995): Os isotope systematics of La Palma, Canary Islands; evidences for recycled crust in the mantle source of HIMU ocean islands. Earth and Planetary Science Letters. 133. pp. 397-410.
Marzoli, A., Renne, P.R., Piccirillo, E.M., Ernesto, M., Bellieni, G. and De Min, A. (1999): Extensive 200-million-year-old continental flood basalts of the Central Atlantic Magmatic Province. Science. 284. pp. 616-618.
McDonough, W.F., Sun, S., Ringwood, A.E., Jagoutz, E. and Hofmann, A.W. (1991): K, Rb and Cs in the earth and moon and the evolution of the earth's mantle. Geochimica et cosmochimica Acta. Ross Taylor Symposium volume.
McDougall, I. and Schmincke, H.-U. (1976): Geochronology of Gran Canaria, Canary Islands: Age of shield-building volcanism and other magmatic phases. Bulletin of Volcanology. 40. pp. 57-77.
Menendez, I., Pablo, G.S., Martín-Betancor, M., Pérez-Torrado, F.J., Guillou, H. and Scaillet, S. (2008): Fluvial dissectionm isostatic uplift, and geomorphological evolution of volcanic islands (Gran Canaria, Canary Islands, Spain). Geomorphology. 102. pp. 189-203.
Mitchell, N.C., Masson, D.G., Watts, A.B., Gee, M.J.R. and Urgeles, R. (2002): The morphology of the submarine flanks of volcanic ocean islands: A comparative study of the Canary and Hawaiian hotspot islands. Journal of Volcanology and Geothermal Research. 115. pp. 83-107.
Morgan, W.J. (1971): Convection plumes in the lower mantle. Nature. 230. pp. 42-43.
Morgan, W.J. (1981): Hotspot tracks and the opening of the Atlantic and Indian Oceans. In: Emiliani C (Ed.): The sea. (The oceanic lithosphere Volume 7) Wiley Interscience. New York. pp. 443-487.
Montelli, R., Nolet, G., Dahlen, F.A., Masters, G., Engdahl, E.R. and Hung, S.H. (2004): Finite-frequency tomography reveals a variety of plumes in the mantle. Science. 303. pp. 338-343.
Montelli, R., Dahlen, F.A. and Masters, G. (2006): A catalogue of deep mantle plumes: new results from finite-frequency tomography. Geochemistry, Geophysics, Geosystems. 7.
Moreira, M., Doucelance, R., Kurz, M.D., Dupré, B. and Allègre, J.C. (1999): Helium and lead isotope geochemistry of the Azores archipelago. Earth and Planetary Science Letters. 169. pp. 189-205.
Morse, S.A. (1980): Basalts and phase diagrams: an introduction to the quantitative use of phase diagrams in igneous petrology. Springer. New York.
Mullen, E.D. (1983): $MnO/TiO_2/P_2O_5$: a minor element discriminant for basaltic rocks of oceanic environments and its implications for petrogenesis. Earth and Planetary Science Letters. 62. pp. 53-62.

Nesse, W.D. (1991): Introduction to optical mineralogy. Oxford University Press. New York.

Neumann, E.-R., Wulff-Pedersen, E., Simonsen, S.L., Pearson, N.J., Martí, J. and Mitjavila, J. (1999): Evidence for fractional crystallization of periodically refilled magma chambers in Tenerife, Canary Islands. Journal of Petrology. 40. pp. 1089–1123.

Oyarzun, R., Doblas, M., López, J. and Cebriá, J.M. (1997): Opening of the central Atlantic and asymmetric mantle upwelling phenomena: implications for long-lived magmatism in western North Africa and Europe. Geology. 25. pp. 727-730.

Pérez-Torrado, F.J. (1990): Roque Nublo non-welded ignimbrite: a type of ignimbrite in Gran Canaria (Canary Islands, Spain). IAVCEI International Volcanology Congress. Mainz. Libro de abstracts.

Pérez-Torrado, F.J. (1992): Volcano-estratigraffa del Grupo Roque Nublo (Gran Canaria). Ph.D. Thesis, Univ. Las Palmas de Gran Canaria, 510 pp. (unpubl.).

Pérez-Torrado, F.J., Carracedo, J.C. and Mangas, J. (1995): Stratigraphy and geochronology of the Roque Nublo Group (Gran Canaria, Canary Islands). Journal of the Geological Society. In press.

Pérez-Torrado, F.J., Martí, J., Queralt, I. and Mangas, J. (1995): Alteration processes of the Roque Nublo ignimbrites (Gran Canaria, Canary Islands). Journal of Volcanology and Geothermal Research. 65. pp. 191-204.

Phillips, W.R. and Griffen, D.T. (1981): Optical mineralogy-The nonopaque minerals. W.H. Freeman and company. San Francisco.

Revenaugh, J. and Meyer, R. (1997): Seismic evidence of partial melt within a possibly ubiquitous low-velocity layer at the base of the mantle. Science. 277. pp. 670–673.

Robertson, A.H.F. and Stillman, C.J. (1979): Submarine volcanic and associated sedimentary rocks of the Fuerteventura Basal Complex, Canary Islands. Geological Magazine. 116. pp. 203-214.

Roeder, P.L. and Emslie, R.F. (1970): Olivine-liquid equilibrium. Contributions to Mineralogy and Petrology. 29. pp. 275-289.

Rollinson, H. (1993): Using geolchemical data: evaluation, presentation, interpretation. Longman Group UK Limited. England.

Rothe, P. (2008): Kanarische Inseln: Lanzarote, Fuerteventura, Gran Canaria, Tenerife, Gomera, La Palma, Hierro. Sammlung Geologischer Führer. Band 81. Gebrüder Bornträger. Stuttgart.

Schmincke, H.-U. (1968a): Faulting versus erosion and reconstruction of the Mid-Miocene shield volcano of Gran Canaria. Geologische Mitteilungen. 8. pp. 23-50.

Schmincke, H.-U. (1976): The geology of the Canary Islands. In: Kunkel, G. (Ed.): Biogeography and ecology of the Canary Islands. Junk. The Hague. pp. 67-184.

Schmincke, H.-U. (1982): Volcanic and chemical evolution of the Canary Islands. In: VON RAD, U., HINZ, K., SARNTHEIN, M.; SEIBOLD, E. (Eds.): Geology of the Northwest African Margin. Spinger, Berlin. pp. 273-306.

Schmincke, H.-U. (1990): Geological field guide. IAVCEI, Int. Volcano. Congr., Mainz. 212 pp.

Schmincke, H.U. and Flower, M.J.F. (1974): Magmenevolution auf atlantischen Vulkaninseln. Naturwissenschaften. 61. pp. 288–297.

Schmincke, H.-U. and Swanson, D.A. (1967a): Laminar viscous flowage structures in ash-flow tuffs from Gran Canaria, Canary Islands. Journal of Geology. 75. pp. 641-664.

Simonsen, S.L., Neumann, E.R. and Seim, K. (2000): Sr-Nd-Pb isotope and trace-element geochemistry evidence for a young HIMU source and assimilation at Tenerife (Canary Islands). Journal of Volcanology and Geothermal Research. 103. pp. 299-312.

Sun, S.S. (1980): Lead isotopic study of young volcanic rocks from mid-ocean ridges, ocean islands and island arcs. In: BAILEY, K., TARNEY,J., DUNHAM, K. (Eds.): The evidence for chemical heterogeneity in the earth`s mantle. Royal society of London. pp. 409-445.

Taylor, S.R. and McLennan, S.M. (1985): The continental crust: its composition and evolution. Blackwell. Oxford.

Thirlwall, M.F., Jenkins, C, Vroon, P.Z. and Mattey, D.P. (1997): Crustal interaction during construction of ocean islands: Pb-Sr-Nd-O isotope geochemistry of the shield basalts of Gran Canaria, Canary Islands. Chemical Geology. 135. pp. 233-262.

Weaver, B.L., Wood, D.A., Tarney, J. and Joron, J.L. (1986): Role of subducted sediment in the genesis of ocean island basalts: geochemical evidence from South Atlantic Ocean islands. Geology. 14. pp. 275-278.

Widom, E., Hoernle, K.A., Shirey, S.B. and Schmincke, H.U. (1999): Os isotope systematics in the Canary Islands and Madeira: lithospheric contamination and mantle plume signatures. Journal of Petrology. 40. pp. 297-314.

Williams, Q. and Garnero, E.J. (1996): Seismic evidence for partial melt at the base of the Earth's mantle. Science. 273. pp. 1528–1530.

Williams, Q., Revenaugh, J. and Garnero, E. (1998): A correlation between ultra-low basal velocities in the mantle and hot spots. Science. 281. pp. 546–549.

Wilson, M. (1991): Igneous petrogenesis- A global

tectonic approach. Chapman & Hall. London.
Wilson, J.T. (1963): A possible origin of the Hawaiian Islands. Canadian Journal of Physics. 41. pp. 863-870.
White, W.M. (1997): Geochemistry. An On-Line Text-Book. Cornell University. Available at http://www.geo.cornell.edu/geology/classes/geo455/Chapters.HTML.
Wulff-Pedersen, E., Neumann, E.-R., Vannucci, R., Bottazzi, P. and Ottolini, L., (1999): Silicic melts produced by reaction between peridotite and infiltrating basaltic melts: ion probe data on glasses and minerals in veined xenoliths from La Palma, Canary Islands. Contributions to Mineralogy and Petrology. 137. pp. 59–82.
Yoder, H.S. and Tilley, C.E. (1962): Origin of basalt magmas: an experimental study of natural and synthetic rock systems. Journal of Petrology. 3. pp. 342-532.
Zindler, A. and Hart, S. (1986): Chemical geodynamics. Annu. Rev. Earth Planet. Sci. 14. pp. 493–571.

Appendix 1 - Geological map of Gran Canaria

Geological map of Gran Canaria taken from Menedez et al. (2008)

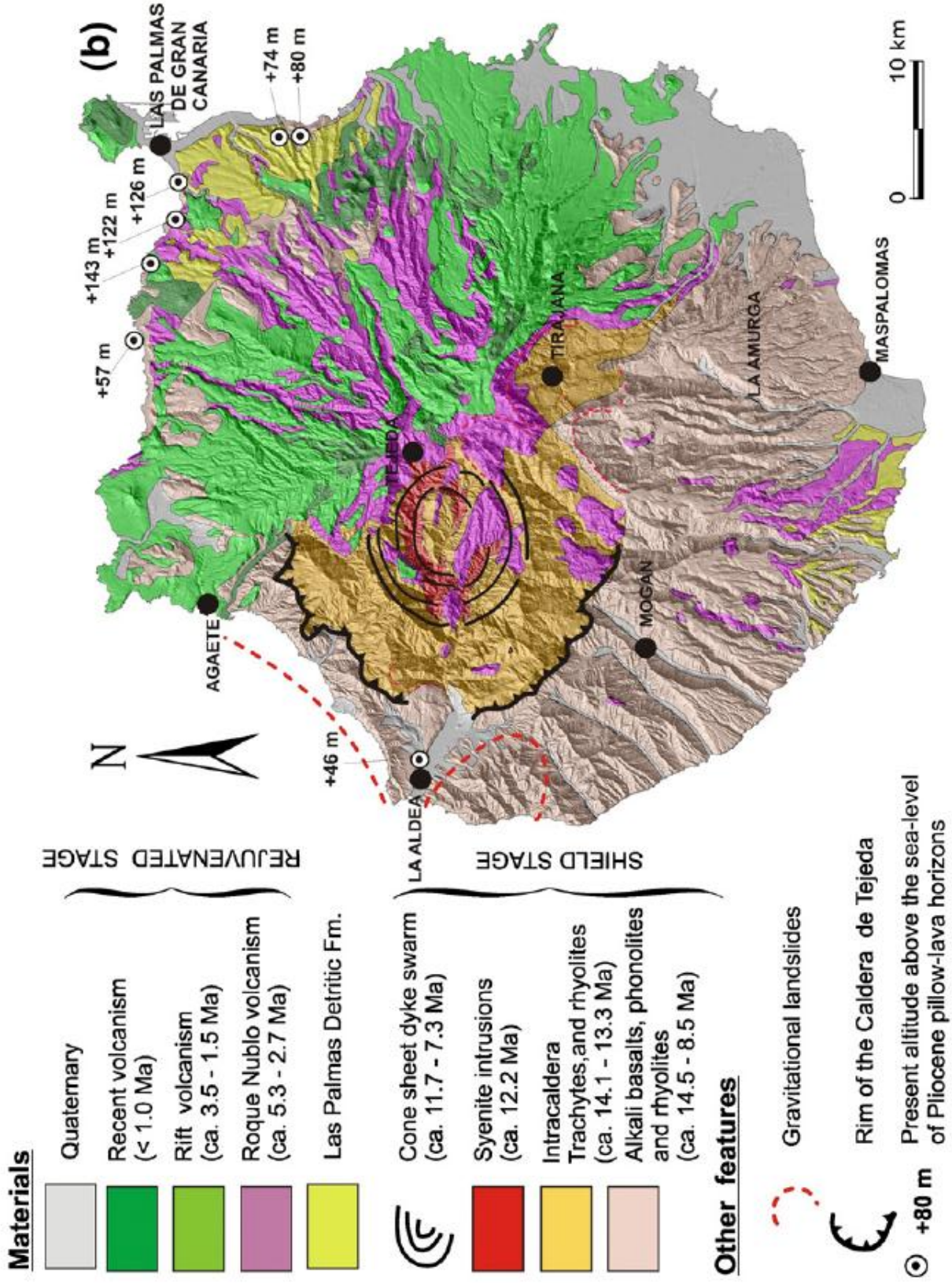

Appendix 2 - Map of the sampled localities at Barranco de Tasártico

Map digitalized using ITGE (1992)

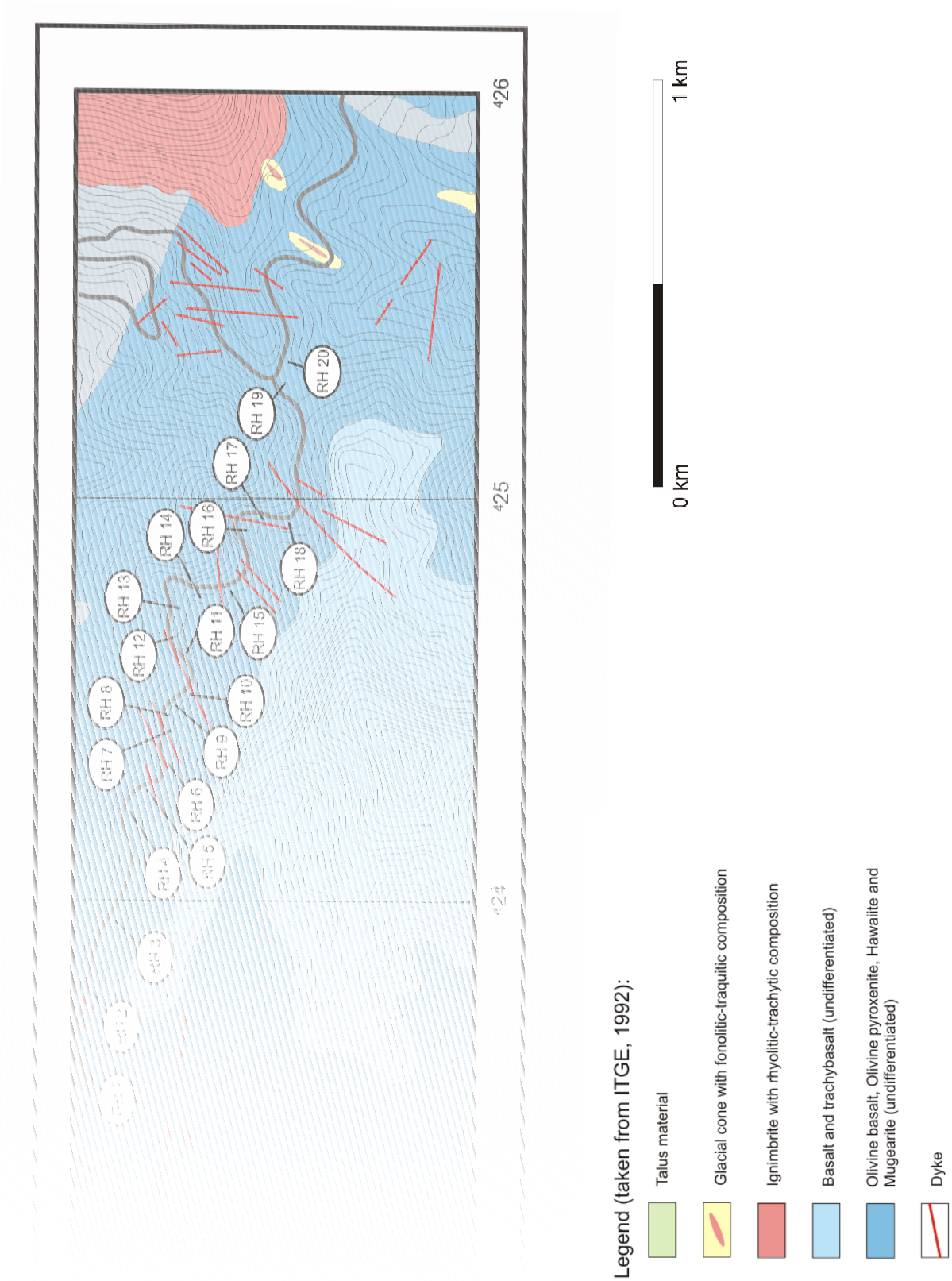

Appendix 3 - Table of the whole rock chemistry

	RH 1	RH 2	RH 3	RH 4	RH 5	RH 6	RH 7
Altitude	399 m	395 m	405 m	413 m	421 m	437 m	445 m
Latitude	27°56.545'N	27°56.555'N	27°56.514'N	27°56.494'N	27°56.453'N	27°56.447'N	27°56.451'N
Longitude	15°46.722'W	15°46.686'W	15°46.465'W	15°46.293'W	15°46.241'W	15°46.201'W	15°46.183'W
major elements in wt%							
SiO_2	47.1	46.4	49.2	49.7	48.7	49.3	45.1
Al_2O_3	10.3	10.7	12.0	12.8	12.9	13.7	9.6
Fe_2O_3	12.6	12.3	12.2	11.6	12.0	11.6	13.1
MnO	0.16	0.16	0.14	0.14	0.14	0.16	0.18
MgO	10.6	9.3	6.0	6.1	6.0	5.1	12.8
CaO	10.1	9.9	9.3	8.7	8.8	9.0	10.0
Na_2O	2.2	2.7	2.7	2.8	2.7	3.0	1.9
K_2O	1.0	1.0	1.3	1.4	1.0	1.2	0.8
Na_2O+K_2O	3.2	3.7	4.0	4.1	3.7	4.2	2.7
TiO_2	3.2	3.1	3.4	3.4	3.5	3.5	2.9
P_2O_5	0.4	0.41	0.45	0.47	0.5	0.51	0.33
trace elements in ppm							
Ba	184	185	228	227	237	251	127
Be	1	1	2	1	1	1	<1
Co	61.4	57.2	48	44.5	44.5	46.2	71.6
Cs	1	1	0.9	0.8	0.4	0.6	0.7
Ga	17.9	18.8	20.2	22	22.2	23.9	17.3
Hf	7.1	7.3	8.2	9.2	8.9	9.6	6.1
Nb	39.7	41.8	44.7	45.9	45	47.6	31.8
Rb	23.1	22.9	34.1	35.9	16.2	22.4	16.9
Sn	2	2	2	3	3	3	2
Sr	455	478	523	551	552	619	386
Ta	2.6	2.6	2.7	2.8	2.7	2.9	1.9
Th	3.2	3	4.1	4.7	5	4.9	2.5
U	0.9	0.9	1.2	1.3	1.1	1.3	0.6
Ti	1924	1846	2032	2038	2092	2122	1726
V	314	326	331	326	322	348	318
Cr	614	503	276	172	163	52	766
W	33.7	30.9	35.1	32.6	38.2	75.1	39.8
Zr	268	279	312	348	339	361	227
Y	25.3	26.5	29.2	32.4	31.4	33.1	23.3
La	30.5	32.3	36.7	40.4	39.7	40.7	24.9
Ce	71.4	74.7	83.4	93.5	92.2	95.7	59.7
Pr	9.4	9.7	10.7	11.9	11.8	12.3	8.0
Nd	42	42.8	46	50.3	51.1	54.8	34.8
Sm	8.2	8.4	9.0	10.1	10.1	10.5	7.4
Eu	2.5	2.5	2.7	3.0	2.9	3.2	2.3
Gd	7.4	7.3	8.0	8.9	8.7	9.4	6.7
Tb	1.1	1.1	1.2	1.3	1.3	1.4	1.0
Dy	5.4	5.6	6.0	6.5	6.6	6.7	5.0
Ho	0.95	0.95	1.08	1.15	1.17	1.25	0.88
Er	2.4	2.3	2.6	2.9	2.9	3.1	2.2
Tm	0.32	0.32	0.36	0.39	0.39	0.41	0.29
Yb	1.9	1.9	2.1	2.3	2.4	2.5	1.7
Lu	0.26	0.27	0.29	0.32	0.33	0.36	0.25
Mo	0.6	0.5	0.8	1	0.4	0.9	0.6

	RH 1	RH 2	RH 3	RH 4	RH 5	RH 6	RH 7
Altitude	399 m	395 m	405 m	413 m	421 m	437 m	445 m
Latitude	27°56.545'N	27°56.555'N	27°56.514'N	27°56.494'N	27°56.453'N	27°56.447'N	27°56.451'N
Longitude	15°46.722'W	15°46.686'W	15°46.465'W	15°46.293'W	15°46.241'W	15°46.201'W	15°46.183'W
trace elements in ppm							
Cu	99	80	134	55	41	47	106
Pb	0.9	1.2	1.5	1.8	1.8	2	1.2
Zn	64	55	70	58	49	53	69
Ni	241	200	108	58	68	19	395
As	0.8	0.7	1.3	1	1.1	0.9	1.1
Cd	<0.1	<0.1	<0.1	<0.1	<0.1	<0.1	<0.1
Sb	0.1	<0.1	0.3	<0.1	0.1	<0.1	<0.1
Bi	<0.1	<0.1	<0.1	<0.1	<0.1	<0.1	<0.1
Ag	<0.1	<0.1	<0.1	<0.1	<0.1	<0.1	<0.1
Au	4.8	5.3	2.9	2.2	1.8	2.7	15.5
Hg	<0.1	<0.1	<0.1	<0.1	<0.1	<0.1	<0.1
Tl	<0.1	<0.1	<0.1	<0.1	<0.1	<0.1	<0.1
Se	<0.5	<0.5	<0.5	<0.5	<0.5	<0.5	<0.5
Zr/Nb	6.75	6.67	6.98	7.57	7.54	7.58	7.13
K/Ba	42.9	46.5	46.9	49.8	36.3	39.4	50.4
Y/Nb	0.64	0.63	0.65	0.71	0.70	0.70	0.73
Ce/Pb	79	62	56	52	51	48	50
Nb/La	1.3	1.3	1.2	1.1	1.1	1.2	1.3
Nb/U	44.1	46.4	37.3	35.3	40.9	36.6	53.0
Nb/Th	12.4	13.9	10.9	9.8	9.0	9.7	12.7
Ba/Nb	4.6	4.4	5.1	4.9	5.3	5.3	4.0
La/Nb	0.77	0.77	0.82	0.88	0.88	0.86	0.78
Zr/Y	10.6	10.5	10.7	10.7	10.8	10.9	9.7
Ba/Th	57.5	61.7	55.6	48.3	47.4	51.2	50.8
K/La	259	266	292	280	217	243	257
Nb/U	44.1	46.4	37.3	35.3	40.9	36.6	53.0
$(La/Sm)_n$	2.3	2.4	2.6	2.5	2.5	2.4	2.1
$(Nb/La)_n$	1.3	1.3	1.2	1.1	1.1	1.2	1.3
$(Ta/La)_n$	1.5	1.4	1.3	1.2	1.2	1.2	1.3
$(K/La)_n$	0.8	0.8	0.9	0.8	0.6	0.7	0.8
$(Pb/La)_n$	0.3	0.4	0.4	0.4	0.5	0.5	0.3
$(La/Lu)_n$	10.6	10.8	11.4	11.4	10.8	10.2	8.9

	RH 8	RH 9	RH 10	RH 11	RH 12	RH 13	RH 14
Altitude	450	456 m	462 m	469 m	465 m	471	484 m
Latitude	27°56.453'N	27°56.428'N	27°56.407'N	27°56.415'N	27°56.443'N	27°56.436'N	27°56.387'N
Longitude	15°46.147'W	15°46.147'W	15°46.138'W	15°46.070'W	15°46.059'W	15°46.013'W	15°45.981'W
major elements in wt%							
SiO_2	46.0	46.9	44.7	46.0	45.7	45.6	45.5
Al_2O_3	14.3	14.6	11.2	12.4	11.6	12.2	11.5
Fe_2O_3	13.0	12.7	13.4	13.2	13.2	12.8	13.2
MnO	0.16	0.17	0.17	0.24	0.16	0.17	0.18
MgO	5.5	5.1	9.1	6.6	8.5	6.9	9.7
CaO	9.3	9.8	10.4	9.9	10.4	10.5	9.7
Na_2O	3.2	3.3	2.5	2.8	2.5	2.8	2.5
K_2O	1.3	1.4	1.1	1.3	1.1	1.2	1.0
Na_2O+K_2O	4.5	4.6	3.6	4.1	3.6	3.9	3.5
TiO_2	4.2	4.3	3.8	4.1	3.9	4.0	3.6

	RH 8	RH 9	RH 10	RH 11	RH 12	RH 13	RH 14
Altitude	450	456 m	462 m	469 m	465 m	471	484 m
Latitude	27°56.453'N	27°56.428'N	27°56.407'N	27°56.415'N	27°56.443'N	27°56.436'N	27°56.387'N
Longitude	15°46.147'W	15°46.147'W	15°46.138'W	15°46.070'W	15°46.059'W	15°46.013'W	15°45.981'W
major elements in wt%							
P_2O_5	0.56	0.57	0.45	0.51	0.46	0.49	0.44
trace elements in ppm							
Ba	239	230	190	213	183	208	163
Be	2	2	1	2	1	2	1
Co	45.9	42	58.8	54.7	56.3	54.9	59.3
Cs	0.2	0.2	0.3	0.3	0.3	0.1	0.2
Ga	24.1	23.1	20.8	21.2	21.4	22.3	19.9
Hf	9.4	9	8.1	8.5	8.2	8.9	7.6
Nb	57.1	55.6	47	51.8	47.5	51.1	39.8
Rb	26.8	26.8	24.4	27.5	23.5	24.7	18.6
Sn	3	3	2	2	2	2	2
Sr	664	653	543	585	522	576	506
Ta	3.5	3.5	3	3.3	3	3.1	2.4
Th	4.7	4.1	3.8	4.2	4	4.1	3.1
U	1.1	1	0.8	1.1	1	1	0.7
Ti	2517	2565	2284	2439	2343	2385	2170
V	367	357	384	370	374	393	357
Cr	47	24	395	257	380	289	453
W	28.1	33.7	22.8	23.4	31.5	27.8	36.4
Zr	363	352	303	332	305	325	295
Y	32.4	31.5	27.1	30	26.6	28.4	26.6
La	41.1	40.9	35.9	38.9	35.5	38.6	30.7
Ce	95.5	95	84.6	89.9	81.9	89.5	74.6
Pr	12.5	12.3	10.7	11.4	10.5	11.4	9.7
Nd	56.2	55	46.4	51.7	47.1	51.5	45.3
Sm	11.1	10.6	9.3	10.1	9.3	10.1	9.2
Eu	3.3	3.3	2.9	3.1	2.8	3.0	2.7
Gd	9.6	9.5	8.3	8.7	8.3	8.8	8.0
Tb	1.4	1.4	1.2	1.3	1.2	1.3	1.2
Dy	7.2	7.1	6.1	6.4	6.0	6.5	6.2
Ho	1.21	1.22	1.03	1.14	1.04	1.12	1.04
Er	3.1	3.0	2.6	2.8	2.6	2.8	2.6
Tm	0.39	0.38	0.33	0.36	0.33	0.36	0.34
Yb	2.5	2.4	2.0	2.2	2.1	2.2	2.0
Lu	0.33	0.31	0.27	0.29	0.27	0.3	0.28
Mo	1	1	0.7	0.7	0.9	0.9	0.8
Cu	157	179	151	95	152	155	93
Pb	0.4	0.4	0.4	0.5	0.5	0.5	0.8
Zn	78	74	75	76	83	87	79
Ni	47	34	185	122	164	132	227
As	1.4	0.9	1.1	1.3	0.9	1	0.7
Cd	<0.1	<0.1	<0.1	<0.1	<0.1	<0.1	<0.1
Sb	<0.1	<0.1	0.1	0.2	0.1	0.1	<0.1
Bi	<0.1	<0.1	<0.1	<0.1	<0.1	<0.1	<0.1
Ag	<0.1	<0.1	<0.1	<0.1	<0.1	<0.1	<0.1
Au	4.3	3.8	2.9	2.8	2.4	1.6	1.5
Hg	<0.1	<0.1	<0.1	<0.1	<0.1	<0.1	<0.1
Tl	<0.1	<0.1	<0.1	<0.1	<0.1	<0.1	<0.1
Se	<0.5	<0.5	<0.5	<0.5	<0.5	<0.5	<0.5

	RH 8	RH 9	RH 10	RH 11	RH 12	RH 13	RH 14
Altitude	450	456 m	462 m	469 m	465 m	471	484 m
Latitude	27°56.453'N	27°56.428'N	27°56.407'N	27°56.415'N	27°56.443'N	27°56.436'N	27°56.387'N
Longitude	15°46.147'W	15°46.147'W	15°46.138'W	15°46.070'W	15°46.059'W	15°46.013'W	15°45.981'W
Zr/Nb	6.35	6.33	6.44	6.42	6.41	6.35	7.41
K/Ba	45.2	48.7	47.4	49.3	49.2	46.6	51.5
Y/Nb	0.57	0.57	0.58	0.58	0.56	0.56	0.67
Ce/Pb	239	238	212	180	164	179	93
Nb/La	1.4	1.4	1.3	1.3	1.3	1.3	1.3
Nb/U	51.9	55.6	58.8	47.1	47.5	51.1	56.9
Nb/Th	12.1	13.6	12.4	12.3	11.9	12.5	12.8
Ba/Nb	4.2	4.1	4.0	4.1	3.9	4.1	4.1
La/Nb	0.72	0.74	0.76	0.75	0.75	0.76	0.77
Zr/Y	11.2	11.2	11.2	11.1	11.4	11.4	11.1
Ba/Th	50.9	56.1	50.0	50.7	45.8	50.7	52.6
K/La	263	274	251	270	254	251	274
Nb/U	51.9	55.6	58.8	47.1	47.5	51.1	56.9
$(La/Sm)_n$	2.3	2.4	2.4	2.4	2.4	2.4	2.1
$(Nb/La)_n$	1.4	1.3	1.3	1.3	1.3	1.3	1.3
$(Ta/La)_n$	1.5	1.5	1.4	1.5	1.5	1.4	1.3
$(K/La)_n$	0.8	0.8	0.7	0.8	0.7	0.7	0.8
$(Pb/La)_n$	0.1	0.1	0.1	0.1	0.1	0.1	0.3
$(La/Lu)_n$	11.2	11.9	11.9	12.1	11.8	11.6	9.9

	RH 15	RH 16	RH 17	RH 18	RH 19	RH 20
Altitude	491 m	497m	500 m	504 m	508 m	515 m
Latitude	27°56.355'N	27°56.340'N	27°56.336'N	27°56.279'N	27°56.264'N	27°56.295'N
Longitude	15°45.945'W	15°45.925'W	15°4.856'W	15°45.870'W	15°45.713'W	15°45.610'W
major elements in wt%						
SiO_2	46.4	46.2	45.7	44.5	44.7	45.7
Al_2O_3	13.7	11.2	11.3	10.6	8.3	10.4
Fe_2O_3	12.8	13.4	13.2	13.5	13.4	13.5
MnO	0.18	0.16	0.17	0.18	0.18	0.18
MgO	5.4	9.0	8.7	9.2	16.0	9.4
CaO	9.1	10.1	10.5	10.3	9.8	10.5
Na_2O	3.2	2.3	2.4	2.2	1.6	2.2
K_2O	1.4	0.9	1.0	0.9	0.7	0.9
Na_2O+K_2O	4.6	3.2	3.5	3.1	2.3	3.1
TiO_2	4.1	3.5	3.6	3.6	2.8	3.3
P_2O_5	0.57	0.4	0.43	0.41	0.28	0.38
trace elements in ppm						
Ba	232	161	170	159	114	148
Be	2	1	1	2	1	2
Co	45.6	60.5	59.8	63	85.7	72.3
Cs	0.2	0.2	0.4	0.2	0.7	0.5
Ga	23.7	19.5	19	19.3	15.2	18.1
Hf	9.5	7.6	7.4	7	5.3	6.8
Nb	54.2	39.5	44	40	28.6	43.7
Rb	27.7	15.7	20.5	17.3	16.3	15.9
Sn	3	2	2	2	2	2
Sr	612	460	491	473	358	449
Ta	3.4	2.6	2.8	2.6	1.8	2.6
Th	4.6	3	3.4	3.1	2.4	3.5

	RH 15	RH 16	RH 17	RH 18	RH 19	RH 20
Altitude	491 m	497m	500 m	504 m	508 m	515 m
Latitude	27°56.355'N	27°56.340'N	27°56.336'N	27°56.279'N	27°56.264'N	27°56.295'N
Longitude	15°45.945'W	15°45.925'W	15°4.856'W	15°45.870'W	15°45.713'W	15°45.610'W
trace elements in ppm						
U	1.1	0.7	0.9	0.7	0.5	0.8
Ti	2457	2080	2158	2158	1690	1996
V	359	331	352	351	297	332
Cr	107	651	501	630	1059	746
W	49.6	17.6	54.4	46.8	46	63
Zr	377	286	283	275	199	262
Y	32.1	25.7	25	24.2	18.8	23.9
La	40.6	29.8	32.5	29.9	22.1	30.5
Ce	96.7	71.7	77.9	72.1	53.7	73.3
Pr	12.5	9.2	9.8	9.1	6.7	9.1
Nd	56.2	42.4	44.6	43	31.2	43.1
Sm	11.1	8.6	8.7	8.4	6.5	8.4
Eu	3.4	2.6	2.6	2.6	2.0	2.5
Gd	9.9	7.6	7.9	7.5	5.8	7.5
Tb	1.5	1.2	1.2	1.1	0.9	1.1
Dy	7.5	5.9	5.9	5.7	4.5	5.5
Ho	1.31	1.02	1.02	0.98	0.76	0.97
Er	3.3	2.6	2.5	2.5	1.8	2.4
Tm	0.44	0.33	0.33	0.3	0.24	0.31
Yb	2.6	2.1	2.0	1.9	1.5	1.9
Lu	0.36	0.27	0.26	0.25	0.19	0.25
Mo	0.8	0.4	0.8	0.5	0.4	0.6
Cu	80	84	132	109	92	133
Pb	0.6	0.7	0.6	1	0.4	0.7
Zn	58	63	69	58	70	71
Ni	58	248	204	263	514	298
As	1.4	1	1.5	1.4	0.8	1.9
Cd	<0.1	<0.1	<0.1	<0.1	<0.1	<0.1
Sb	0.2	<0.1	0.1	<0.1	<0.1	<0.1
Bi	<0.1	<0.1	<0.1	<0.1	<0.1	<0.1
Ag	<0.1	<0.1	<0.1	<0.1	<0.1	<0.1
Au	2.5	3	2.3	3.3	0.7	12.4
Hg	<0.1	<0.1	<0.1	<0.1	<0.1	<0.1
Tl	<0.1	<0.1	<0.1	<0.1	<0.1	<0.1
Se	<0.5	<0.5	<0.5	<0.5	<0.5	<0.5
Zr/Nb	6.96	7.25	6.43	6.86	6.95	5.98
K/Ba	50.9	47.2	50.6	49.1	50.9	49.3
Y/Nb	0.59	0.65	0.57	0.61	0.66	0.55
Ce/Pb	161	102	130	72	134	105
Nb/La	1.3	1.3	1.4	1.3	1.3	1.4
Nb/U	49.3	56.4	48.9	57.1	57.2	54.6
Nb/Th	11.8	13.2	12.9	12.9	11.9	12.5
Ba/Nb	4.3	4.1	3.9	4.0	4.0	3.4
La/Nb	0.75	0.75	0.74	0.75	0.77	0.70
Zr/Y	11.8	11.1	11.3	11.3	10.6	10.9
Ba/Th	50.4	53.7	50.0	51.3	47.5	42.3
K/La	291	255	265	261	262	239
Nb/U	49.3	56.4	48.9	57.1	57.2	54.6
$(La/Sm)_n$	2.3	2.2	2.3	2.2	2.1	2.3

	RH 15	RH 16	RH 17	RH 18	RH 19	RH 20
Altitude	491 m	497m	500 m	504 m	508 m	515 m
Latitude	27°56.355'N	27°56.340'N	27°56.336'N	27°56.279'N	27°56.264'N	27°56.295'N
Longitude	15°45.945'W	15°45.925'W	15°4.856'W	15°45.870'W	15°45.713'W	15°45.610'W
$(Nb/La)_n$	1.3	1.3	1.3	1.3	1.3	1.4
$(Ta/La)_n$	1.4	1.5	1.5	1.5	1.4	1.5
$(K/La)_n$	0.9	0.8	0.8	0.8	0.8	0.7
$(Pb/La)_n$	0.1	0.2	0.2	0.3	0.2	0.2
$(La/Lu)_n$	10.1	9.9	11.3	10.8	10.5	10.9

Appendix 4 - Table of the normative minerals

	Ap	Il	Or	Ab	An	Mt	Di	Hy	Qz	Ol	Ne
RH 1	0.88	5.7	5.3	17.5	14.0	16.4	23.3	15.4		1.1	
RH 2	0.92	5.5	5.7	21.2	13.5	16.9	23.5	9.2		3.6	
RH 3	0.99	6.0	7.2	21.3	15.8	16.6	19.2	7.8	5.1		
RH 4	1.04	6.1	7.6	22.1	17.2	15.9	15.7	9.3	5.1		
RH 5	1.11	6.3	5.8	21.6	18.8	16.4	15.3	9.3	5.6		
RH 6	1.14	6.3	6.6	23.6	19.2	15.8	15.3	6.9	5.2		
RH 7	0.73	5.1	4.3	14.9	14.4	17.7	23.3	11.4		8.2	
RH 8	1.23	7.4	7.1	25.0	19.3	17.4	15.4	6.5		0.6	
RH 9	1.46	7.4	7.3	25.2	19.2	16.9	16.3	6.1	0.06		
RH 10	0.99	6.7	5.9	19.6	15.0	18.1	23.3	3.9		6.5	
RH 11	1.11	7.2	6.9	21.9	16.2	17.8	20.4	8.1	0.33		
RH 12	1.02	6.9	6.0	19.3	16.0	17.7	22.6	8.3		2.3	
RH 13	1.08	7.0	6.4	24.5	14.7	17.3	23.9			5.2	0.04
RH 14	0.97	6.4	5.5	19.3	16.1	17.7	20.2	9.0		5.0	
RH 15	1.25	7.3	7.6	25.4	17.4	17.3	16.5	6.8	0.34		
RH 16	0.94	5.7	5.2	19.6	15.6	17.4	22.2	12.0		1.4	
RH 17	0.95	6.4	5.7	19.2	15.4	17.7	23.4	8.6		2.6	
RH 18	0.92	6.4	5.2	17.4	15.4	18.3	23.5	10.4		2.5	
RH 19	0.62	4.9	3.8	12.2	12.5	17.9	23.9	10.4		13.9	
RH 20	0.83	5.9	4.9	17.6	14.7	18.3	24.4	12.3		1.3	

Norm mineral	Abbreviation
Apatite	Ap
Ilmenite	Il
Orthoclase	Or
Albite	Ab
Anorthite	An
Magnetite	Mt
Diopside	Di
Hypersthene	Hy
Quartz	Qz
Olivine	Ol
Nepheline	Ne

Appendix 5 - Table of the chemical composition of the clinopyroxene phenocrysts (in number of ions calculated for 6 oxygen)

	Na	Mg	Al	Si	Ca	Ti	Cr	Fe	O	Cation sum	Totals
RH_2_PYX_2_1	0.05	0.86	0.17	1.9	0.8	0.05	0.01	0.23	6	4.03	99.3
RH_2_PYX_2_2	0.05	0.87	0.18	1.9	0.81	0.04	0.02	0.21	6	4.03	99.6
RH_2_PYX_2_3	0.05	0.87	0.17	1.9	0.81	0.05	0.02	0.22	6	4.03	100.1
RH_2_PYX_2_4	0.05	0.85	0.19	1.8	0.81	0.05	0.03	0.22	6	4.03	100.3
RH_2_PYX_3_1	0.05	0.88	0.13	1.9	0.77	0.04	0.01	0.26	6	4.03	100.3
RH_2_PYX_3_2	0.05	0.89	0.14	1.9	0.82	0.04	0.02	0.19	6	4.03	100.3
RH_2_PYX_3_3	0.05	0.88	0.14	1.9	0.79	0.04	0.02	0.23	6	4.03	100.0
RH_2_PYX_3_4	0.05	0.88	0.14	1.9	0.79	0.04	0.01	0.23	6	4.03	99.5
RH_2_PYX_5_3	0.03	0.89	0.13	1.9	0.86	0.04		0.17	6	4.02	97.0
RH_2_PYX_5_4	0.03	0.89	0.13	1.9	0.85	0.04		0.15	6	4.01	99.2
RH_2_PYX_5_5	0.03	0.89	0.16	1.9	0.84	0.04		0.18	6	4.02	99.2
RH_2_PYX_7_1	0.05	0.86	0.17	1.9	0.8	0.05	0.01	0.23	6	4.03	99.3
RH_2_PYX_7_2	0.05	0.87	0.18	1.9	0.81	0.04	0.02	0.21	6	4.03	99.6
RH_2_PYX_7_3	0.05	0.87	0.17	1.9	0.81	0.05	0.02	0.22	6	4.03	100.1
RH_2_PYX_7_4	0.05	0.85	0.19	1.8	0.81	0.05	0.03	0.22	6	4.03	100.3
RH_2_PYX_8_1	0.05	0.88	0.13	1.9	0.77	0.04	0.01	0.26	6	4.03	100.3
RH_2_PYX_8_2	0.05	0.89	0.14	1.9	0.82	0.04	0.02	0.19	6	4.03	100.3
RH_2_PYX_8_3	0.05	0.88	0.14	1.9	0.79	0.04	0.02	0.23	6	4.03	100.0
RH_2_PYX_8_4	0.05	0.88	0.14	1.9	0.79	0.04	0.01	0.23	6	4.03	99.5
RH_2_PYX_9_1	0.05	0.81	0.2	1.8	0.81	0.07	0.01	0.28	6	4.04	100.3
RH_2_PYX_9_2	0.04	0.85	0.19	1.8	0.83	0.05	0.03	0.21	6	4.03	100.7
RH_2_PYX_9_3	0.05	0.82	0.19	1.8	0.82	0.06	0.01	0.26	6	4.04	100.3
RH_2_PYX_9_4	0.05	0.85	0.17	1.9	0.81	0.06	0.02	0.24	6	4.03	100.4
RH_2_PYX_9_5	0.04	0.9	0.14	1.9	0.79	0.04	0.02	0.21	6	4.03	100.1
RH_2_PYX_10_1	0.05	0.86	0.11	1.9	0.78	0.04	0.01	0.29	6	4.02	100.0
RH_2_PYX_10_2	0.05	0.89	0.14	1.9	0.81	0.04	0.02	0.2	6	4.03	100.8
RH_2_PYX_10_3	0.04	0.9	0.13	1.9	0.8	0.04	0.02	0.21	6	4.02	100.1
RH_2_PYX_10_4	0.06	0.85	0.16	1.9	0.8	0.05	0.01	0.25	6	4.04	100.1
RH_2_PYX_10_5	0.05	0.9	0.14	1.9	0.8	0.04	0.02	0.21	6	4.03	100.0
RH_3_PYX_2_1	0.02	0.9	0.07	1.9	0.76	0.03		0.3	6	4.01	100.1
RH_3_PYX_2_2	0.03	0.93	0.09	1.9	0.79	0.03		0.22	6	4.01	99.6
RH_3_PYX_2_3	0.03	0.89	0.16	1.9	0.82	0.04	0.03	0.2	6	4.02	100.0
RH_3_PYX_2_4	0.03	0.88	0.16	1.9	0.82	0.05	0.02	0.19	6	4.01	99.2
RH_3_PYX_3_1	0.02	0.9	0.13	1.9	0.79	0.05	0.02	0.22	6	4.01	99.2
RH_3_PYX_3_2	0.03	0.8	0.13	1.9	0.79	0.05	0.01	0.24	6	4.01	99.6
RH_3_PYX_3_3	0.02	0.9	0.13	1.9	0.79	0.04	0.02	0.23	6	4.01	99.8
RH_3_PYX_4_1	0.03	0.9	0.08	1.9	0.77	0.04		0.27	6	4.01	99.5
RH_3_PYX_4_2	0.02	0.92	0.09	1.9	0.79	0.04		0.22	6	4.01	98.7
RH_3_PYX_4_3	0.02	0.92	0.1	1.9	0.79	0.04	0.01	0.23	6	4.01	98.5
RH_3_PYX_4_4	0.03	0.91	0.1	1.9	0.77	0.04	0.01	0.21	6	3.99	97.5
RH_3_PYX_5_5	0.03	0.9	0.11	1.9	0.78	0.04	0.01	0.23	6	4	98.1
RH_3_PYX_6_1	0.02	0.88	0.12	1.9	0.78	0.05		0.29	6	4.02	102.1
RH_3_PYX_6_3	0.03	0.88	0.14	1.9	0.81	0.04	0.02	0.21	6	4.01	101.4
RH_3_PYX_6_4	0.03	0.9	0.12	1.9	0.8	0.04	0.02	0.22	6	4.02	102.5
RH_3_PYX_6_5	0.03	0.88	0.14	1.9	0.8	0.04	0.01	0.22	6	4.01	101.2
RH_3_PYX_6_6	0.03	0.87	0.14	1.9	0.81	0.05	0.02	0.23	6	4.01	101.8
RH_3_PYX_6_7	0.04	0.88	0.14	1.9	0.8	0.04	0.03	0.21	6	4.02	100.5
RH_3_PYX_7_1	0.02	0.91	0.08	1.9	0.75	0.04		0.27	6	4	100.1
RH_3_PYX_7_2	0.03	0.93	0.1	1.9	0.77	0.03	0.01	0.22	6	4.01	100.5
RH_3_PYX_7_3	0.02	0.89	0.12	1.9	0.81	0.04	0.02	0.22	6	4.01	100.5
RH_3_PYX_8_1	0.03	0.83	0.1	1.9	0.75	0.04		0.34	6	4.01	101.6

	Na	Mg	Al	Si	Ca	Ti	Cr	Fe	O	Cation sum	Totals
RH_3_PYX_8_2	0.03	0.9	0.13	1.9	0.8	0.05		0.23	6	4.01	99.8
RH_3_PYX_8_3	0.02	0.9	0.13	1.9	0.79	0.04	0.01	0.23	6	4.01	100.6
RH_3_PYX_8_4	0.02	0.88	0.14	1.9	0.79	0.04	0.02	0.21	6	4	100.6
RH_3_PYX_9_1	0.03	0.87	0.12	1.9	0.77	0.05		0.27	6	4.01	101.7
RH_3_PYX_9_2	0.02	0.89	0.12	1.9	0.79	0.05		0.25	6	4.01	102.2
RH_3_PYX_9_4	0.02	0.9	0.11	1.9	0.82	0.03		0.22	6	4.02	101.1
RH_6_PYX_1_1	0.02	0.9	0.07	2.0	0.69	0.03		0.34	6	4	98.1
RH_6_PYX_1_2	0.03	0.91	0.07	1.9	0.7	0.03		0.35	6	4.02	97.6
RH_6_PYX_1_3	0.02	0.87	0.07	1.9	0.72	0.03		0.34	6	4	97.9
RH_6_PYX_1_5	0.02	0.88	0.08	1.9	0.74	0.03		0.33	6	4.01	97.6
RH_6_PYX_2_1	0.03	0.86	0.1	1.9	0.75	0.04		0.31	6	4.02	100.1
RH_6_PYX_2_2	0.02	0.87	0.1	1.9	0.68	0.04		0.37	6	4	99.1
RH_6_PYX_2_3	0.02	0.87	0.12	1.9	0.74	0.03		0.33	6	4.02	99.9
RH_6_PYX_2_4	0.03	0.86	0.13	1.9	0.79	0.03		0.29	6	4.01	99.3
RH_6_PYX_2_5	0.03	0.88	0.12	1.9	0.74	0.04		0.31	6	4.02	99.5
RH_6_PYX_2_6	0.03	0.85	0.15	1.9	0.78	0.05		0.3	6	4.02	97.4
RH_6_PYX_3_1	0.03	0.89	0.06	1.9	0.69	0.03		0.36	6	4.01	100.1
RH_6_PYX_3_2	0.02	0.91	0.06	1.9	0.69	0.03		0.35	6	4.01	99.2
RH_6_PYX_3_3	0.02	0.9	0.07	1.9	0.72	0.03		0.32	6	4	99.0
RH_6_PYX_3_4	0.02	0.9	0.07	2.0	0.68	0.02		0.35	6	4	99.4
RH_6_PYX_3_5	0.02	0.87	0.07	1.9	0.71	0.03		0.34	6	4	97.9
RH_6_PYX_3_6	0.03	0.86	0.07	1.9	0.72	0.03		0.34	6	4.01	98.4
RH_6_PYX_4_1	0.03	0.81	0.1	1.9	0.73	0.05		0.37	6	4	98.0
RH_6_PYX_4_2	0.02	0.86	0.09	1.9	0.76	0.04		0.32	6	4.01	98.0
RH_6_PYX_4_3	0.03	0.85	0.1	1.9	0.73	0.04		0.35	6	4	98.1
RH_6_PYX_4_4	0.02	0.87	0.09	1.9	0.73	0.04		0.33	6	4	97.1
RH_6_PYX_5_1	0.02	0.88	0.06	1.9	0.73	0.03		0.34	6	4	97.5
RH_6_PYX_5_2	0.02	0.88	0.07	1.9	0.71	0.03		0.34	6	4	97.3
RH_6_PYX_5_3	0.02	0.88	0.07	1.9	0.72	0.03		0.36	6	4.02	97.3
RH_6_PYX_5_4	0.02	0.9	0.06	2.0	0.68	0.03		0.34	6	4	97.9
RH_6_PYX_5_5	0.02	0.92	0.06	1.9	0.69	0.03		0.34	6	4.01	97.7
RH_6_PYX_6_1	0.02	0.82	0.11	1.9	0.75	0.05		0.35	6	4	100.2
RH_6_PYX_6_2	0.03	0.87	0.1	1.9	0.77	0.03		0.32	6	4.03	101.0
RH_6_PYX_6_3	0.03	0.86	0.13	1.9	0.78	0.04		0.28	6	4.01	100.6
RH_6_PYX_6_4	0.02	0.86	0.12	1.9	0.78	0.03		0.28	6	4.01	99.6
RH_6_PYX_6_5	0.03	0.88	0.1	1.9	0.74	0.03		0.31	6	4.02	99.8
RH_6_PYX_7_1	0.02	0.9	0.06	1.9	0.71	0.03		0.33	6	4	99.1
RH_6_PYX_7_2	0.02	0.88	0.07	1.9	0.72	0.03		0.34	6	4.01	98.7
RH_6_PYX_7_3	0.02	0.87	0.08	1.9	0.75	0.03		0.33	6	4.01	98.1
RH_6_PYX_7_4	0.03	0.89	0.07	1.9	0.73	0.03		0.33	6	4.01	98.3
RH_6_PYX_7_5	0.02	0.87	0.11	1.9	0.78	0.03		0.28	6	4.01	97.6
RH_6_PYX_8_1	0.02	0.88	0.07	1.9	0.71	0.03		0.36	6	4.01	99.8
RH_6_PYX_8_2	0.02	0.88	0.08	1.9	0.74	0.04		0.31	6	4	100.0
RH_6_PYX_8_3	0.03	0.87	0.07	1.9	0.72	0.03		0.33	6	4	100.7
RH_6_PYX_8_4	0.02	0.87	0.08	1.9	0.74	0.02		0.34	6	4.01	99.6
RH_6_PYX_8_5	0.02	0.87	0.08	1.9	0.71	0.02		0.36	6	4	99.6
RH_6_PYX_8_6	0.03	0.89	0.08	1.9	0.69	0.03		0.36	6	4.01	99.8
RH_6_PYX_9_1	0.02	0.87	0.1	1.9	0.75	0.04		0.31	6	4.01	101.9
RH_6_PYX_9_2	0.02	0.87	0.1	1.9	0.72	0.04		0.35	6	4.01	100.9
RH_6_PYX_9_3	0.03	0.85	0.08	1.9	0.72	0.04		0.35	6	4	100.2
RH_6_PYX_9_4	0.02	0.85	0.08	1.9	0.71	0.03		0.36	6	4	100.6
RH_6_PYX_9_5	0.02	0.86	0.08	1.9	0.74	0.03		0.35	6	4.01	100.5
RH_6_PYX_10_1	0.03	0.84	0.1	1.9	0.75	0.04		0.33	6	4	99.6
RH_6_PYX_10_2	0.03	0.87	0.11	1.9	0.75	0.04		0.31	6	4.01	99.0

	Na	Mg	Al	Si	Ca	Ti	Cr	Fe	O	Cation sum	Totals
RH_6_PYX_10_5	0.02	0.86	0.1	1.9	0.74	0.04		0.33	6	4.01	100.4
RH_6_PYX_11_1	0.03	0.84	0.12	1.9	0.77	0.05		0.32	6	4.01	102.0
RH_6_PYX_11_2	0.02	0.87	0.11	1.9	0.81	0.03		0.26	6	4.02	100.9
RH_6_PYX_11_3	0.01	0.9	0.07	1.9	0.77	0.03		0.3	6	4.01	101.7
RH_6_PYX_11_4	0.02	0.88	0.09	1.9	0.75	0.03		0.29	6	3.99	100.8
RH_6_PYX_11_5	0.02	0.86	0.1	1.9	0.79	0.04		0.28	6	4.01	101.1
RH_8_PYX_1_1	0.03	0.82	0.16	1.9	0.84	0.06		0.24	6	4.01	98.6
RH_8_PYX_1_2	0.04	0.77	0.23	1.8	0.85	0.08		0.26	6	4.03	99.4
RH_8_PYX_1_3	0.04	0.78	0.2	1.8	0.85	0.07		0.25	6	4.02	99.9
RH_8_PYX_1_4	0.03	0.77	0.22	1.8	0.86	0.07		0.24	6	4.01	99.3
RH_8_PYX_1_5	0.04	0.75	0.21	1.8	0.87	0.08		0.26	6	4.02	100.4
RH_8_PYX_2_1	0.03	0.8	0.14	1.9	0.85	0.06		0.27	6	4.02	98.1
RH_8_PYX_2_2	0.05	0.73	0.27	1.8	0.84	0.11		0.29	6	4.03	97.6
RH_8_PYX_2_3	0.04	0.79	0.19	1.8	0.84	0.08		0.26	6	4.02	98.8
RH_8_PYX_2_4	0.04	0.79	0.19	1.8	0.84	0.07		0.26	6	4.02	99.5
RH_8_PYX_2_5	0.03	0.8	0.18	1.8	0.84	0.07		0.26	6	4.01	99.2
RH_8_PYX_3_1	0.04	0.78	0.21	1.8	0.83	0.08		0.28	6	4.02	100.4
RH_8_PYX_3_2	0.04	0.78	0.2	1.8	0.86	0.07		0.26	6	4.03	101.0
RH_8_PYX_3_3	0.03	0.78	0.2	1.8	0.85	0.08		0.25	6	4.01	100.5
RH_8_PYX_3_4	0.03	0.79	0.18	1.9	0.85	0.07		0.24	6	4.01	101.2
RH_8_PYX_3_5	0.03	0.83	0.13	1.9	0.84	0.05		0.25	6	4.01	102.0
RH_8_PYX_4_1	0.03	0.83	0.15	1.9	0.85	0.05		0.25	6	4.02	101.2
RH_8_PYX_4_2	0.03	0.83	0.14	1.9	0.85	0.05		0.25	6	4.02	101.5
RH_8_PYX_4_3	0.03	0.77	0.22	1.8	0.86	0.08		0.26	6	4.03	100.8
RH_8_PYX_4_4	0.04	0.77	0.21	1.8	0.85	0.08		0.27	6	4.03	101.7
RH_8_PYX_5_1	0.03	0.82	0.15	1.9	0.85	0.06		0.25	6	4.02	100.6
RH_8_PYX_5_2	0.02	0.88	0.12	1.9	0.87	0.03	0.02	0.18	6	4.02	101.0
RH_8_PYX_5_3	0.02	0.88	0.12	1.9	0.87	0.04	0.01	0.18	6	4.01	101.3
RH_8_PYX_5_4	0.03	0.89	0.11	1.9	0.89	0.03	0.01	0.18	6	4.03	100.6
RH_8_PYX_6_1	0.04	0.84	0.18	1.9	0.87	0.05	0.01	0.21	6	4.03	100.9
RH_8_PYX_6_2	0.03	0.86	0.17	1.9	0.86	0.05	0.01	0.2	6	4.03	101.6
RH_8_PYX_6_3	0.02	0.87	0.15	1.9	0.85	0.04	0.01	0.21	6	4.02	100.9
RH_8_PYX_6_4	0.03	0.85	0.17	1.9	0.84	0.05	0.01	0.21	6	4.02	101.1
RH_8_PYX_7_1	0.03	0.81	0.17	1.9	0.83	0.07		0.25	6	4.01	102.2
RH_8_PYX_7_2	0.03	0.84	0.14	1.9	0.82	0.05		0.25	6	4.01	101.7
RH_8_PYX_7_3	0.03	0.81	0.14	1.9	0.86	0.06		0.25	6	4.01	99.1
RH_8_PYX_7_4	0.03	0.84	0.13	1.9	0.84	0.05		0.25	6	4.02	102.1
RH_8_PYX_8_1	0.03	0.8	0.17	1.9	0.84	0.07		0.25	6	4.01	100.6
RH_8_PYX_8_2	0.04	0.79	0.19	1.8	0.85	0.07		0.26	6	4.02	101.4
RH_8_PYX_8_3	0.03	0.78	0.2	1.8	0.86	0.07		0.24	6	4.01	101.3
RH_8_PYX_8_4	0.03	0.82	0.17	1.9	0.86	0.06		0.24	6	4.02	101.4
RH_10 PYX_1_1	0.03	0.95	0.05	1.9	0.87	0.02	0.02	0.13	6	4.01	99.9
RH_10_PYX_1_2	0.03	0.8	0.23	1.8	0.83	0.07	0.01	0.25	6	4.02	99.9
RH_10_PYX_1_3	0.02	0.95	0.06	1.9	0.87	0.03	0.03	0.13	6	4.01	101.3
RH_10_PYX_1_4	0.01	0.95	0.06	2.0	0.87	0.02	0.02	0.13	6	4	101.5
RH_10_PYX_1_5	0.02	0.95	0.06	2.0	0.86	0.02	0.02	0.12	6	4.01	102.0
RH_10_PYX_2_1	0.03	0.78	0.16	1.9	0.83	0.06	0.01	0.28	6	4.01	99.8
RH_10_PYX_2_2	0.03	0.83	0.18	1.8	0.85	0.06	0.02	0.22	6	4.02	100.0
RH_10_PYX_2_3	0.03	0.9	0.12	1.9	0.88	0.04	0.02	0.16	6	4.03	100.1
RH_10_PYX_2_4	0.02	0.89	0.11	1.9	0.89	0.04	0.01	0.17	6	4.02	100.3
RH_10_PYX_3_1	0.03	0.78	0.16	1.8	0.82	0.07		0.3	6	4.02	97.3
RH_10_PYX_3_2	0.03	0.86	0.14	1.9	0.86	0.04	0.01	0.19	6	4.02	99.9
RH_10_PYX_3_3	0.02	0.89	0.11	1.9	0.88	0.04	0.02	0.16	6	4.01	99.9
RH_10_PYX_3_4	0.03	0.84	0.14	1.9	0.85	0.05	0.01	0.21	6	4.01	99.5

	Na	Mg	Al	Si	Ca	Ti	Cr	Fe	O	Cation sum	Totals
RH_10_PYX_3_5	0.02	0.86	0.15	1.9	0.87	0.05	0.02	0.19	6	4.02	99.9
RH_10_PYX_4_1	0.03	0.9	0.09	1.9	0.85	0.04		0.21	6	4.02	101.0
RH_10_PYX_4_2	0.03	0.86	0.14	1.9	0.84	0.04		0.22	6	4.02	101.0
RH_10_PYX_4_3	0.04	0.86	0.11	1.9	0.84	0.04		0.22	6	4.01	100.9
RH_10_PYX_4_4	0.04	0.79	0.18	1.9	0.85	0.05		0.26	6	4.03	100.6
RH_10_PYX_4_5	0.04	0.82	0.17	1.9	0.83	0.05		0.25	6	4.03	100.0
RH_10_PYX_4_6	0.04	0.8	0.19	1.9	0.86	0.05		0.24	6	4.03	98.7
RH_10_PYX_5_1	0.02	0.89	0.12	1.9	0.84	0.03	0.02	0.19	6	4.01	100.2
RH_10_PYX_5_2	0.01	0.92	0.1	1.9	0.84	0.04	0.02	0.19	6	4.01	100.1
RH_10_PYX_5_3	0.02	0.86	0.15	1.9	0.86	0.04	0.01	0.21	6	4.01	99.8
RH_10_PYX_5_4	0.03	0.8	0.22	1.8	0.86	0.07		0.24	6	4.03	99.8
RH_10_PYX_5_5	0.02	0.81	0.21	1.8	0.87	0.06		0.23	6	4.02	99.8
RH_10_PYX_6_1	0.02	0.86	0.15	1.9	0.85	0.05	0.02	0.2	6	4.01	100.4
RH_10_PYX_6_2	0.04	0.81	0.18	1.9	0.86	0.05		0.24	6	4.03	99.1
RH_10_PYX_6_3	0.04	0.83	0.17	1.9	0.85	0.06	0.01	0.23	6	4.02	99.4
RH_10_PYX_6_4	0.04	0.82	0.14	1.9	0.86	0.05		0.25	6	4.03	99.3
RH_10_PYX_7_1	0.02	0.9	0.12	1.9	0.83	0.04	0.01	0.21	6	4.01	100.9
RH_10_PYX_7_2	0.02	0.94	0.07	1.9	0.88	0.02	0.02	0.13	6	4.01	100.4
RH_10_PYX_7_3	0.02	0.93	0.06	1.9	0.87	0.03	0.02	0.13	6	4	100.0
RH_10_PYX_7_4	0.02	0.94	0.07	1.9	0.87	0.02	0.02	0.14	6	4.01	99.1
RH_10_PYX_8_1	0.02	0.81	0.18	1.9	0.88	0.05		0.23	6	4.02	101.6
RH_10_PYX_8_2	0.03	0.81	0.22	1.8	0.86	0.06		0.23	6	4.03	99.9
RH_10_PYX_8_3	0.03	0.78	0.23	1.8	0.86	0.07		0.25	6	4.03	99.2
RH_10_PYX_8_4	0.04	0.79	0.21	1.8	0.86	0.07		0.25	6	4.04	100.2
RH_10_PYX_9_1	0.03	0.83	0.11	1.9	0.84	0.05		0.25	6	4.01	99.6
RH_10_PYX_9_2	0.03	0.84	0.16	1.9	0.85	0.04		0.21	6	4.01	99.9
RH_10_PYX_9_3	0.03	0.84	0.18	1.9	0.85	0.05		0.21	6	4.02	99.5
RH_10_PYX_9_4	0.03	0.82	0.21	1.8	0.84	0.07		0.24	6	4.03	101.5
RH_10_PYX_9_5	0.04	0.86	0.16	1.9	0.84	0.04	0.02	0.21	6	4.03	102.4
RH_11_PYX_1_1	0.02	0.81	0.19	1.8	0.86	0.06		0.23	6	4.02	98.6
RH_11_PYX_1_2	0.03	0.81	0.19	1.8	0.87	0.06	0.01	0.23	6	4.03	99.2
RH_11_PYX_1_3	0.03	0.79	0.21	1.8	0.86	0.07	0.01	0.24	6	4.02	100.6
RH_11_PYX_1_4	0.03	0.81	0.19	1.8	0.85	0.06	0.01	0.25	6	4.02	101.5
RH_11_PYX_1_5	0.03	0.81	0.18	1.8	0.87	0.06	0.02	0.22	6	4.02	100.2
RH_11_PYX_2_1	0.04	0.81	0.16	1.9	0.85	0.07		0.25	6	4.02	99.3
RH_11_PYX_2_2	0.04	0.79	0.2	1.8	0.86	0.07		0.24	6	4.03	100.5
RH_11_PYX_2_3	0.04	0.77	0.24	1.8	0.86	0.07	0.01	0.25	6	4.03	100.3
RH_11_PYX_2_4	0.03	0.82	0.18	1.9	0.85	0.06		0.24	6	4.02	99.9
RH_11_PYX_2_5	0.03	0.81	0.22	1.8	0.84	0.07		0.24	6	4.03	100.1
RH_11_PYX_2_6	0.03	0.82	0.19	1.8	0.86	0.07	0.02	0.24	6	4.03	101.0
RH_11_PYX_3_1	0.04	0.85	0.14	1.9	0.85	0.04		0.22	6	4.03	100.8
RH_11_PYX_3_2	0.03	0.82	0.15	1.9	0.85	0.05		0.25	6	4.02	99.4
RH_11_PYX_3_3	0.04	0.84	0.15	1.9	0.84	0.05		0.24	6	4.02	100.8
RH_11_PYX_3_4	0.03	0.84	0.16	1.9	0.86	0.05		0.24	6	4.03	99.2
RH_11_PYX_4_1	0.03	0.85	0.17	1.9	0.86	0.05	0.02	0.19	6	4.02	102.9
RH_11_PYX_4_2	0.03	0.84	0.14	1.9	0.85	0.04		0.23	6	4.02	101.0
RH_11_PYX_4_3	0.04	0.8	0.2	1.8	0.85	0.06		0.25	6	4.03	101.7
RH_11_PYX_4_4	0.03	0.86	0.14	1.9	0.83	0.05	0.01	0.22	6	4.02	102.0
RH_11_PYX_5_1	0.03	0.81	0.22	1.8	0.85	0.06		0.24	6	4.03	102.1
RH_11_PYX_5_2	0.04	0.83	0.16	1.9	0.85	0.05		0.23	6	4.03	101.2
RH_11_PYX_5_3	0.06	0.82	0.16	1.9	0.86	0.05		0.24	6	4.04	100.2
RH_11_PYX_5_4	0.03	0.85	0.15	1.9	0.85	0.05		0.23	6	4.02	101.1
RH_11_PYX_6_1	0.03	0.84	0.15	1.9	0.87	0.05	0.02	0.2	6	4.02	102.8
RH_11_PYX_6_2	0.03	0.82	0.2	1.8	0.87	0.05	0.02	0.2	6	4.02	101.9

	Na	Mg	Al	Si	Ca	Ti	Cr	Fe	O	Cation sum	Totals
RH_11_PYX_6_3	0.03	0.88	0.12	1.9	0.86	0.03	0.02	0.18	6	4.02	102.9
RH_11_PYX_6_4	0.02	0.87	0.14	1.9	0.88	0.04	0.02	0.18	6	4.02	101.3
RH_11_PYX_6_5	0.02	0.86	0.15	1.9	0.88	0.05	0.02	0.17	6	4.01	100.5
RH_11_PYX_7_1	0.02	0.8	0.18	1.8	0.86	0.06		0.25	6	4.02	102.5
RH_11_PYX_7_2	0.04	0.8	1.84	0.9	0.86	0.06		0.25	6	4.03	102.7
RH_11_PYX_7_3	0.03	0.79	0.19	1.8	0.86	0.06		0.25	6	4.02	100.4
RH_11_PYX_7_4	0.05	0.82	0.18	1.8	0.86	0.06		0.24	6	4.04	99.5
RH_11_PYX_7_5	0.03	0.78	0.19	1.8	0.86	0.06		0.24	6	4.02	99.0
RH_11_PYX_8_1	0.03	0.79	0.19	1.8	0.86	0.07		0.25	6	4.03	99.7
RH_11_PYX_8_2	0.04	0.79	0.19	1.8	0.85	0.06		0.25	6	4.02	100.3
RH_11_PYX_8_3	0.03	0.82	0.17	1.9	0.86	0.06		0.22	6	4.01	99.6
RH_11_PYX_8_4	0.04	0.78	0.19	1.8	0.86	0.06		0.25	6	4.02	100.1
RH_11_PYX_8_5	0.04	0.78	0.21	1.8	0.86	0.07		0.25	6	4.03	99.6
RH_11_PYX_9_1	0.04	0.79	0.19	1.8	0.87	0.06		0.25	6	4.03	98.9
RH_11_PYX_9_2	0.04	0.78	0.22	1.8	0.85	0.07		0.26	6	4.03	100.6
RH_11_PYX_9_3	0.03	0.84	0.15	1.9	0.85	0.05		0.24	6	4.03	100.5
RH_11_PYX_10_1	0.03	0.84	0.14	1.9	0.84	0.05		0.24	6	4.02	101.3
RH_11_PYX_10_2	0.03	0.81	0.14	1.9	0.85	0.06		0.24	6	4.01	98.0
RH_11_PYX_10_3	0.03	0.84	0.15	1.9	0.83	0.05		0.25	6	4.01	101.2
RH_11_PYX_10_4	0.03	0.83	0.14	1.9	0.85	0.05		0.24	6	4.02	100.4
RH_11_PYX_11_1	0.04	0.78	0.2	1.8	0.87	0.07		0.26	6	4.04	101.1
RH_11_PYX_11_2	0.03	0.84	0.15	1.9	0.85	0.05		0.25	6	4.03	102.4
RH_11_PYX_11_3	0.03	0.83	0.14	1.9	0.85	0.05		0.24	6	4.02	102.8
RH_11_PYX_11_4	0.03	0.84	0.15	1.9	0.85	0.05		0.24	6	4.03	102.7
RH_13_PYX_1_1	0.05	0.79	0.2	1.8	0.84	0.07		0.26	6	4.04	99.7
RH_13_PYX_1_2	0.04	0.8	0.2	1.8	0.84	0.07		0.24	6	4.02	98.9
RH_13_PYX_1_3	0.03	0.89	0.12	1.9	0.87	0.04		0.16	6	4.02	99.7
RH_13_PYX_1_4	0.03	0.8	0.19	1.8	0.86	0.07		0.23	6	4.01	99.8
RH_13_PYX_1_5	0.03	0.84	0.15	1.9	0.85	0.05		0.21	6	4.01	99.7
RH_13_PYX_2_2	0.03	0.84	0.17	1.9	0.85	0.06		0.22	6	4.02	101.4
RH_13_PYX_2_3	0.04	0.8	0.2	1.8	0.85	0.07		0.25	6	4.02	102.2
RH_13_PYX_2_4	0.02	0.84	0.17	1.8	0.88	0.06		0.22	6	4.02	102.3
RH_13_PYX_3_1	0.03	0.79	0.17	1.9	0.85	0.07		0.26	6	4.01	102.6
RH_13_PYX_3_2	0.03	0.85	0.15	1.9	0.86	0.04		0.19	6	4	101.8
RH_13_PYX_3_3	0.02	0.86	0.18	1.9	0.83	0.05		0.22	6	4.01	100.1
RH_13_PYX_3_4	0.03	0.86	0.17	1.9	0.84	0.05		0.21	6	4.02	98.4
RH_13_PYX_3_5	0.02	0.84	0.19	1.8	0.86	0.06		0.2	6	4.01	98.5
RH_13_PYX_4_2	0.03	0.86	0.13	1.9	0.86	0.04	0.02	0.17	6	4.01	100.7
RH_13_PYX_4_3	0.04	0.74	0.28	1.8	0.86	0.09		0.25	6	4.02	100.6
RH_13_PYX_4_4	0.03	0.79	0.22	1.8	0.83	0.08		0.26	6	4.02	100.7
RH_13_PYX_4_5	0.04	0.79	0.23	1.8	0.83	0.07		0.27	6	4.03	100.1
RH_13_PYX_4_6	0.02	0.86	0.14	1.9	0.87	0.04		0.18	6	4.01	98.9
RH_13_PYX_4_7	0.02	0.86	0.16	1.9	0.85	0.04		0.19	6	4	98.7
RH_13_PYX_5_1	0.02	0.88	0.13	1.9	0.83	0.05		0.19	6	4	101.0
RH_13_PYX_5_2	0.03	0.89	0.12	1.9	0.83	0.04		0.21	6	4.02	101.0
RH_13_PYX_5_3	0.03	0.88	0.12	1.9	0.86	0.04	0.03	0.18	6	4.02	100.1
RH_13_PYX_5_4	0.03	0.85	0.15	1.9	0.86	0.05		0.21	6	4.02	98.9
RH_13_PYX_5_5	0.03	0.84	0.16	1.9	0.85	0.05	0.02	0.19	6	4.01	100.2
RH_13_PYX_6_1	0.04	0.79	0.18	1.8	0.83	0.07		0.25	6	4.01	100.2
RH_13_PYX_6_2	0.04	0.78	0.22	1.8	0.86	0.07	0.02	0.25	6	4.04	100.6
RH_13_PYX_6_3	0.04	0.8	0.2	1.8	0.86	0.06		0.24	6	4.03	99.2
RH_13_PYX_6_4	0.04	0.79	0.21	1.8	0.85	0.07		0.24	6	4.02	101.2
RH_13_PYX_6_5	0.03	0.78	0.2	1.8	0.86	0.07		0.26	6	4.02	100.2
RH_13_PYX_7_1	0.03	0.86	0.14	1.9	0.84	0.04		0.18	6	4	102.8

	Na	Mg	Al	Si	Ca	Ti	Cr	Fe	O	Cation sum	Totals
RH_13_PYX_7_2	0.03	0.88	0.13	1.9	0.85	0.05		0.21	6	4.02	102.3
RH_13_PYX_7_3	0.04	0.85	0.14	1.9	0.82	0.05		0.23	6	4.01	102.0
RH_13_PYX_7_4	0.04	0.85	0.14	1.9	0.84	0.05		0.24	6	4.03	102.2
RH_13_PYX_7_5	0.03	0.81	0.18	1.9	0.86	0.06		0.23	6	4.02	102.0
RH_13_PYX_7_6	0.02	0.8	0.22	1.8	0.84	0.08		0.24	6	4.01	101.9
RH_13_PYX_8_1	0.03	0.83	0.18	1.9	0.85	0.06		0.21	6	4.02	102.4
RH_13_PYX_8_2	0.03	0.81	0.21	1.8	0.85	0.05		0.24	6	4.02	100.9
RH_13_PYX_8_3	0.04	0.82	0.19	1.8	0.84	0.06		0.24	6	4.03	102.4
RH_13_PYX_8_4	0.03	0.82	0.17	1.9	0.86	0.05		0.24	6	4.02	100.9
RH_13_PYX_8_5	0.04	0.83	0.19	1.8	0.85	0.06		0.23	6	4.03	102.6
RH_16_PYX_1_1	0.02	0.86	0.17	1.8	0.84	0.05	0.02	0.22	6	4.02	102.4
RH_16_PYX_1_3	0.03	0.84	0.16	1.9	0.87	0.04	0.03	0.19	6	4.02	101.5
RH_16_PYX_1_4	0.04	0.83	0.18	1.9	0.85	0.06		0.2	6	4.01	101.0
RH_16_PYX_1_5	0.03	0.84	0.17	1.8	0.87	0.05	0.02	0.21	6	4.03	99.9
RH_16_PYX_1_6	0.03	0.83	0.18	1.9	0.85	0.06		0.21	6	4.02	100.3
RH_16_PYX_1_7	0.03	0.84	0.18	1.8	0.85	0.05	0.02	0.22	6	4.03	101.0
RH_16_PYX_2_1	0.03	0.77	0.31	1.7	0.83	0.09		0.25	6	4.03	99.5
RH_16_PYX_2_2	0.03	0.85	0.16	1.8	0.86	0.05	0.03	0.2	6	4.03	102.6
RH_16_PYX_2_3	0.03	0.86	0.16	1.9	0.86	0.04		0.2	6	4.02	99.8
RH_16_PYX_2_4	0.03	0.88	0.13	1.9	0.88	0.02		0.2	6	4.03	99.1
RH_16_PYX_2_5	0.03	0.86	0.17	1.9	0.86	0.05	0.02	0.19	6	4.02	98.6
RH_16_PYX_3_1	0.03	0.82	0.19	1.9	0.82	0.06		0.25	6	4.01	99.9
RH_16_PYX_3_2	0.03	0.88	0.15	1.9	0.86	0.04	0.02	0.18	6	4.03	99.3
RH_16_PYX_3_3	0.04	0.85	0.18	1.9	0.83	0.05	0.02	0.18	6	4.01	99.8
RH_16_PYX_3_4	0.03	0.87	0.18	1.9	0.84	0.04	0.02	0.18	6	4.02	99.4
RH_16_PYX_3_5	0.03	0.86	0.16	1.9	0.85	0.04	0.02	0.2	6	4.02	100.5
RH_16_PYX_3_6	0.03	0.86	0.18	1.8	0.87	0.05	0.02	0.2	6	4.03	99.8
RH_16_PYX_4_1	0.03	0.87	0.16	1.9	0.86	0.04	0.03	0.2	6	4.03	98.9
RH_16_PYX_4_2	0.02	0.84	0.17	1.9	0.82	0.06		0.23	6	4	98.9
RH_16_PYX_4_3	0.02	0.84	0.19	1.8	0.83	0.05		0.23	6	4.02	99.0
RH_16_PYX_4_4	0.03	0.92	0.1	1.9	0.85	0.03	0.03	0.16	6	4.02	100.0
RH_16_PYX_4_5	0.02	0.93	0.09	1.9	0.86	0.02	0.02	0.14	6	4.01	99.8
RH_16_PYX_5_1	0.02	0.88	0.12	1.9	0.88	0.04	0.02	0.17	6	4.02	99.5
RH_16_PYX_5_2	0.02	0.94	0.09	1.9	0.84	0.03	0.02	0.14	6	4.01	98.3
RH_16_PYX_5_3	0.02	0.93	0.09	1.9	0.85	0.02	0.02	0.14	6	4	99.0
RH_16_PYX_5_4	0.02	0.93	0.09	1.9	0.85	0.02	0.02	0.15	6	4	97.5
RH_16_PYX_5_5	0.03	0.87	0.16	1.9	0.86	0.04		0.2	6	4.03	98.8
RH_16_PYX_6_1	0.02	0.9	0.1	1.9	0.83	0.04		0.21	6	4.01	99.7
RH_16_PYX_6_2	0.03	0.9	0.09	1.9	0.88	0.03	0.02	0.17	6	4.02	99.0
RH_16_PYX_6_3	0.03	0.86	0.17	1.9	0.85	0.05		0.2	6	4.02	101.0
RH_16_PYX_6_4	0.02	0.9	0.14	1.9	0.85	0.04		0.18	6	4.01	100.5
RH_16_PYX_6_5	0.02	0.9	0.11	1.9	0.87	0.04	0.02	0.16	6	4.01	100.4
RH_16_PYX_7_1	0.04	0.81	0.18	1.9	0.84	0.05		0.24	6	4.02	100.2
RH_16_PYX_7_2	0.03	0.7	0.24	1.8	0.83	0.09		0.26	6	4.01	98.2
RH_16_PYX_7_3	0.03	0.86	0.16	1.9	0.85	0.05		0.2	6	4.02	98.8
RH_16_PYX_7_4	0.03	0.83	0.18	1.9	0.84	0.06		0.24	6	4.02	99.4
RH_16_PYX_7_5	0.02	0.84	0.18	1.8	0.85	0.06		0.25	6	4.03	100.2
RH_16_PYX_8_1	0.03	0.78	0.2	1.8	0.84	0.09		0.28	6	4.03	100.5
RH_16_PYX_8_2	0.04	0.79	0.17	1.8	0.83	0.08		0.28	6	4.02	99.1
RH_16_PYX_8_3	0.04	0.75	0.27	1.8	0.84	0.09		0.29	6	4.03	98.8
RH_16_PYX_8_4	0.03	0.79	0.25	1.8	0.84	0.08	0.01	0.23	6	4.02	98.7
RH_16_PYX_8_5	0.04	0.81	0.22	1.8	0.83	0.06	0.01	0.21	6	4.02	98.2
RH_16_PYX_8_6	0.02	0.82	0.21	1.8	0.85	0.06	0.02	0.21	6	4.02	99.5
RH_16_PYX_8_7	0.02	0.82	0.22	1.8	0.85	0.06	0.02	0.21	6	4.02	98.9

	Na	Mg	Al	Si	Ca	Ti	Cr	Fe	O	Cation sum	Totals
RH_16_PYX_8_8	0.03	0.82	0.2	1.8	0.87	0.06	0.02	0.21	6	4.03	99.6
RH_16_PYX_9_1	0.03	0.77	0.29	1.8	0.83	0.09	0.01	0.24	6	4.02	102.3
RH_16_PYX_9_2	0.03	0.84	0.18	1.8	0.87	0.05	0.02	0.21	6	4.03	102.8
RH_16_PYX_9_3	0.03	0.84	0.16	1.9	0.84	0.05		0.23	6	4.02	102.3
RH_16_PYX_9_4	0.03	0.86	0.13	1.9	0.84	0.05		0.22	6	4.02	102.7
RH_16_PYX_9_5	0.03	0.86	0.18	1.8	0.85	0.06		0.2	6	4.03	100.8
RH_18_PYX_1_1	0.03	0.78	0.2	1.8	0.84	0.09		0.28	6	4.03	100.5
RH_18_PYX_1_2	0.04	0.79	0.17	1.8	0.83	0.08		0.28	6	4.02	99.1
RH_18_PYX_1_3	0.04	0.75	0.27	1.8	0.84	0.09		0.29	6	4.03	98.8
RH_18_PYX_1_4	0.03	0.79	0.25	1.8	0.84	0.08	0.01	0.23	6	4.02	98.7
RH_18_PYX_1_5	0.04	0.81	0.22	1.8	0.83	0.06	0.01	0.21	6	4.02	98.2
RH_18_PYX_1_6	0.02	0.82	0.21	1.8	0.85	0.06	0.02	0.21	6	4.02	99.5
RH_18_PYX_1_7	0.02	0.82	0.22	1.8	0.85	0.06	0.02	0.21	6	4.02	98.9
RH_18_PYX_1_8	0.03	0.82	0.2	1.8	0.87	0.06	0.02	0.21	6	4.03	99.6
RH_18_PYX_2_1	0.04	0.82	0.19	1.8	0.86	0.07		0.23	6	4.03	101.1
RH_18_PYX_2_2	0.04	0.76	0.22	1.8	0.83	0.08		0.28	6	4.02	101.7
RH_18_PYX_2_3	0.03	0.82	0.23	1.8	0.84	0.06		0.24	6	4.03	100.2
RH_18_PYX_2_4	0.04	0.81	0.18	1.8	0.85	0.07		0.24	6	4.02	101.7
RH_18_PYX_2_5	0.03	0.8	0.19	1.8	0.85	0.06		0.25	6	4.02	102.0
RH_18_PYX_2_6	0.04	0.82	0.19	1.8	0.86	0.06		0.22	6	4.03	101.2
RH_18_PYX_2_7	0.03	0.84	0.17	1.8	0.86	0.06	0.01	0.23	6	4.03	102.0
RH_18_PYX_2_8	0.04	0.84	0.16	1.9	0.85	0.05	0.01	0.22	6	4.03	101.7
RH_18_PYX_3_1	0.03	0.78	0.24	1.8	0.85	0.07	0.02	0.24	6	4.03	102.2
RH_18_PYX_3_2	0.04	0.79	0.22	1.8	0.84	0.08		0.24	6	4.02	100.6
RH_18_PYX_3_3	0.03	0.89	0.14	1.9	0.83	0.01		0.21	6	4.02	100.6
RH_18_PYX_3_4	0.04	0.92	0.13	1.9	0.8	0.03		0.23	6	4.04	100.6
RH_18_PYX_3_5	0.03	0.84	0.17	1.9	0.82	0.06		0.24	6	4.02	101.1
RH_18_PYX_4_1	0.03	0.77	0.29	1.8	0.83	0.09	0.01	0.24	6	4.02	102.3
RH_18_PYX_4_2	0.03	0.84	0.18	1.8	0.87	0.05	0.02	0.21	6	4.03	102.8
RH_18_PYX_4_3	0.03	0.84	0.16	1.9	0.84	0.05		0.23	6	4.02	102.3
RH_18_PYX_4_4	0.03	0.86	0.13	1.9	0.84	0.05		0.22	6	4.02	102.7
RH_18_PYX_4_5	0.03	0.86	0.18	1.8	0.85	0.06		0.22	6	4.03	100.8
RH_18_PYX_5_1	0.03	0.75	0.28	1.8	0.86	0.08		0.26	6	4.03	100.3
RH_18_PYX_5_2	0.04	0.81	0.22	1.8	0.84	0.08		0.24	6	4.03	101.4
RH_18_PYX_5_3	0.03	0.9	0.14	1.9	0.84	0.05		0.21	6	4.03	101.3
RH_18_PYX_5_4	0.02	0.86	0.16	1.9	0.84	0.05		0.21	6	4.02	101.1
RH_18_PYX_6_1	0.04	0.79	0.21	1.8	0.86	0.07		0.24	6	4.03	101.0
RH_18_PYX_6_2	0.04	0.75	0.27	1.7	0.82	0.11		0.31	6	4.04	102.0
RH_18_PYX_6_3	0.03	0.82	0.22	1.8	0.85	0.06	0.02	0.23	6	4.03	101.2
RH_18_PYX_6_4	0.03	0.81	0.22	1.8	0.86	0.06	0.02	0.23	6	4.03	101.8
RH_18_PYX_6_5	0.03	0.76	0.28	1.8	0.84	0.09	0.01	0.26	6	4.03	101.0
RH_18_PYX_6_6	0.04	0.8	0.2	1.8	0.85	0.07		0.23	6	4.02	101.2
RH_18_PYX_6_7	0.03	0.8	0.21	1.8	0.86	0.07		0.23	6	4.02	100.3
RH_18_PYX_7_1	0.02	0.87	0.13	1.9	0.84	0.05		0.21	6	4.01	101.0
RH_18_PYX_7_2	0.02	0.88	0.13	1.9	0.83	0.04	0.01	0.21	6	4.01	101.8
RH_18_PYX_7_3	0.03	0.87	0.14	1.9	0.81	0.05		0.22	6	4.01	100.5
RH_18_PYX_7_4	0.03	0.89	0.11	1.9	0.85	0.05		0.2	6	4.01	102.0
RH_18_PYX_7_5	0.03	0.82	0.2	1.8	0.87	0.06	0.02	0.19	6	4.02	102.5
RH_18_PYX_7_6	0.03	0.85	0.17	1.9	0.87	0.05	0.02	0.19	6	4.02	101.3
RH_18_PYX_8_1	0.03	0.78	0.25	1.8	0.84	0.08	0.01	0.24	6	4.02	100.5
RH_18_PYX_8_2	0.03	0.76	0.29	1.8	0.83	0.09		0.26	6	4.03	101.2
RH_18_PYX_8_3	0.03	0.83	0.2	1.8	0.85	0.06	0.02	0.22	6	4.02	101.0
RH_18_PYX_8_4	0.03	0.8	0.22	1.8	0.85	0.07		0.24	6	4.02	99.9
RH_18_PYX_8_5	0.03	0.81	0.2	1.8	0.85	0.07		0.24	6	4.02	99.8

	Na	Mg	Al	Si	Ca	Ti	Cr	Fe	O	Cation sum	Totals
RH_18_PYX_8_6	0.03	0.88	0.11	1.9	0.82	0.05		0.24	6	4.02	100.6
RH_18_PYX_9_1	0.03	0.83	0.2	1.8	0.87	0.06	0.01	0.21	6	4.02	99.8
RH_18_PYX_9_2	0.03	0.79	0.27	1.8	0.84	0.08	0.01	0.25	6	4.03	99.9
RH_18_PYX_9_3	0.03	0.85	0.17	1.9	0.85	0.05		0.21	6	4.02	100.2
RH_18_PYX_9_4	0.03	0.84	0.19	1.8	0.85	0.06		0.22	6	4.03	99.9
RH_18_PYX_9_5	0.03	0.83	0.19	1.8	0.85	0.06	0.01	0.22	6	4.02	101.4
RH_18_PYX_9_6	0.03	0.82	0.19	1.9	0.85	0.05		0.22	6	4.02	100.4
RH_18_PYX_10_1	0.03	0.74	0.3	1.7	0.84	0.1	0.01	0.27	6	4.03	99.6
RH_18_PYX_10_2	0.03	0.75	0.3	1.7	0.83	0.09	0.01	0.26	6	4.03	99.4
RH_18_PYX_10_3	0.03	0.84	0.18	1.9	0.84	0.06		0.23	6	4.02	101.1
RH_18_PYX_10_4	0.03	0.85	0.16	1.9	0.85	0.04		0.23	6	4.03	100.3
RH_18_PYX_11_2	0.03	0.83	0.19	1.8	0.85	0.05	0.02	0.21	6	4.02	102.4
RH_18_PYX_11_3	0.03	0.8	0.24	1.8	0.83	0.07		0.25	6	4.02	100.7
RH_18_PYX_11_4	0.03	0.84	0.18	1.9	0.86	0.05		0.23	6	4.03	100.3
RH_18_PYX_11_5	0.03	0.84	0.18	1.8	0.85	0.05		0.24	6	4.03	100.6
RH_20_PYX_1_1	0.02	0.87	0.14	1.9	0.81	0.05		0.24	6	4.01	102.6
RH_20_PYX_1_2	0.03	0.87	0.15	1.9	0.83	0.04	0.01	0.21	6	4.02	99.7
RH_20_PYX_1_3	0.03	0.86	0.16	1.9	0.84	0.04		0.23	6	4.03	101.8
RH_20_PYX_1_4	0.04	0.81	0.22	1.8	0.85	0.06		0.25	6	4.03	100.7
RH_20_PYX_2_1	0.02	0.9	0.08	1.9	0.87	0.02	0.02	0.16	6	4.01	100.7
RH_20_PYX_2_2	0.03	0.88	0.1	1.9	0.88	0.02	0.02	0.17	6	4.02	100.2
RH_20_PYX_2_3	0.02	0.9	0.09	1.9	0.87	0.02	0.02	0.17	6	4.01	100.3
RH_20_PYX_2_4	0.01	0.9	0.08	1.9	0.86	0.03	0.02	0.16	6	4	101.2
RH_20_PYX_2_5	0.02	0.9	0.08	1.9	0.86	0.02	0.02	0.17	6	4.01	100.8
RH_20_PYX_3_1	0.02	0.89	0.14	1.9	0.81	0.04		0.24	6	4.02	99.0
RH_20_PYX_3_2	0.03	0.86	0.18	1.9	0.83	0.05		0.21	6	4.02	98.7
RH_20_PYX_3_3	0.03	0.9	0.12	1.9	0.83	0.04	0.01	0.2	6	4.02	98.8
RH_20_PYX_3_4	0.03	0.86	0.17	1.9	0.85	0.04	0.02	0.2	6	4.02	99.8
RH_20_PYX_3_5	0.03	0.84	0.21	1.8	0.85	0.05	0.02	0.22	6	4.03	99.5
RH_20_PYX_3_6	0.03	0.85	0.18	1.9	0.85	0.05	0.01	0.2	6	4.02	98.8
RH_20_PYX_4_1	0.03	0.84	0.21	1.8	0.84	0.05	0.02	0.22	6	4.03	99.4
RH_20_PYX_4_2	0.03	0.85	0.19	1.8	0.85	0.05	0.01	0.23	6	4.04	99.9
RH_20_PYX_4_3	0.03	0.82	0.22	1.8	0.85	0.06		0.23	6	4.03	98.4
RH_20_PYX_4_4	0.04	0.81	0.23	1.8	0.86	0.06	0.01	0.23	6	4.04	98.8
RH_20_PYX_4_5	0.04	0.84	0.2	1.8	0.84	0.06	0.01	0.21	6	4.03	98.5
RH_20_PYX_5_1	0.03	0.82	0.2	1.8	0.84	0.05		0.24	6	4.03	98.5
RH_20_PYX_5_2	0.03	0.87	0.14	1.9	0.86	0.04	0.02	0.18	6	4.02	98.5
RH_20_PYX_5_3	0.04	0.82	0.2	1.8	0.85	0.06	0.01	0.25	6	4.04	99.8
RH_20_PYX_5_4	0.03	0.83	0.21	1.8	0.85	0.06		0.23	6	4.03	98.6
RH_20_PYX_5_5	0.03	0.83	0.21	1.8	0.85	0.06		0.24	6	4.03	99.1
RH_20_PYX_6_1	0.02	0.93	0.09	1.9	0.86	0.03	0.01	0.15	6	4.01	99.6
RH_20_PYX_6_2	0.02	0.93	0.08	1.9	0.86	0.02	0.02	0.15	6	4.01	99.7
RH_20_PYX_6_3	0.02	0.91	0.07	1.9	0.87	0.03	0.02	0.14	6	4	100.1
RH_20_PYX_6_4	0.03	0.92	0.07	1.9	0.87	0.02	0.02	0.15	6	4.01	99.8
RH_20_PYX_6_5	0.03	0.87	0.15	1.9	0.85	0.05	0.01	0.2	6	4.02	100.5
RH_20_PYX_7_1	0.04	0.78	0.28	1.8	0.84	0.09		0.26	6	4.03	100.1
RH_20_PYX_7_2	0.03	0.84	0.19	1.9	0.86	0.05	0.02	0.2	6	4.02	100.4
RH_20_PYX_7_3	0.02	0.87	0.16	1.9	0.86	0.04	0.01	0.19	6	4.02	100.1
RH_20_PYX_7_4	0.03	0.86	0.16	1.9	0.86	0.04		0.2	6	4.02	98.8
RH_20_PYX_7_5	0.03	0.83	0.21	1.8	0.86	0.04	0.02	0.21	6	4.03	100.4
RH_20_PYX_7_6	0.03	0.86	0.18	1.9	0.84	0.05	0.01	0.21	6	4.02	99.4
RH_20_PYX_8_1	0.03	0.86	0.16	1.9	0.82	0.05		0.23	6	4.02	98.0
RH_20_PYX_8_2	0.04	0.82	0.2	1.8	0.85	0.06		0.23	6	4.03	100.1
RH_20_PYX_8_3	0.02	0.81	0.22	1.8	0.84	0.07		0.25	6	4.02	98.9

	Na	Mg	Al	Si	Ca	Ti	Cr	Fe	O	Cation sum	Totals
RH_20_PYX_8_4	0.03	0.81	0.2	1.8	0.85	0.06		0.25	6	4.03	98.8
RH_20_PYX_9_1	0.02	0.87	0.13	1.9	0.81	0.04		0.25	6	4.02	100.9
RH_20_PYX_9_2	0.02	0.92	0.1	1.9	0.84	0.03		0.2	6	4.02	100.1
RH_20_PYX_9_3	0.02	0.86	0.16	1.9	0.83	0.05		0.22	6	4.02	99.7
RH_20_PYX_9_4	0.03	0.89	0.13	1.9	0.82	0.05		0.24	6	4.02	97.7
RH_20_PYX_10_1	0.03	0.86	0.14	1.9	0.88	0.04	0.02	0.19	6	4.02	99.7
RH_10_PYX_10_2	0.03	0.82	0.22	1.8	0.86	0.06	0.01	0.23	6	4.03	99.4
RH_20_PYX_10_3	0.03	0.86	0.18	1.8	0.86	0.05	0.02	0.2	6	4.03	100.4
RH_20_PYX_10_4	0.03	0.88	0.15	1.9	0.86	0.04		0.2	6	4.03	100.0
RH_20_PYX_10_5	0.02	0.84	0.2	1.8	0.87	0.05	0.02	0.21	6	4.03	98.7
RH_20_PYX_11_1	0.03	0.82	0.2	1.8	0.86	0.06	0.02	0.22	6	4.02	99.9
RH_20_PYX_11_2	0.02	0.83	0.19	1.8	0.86	0.05		0.22	6	4.02	98.9
RH_20_PYX_11_3	0.03	0.86	0.16	1.9	0.86	0.04	0.02	0.2	6	4.02	98.9
RH_20_PYX_11_4	0.03	0.83	0.19	1.8	0.85	0.05	0.01	0.23	6	4.03	98.8
RH_20_PYX_11_5	0.04	0.85	0.18	1.9	0.84	0.05	0.02	0.2	6	4.03	99.2
RH_20_PYX_12_1	0.03	0.94	0.07	1.9	0.87	0.03	0.02	0.14	6	4.02	101.2
RH_20_PYX_12_2	0.03	0.82	0.18	1.8	0.84	0.07		0.27	6	4.03	100.1
RH_20_PYX_12_3	0.03	0.88	0.12	1.9	0.83	0.05		0.22	6	4.02	99.7
RH_20_PYX_12_4	0.02	0.94	0.08	1.9	0.87	0.03	0.02	0.13	6	4.01	100.5
RH_20_PYX_12_5	0.03	0.93	0.09	1.9	0.87	0.02	0.02	0.13	6	4.02	99.6
RH_20_PYX_13_1	0.02	0.89	0.13	1.9	0.87	0.03	0.02	0.19	6	4.03	99.3
RH_20_PYX_13_2	0.02	0.89	0.13	1.9	0.86	0.04	0.02	0.19	6	4.03	99.3
RH_20_PYX_13_3	0.02	0.87	0.14	1.9	0.87	0.04	0.02	0.2	6	4.02	99.0
RH_20_PYX_13_4	0.03	0.87	0.14	1.9	0.86	0.04	0.02	0.19	6	4.02	99.5
RH_20_PYX_14_1	0.03	0.82	0.2	1.8	0.85	0.06	0.01	0.21	6	4.01	99.3
RH_20_PYX_14_2	0.03	0.83	0.19	1.8	0.86	0.06		0.23	6	4.02	98.3
RH_20_PYX_14_3	0.03	0.82	0.21	1.8	0.84	0.06		0.24	6	4.02	99.7
RH_20_PYX_14_4	0.03	0.83	0.19	1.8	0.85	0.06	0.01	0.23	6	4.03	99.5
RH_20_PYX_14_5	0.03	0.86	0.14	1.9	0.87	0.04	0.02	0.19	6	4.03	100.1
RH_20_PYX_14_6	0.03	0.84	0.19	1.8	0.86	0.06		0.22	6	4.03	98.9
RH_20_PYX_15_1	0.03	0.86	0.14	1.9	0.84	0.05		0.23	6	4.02	99.1
RH_20_PYX_15_2	0.04	0.84	0.17	1.9	0.84	0.05		0.22	6	4.02	98.5
RH_20_PYX_15_3	0.02	0.89	0.15	1.9	0.84	0.04		0.2	6	4.02	98.9
RH_20_PYX_15_4	0.03	0.92	0.12	1.9	0.84	0.04		0.2	6	4.03	98.2
RH_20_PYX_16_1	0.03	0.83	0.2	1.8	0.85	0.06		0.23	6	4.02	100.3
RH_20_PYX_16_2	0.03	0.82	0.2	1.8	0.84	0.05		0.24	6	4.02	98.9
RH_20_PYX_16_3	0.03	0.86	0.17	1.9	0.85	0.05	0.02	0.2	6	4.02	97.2

Appendix 6 - Table of the calculated aegirine component and Tschermak's substitution (in number of ions calculated for 6 oxygen)

	Al (tetr.)	Al (oct.)	Al (Jadeite)	Na (Jadeite)	Na (Aegirine)
RH_2_PYX_2_1	0.15	0.02	0	0	0.05
RH_2_PYX_2_2	0.15	0.03	0	0	0.05
RH_2_PYX_2_3	0.15	0.02	0	0	0.05
RH_2_PYX_2_4	0.16	0.03	0	0	0.05
RH_2_PYX_3_1	0.12	0.01	0	0	0.05
RH_2_PYX_3_2	0.12	0.02	0	0	0.05
RH_2_PYX_3_3	0.13	0.01	0	0	0.05
RH_2_PYX_3_4	0.13	0.01	0	0	0.05
RH_2_PYX_4_3	0.13	0.02	0	0	0.03
RH_2_PYX_4_4	0.13	0.04	0	0	0.03
RH_2_PYX_5_4	0.11	0.02	0	0	0.03
RH_2_PYX_5_5	0.14	0.02	0	0	0.03
RH_2_PYX_7_1	0.15	0.02	0	0	0.05
RH_2_PYX_7_2	0.15	0.03	0	0	0.05
RH_2_PYX_7_3	0.15	0.02	0	0	0.05
RH_2_PYX_7_4	0.16	0.03	0	0	0.05
RH_2_PYX_8_1	0.12	0.01	0	0	0.05
RH_2_PYX_8_2	0.12	0.02	0	0	0.05
RH_2_PYX_8_3	0.13	0.01	0	0	0.05
RH_2_PYX_8_4	0.13	0.01	0	0	0.05
RH_2_PYX_9_1	0.18	0.02	0	0	0.05
RH_2_PYX_9_2	0.17	0.02	0	0	0.04
RH_2_PYX_9_3	0.17	0.02	0	0	0.05
RH_2_PYX_9_4	0.15	0.02	0	0	0.05
RH_2_PYX_9_5	0.12	0.02	0	0	0.04
RH_2_PYX_10_1	0.1	0.01	0	0	0.05
RH_2_PYX_10_2	0.13	0.01	0	0	0.05
RH_2_PYX_10_3	0.12	0.01	0	0	0.04
RH_2_PYX_10_4	0.14	0.02	0	0	0.06
RH_2_PYX_10_5	0.12	0.02	0	0	0.05
RH_3_PYX_2_1	0.07	0	0	0	0.02
RH_3_PYX_2_2	0.08	0.01	0	0	0.03
RH_3_PYX_2_3	0.14	0.02	0	0	0.03
RH_3_PYX_2_4	0.14	0.02	0	0	0.03
RH_3_PYX_3_1	0.12	0.01	0	0	0.02
RH_3_PYX_3_2	0.12	0.01	0	0	0.03
RH_3_PYX_3_3	0.11	0.02	0	0	0.02
RH_3_PYX_4_1	0.07	0.01	0	0	0.03
RH_3_PYX_4_2	0.08	0.01	0	0	0.02
RH_3_PYX_4_3	0.09	0.01	0	0	0.02
RH_3_PYX_4_4	0.07	0.03	0	0	0.03
RH_3_PYX_5_5	0.09	0.02	0	0	0.03
RH_3_PYX_6_1	0.11	0.01	0	0	0.02
RH_3_PYX_6_3	0.12	0.02	0	0	0.03
RH_3_PYX_6_4	0.11	0.01	0	0	0.03
RH_3_PYX_6_5	0.12	0.02	0	0	0.03
RH_3_PYX_6_6	0.12	0.02	0	0	0.03
RH_3_PYX_6_7	0.12	0.02	0	0	0.04
RH_3_PYX_7_1	0.08	0	0	0	0.02
RH_3_PYX_7_2	0.09	0.01	0	0	0.03
RH_3_PYX_7_3	0.11	0.01	0	0	0.02

	Al (tetr.)	Al (oct.)	Al (Jadeite)	Na (Jadeite)	Na (Aegirine)
RH_3_PYX_8_1	0.09	0.01	0	0	0.03
RH_3_PYX_8_2	0.11	0.02	0	0	0.03
RH_3_PYX_8_3	0.11	0.02	0	0	0.02
RH_3_PYX_8_4	0.12	0.02	0	0	0.02
RH_3_PYX_9_1	0.1	0.02	0	0	0.03
RH_3_PYX_9_2	0.1	0.02	0	0	0.02
RH_3_PYX_9_4	0.1	0.01	0	0	0.02
RH_6_PYX_1_1	0.05	0.02	0	0	0.02
RH_6_PYX_1_2	0.06	0.01	0	0	0.03
RH_6_PYX_1_3	0.06	0.01	0	0	0.02
RH_6_PYX_1_5	0.07	0.01	0	0	0.02
RH_6_PYX_2_1	0.1	0	0	0	0.03
RH_6_PYX_2_2	0.08	0.02	0	0	0.02
RH_6_PYX_2_3	0.1	0.02	0	0	0.02
RH_6_PYX_2_4	0.11	0.02	0	0	0.03
RH_6_PYX_2_5	0.11	0.01	0	0	0.03
RH_6_PYX_2_6	0.13	0.02	0	0	0.03
RH_6_PYX_3_1	0.06	0	0	0	0.03
RH_6_PYX_3_2	0.06	0	0	0	0.02
RH_6_PYX_3_3	0.06	0.01	0	0	0.02
RH_6_PYX_3_4	0.05	0.02	0	0	0.02
RH_6_PYX_3_5	0.06	0.01	0	0	0.02
RH_6_PYX_3_6	0.06	0.01	0	0	0.03
RH_6_PYX_4_1	0.09	0.01	0	0	0.03
RH_6_PYX_4_2	0.08	0.01	0	0	0.02
RH_6_PYX_4_3	0.08	0.02	0	0	0.03
RH_6_PYX_4_4	0.07	0.02	0	0	0.02
RH_6_PYX_5_1	0.06	0	0	0	0.02
RH_6_PYX_5_2	0.06	0.01	0	0	0.02
RH_6_PYX_5_3	0.07	0	0	0	0.02
RH_6_PYX_5_4	0.04	0.02	0	0	0.02
RH_6_PYX_5_5	0.06	0	0	0	0.02
RH_6_PYX_6_1	0.1	0.01	0	0	0.02
RH_6_PYX_6_2	0.1	0	0	0	0.03
RH_6_PYX_6_3	0.1	0.03	0	0	0.03
RH_6_PYX_6_4	0.09	0.03	0	0	0.02
RH_6_PYX_6_5	0.08	0.02	0	0	0.03
RH_6_PYX_7_1	0.06	0	0	0	0.02
RH_6_PYX_7_2	0.06	0.01	0	0	0.02
RH_6_PYX_7_3	0.07	0.01	0	0	0.02
RH_6_PYX_7_4	0.06	0.01	0	0	0.03
RH_6_PYX_7_5	0.09	0.02	0	0	0.02
RH_6_PYX_8_1	0.07	0	0	0	0.02
RH_6_PYX_8_2	0.07	0.01	0	0	0.02
RH_6_PYX_8_3	0.06	0.01	0	0	0.03
RH_6_PYX_8_4	0.06	0.02	0	0	0.02
RH_6_PYX_8_5	0.06	0.02	0	0	0.02
RH_6_PYX_8_6	0.07	0.01	0	0	0.03
RH_6_PYX_9_1	0.09	0.01	0	0	0.02
RH_6_PYX_9_2	0.09	0.01	0	0	0.02
RH_6_PYX_9_3	0.07	0.01	0	0	0.03
RH_6_PYX_9_4	0.06	0.02	0	0	0.02
RH_6_PYX_9_5	0.08	0	0	0	0.02
RH_6_PYX_10_1	0.08	0.02	0	0	0.03

	Al (tetr.)	Al (oct.)	Al (Jadeite)	Na (Jadeite)	Na (Aegirine)
RH_6_PYX_10_2	0.09	0.02	0	0	0.03
RH_6_PYX_10_5	0.08	0.02	0	0	0.02
RH_6_PYX_11_1	0.11	0.01	0	0	0.03
RH_6_PYX_11_2	0.09	0.02	0	0	0.02
RH_6_PYX_11_3	0.07	0	0	0	0.01
RH_6_PYX_11_4	0.06	0.03	0	0	0.02
RH_6_PYX_11_5	0.09	0.01	0	0	0.02
RH_8_PYX_1_1	0.13	0.03	0	0	0.03
RH_8_PYX_1_2	0.21	0.02	0	0	0.04
RH_8_PYX_1_3	0.17	0.03	0	0	0.04
RH_8_PYX_1_4	0.18	0.04	0	0	0.03
RH_8_PYX_1_5	0.19	0.02	0	0	0.04
RH_8_PYX_2_1	0.14	0	0	0	0.03
RH_8_PYX_2_2	0.25	0.02	0	0	0.05
RH_8_PYX_2_3	0.17	0.02	0	0	0.04
RH_8_PYX_2_4	0.17	0.02	0	0	0.04
RH_8_PYX_2_5	0.16	0.02	0	0	0.03
RH_8_PYX_3_1	0.19	0.02	0	0	0.04
RH_8_PYX_3_2	0.19	0.01	0	0	0.04
RH_8_PYX_3_3	0.17	0.03	0	0	0.03
RH_8_PYX_3_4	0.15	0.03	0	0	0.03
RH_8_PYX_3_5	0.12	0.01	0	0	0.03
RH_8_PYX_4_1	0.14	0.01	0	0	0.03
RH_8_PYX_4_2	0.13	0.01	0	0	0.03
RH_8_PYX_4_3	0.2	0.02	0	0	0.03
RH_8_PYX_4_4	0.2	0.01	0	0	0.04
RH_8_PYX_5_1	0.13	0.02	0	0	0.03
RH_8_PYX_5_2	0.11	0.01	0	0	0.02
RH_8_PYX_5_3	0.11	0.01	0	0	0.02
RH_8_PYX_5_4	0.11	0	0	0	0.03
RH_8_PYX_6_1	0.15	0.03	0	0	0.04
RH_8_PYX_6_2	0.15	0.02	0	0	0.03
RH_8_PYX_6_3	0.13	0.02	0	0	0.02
RH_8_PYX_6_4	0.15	0.02	0	0	0.03
RH_8_PYX_7_1	0.15	0.02	0	0	0.03
RH_8_PYX_7_2	0.11	0.03	0	0	0.03
RH_8_PYX_7_3	0.12	0.02	0	0	0.03
RH_8_PYX_7_4	0.12	0.01	0	0	0.03
RH_8_PYX_8_1	0.15	0.02	0	0	0.03
RH_8_PYX_8_2	0.16	0.03	0	0	0.04
RH_8_PYX_8_3	0.16	0.04	0	0	0.03
RH_8_PYX_8_4	0.15	0.02	0	0	0.03
RH_10_PYX_1_2	0.2	0.03	0	0	0.03
RH_10_PYX_1_4	0.05	0.01	0	0	0.01
RH_10_PYX_1_5	0.05	0.01	0	0	0.02
RH_10_PYX_2_1	0.15	0.01	0	0	0.03
RH_10_PYX_2_2	0.17	0.01	0	0	0.03
RH_10_PYX_2_3	0.11	0.01	0	0	0.03
RH_10_PYX_2_4	0.11	0	0	0	0.02
RH_10_PYX_3_1	0.16	0	0	0	0.03
RH_10_PYX_3_2	0.12	0.02	0	0	0.03
RH_10_PYX_3_3	0.11	0	0	0	0.02
RH_10_PYX_3_4	0.12	0.02	0	0	0.03
RH_10_PYX_3_5	0.14	0.01	0	0	0.02

	Al (tetr.)	Al (oct.)	Al (Jadeite)	Na (Jadeite)	Na (Aegirine)
RH_10_PYX_4_1	0.09	0	0	0	0.03
RH_10_PYX_4_2	0.11	0.03	0	0	0.03
RH_10_PYX_4_3	0.09	0.02	0	0	0.04
RH_10_PYX_4_4	0.15	0.03	0	0	0.04
RH_10_PYX_4_5	0.14	0.03	0	0	0.04
RH_10_PYX_4_6	0.15	0.04	0	0	0.04
RH_10_PYX_5_1	0.1	0.02	0	0	0.02
RH_10_PYX_5_2	0.1	0	0	0	0.01
RH_10_PYX_5_3	0.12	0.03	0	0	0.02
RH_10_PYX_5_4	0.2	0.02	0	0	0.03
RH_10_PYX_5_5	0.18	0.03	0	0	0.02
RH_10_PYX_6_1	0.14	0.01	0	0	0.02
RH_10_PYX_6_2	0.15	0.03	0	0	0.04
RH_10_PYX_6_3	0.15	0.02	0	0	0.04
RH_10_PYX_6_4	0.13	0.01	0	0	0.04
RH_10_PYX_7_1	0.11	0.01	0	0	0.02
RH_10_PYX_7_2	0.07	0	0	0	0.02
RH_10_PYX_7_3	0.06	0	0	0	0.02
RH_10_PYX_7_4	0.07	0	0	0	0.02
RH_10_PYX_8_1	0.15	0.03	0	0	0.02
RH_10_PYX_8_2	0.18	0.04	0	0	0.03
RH_10_PYX_8_3	0.2	0.03	0	0	0.03
RH_10_PYX_8_4	0.19	0.02	0	0	0.04
RH_10_PYX_9_1	0.1	0.01	0	0	0.03
RH_10_PYX_9_2	0.13	0.03	0	0	0.03
RH_10_PYX_9_3	0.14	0.04	0	0	0.03
RH_10_PYX_9_4	0.19	0.02	0	0	0.03
RH_10_PYX_9_5	0.14	0.02	0	0	0.04
RH_11_PYX_1_1	0.17	0.02	0	0	0.02
RH_11_PYX_1_2	0.17	0.02	0	0	0.03
RH_11_PYX_1_3	0.18	0.03	0	0	0.03
RH_11_PYX_1_4	0.17	0.02	0	0	0.03
RH_11_PYX_1_5	0.17	0.01	0	0	0.03
RH_11_PYX_2_1	0.14	0.02	0	0	0.04
RH_11_PYX_2_2	0.18	0.02	0	0	0.04
RH_11_PYX_2_3	0.21	0.03	0	0	0.04
RH_11_PYX_2_4	0.15	0.03	0	0	0.03
RH_11_PYX_2_5	0.19	0.03	0	0	0.03
RH_11_PYX_2_6	0.19	0	0	0	0.03
RH_11_PYX_3_1	0.12	0.02	0	0	0.04
RH_11_PYX_3_2	0.13	0.02	0	0	0.03
RH_11_PYX_3_3	0.13	0.02	0	0	0.04
RH_11_PYX_3_4	0.14	0.02	0	0	0.03
RH_11_PYX_4_1	0.15	0.02	0	0	0.03
RH_11_PYX_4_2	0.12	0.02	0	0	0.03
RH_11_PYX_4_3	0.18	0.02	0	0	0.04
RH_11_PYX_4_4	0.13	0.01	0	0	0.03
RH_11_PYX_5_1	0.18	0.04	0	0	0.03
RH_11_PYX_5_2	0.14	0.02	0	0	0.04
RH_11_PYX_5_3	0.14	0.02	0	0	0.06
RH_11_PYX_5_4	0.13	0.02	0	0	0.03
RH_11_PYX_6_1	0.14	0.01	0	0	0.03
RH_11_PYX_6_2	0.17	0.03	0	0	0.03
RH_11_PYX_6_3	0.11	0.01	0	0	0.03

	Al (tetr.)	Al (oct.)	Al (Jadeite)	Na (Jadeite)	Na (Aegirine)
RH_11_PYX_6_4	0.13	0.01	0	0	0.02
RH_11_PYX_6_5	0.13	0.02	0	0	0.02
RH_11_PYX_7_1	0.16	0.02	0	0	0.02
RH_11_PYX_7_3	0.16	0.03	0	0	0.03
RH_11_PYX_7_4	0.16	0.02	0	0	0.05
RH_11_PYX_7_5	0.16	0.03	0	0	0.03
RH_11_PYX_8_1	0.18	0.01	0	0	0.03
RH_11_PYX_8_2	0.16	0.03	0	0	0.04
RH_11_PYX_8_3	0.14	0.03	0	0	0.03
RH_11_PYX_8_4	0.16	0.03	0	0	0.04
RH_11_PYX_8_5	0.19	0.02	0	0	0.04
RH_11_PYX_9_1	0.17	0.02	0	0	0.04
RH_11_PYX_9_2	0.19	0.03	0	0	0.04
RH_11_PYX_9_3	0.14	0.01	0	0	0.03
RH_11_PYX_10_1	0.13	0.01	0	0	0.03
RH_11_PYX_10_2	0.13	0.01	0	0	0.03
RH_11_PYX_10_3	0.13	0.02	0	0	0.03
RH_11_PYX_10_4	0.13	0.01	0	0	0.03
RH_11_PYX_11_1	0.19	0.01	0	0	0.04
RH_11_PYX_11_2	0.13	0.02	0	0	0.03
RH_11_PYX_11_3	0.12	0.02	0	0	0.03
RH_11_PYX_11_4	0.13	0.02	0	0	0.03
RH_13_PYX_1_1	0.18	0.02	0	0	0.05
RH_13_PYX_1_2	0.17	0.03	0	0	0.04
RH_13_PYX_1_3	0.11	0.01	0	0	0.03
RH_13_PYX_1_4	0.17	0.02	0	0	0.03
RH_13_PYX_1_5	0.12	0.03	0	0	0.03
RH_13_PYX_2_2	0.14	0.03	0	0	0.03
RH_13_PYX_2_3	0.17	0.03	0	0	0.04
RH_13_PYX_2_4	0.16	0.01	0	0	0.02
RH_13_PYX_3_1	0.15	0.02	0	0	0.03
RH_13_PYX_3_2	0.11	0.04	0	0	0.03
RH_13_PYX_3_3	0.14	0.04	0	0	0.02
RH_13_PYX_3_4	0.13	0.04	0	0	0.03
RH_13_PYX_3_5	0.16	0.03	0	0	0.02
RH_13_PYX_4_2	0.11	0.02	0	0	0.03
RH_13_PYX_4_3	0.23	0.05	0	0	0.04
RH_13_PYX_4_4	0.2	0.02	0	0	0.03
RH_13_PYX_4_5	0.2	0.03	0	0	0.04
RH_13_PYX_4_6	0.11	0.03	0	0	0.02
RH_13_PYX_4_7	0.12	0.04	0	0	0.02
RH_13_PYX_5_1	0.1	0.03	0	0	0.02
RH_13_PYX_5_2	0.1	0.02	0	0	0.03
RH_13_PYX_5_3	0.11	0.01	0	0	0.03
RH_13_PYX_5_4	0.13	0.02	0	0	0.03
RH_13_PYX_5_5	0.13	0.03	0	0	0.03
RH_13_PYX_6_1	0.16	0.02	0	0	0.04
RH_13_PYX_6_2	0.2	0.02	0	0	0.04
RH_13_PYX_6_3	0.18	0.02	0	0	0.04
RH_13_PYX_6_4	0.18	0.03	0	0	0.04
RH_13_PYX_6_5	0.17	0.03	0	0	0.03
RH_13_PYX_7_1	0.1	0.04	0	0	0.03
RH_13_PYX_7_2	0.12	0.01	0	0	0.03
RH_13_PYX_7_3	0.11	0.03	0	0	0.04

	Al (tetr.)	Al (oct.)	Al (Jadeite)	Na (Jadeite)	Na (Aegirine)
RH_13_PYX_7_4	0.13	0.01	0	0	0.04
RH_13_PYX_7_5	0.15	0.03	0	0	0.03
RH_13_PYX_7_6	0.19	0.03	0	0	0.02
RH_13_PYX_8_1	0.15	0.03	0	0	0.03
RH_13_PYX_8_2	0.17	0.04	0	0	0.03
RH_13_PYX_8_3	0.16	0.03	0	0	0.04
RH_13_PYX_8_4	0.14	0.03	0	0	0.03
RH_13_PYX_8_5	0.16	0.03	0	0	0.04
RH_16_PYX_1_1	0.16	0.01	0	0	0.02
RH_16_PYX_1_3	0.14	0.02	0	0	0.03
RH_16_PYX_1_4	0.14	0.04	0	0	0.04
RH_16_PYX_1_5	0.16	0.01	0	0	0.03
RH_16_PYX_1_6	0.15	0.03	0	0	0.03
RH_16_PYX_1_7	0.16	0.02	0	0	0.03
RH_16_PYX_2_1	0.26	0.05	0	0	0.03
RH_16_PYX_2_2	0.16	0	0	0	0.03
RH_16_PYX_2_3	0.13	0.03	0	0	0.03
RH_16_PYX_2_4	0.1	0.03	0	0	0.03
RH_16_PYX_2_5	0.15	0.02	0	0	0.03
RH_16_PYX_3_1	0.15	0.04	0	0	0.03
RH_16_PYX_3_2	0.14	0.01	0	0	0.03
RH_16_PYX_3_3	0.14	0.04	0	0	0.04
RH_16_PYX_3_4	0.14	0.04	0	0	0.03
RH_16_PYX_3_5	0.14	0.02	0	0	0.03
RH_16_PYX_3_6	0.17	0.01	0	0	0.03
RH_16_PYX_4_1	0.15	0.01	0	0	0.03
RH_16_PYX_4_2	0.14	0.03	0	0	0.02
RH_16_PYX_4_3	0.16	0.03	0	0	0.02
RH_16_PYX_4_4	0.1	0	0	0	0.03
RH_16_PYX_4_5	0.07	0.02	0	0	0.02
RH_16_PYX_5_1	0.11	0.01	0	0	0.02
RH_16_PYX_5_2	0.08	0.01	0	0	0.02
RH_16_PYX_5_3	0.07	0.02	0	0	0.02
RH_16_PYX_5_4	0.07	0.02	0	0	0.02
RH_16_PYX_5_5	0.13	0.03	0	0	0.03
RH_16_PYX_6_1	0.09	0.01	0	0	0.02
RH_16_PYX_6_2	0.09	0	0	0	0.03
RH_16_PYX_6_3	0.14	0.03	0	0	0.03
RH_16_PYX_6_4	0.12	0.02	0	0	0.02
RH_16_PYX_6_5	0.1	0.01	0	0	0.02
RH_16_PYX_7_1	0.14	0.04	0	0	0.04
RH_16_PYX_7_2	0.21	0.03	0	0	0.03
RH_16_PYX_7_3	0.14	0.02	0	0	0.03
RH_16_PYX_7_4	0.15	0.03	0	0	0.03
RH_16_PYX_7_5	0.17	0.01	0	0	0.02
RH_16_PYX_8_1	0.2	0	0	0	0.03
RH_16_PYX_8_2	0.16	0.01	0	0	0.04
RH_16_PYX_8_3	0.24	0.03	0	0	0.04
RH_16_PYX_8_4	0.21	0.04	0	0	0.03
RH_16_PYX_8_5	0.17	0.05	0	0	0.04
RH_16_PYX_8_6	0.18	0.03	0	0	0.02
RH_16_PYX_8_7	0.19	0.03	0	0	0.02
RH_16_PYX_8_8	0.19	0.01	0	0	0.03
RH_16_PYX_9_1	0.25	0.04	0	0	0.03

	Al (tetr.)	Al (oct.)	Al (Jadeite)	Na (Jadeite)	Na (Aegirine)
RH_16_PYX_9_2	0.17	0.01	0	0	0.03
RH_16_PYX_9_3	0.13	0.03	0	0	0.03
RH_16_PYX_9_4	0.12	0.01	0	0	0.03
RH_16_PYX_9_5	0.16	0.02	0	0	0.03
RH_18_PYX_1_1	0.2	0	0	0	0.03
RH_18_PYX_1_2	0.16	0.01	0	0	0.04
RH_18_PYX_1_3	0.24	0.03	0	0	0.04
RH_18_PYX_1_4	0.21	0.04	0	0	0.03
RH_18_PYX_1_5	0.17	0.05	0	0	0.04
RH_18_PYX_1_6	0.18	0.03	0	0	0.02
RH_18_PYX_1_7	0.19	0.03	0	0	0.02
RH_18_PYX_1_8	0.19	0.01	0	0	0.03
RH_18_PYX_2_1	0.18	0.01	0	0	0.04
RH_18_PYX_2_2	0.2	0.02	0	0	0.04
RH_18_PYX_2_3	0.19	0.04	0	0	0.03
RH_18_PYX_2_4	0.16	0.02	0	0	0.04
RH_18_PYX_2_5	0.16	0.03	0	0	0.03
RH_18_PYX_2_6	0.16	0.03	0	0	0.04
RH_18_PYX_2_7	0.16	0.01	0	0	0.03
RH_18_PYX_2_8	0.15	0.01	0	0	0.04
RH_18_PYX_3_1	0.21	0.03	0	0	0.03
RH_18_PYX_3_2	0.19	0.03	0	0	0.04
RH_18_PYX_3_3	0.12	0.02	0	0	0.03
RH_18_PYX_3_4	0.11	0.02	0	0	0.04
RH_18_PYX_3_5	0.14	0.03	0	0	0.03
RH_18_PYX_4_1	0.25	0.04	0	0	0.03
RH_18_PYX_4_2	0.17	0.01	0	0	0.03
RH_18_PYX_4_3	0.13	0.03	0	0	0.03
RH_18_PYX_4_4	0.12	0.01	0	0	0.03
RH_18_PYX_4_5	0.16	0.02	0	0	0.03
RH_18_PYX_5_1	0.24	0.04	0	0	0.03
RH_18_PYX_5_2	0.2	0.02	0	0	0.04
RH_18_PYX_5_3	0.13	0.01	0	0	0.03
RH_18_PYX_5_4	0.13	0.03	0	0	0.02
RH_18_PYX_6_1	0.19	0.02	0	0	0.04
RH_18_PYX_6_2	0.26	0.01	0	0	0.04
RH_18_PYX_6_3	0.19	0.03	0	0	0.03
RH_18_PYX_6_4	0.2	0.02	0	0	0.03
RH_18_PYX_6_5	0.25	0.03	0	0	0.03
RH_18_PYX_6_6	0.17	0.03	0	0	0.04
RH_18_PYX_6_7	0.19	0.02	0	0	0.03
RH_18_PYX_7_1	0.11	0.02	0	0	0.02
RH_18_PYX_7_2	0.11	0.02	0	0	0.02
RH_18_PYX_7_3	0.11	0.03	0	0	0.03
RH_18_PYX_7_4	0.11	0	0	0	0.03
RH_18_PYX_7_5	0.17	0.03	0	0	0.03
RH_18_PYX_7_6	0.15	0.02	0	0	0.03
RH_18_PYX_8_1	0.21	0.04	0	0	0.03
RH_18_PYX_8_2	0.24	0.05	0	0	0.03
RH_18_PYX_8_3	0.18	0.02	0	0	0.03
RH_18_PYX_8_4	0.18	0.04	0	0	0.03
RH_18_PYX_8_5	0.18	0.02	0	0	0.03
RH_18_PYX_8_6	0.11	0	0	0	0.03
RH_18_PYX_9_1	0.17	0.03	0	0	0.03

	Al (tetr.)	Al (oct.)	Al (Jadeite)	Na (Jadeite)	Na (Aegirine)
RH_18_PYX_9_2	0.23	0.04	0	0	0.03
RH_18_PYX_9_3	0.14	0.03	0	0	0.03
RH_18_PYX_9_4	0.16	0.03	0	0	0.03
RH_18_PYX_9_5	0.17	0.02	0	0	0.03
RH_18_PYX_9_6	0.15	0.04	0	0	0.03
RH_18_PYX_10_1	0.27	0.03	0	0	0.03
RH_18_PYX_10_2	0.26	0.04	0	0	0.03
RH_18_PYX_10_3	0.15	0.03	0	0	0.03
RH_18_PYX_10_4	0.13	0.03	0	0	0.03
RH_18_PYX_11_2	0.16	0.03	0	0	0.03
RH_18_PYX_11_3	0.19	0.05	0	0	0.03
RH_18_PYX_11_4	0.15	0.03	0	0	0.03
RH_18_PYX_11_5	0.16	0.02	0	0	0.03
RH_20_PYX_1_1	0.12	0.02	0	0	0.02
RH_20_PYX_1_2	0.13	0.02	0	0	0.03
RH_20_PYX_1_3	0.13	0.03	0	0	0.03
RH_20_PYX_1_4	0.19	0.03	0	0	0.04
RH_20_PYX_2_1	0.07	0.01	0	0	0.02
RH_20_PYX_2_2	0.08	0.02	0	0	0.03
RH_20_PYX_2_3	0.08	0.01	0	0	0.02
RH_20_PYX_2_4	0.06	0.02	0	0	0.01
RH_20_PYX_2_5	0.07	0.01	0	0	0.02
RH_20_PYX_3_1	0.12	0.02	0	0	0.02
RH_20_PYX_3_2	0.14	0.04	0	0	0.03
RH_20_PYX_3_3	0.11	0.01	0	0	0.03
RH_20_PYX_3_4	0.15	0.02	0	0	0.03
RH_20_PYX_3_5	0.19	0.02	0	0	0.03
RH_20_PYX_3_6	0.15	0.03	0	0	0.03
RH_20_PYX_4_1	0.18	0.03	0	0	0.03
RH_20_PYX_4_2	0.18	0.01	0	0	0.03
RH_20_PYX_4_3	0.18	0.04	0	0	0.03
RH_20_PYX_4_4	0.2	0.03	0	0	0.04
RH_20_PYX_4_5	0.17	0.03	0	0	0.04
RH_20_PYX_5_1	0.16	0.04	0	0	0.03
RH_20_PYX_5_2	0.13	0.01	0	0	0.03
RH_20_PYX_5_3	0.18	0.02	0	0	0.04
RH_20_PYX_5_4	0.18	0.03	0	0	0.03
RH_20_PYX_5_5	0.18	0.03	0	0	0.03
RH_20_PYX_6_1	0.08	0.01	0	0	0.02
RH_20_PYX_6_2	0.07	0.01	0	0	0.02
RH_20_PYX_6_3	0.06	0.01	0	0	0.02
RH_20_PYX_6_4	0.07	0	0	0	0.03
RH_20_PYX_6_5	0.14	0.01	0	0	0.03
RH_20_PYX_7_1	0.24	0.04	0	0	0.04
RH_20_PYX_7_2	0.15	0.04	0	0	0.03
RH_20_PYX_7_3	0.14	0.02	0	0	0.02
RH_20_PYX_7_4	0.13	0.03	0	0	0.03
RH_20_PYX_7_5	0.17	0.04	0	0	0.03
RH_20_PYX_7_6	0.15	0.03	0	0	0.03
RH_20_PYX_8_1	0.13	0.03	0	0	0.03
RH_20_PYX_8_2	0.17	0.03	0	0	0.04
RH_20_PYX_8_3	0.19	0.03	0	0	0.02
RH_20_PYX_8_4	0.18	0.02	0	0	0.03
RH_20_PYX_9_1	0.11	0.02	0	0	0.02

	Al (tetr.)	Al (oct.)	Al (Jadeite)	Na (Jadeite)	Na (Aegirine)
RH_20_PYX_9_2	0.09	0.01	0	0	0.02
RH_20_PYX_9_3	0.13	0.03	0	0	0.02
RH_20_PYX_9_4	0.12	0.01	0	0	0.03
RH_20_PYX_10_1	0.12	0.02	0	0	0.03
RH_10_PYX_10_2	0.19	0.03	0	0	0.03
RH_20_PYX_10_3	0.16	0.02	0	0	0.03
RH_20_PYX_10_4	0.13	0.02	0	0	0.03
RH_20_PYX_10_5	0.17	0.03	0	0	0.02
RH_20_PYX_11_1	0.17	0.03	0	0	0.03
RH_20_PYX_11_2	0.16	0.03	0	0	0.02
RH_20_PYX_11_3	0.14	0.02	0	0	0.03
RH_20_PYX_11_4	0.17	0.02	0	0	0.03
RH_20_PYX_11_5	0.15	0.03	0	0	0.04
RH_20_PYX_12_2	0.17	0.01	0	0	0.03
RH_20_PYX_12_3	0.11	0.01	0	0	0.03
RH_20_PYX_12_4	0.07	0.01	0	0	0.02
RH_20_PYX_12_5	0.08	0.01	0	0	0.03
RH_20_PYX_13_1	0.12	0.01	0	0	0.02
RH_20_PYX_13_2	0.13	0	0	0	0.02
RH_20_PYX_13_3	0.13	0.01	0	0	0.02
RH_20_PYX_13_4	0.13	0.01	0	0	0.03
RH_20_PYX_14_1	0.16	0.04	0	0	0.03
RH_20_PYX_14_2	0.16	0.03	0	0	0.03
RH_20_PYX_14_3	0.18	0.03	0	0	0.03
RH_20_PYX_14_4	0.17	0.02	0	0	0.03
RH_20_PYX_14_5	0.14	0	0	0	0.03
RH_20_PYX_14_6	0.17	0.02	0	0	0.03
RH_20_PYX_15_1	0.12	0.02	0	0	0.03
RH_20_PYX_15_2	0.14	0.03	0	0	0.04
RH_20_PYX_15_3	0.12	0.03	0	0	0.02
RH_20_PYX_15_4	0.12	0	0	0	0.03
RH_20_PYX_16_1	0.16	0.04	0	0	0.03
RH_20_PYX_16_2	0.16	0.04	0	0	0.03
RH_20_PYX_16_3	0.15	0.02	0	0	0.03

Appendix 7 - Table of the chemical composition of the olivine phenocrysts (in number of ions calculated for 4 oxygen)

	Mg	Si	Ca	Fe	O	Cation sum	Totals
RH_2_OL_1_1	1.6	1	0.01	0.36	4	3	98.0
RH_2_OL_1_2	1.6	1.01	0.01	0.38	4	2.99	97.6
RH_2_OL_1_3	1.6	1.01	0.01	0.39	4	2.99	98.1
RH_2_OL_1_4	1.6	1.01	0.01	0.4	4	2.99	97.8
RH_2_OL_2_1	1.6	1		0.38	4	3	98.4
RH_2_OL_2_2	1.6	1	0.01	0.39	4	3	100.5
RH_2_OL_2_3	1.6	1	0.01	0.38	4	3	100.2
RH_2_OL_2_4	1.6	1	0.01	0.37	4	3	99.1
RH_2_OL_2_5	1.6	1	0.01	0.37	4	3	99.7
RH_2_OL_2_6	1.6	1	0.01	0.36	4	3	99.5
RH_2_OL_3_1	1.6	1	0.01	0.38	4	3	100.0
RH_2_OL_3_2	1.6	1	0.01	0.39	4	3	99.8
RH_2_OL_3_3	1.6	1		0.39	4	3	99.1
RH_2_OL_3_4	1.6	1.01		0.38	4	2.99	98.5
RH_2_OL_3_5	1.6	1	0.01	0.39	4	3	99.6
RH_2_OL_3_6	1.6	1	0.01	0.38	4	3	99.2
RH_2_OL_3_7	1.6	0.99	0.01	0.38	4	3.01	99.1
RH_10_OL_1_1	1.8	1	0	0.24	4	3	98.4
RH_10_OL_1_2	1.8	1	0.01	0.24	4	3	98.3
RH_10_OL_1_3	1.8	1.01	0.01	0.23	4	2.99	97.1
RH_10_OL_1_4	1.7	1.01	0.01	0.24	4	2.99	99.1
RH_10_OL_1_5	1.8	1.01	0.01	0.24	4	2.99	97.2
RH_10_OL_2_1	1.8	1	0.01	0.24	4	3	99.8
RH_10_OL_2_2	1.8	1	0.01	0.24	4	3	101.0
RH_10_OL_2_3	1.8	1	0.01	0.23	4	3	99.9
RH_10_OL_2_4	1.8	1	0.01	0.23	4	3	99.9
RH_10_OL_3_2	1.7	1	0.01	0.33	4	3	99.4
RH_10_OL_3_3	1.7	1	0.01	0.33	4	3	99.9
RH_10_OL_3_4	1.6	1	0.01	0.36	4	3	100.0
RH_10_OL_3_5	1.7	1	0.01	0.34	4	3	98.9
RH_10_OL_3_6	1.7	1	0.01	0.3	4	3	100.0
RH_10_OL_4_1	1.7	1	0.01	0.3	4	3	98.6
RH_10_OL_4_2	1.7	1	0.01	0.29	4	3	99.4
RH_10_OL_4_3	1.7	1.01	0.01	0.3	4	2.99	99.8
RH_10_OL_4_4	1.7	1	0.01	0.28	4	3	99.6
RH_10_OL_4_5	1.7	0.99	0.01	0.29	4	3.01	99.6
RH_10_OL_5_1	1.7	0.99	0.01	0.27	4	3.01	99.8
RH_10_OL_5_2	1.7	1	0.01	0.26	4	3	99.3
RH_10_OL_5_3	1.7	1	0.01	0.26	4	3	99.4
RH_10_OL_5_4	1.7	1.01	0.01	0.25	4	2.99	98.8
RH_10_OL_5_5	1.7	1	0.01	0.26	4	3	99.2
RH_10_OL_6_1	1.7	1	0.01	0.28	4	3	101.3
RH_10_OL_6_2	1.7	1	0.01	0.28	4	3	100.6
RH_10_OL_6_3	1.7	1	0.01	0.27	4	3	102.3
RH_10_OL_6_4	1.7	1	0.01	0.28	4	3	100.7
RH_10_OL_6_5	1.7	1	0.01	0.28	4	3	102.0
RH_10_OL_7_1	1.7	1	0.01	0.31	4	3	101.9
RH_10_OL_7_2	1.7	1	0.01	0.29	4	3	102.0
RH_10_OL_7_3	1.7	1	0.01	0.3	4	3	101.6
RH_10_OL_7_4	1.7	1	0.01	0.29	4	3	101.3
RH_10_OL_7_5	1.7	1	0.01	0.3	4	3	101.4

	Mg	Si	Ca	Fe	O	Cation sum	Totals
RH_10_OL_7_6	1.7	1	0.01	0.3	4	3	101.3
RH_10_OL_7_7	1.7	1	0.01	0.3	4	3	100.6
RH_10_OL_8_1	1.7	1	0.01	0.29	4	3	99.8
RH_10_OL_8_2	1.7	1	0.01	0.28	4	3	99.9
RH_10_OL_8_3	1.7	1	0.01	0.29	4	3	99.8
RH_10_OL_8_4	1.7	1	0.01	0.28	4	3	100.9
RH_10_OL_8_5	1.7	1.01	0.01	0.27	4	2.99	99.7
RH_10_OL_9_1	1.7	1	0.01	0.26	4	3	100.2
RH_10_OL_9_2	1.7	1	0.01	0.26	4	3	101.0
RH_10_OL_9_3	1.7	1	0.01	0.26	4	3	98.7
RH_10_OL_9_4	1.7	1	0.01	0.26	4	3	101.4
RH_10_OL_9_5	1.7	1	0.01	0.26	4	3	100.1
RH_10_OL_9_6	1.7	1.01	0.01	0.25	4	2.99	99.1
RH_10_OL_9_7	1.7	1	0.01	0.26	4	3	99.5
RH_10_OL_10_1	1.7	1	0.01	0.28	4	3	99.7
RH_10_OL_10_2	1.7	1	0.01	0.27	4	3	97.7
RH_10_OL_10_3	1.7	1	0.01	0.28	4	3	98.9
RH_10_OL_10_4	1.7	1.01	0.01	0.28	4	2.99	99.8
RH_10_OL_11_1	1.7	1	0.01	0.27	4	3	101.0
RH_10_OL_11_2	1.7	1	0.01	0.26	4	3	100.7
RH_10_OL_11_3	1.7	1	0.01	0.26	4	3	100.9
RH_10_OL_11_4	1.7	1	0.01	0.26	4	3	98.7
RH_10_OL_12_1	1.7	1	0.01	0.29	4	3	101.1
RH_10_OL_12_2	1.7	1	0.01	0.3	4	3	100.7
RH_10_OL_12_3	1.7	1	0.01	0.3	4	3	101.0
RH_10_OL_12_4	1.7	1	0.01	0.3	4	3	100.7
RH_10_OL_12_5	1.7	1	0.01	0.28	4	3	100.2
RH_10_OL_12_6	1.7	1	0.01	0.29	4	3	101.2
RH_10_OL_12_7	1.7	1	0.01	0.29	4	3	100.1
RH_10_OL_13_1	1.7	1	0.01	0.28	4	3	101.8
RH_10_OL_13_2	1.7	1.01	0.01	0.26	4	2.99	101.4
RH_10_OL_13_3	1.7	1	0.01	0.27	4	3	102.3
RH_10_OL_13_4	1.7	1	0.01	0.27	4	3	102.2
RH_10_OL_13_5	1.7	1	0.01	0.27	4	3	102.3
RH_10_OL_13_6	1.7	1	0.01	0.27	4	3	101.3
RH_10_OL_13_7	1.7	1	0.01	0.27	4	3	101.7
RH_10_OL_13_8	1.7	1	0.01	0.26	4	3	101.8
RH_16_OL_1_1	1.6	1	0.01	0.36	4	3	101.4
RH_16_OL_1_2	1.7	1	0.01	0.32	4	3	99.5
RH_16_OL_1_3	1.7	1.01	0.01	0.31	4	2.99	99.4
RH_16_OL_1_4	1.7	1	0.01	0.32	4	3	101.4
RH_16_OL_1_5	1.7	0.99	0.01	0.35	4	3.01	101.9
RH_16_OL_1_6	1.7	0.99	0.01	0.35	4	3.01	102.0
RH_16_OL_2_1	1.6	1	0.01	0.36	4	3	101.4
RH_16_OL_2_2	1.7	1	0.01	0.32	4	3	98.7
RH_16_OL_2_3	1.7	0.99	0.01	0.34	4	3.01	99.3
RH_16_OL_2_4	1.7	1	0.01	0.33	4	3	98.0
RH_16_OL_2_5	1.7	1		0.34	4	3	98.3
RH_16_OL_2_6	1.6	1.01	0.01	0.33	4	2.99	97.8
RH_16_OL_2_7	1.7	1	0.01	0.33	4	3	98.0
RH_16_OL_2_8	1.7	1	0.01	0.33	4	3	98.7
RH_16_OL_3_1	1.7	1	0.01	0.33	4	3	99.6
RH_16_OL_3_2	1.7	1	0.01	0.34	4	3	100.7
RH_16_OL_3_3	1.7	1	0.01	0.34	4	3	101.5

	Mg	Si	Ca	Fe	O	Cation sum	Totals
RH_16_OL_3_4	1.7	1	0.01	0.34	4	3	101.5
RH_16_OL_3_5	1.7	1	0.01	0.33	4	3	100.0
RH_16_OL_4_1	1.7	1.01	0.01	0.3	4	2.99	99.6
RH_16_OL_4_2	1.7	1	0.01	0.3	4	3	100.7
RH_16_OL_4_3	1.7	0.99	0.01	0.3	4	3.01	100.3
RH_16_OL_4_4	1.7	1.01	0.01	0.29	4	2.99	100.2
RH_16_OL_4_5	1.7	0.99	0.01	0.31	4	3.01	101.2
RH_16_OL_4_6	1.7	1	0.01	0.3	4	3	100.7
RH_16_OL_4_7	1.7	1	0.01	0.31	4	3	101.8
RH_16_OL_4_8	1.7	1.01	0.01	0.29	4	3	99.3
RH_16_OL_4_9	1.7	1	0.01	0.33	4	3	97.2
RH_16_OL_5_1	1.7	1	0.01	0.35	4	3	102.7
RH_16_OL_5_2	1.6	1	0.01	0.34	4	3	100.3
RH_16_OL_5_3	1.6	1	0.01	0.35	4	3	100.5
RH_16_OL_5_4	1.6	1		0.35	4	3	100.6
RH_16_OL_5_5	1.7	1	0.01	0.34	4	3	98.7
RH_16_OL_5_6	1.6	1	0.01	0.35	4	3	99.9
RH_16_OL_5_7	1.6	1	0.01	0.34	4	3	99.0
RH_16_OL_5_8	1.7	1	0.01	0.35	4	3	100.4
RH_16_OL_6_1	1.6	1	0.01	0.35	4	3	100.9
RH_16_OL_6_2	1.7	1.01		0.34	4	2.99	99.4
RH_16_OL_6_3	1.7	1	0.01	0.34	4	3	101.2
RH_16_OL_6_4	1.7	0.99	0.01	0.35	4	3.01	101.6
RH_16_OL_6_5	1.6	1	0.01	0.36	4	3	102.8
RH_16_OL_7_1	1.7	1	0.01	0.28	4	3	102.3
RH_16_OL_7_2	1.7	0.99	0.02	0.27	4	3.01	101.0
RH_16_OL_7_3	1.7	0.99	0.01	0.28	4	3.01	101.1
RH_16_OL_7_4	1.7	1.01	0.01	0.26	4	2.99	98.3
RH_16_OL_7_5	1.7	0.99	0.01	0.26	4	3.01	98.2
RH_16_OL_7_6	1.7	0.99	0.01	0.27	4	3.01	100.4
RH_16_OL_7_7	1.7	1	0.01	0.27	4	3	99.6
RH_16_OL_8_1	1.6	1	0.01	0.39	4	3	99.3
RH_16_OL_8_2	1.6	1	0.01	0.39	4	3	98.1
RH_16_OL_8_3	1.6	1	0.01	0.39	4	3	99.0
RH_16_OL_8_4	1.6	1	0.01	0.39	4	3	98.8
RH_16_OL_8_5	1.6	1.01	0.01	0.38	4	2.99	99.0
RH_16_OL_8_6	1.6	1	0.01	0.39	4	3	98.6
RH_16_OL_9_1	1.6	0.99	0.01	0.36	4	3.01	97.7
RH_16_OL_9_2	1.6	1.01	0.01	0.35	4	2.99	98.9
RH_16_OL_9_3	1.6	1.01	0.01	0.36	4	2.99	97.8
RH_16_OL_9_4	1.6	1	0.01	0.36	4	3	97.9
RH_16_OL_9_5	1.6	1.02	0.01	0.35	4	2.98	98.0
RH_16_OL_9_6	1.6	0.99	0.01	0.37	4	3.01	97.1
RH_16_OL_10_1	1.7	1.01	0.01	0.28	4	2.99	101.5
RH_16_OL_10_2	1.7	0.99	0.01	0.3	4	3.01	102.7
RH_16_OL_10_3	1.7	1.01	0.01	0.29	4	2.99	101.5
RH_16_OL_10_4	1.7	1	0.01	0.3	4	3	99.9
RH_16_OL_10_5	1.7	0.99	0.01	0.3	4	3.01	100.6
RH_16_OL_10_6	1.7	1.01	0.01	0.3	4	2.99	101.2
RH_16_OL_10_7	1.7	1	0.01	0.29	4	3	100.4
RH_16_OL_10_8	1.7	1	0.01	0.3	4	3	100.9
RH_16_OL_11_1	1.6	1.01	0.01	0.36	4	2.99	101.6
RH_16_OL_11_2	1.6	1	0.01	0.37	4	3	101.3
RH_16_OL_11_3	1.6	1		0.37	4	3	101.1

	Mg	Si	Ca	Fe	O	Cation sum	Totals
RH_16_OL_11_4	1.6	1	0.01	0.36	4	3	100.8
RH_16_OL_11_5	1.6	1.01	0.01	0.36	4	2.99	100.6
RH_16_OL_11_6	1.6	1	0.01	0.37	4	3	100.6
RH_16_OL_11_7	1.6	1.01	0.01	0.34	4	2.99	100.5
RH_16_OL_12_1	1.6	1	0.01	0.38	4	3	102.4
RH_16_OL_12_2	1.6	1	0.01	0.38	4	3	101.8
RH_16_OL_12_3	1.6	1	0.01	0.37	4	3	101.6
RH_16_OL_12_4	1.6	1	0.01	0.38	4	3	101.6
RH_16_OL_12_5	1.6	1	0.01	0.39	4	3	101.1
RH_16_OL_12_6	1.6	1	0.01	0.39	4	3	102.1
RH_16_OL_12_7	1.6	1.01	0.01	0.38	4	2.99	101.0
RH_16_OL_13_1	1.7	0.99	0.01	0.34	4	3.01	99.8
RH_16_OL_13_2	1.6	0.99	0.01	0.36	4	3.01	102.0
RH_16_OL_13_3	1.7	0.99	0.01	0.36	4	3.01	102.4
RH_16_OL_13_4	1.6	1	0.01	0.34	4	3	101.2
RH_16_OL_13_5	1.7	1	0.01	0.34	4	3	102.3
RH_16_OL_13_6	1.6	1.01	0.01	0.34	4	2.99	99.3
RH_16_OL_14_1	1.6	1	0.01	0.38	4	3	102.6
RH_16_OL_14_4	1.6	1	0.01	0.37	4	3	99.9
RH_16_OL_14_5	1.6	1	0.01	0.39	4	3	99.6
RH_16_OL_14_6	1.6	1	0.01	0.38	4	3	100.2
RH_16_OL_14_7	1.6	1		0.38	4	3	99.1
RH_16_OL_14_8	1.6	0.99	0.01	0.39	4	3.01	99.8
RH_16_OL_14_9	1.6	1	0.01	0.38	4	3	100.2
RH_16_OL_14_10	1.6	1	0.01	0.38	4	3	100.9
RH_16_OL_14_11	1.6	1	0.01	0.38	4	3	102.9
RH_16_OL_15_1	1.6	1	0.01	0.35	4	3	99.0
RH_16_OL_15_2	1.6	0.99	0.01	0.37	4	3.01	101.6
RH_16_OL_15_3	1.6	1	0.01	0.36	4	3	100.7
RH_16_OL_15_4	1.6	1.01	0.01	0.35	4	2.99	101.9
RH_16_OL_15_5	1.6	1	0.01	0.36	4	3	101.3
RH_16_OL_15_6	1.6	1	0.01	0.37	4	3	102.1
RH_16_OL_16_1	1.6	1	0.01	0.37	4	3	100.6
RH_16_OL_16_2	1.6	1	0.01	0.37	4	3	100.4
RH_16_OL_16_3	1.6	1	0.01	0.36	4	3	100.9
RH_16_OL_16_4	1.6	1	0.01	0.37	4	3	100.6
RH_16_OL_16_5	1.6	1	0.01	0.36	4	3	100.9
RH_16_OL_16_6	1.6	1.01	0.01	0.36	4	2.99	99.4
RH_16_OL_16_7	1.6	1	0.01	0.36	4	3	100.2
RH_16_OL_16_8	1.6	1	0.01	0.37	4	3	100.1
RH_16_OL_16_9	1.6	1.01	0.01	0.37	4	2.99	100.2
RH_16_OL_17_1	1.6	1.01	0.01	0.37	4	2.99	100.4
RH_16_OL_17_2	1.6	1	0.01	0.38	4	3	100.9
RH_16_OL_17_3	1.6	1	0.01	0.39	4	3	101.0
RH_16_OL_17_4	1.6	1	0.01	0.39	4	3	100.7
RH_16_OL_17_5	1.6	0.99	0.01	0.38	4	3.01	99.8
RH_16_OL_17_6	1.6	1	0.01	0.38	4	3	100.2
RH_16_OL_17_7	1.6	1	0.01	0.38	4	3	100.9
RH_16_OL_17_8	1.6	1	0.01	0.38	4	3	100.8
RH_16_OL_17_9	1.6	1	0.01	0.38	4	3	99.3
RH_20_OL_1_1	1.7	1	0.01	0.25	4	3	99.8
RH_20_OL_1_2	1.7	1.01	0.01	0.25	4	2.99	99.9
RH_20_OL_1_3	1.7	1	0.01	0.24	4	3	99.8
RH_20_OL_1_4	1.8	1	0.01	0.24	4	3	100.2

	Mg	Si	Ca	Fe	O	Cation sum	Totals
RH_20_OL_1_5	1.8	1	0.01	0.24	4	3	100.1
RH_20_OL_1_6	1.8	1	0.01	0.23	4	3	100.3
RH_20_OL_1_7	1.7	1	0.01	0.25	4	3	100.8
RH_20_OL_2_1	1.7	1.01	0.01	0.29	4	2.99	100.3
RH_20_OL_2_2	1.7	1	0.02	0.29	4	3	99.7
RH_20_OL_2_3	1.7	0.99	0.01	0.29	4	3.01	100.1
RH_20_OL_2_4	1.7	1	0.01	0.29	4	3	100.0
RH_20_OL_2_5	1.7	1	0.01	0.29	4	3	99.8
RH_20_OL_2_6	1.7	1	0.01	0.29	4	3	100.9
RH_20_OL_2_8	1.7	1	0.01	0.26	4	3	99.8
RH_20_OL_3_1	1.7	1	0.01	0.31	4	3	100.2
RH_20_OL_3_2	1.7	1	0.01	0.3	4	3	100.1
RH_20_OL_3_3	1.7	1	0.01	0.29	4	3	99.8
RH_20_OL_3_4	1.7	1	0.01	0.29	4	3	100.4
RH_20_OL_3_5	1.7	1	0.01	0.29	4	3	100.7
RH_20_OL_3_6	1.7	1	0.01	0.29	4	3	99.8
RH_20_OL_3_7	1.7	1	0.01	0.3	4	3	99.4
RH_20_OL_3_8	1.7	1	0.01	0.3	4	3	100.1
RH_20_OL_3_9	1.7	1	0.01	0.3	4	3	99.8
RH_20_OL_4_1	1.7	1	0.01	0.29	4	3	99.2
RH_20_OL_4_2	1.7	1.01	0.01	0.29	4	2.99	99.3
RH_20_OL_4_3	1.7	1	0.01	0.3	4	3	99.5
RH_20_OL_4_4	1.7	1	0.01	0.29	4	3	99.2
RH_20_OL_4_5	1.7	1	0.01	0.3	4	3	99.7
RH_20_OL_4_6	1.7	1	0.01	0.3	4	3	98.9
RH_20_OL_5_1	1.7	1	0.01	0.31	4	3	100.0
RH_20_OL_5_2	1.7	1.01	0.01	0.29	4	2.99	98.7
RH_20_OL_5_3	1.7	1	0.01	0.29	4	3	99.4
RH_20_OL_5_4	1.7	1	0.01	0.29	4	3	98.6
RH_20_OL_5_5	1.7	1	0.01	0.3	4	3	99.6
RH_20_OL_5_6	1.7	1	0.01	0.29	4	3	99.2
RH_20_OL_5_7	1.7	1	0.01	0.29	4	3	100.1
RH_20_OL_5_8	1.7	1.01	0.01	0.29	4	2.99	99.1
RH_20_OL_5_9	1.7	1	0.01	0.29	4	3	99.7
RH_20_OL_6_1	1.7	1	0.01	0.28	4	3	100.0
RH_20_OL_6_2	1.7	1	0.01	0.28	4	3	101.1
RH_20_OL_6_3	1.7	1	0.01	0.27	4	3	99.6
RH_20_OL_6_4	1.7	1	0.01	0.28	4	3	99.7
RH_20_OL_6_5	1.7	1	0.01	0.27	4	3	98.6
RH_20_OL_6_6	1.7	1	0.01	0.28	4	3	98.7
RH_20_OL_7_1	1.7	1	0.01	0.31	4	3	101.0
RH_20_OL_7_2	1.7	1.01	0.01	0.32	4	2.99	102.6
RH_20_OL_7_3	1.7	1	0.01	0.32	4	3	101.2
RH_20_OL_7_4	1.7	1	0.01	0.33	4	3	101.3
RH_20_OL_7_5	1.7	1	0.01	0.33	4	3	101.6
RH_20_OL_7_6	1.7	1	0.01	0.33	4	3	101.4
RH_20_OL_7_7	1.7	1	0.01	0.34	4	3	101.6
RH_20_OL_8_1	1.7	1	0.01	0.33	4	3	101.1
RH_20_OL_8_2	1.7	1.01	0.01	0.32	4	2.99	99.7
RH_20_OL_8_3	1.7	1	0.01	0.33	4	3	101.3
RH_20_OL_8_4	1.7	1	0.01	0.32	4	3	100.1
RH_20_OL_8_5	1.7	1.01	0.01	0.33	4	2.99	102.6
RH_20_OL_8_6	1.7	1	0.01	0.32	4	3	100.7

Appendix 8 - Table with calculated olivine crystallization temperatures

	$K_{D\ Mg}$	$\log K_{D\ Mg}$	T in °C (Mg)	$K_{D\ Fe}$	$\log K_{D\ Fe}$	T in °C (Mg)
	Mg equation Roeder and Emslie (1971)			Fe equation Roeder and Emslie (1971)		
RH_2_OL_1_1	4.35	0.64	1218	1.64	0.22	1167
RH_2_OL_1_2	4.35	0.64	1218	1.71	0.23	1157
RH_2_OL_1_3	4.35	0.64	1218	1.79	0.25	1148
RH_2_OL_1_4	4.35	0.64	1218	1.79	0.25	1148
RH_2_OL_2_1	4.35	0.64	1218	1.71	0.23	1157
RH_2_OL_2_2	4.78	0.68	1194	1.79	0.25	1148
RH_2_OL_2_3	4.35	0.64	1218	1.79	0.25	1148
RH_2_OL_2_4	4.35	0.64	1218	1.71	0.23	1157
RH_2_OL_2_5	4.78	0.68	1194	1.71	0.23	1157
RH_2_OL_2_6	4.78	0.68	1194	1.71	0.23	1157
RH_2_OL_3_1	4.78	0.68	1194	1.79	0.25	1148
RH_2_OL_3_2	4.35	0.64	1218	1.79	0.25	1148
RH_2_OL_3_3	4.35	0.64	1218	1.79	0.25	1148
RH_2_OL_3_4	4.35	0.64	1218	1.71	0.23	1157
RH_2_OL_3_5	4.35	0.64	1218	1.86	0.27	1140
RH_2_OL_3_6	4.35	0.64	1218	1.71	0.23	1157
RH_2_OL_3_7	4.78	0.68	1194	1.79	0.25	1148
RH_10_OL_1_1	5.22	0.72	1172	1.14	0.06	1256
RH_10_OL_1_2	5.22	0.72	1172	1.14	0.06	1256
RH_10_OL_1_3	5.22	0.72	1172	1.07	0.03	1273
RH_10_OL_1_4	5.22	0.72	1172	1.14	0.06	1256
RH_10_OL_1_5	4.78	0.68	1194	1.07	0.03	1273
RH_10_OL_2_1	5.22	0.72	1172	1.14	0.06	1256
RH_10_OL_2_2	5.22	0.72	1172	1.14	0.06	1256
RH_10_OL_2_3	5.22	0.72	1172	1.14	0.06	1256
RH_10_OL_2_4	5.22	0.72	1172	1.14	0.06	1256
RH_10_OL_3_2	4.78	0.68	1194	1.50	0.18	1188
RH_10_OL_3_3	4.78	0.68	1194	1.57	0.20	1178
RH_10_OL_3_4	4.78	0.68	1194	1.71	0.23	1157
RH_10_OL_3_5	4.78	0.68	1194	1.57	0.20	1178
RH_10_OL_3_6	4.78	0.68	1194	1.43	0.15	1200
RH_10_OL_4_1	4.78	0.68	1194	1.43	0.15	1200
RH_10_OL_4_2	4.78	0.68	1194	1.36	0.13	1213
RH_10_OL_4_3	4.78	0.68	1194	1.43	0.15	1200
RH_10_OL_4_4	4.78	0.68	1194	1.36	0.13	1213
RH_10_OL_4_5	4.78	0.68	1194	1.36	0.13	1213
RH_10_OL_5_1	5.22	0.72	1172	1.29	0.11	1226
RH_10_OL_5_2	4.78	0.68	1194	1.21	0.08	1240
RH_10_OL_5_3	5.22	0.72	1172	1.29	0.11	1226
RH_10_OL_5_4	5.22	0.72	1172	1.21	0.08	1240
RH_10_OL_5_5	4.78	0.68	1194	1.21	0.08	1240
RH_10_OL_6_1	4.78	0.68	1194	1.36	0.13	1213
RH_10_OL_6_2	4.78	0.68	1194	1.36	0.13	1213
RH_10_OL_6_3	5.22	0.72	1172	1.36	0.13	1213
RH_10_OL_6_4	5.22	0.72	1172	1.36	0.13	1213
RH_10_OL_6_5	5.22	0.72	1172	1.36	0.13	1213
RH_10_OL_7_1	4.78	0.68	1194	1.50	0.18	1188
RH_10_OL_7_2	5.22	0.72	1172	1.43	0.15	1200
RH_10_OL_7_3	4.78	0.68	1194	1.43	0.15	1200
RH_10_OL_7_4	4.78	0.68	1194	1.43	0.15	1200
RH_10_OL_7_5	4.78	0.68	1194	1.43	0.15	1200

	$K_{D\ Mg}$	log $K_{D\ Mg}$	T in °C (Mg)	$K_{D\ Fe}$	log $K_{D\ Fe}$	T in °C (Mg)
	Mg equation Roeder and Emslie (1971)			Fe equation Roeder and Emslie (1971)		
RH_10_OL_7_6	4.78	0.68	1194	1.43	0.15	1200
RH_10_OL_7_7	4.78	0.68	1194	1.43	0.15	1200
RH_10_OL_8_1	4.78	0.68	1194	1.36	0.13	1213
RH_10_OL_8_2	4.78	0.68	1194	1.36	0.13	1213
RH_10_OL_8_3	4.78	0.68	1194	1.36	0.13	1213
RH_10_OL_8_4	5.22	0.72	1172	1.36	0.13	1213
RH_10_OL_8_5	4.78	0.68	1194	1.29	0.11	1226
RH_10_OL_9_1	5.22	0.72	1172	1.21	0.08	1240
RH_10_OL_9_2	5.22	0.72	1172	1.21	0.08	1240
RH_10_OL_9_3	4.78	0.68	1194	1.21	0.08	1240
RH_10_OL_9_4	5.22	0.72	1172	1.29	0.11	1226
RH_10_OL_9_5	5.22	0.72	1172	1.29	0.11	1226
RH_10_OL_9_6	5.22	0.72	1172	1.21	0.08	1240
RH_10_OL_9_7	5.22	0.72	1172	1.21	0.08	1240
RH_10_OL_10_1	4.35	0.64	1218	1.36	0.13	1213
RH_10_OL_10_2	4.78	0.68	1194	1.29	0.11	1226
RH_10_OL_10_3	4.78	0.68	1194	1.36	0.13	1213
RH_10_OL_10_4	4.78	0.68	1194	1.29	0.11	1226
RH_10_OL_11_1	5.22	0.72	1172	1.29	0.11	1226
RH_10_OL_11_2	5.22	0.72	1172	1.29	0.11	1226
RH_10_OL_11_3	5.22	0.72	1172	1.29	0.11	1226
RH_10_OL_11_4	4.78	0.68	1194	1.21	0.08	1240
RH_10_OL_12_1	4.78	0.68	1194	1.43	0.15	1200
RH_10_OL_12_2	4.78	0.68	1194	1.43	0.15	1200
RH_10_OL_12_3	4.78	0.68	1194	1.43	0.15	1200
RH_10_OL_12_4	4.78	0.68	1194	1.43	0.15	1200
RH_10_OL_12_5	4.78	0.68	1194	1.36	0.13	1213
RH_10_OL_12_6	4.78	0.68	1194	1.43	0.15	1200
RH_10_OL_12_7	4.78	0.68	1194	1.36	0.13	1213
RH_10_OL_13_1	5.22	0.72	1172	1.36	0.13	1213
RH_10_OL_13_2	5.22	0.72	1172	1.29	0.11	1226
RH_10_OL_13_3	5.22	0.72	1172	1.29	0.11	1226
RH_10_OL_13_4	5.22	0.72	1172	1.29	0.11	1226
RH_10_OL_13_5	5.22	0.72	1172	1.29	0.11	1226
RH_10_OL_13_6	5.22	0.72	1172	1.29	0.11	1226
RH_10_OL_13_7	5.22	0.72	1172	1.29	0.11	1226
RH_10_OL_13_8	5.22	0.72	1172	1.29	0.11	1226
RH_16_OL_1_1	4.78	0.68	1194	1.71	0.23	1157
RH_16_OL_1_2	4.78	0.68	1194	1.50	0.18	1188
RH_16_OL_1_3	4.78	0.68	1194	1.43	0.15	1200
RH_16_OL_1_4	4.78	0.68	1194	1.57	0.20	1178
RH_16_OL_1_5	4.78	0.68	1194	1.64	0.22	1167
RH_16_OL_1_6	4.78	0.68	1194	1.64	0.22	1167
RH_16_OL_2_1	4.78	0.68	1194	1.71	0.23	1157
RH_16_OL_2_2	4.78	0.68	1194	1.50	0.18	1188
RH_16_OL_2_3	4.78	0.68	1194	1.57	0.20	1178
RH_16_OL_2_4	4.78	0.68	1194	1.57	0.20	1178
RH_16_OL_2_5	4.78	0.68	1194	1.57	0.20	1178
RH_16_OL_2_6	4.78	0.68	1194	1.50	0.18	1188
RH_16_OL_2_7	4.78	0.68	1194	1.50	0.18	1188
RH_16_OL_2_8	4.78	0.68	1194	1.57	0.20	1178
RH_16_OL_3_1	4.78	0.68	1194	1.57	0.20	1178
RH_16_OL_3_2	4.78	0.68	1194	1.57	0.20	1178

	$K_{D\ Mg}$	log $K_{D\ Mg}$	T in °C (Mg)	$K_{D\ Fe}$	log $K_{D\ Fe}$	T in °C (Mg)
	Mg equation Roeder and Emslie (1971)			Fe equation Roeder and Emslie (1971)		
RH_16_OL_3_3	4.78	0.68	1194	1.64	0.22	1167
RH_16_OL_3_4	4.78	0.68	1194	1.64	0.22	1167
RH_16_OL_3_5	4.78	0.68	1194	1.57	0.20	1178
RH_16_OL_4_1	4.78	0.68	1194	1.43	0.15	1200
RH_16_OL_4_2	4.78	0.68	1194	1.43	0.15	1200
RH_16_OL_4_3	4.78	0.68	1194	1.43	0.15	1200
RH_16_OL_4_4	4.78	0.68	1194	1.36	0.13	1213
RH_16_OL_4_5	4.78	0.68	1194	1.50	0.18	1188
RH_16_OL_4_6	4.78	0.68	1194	1.43	0.15	1200
RH_16_OL_4_7	4.78	0.68	1194	1.50	0.18	1188
RH_16_OL_4_8	4.78	0.68	1194	1.36	0.13	1213
RH_16_OL_4_9	4.78	0.68	1194	1.50	0.18	1188
RH_16_OL_5_1	4.78	0.68	1194	1.64	0.22	1167
RH_16_OL_5_2	4.78	0.68	1194	1.64	0.22	1167
RH_16_OL_5_3	4.78	0.68	1194	1.64	0.22	1167
RH_16_OL_5_4	4.78	0.68	1194	1.64	0.22	1167
RH_16_OL_5_5	4.78	0.68	1194	1.57	0.20	1178
RH_16_OL_5_6	4.78	0.68	1194	1.64	0.22	1167
RH_16_OL_5_7	4.78	0.68	1194	1.64	0.22	1167
RH_16_OL_5_8	4.78	0.68	1194	1.64	0.22	1167
RH_16_OL_6_1	4.78	0.68	1194	1.64	0.22	1167
RH_16_OL_6_2	4.78	0.68	1194	1.57	0.20	1178
RH_16_OL_6_3	4.78	0.68	1194	1.64	0.22	1167
RH_16_OL_6_4	4.78	0.68	1194	1.64	0.22	1167
RH_16_OL_6_5	4.78	0.68	1194	1.71	0.23	1157
RH_16_OL_7_1	5.22	0.72	1172	1.36	0.13	1213
RH_16_OL_7_2	5.22	0.72	1172	1.29	0.11	1226
RH_16_OL_7_3	5.22	0.72	1172	1.36	0.13	1213
RH_16_OL_7_4	4.78	0.68	1194	1.21	0.08	1240
RH_16_OL_7_5	4.78	0.68	1194	1.21	0.08	1240
RH_16_OL_7_6	5.22	0.72	1172	1.29	0.11	1226
RH_16_OL_7_7	4.78	0.68	1194	1.29	0.11	1226
RH_16_OL_8_1	4.35	0.64	1218	1.79	0.25	1148
RH_16_OL_8_2	4.35	0.64	1218	1.79	0.25	1148
RH_16_OL_8_3	4.35	0.64	1218	1.79	0.25	1148
RH_16_OL_8_4	4.35	0.64	1218	1.79	0.25	1148
RH_16_OL_8_5	4.35	0.64	1218	1.79	0.25	1148
RH_16_OL_8_6	4.35	0.64	1218	1.79	0.25	1148
RH_16_OL_9_1	4.35	0.64	1218	1.64	0.22	1167
RH_16_OL_9_2	4.35	0.64	1218	1.64	0.22	1167
RH_16_OL_9_3	4.35	0.64	1218	1.64	0.22	1167
RH_16_OL_9_4	4.35	0.64	1218	1.64	0.22	1167
RH_16_OL_9_5	4.35	0.64	1218	1.57	0.20	1178
RH_16_OL_9_6	4.35	0.64	1218	1.64	0.22	1167
RH_16_OL_10_1	5.22	0.72	1172	1.36	0.13	1213
RH_16_OL_10_2	5.22	0.72	1172	1.50	0.18	1188
RH_16_OL_10_3	4.78	0.68	1194	1.43	0.15	1200
RH_16_OL_10_4	4.78	0.68	1194	1.43	0.15	1200
RH_16_OL_10_5	4.78	0.68	1194	1.43	0.15	1200
RH_16_OL_10_6	4.78	0.68	1194	1.43	0.15	1200
RH_16_OL_10_7	4.78	0.68	1194	1.43	0.15	1200
RH_16_OL_10_8	4.78	0.68	1194	1.43	0.15	1200
RH_16_OL_11_1	4.78	0.68	1194	1.71	0.23	1157

	$K_{D\ Mg}$	log $K_{D\ Mg}$	T in °C (Mg)	$K_{D\ Fe}$	log $K_{D\ Fe}$	T in °C (Mg)
	Mg equation Roeder and Emslie (1971)			Fe equation Roeder and Emslie (1971)		
RH_16_OL_11_2	4.78	0.68	1194	1.71	0.23	1157
RH_16_OL_11_3	4.78	0.68	1194	1.79	0.25	1148
RH_16_OL_11_4	4.78	0.68	1194	1.71	0.23	1157
RH_16_OL_11_5	4.78	0.68	1194	1.71	0.23	1157
RH_16_OL_11_6	4.78	0.68	1194	1.71	0.23	1157
RH_16_OL_11_7	4.78	0.68	1194	1.64	0.22	1167
RH_16_OL_12_1	4.78	0.68	1194	1.86	0.27	1140
RH_16_OL_12_2	4.78	0.68	1194	1.79	0.25	1148
RH_16_OL_12_3	4.78	0.68	1194	1.79	0.25	1148
RH_16_OL_12_4	4.78	0.68	1194	1.79	0.25	1148
RH_16_OL_12_5	4.78	0.68	1194	1.79	0.25	1148
RH_16_OL_12_6	4.78	0.68	1194	1.86	0.27	1140
RH_16_OL_12_7	4.78	0.68	1194	1.79	0.25	1148
RH_16_OL_13_1	4.78	0.68	1194	1.57	0.20	1178
RH_16_OL_13_2	4.78	0.68	1194	1.71	0.23	1157
RH_16_OL_13_3	4.78	0.68	1194	1.71	0.23	1157
RH_16_OL_13_4	4.78	0.68	1194	1.64	0.22	1167
RH_16_OL_13_5	4.78	0.68	1194	1.64	0.22	1167
RH_16_OL_13_6	4.78	0.68	1194	1.64	0.22	1167
RH_16_OL_14_1	4.78	0.68	1194	1.79	0.25	1148
RH_16_OL_14_4	4.78	0.68	1194	1.71	0.23	1157
RH_16_OL_14_5	4.35	0.64	1218	1.79	0.25	1148
RH_16_OL_14_6	4.78	0.68	1194	1.79	0.25	1148
RH_16_OL_14_7	4.78	0.68	1194	1.71	0.23	1157
RH_16_OL_14_8	4.78	0.68	1194	1.79	0.25	1148
RH_16_OL_14_9	4.78	0.68	1194	1.79	0.25	1148
RH_16_OL_14_10	4.78	0.68	1194	1.79	0.25	1148
RH_16_OL_14_11	4.78	0.68	1194	1.86	0.27	1140
RH_16_OL_15_1	4.78	0.68	1194	1.64	0.22	1167
RH_16_OL_15_2	4.78	0.68	1194	1.71	0.23	1157
RH_16_OL_15_3	4.78	0.68	1194	1.71	0.23	1157
RH_16_OL_15_4	4.78	0.68	1194	1.71	0.23	1157
RH_16_OL_15_5	4.78	0.68	1194	1.71	0.23	1157
RH_16_OL_15_6	4.78	0.68	1194	1.71	0.23	1157
RH_16_OL_16_1	4.78	0.68	1194	1.71	0.23	1157
RH_16_OL_16_2	4.78	0.68	1194	1.79	0.25	1148
RH_16_OL_16_3	4.78	0.68	1194	1.71	0.23	1157
RH_16_OL_16_4	4.78	0.68	1194	1.71	0.23	1157
RH_16_OL_16_5	4.78	0.68	1194	1.71	0.23	1157
RH_16_OL_16_6	4.78	0.68	1194	1.64	0.22	1167
RH_16_OL_16_7	4.78	0.68	1194	1.71	0.23	1157
RH_16_OL_16_8	4.78	0.68	1194	1.71	0.23	1157
RH_16_OL_16_9	4.35	0.64	1218	1.79	0.25	1148
RH_16_OL_17_1	4.78	0.68	1194	1.79	0.25	1148
RH_16_OL_17_2	4.78	0.68	1194	1.79	0.25	1148
RH_16_OL_17_3	4.78	0.68	1194	1.86	0.27	1140
RH_16_OL_17_4	4.78	0.68	1194	1.79	0.25	1148
RH_16_OL_17_5	4.78	0.68	1194	1.79	0.25	1148
RH_16_OL_17_6	4.78	0.68	1194	1.79	0.25	1148
RH_16_OL_17_7	4.78	0.68	1194	1.79	0.25	1148
RH_16_OL_17_8	4.78	0.68	1194	1.79	0.25	1148
RH_16_OL_17_9	4.35	0.64	1218	1.79	0.25	1148
RH_20_OL_1_1	5.22	0.72	1172	1.21	0.08	1240

	$K_{D\ Mg}$	log $K_{D\ Mg}$	T in °C (Mg)	$K_{D\ Fe}$	log $K_{D\ Fe}$	T in °C (Mg)
	Mg equation Roeder and Emslie (1971)			Fe equation Roeder and Emslie (1971)		
RH_20_OL_1_2	5.22	0.72	1172	1.21	0.08	1240
RH_20_OL_1_3	5.22	0.72	1172	1.14	0.06	1256
RH_20_OL_1_4	5.22	0.72	1172	1.14	0.06	1256
RH_20_OL_1_5	5.22	0.72	1172	1.14	0.06	1256
RH_20_OL_1_6	5.22	0.72	1172	1.14	0.06	1256
RH_20_OL_1_7	5.22	0.72	1172	1.21	0.08	1240
RH_20_OL_2_1	4.78	0.68	1194	1.36	0.13	1213
RH_20_OL_2_2	4.78	0.68	1194	1.36	0.13	1213
RH_20_OL_2_3	4.78	0.68	1194	1.36	0.13	1213
RH_20_OL_2_4	4.78	0.68	1194	1.36	0.13	1213
RH_20_OL_2_5	4.78	0.68	1194	1.36	0.13	1213
RH_20_OL_2_6	4.78	0.68	1194	1.43	0.15	1200
RH_20_OL_2_8	5.22	0.72	1172	1.36	0.13	1213
RH_20_OL_3_1	4.78	0.68	1194	1.50	0.18	1188
RH_20_OL_3_2	4.78	0.68	1194	1.43	0.15	1200
RH_20_OL_3_3	4.78	0.68	1194	1.43	0.15	1200
RH_20_OL_3_4	4.78	0.68	1194	1.36	0.13	1213
RH_20_OL_3_5	4.78	0.68	1194	1.36	0.13	1213
RH_20_OL_3_6	4.78	0.68	1194	1.36	0.13	1213
RH_20_OL_3_7	4.78	0.68	1194	1.43	0.15	1200
RH_20_OL_3_8	4.78	0.68	1194	1.43	0.15	1200
RH_20_OL_3_9	4.78	0.68	1194	1.43	0.15	1200
RH_20_OL_4_1	4.78	0.68	1194	1.36	0.13	1213
RH_20_OL_4_2	4.78	0.68	1194	1.36	0.13	1213
RH_20_OL_4_3	4.78	0.68	1194	1.43	0.15	1200
RH_20_OL_4_4	4.78	0.68	1194	1.36	0.13	1213
RH_20_OL_4_5	4.78	0.68	1194	1.43	0.15	1200
RH_20_OL_4_6	4.78	0.68	1194	1.43	0.15	1200
RH_20_OL_5_1	4.78	0.68	1194	1.50	0.18	1188
RH_20_OL_5_2	4.78	0.68	1194	1.36	0.13	1213
RH_20_OL_5_3	4.78	0.68	1194	1.36	0.13	1213
RH_20_OL_5_4	4.78	0.68	1194	1.36	0.13	1213
RH_20_OL_5_5	4.78	0.68	1194	1.43	0.15	1200
RH_20_OL_5_6	4.78	0.68	1194	1.36	0.13	1213
RH_20_OL_5_7	4.78	0.68	1194	1.43	0.15	1200
RH_20_OL_5_8	4.78	0.68	1194	1.36	0.13	1213
RH_20_OL_5_9	4.78	0.68	1194	1.36	0.13	1213
RH_20_OL_6_1	4.78	0.68	1194	1.36	0.13	1213
RH_20_OL_6_2	5.22	0.72	1172	1.36	0.13	1213
RH_20_OL_6_3	4.78	0.68	1194	1.29	0.11	1226
RH_20_OL_6_4	4.78	0.68	1194	1.36	0.13	1213
RH_20_OL_6_5	4.78	0.68	1194	1.29	0.11	1226
RH_20_OL_6_6	4.78	0.68	1194	1.29	0.11	1226
RH_20_OL_7_1	4.78	0.68	1194	1.50	0.18	1188
RH_20_OL_7_2	4.78	0.68	1194	1.57	0.20	1178
RH_20_OL_7_3	4.78	0.68	1194	1.57	0.20	1178
RH_20_OL_7_4	4.78	0.68	1194	1.57	0.20	1178
RH_20_OL_7_5	4.78	0.68	1194	1.57	0.20	1178
RH_20_OL_7_6	4.78	0.68	1194	1.57	0.20	1178
RH_20_OL_7_7	4.78	0.68	1194	1.57	0.20	1178
RH_20_OL_8_1	4.78	0.68	1194	1.57	0.20	1178
RH_20_OL_8_2	4.78	0.68	1194	1.50	0.18	1188
RH_20_OL_8_3	4.78	0.68	1194	1.57	0.20	1178

	$K_{D\ Mg}$	log $K_{D\ Mg}$	T in °C (Mg)	$K_{D\ Fe}$	log $K_{D\ Fe}$	T in °C (Mg)
	Mg equation Roeder and Emslie (1971)			**Fe equation Roeder and Emslie (1971)**		
RH_20_OL_8_4	4.78	0.68	1194	1.50	0.18	1188
RH_20_OL_8_5	4.78	0.68	1194	1.57	0.20	1178
RH_20_OL_8_6	4.78	0.68	1194	1.50	0.18	1188

Appendix 9 - Table of the chemical composition of the plagioclase phenocrysts (in number of ions calculated for 8 oxygen)

	Na	Al	Si	K	Ca	O	Cation sum	Totals
RH_3_FSP_3_1	0.7	1.1	2.9	0.14	0.13	8	4.97	100.1
RH_3_FSP_3_2	0.51	1.5	2.5	0.03	0.48	8	5.01	99.3
RH_3_FSP_3_3	0.39	1.6	2.4	0.02	0.6	8	5.01	99.1
RH_3_FSP_3_4	0.37	1.6	2.4	0.01	0.62	8	5	98.7
RH_3_FSP_4_1	0.6	1.4	2.6	0.05	0.36	8	5.01	98.3
RH_3_FSP_4_2	0.38	1.6	2.4	0.02	0.63	8	5.01	97.3
RH_3_FSP_5_1	0.45	1.5	2.5	0.02	0.54	8	5	101.0
RH_3_FSP_5_2	0.38	1.6	2.4	0.02	0.6	8	4.99	100.8
RH_3_FSP_5_3	0.38	1.6	2.4	0.01	0.63	8	5	100.2
RH_3_FSP_5_4	0.37	1.6	2.4	0.01	0.63	8	5	101.0
RH_3_FSP_6_1	0.42	1.5	2.5	0.02	0.57	8	5	98.1
RH_3_FSP_6_2	0.41	1.6	2.4	0.02	0.59	8	5.01	98.1
RH_3_FSP_6_3	0.38	1.6	2.4	0.02	0.63	8	5.01	97.5
RH_3_FSP_6_4	0.38	1.6	2.4	0.02	0.63	8	5.01	97.2
RH_3_FSP_7_1	0.4	1.5	2.5	0.02	0.57	8	4.99	101.7
RH_3_FSP_7_2	0.39	1.6	2.4	0.02	0.62	8	5.01	100.9
RH_3_FSP_7_3	0.4	1.6	2.4	0.02	0.6	8	5.01	100.4
RH_3_FSP_7_4	0.38	1.6	2.4	0.02	0.63	8	5.01	100.7
RH_3_FSP_8_1	0.67	1.3	2.7	0.06	0.3	8	5.01	102.1
RH_3_FSP_8_2	0.45	1.5	2.5	0.03	0.55	8	5.01	101.1
RH_3_FSP_8_3	0.39	1.6	2.4	0.02	0.59	8	4.99	100.9
RH_3_FSP_8_4	0.38	1.6	2.4	0.01	0.62	8	5	101.1
RH_6_FSP_1_2	0.44	1.5	2.5	0.02	0.54	8	5	100.1
RH_6_FSP_1_3	0.48	1.5	2.5	0.03	0.51	8	5	98.6
RH_6_FSP_1_4	0.45	1.5	2.5	0.03	0.54	8	5	98.5
RH_6_FSP_1_5	0.46	1.5	2.5	0.03	0.52	8	4.99	97.7
RH_6_FSP_1_6	0.46	1.5	2.5	0.03	0.52	8	5	98.2
RH_6_FSP_1_7	0.46	1.5	2.5	0.02	0.53	8	5.01	99.2
RH_6_FSP_2_1	0.54	1.4	2.6	.0.04	0.43	8	5	97.8
RH_6_FSP_2_3	0.44	1.5	2.5	0.03	0.55	8	5.01	98.1
RH_6_FSP_2_4	0.47	1.5	2.5	0.03	0.54	8	5.01	98.1
RH_6_FSP_2_5	0.43	1.5	2.5	0.03	0.55	8	5	98.3
RH_6_FSP_3_1	0.49	1.5	2.5	0.03	0.51	8	5.01	100.8
RH_6_FSP_3_2	0.48	1.5	2.5	0.03	0.51	8	5.01	99.6
RH_6_FSP_3_3	0.44	1.5	2.5	0.02	0.55	8	4.99	99.1
RH_6_FSP_3_4	0.44	1.5	2.5	0.03	0.53	8	4.99	100.0
RH_6_FSP_3_5	0.45	1.5	2.5	0.03	0.54	8	5	99.6
RH_6_FSP_4_1	0.46	1.5	2.5	0.03	0.54	8	5.01	98.1
RH_6_FSP_4_2	0.44	1.5	2.5	0.02	0.55	8	5.01	98.1
RH_6_FSP_4_3	0.46	1.5	2.5	0.03	0.53	8	5	98.4
RH_6_FSP_4_4	0.43	1.5	2.5	0.03	0.56	8	5.01	98.2
RH_6_FSP_4_5	0.49	1.5	2.5	0.03	0.51	8	5.01	97.7
RH_6_FSP_5_1	0.44	1.5	2.5	0.03	0.55	8	5	97.4
RH_6_FSP_5_3	0.4	1.5	2.5	0.02	0.58	8	4.99	97.6
RH_6_FSP_5_4	0.45	1.5	2.5	0.02	0.55	8	5	98.5
RH_6_FSP_5_5	0.44	1.5	2.5	0.03	0.53	8	4.99	97.8
RH_6_FSP_6_1	0.48	1.5	2.5	0.03	0.5	8	5	100.9
RH_6_FSP_6_2	0.44	1.5	2.5	0.02	0.54	8	5	101.2
RH_6_FSP_6_3	0.45	1.5	2.5	0.02	0.55	8	5.01	101.1
RH_6_FSP_6_4	0.44	1.5	2.5	0.03	0.54	8	5	100.4
RH_6_FSP_6_5	0.46	1.5	2.5	0.03	0.54	8	5	99.8

	Na	Al	Si	K	Ca	O	Cation sum	Totals
RH_6_FSP_6_6	0.45	1.5	2.5	0.03	0.54	8	5.01	101.3
RH_6_FSP_6_7	0.46	1.5	2.5	0.02	0.52	8	5	101.3
RH_6_FSP_7_1	0.47	1.5	2.5	0.02	0.53	8	5.01	99.6
RH_6_FSP_7_2	0.46	1.5	2.5	0.03	0.55	8	5.01	100.4
RH_6_FSP_7_3	0.46	1.5	2.5	0.03	0.54	8	5.01	99.8
RH_6_FSP_7_4	0.44	1.5	2.5	0.03	0.54	8	5	99.4
RH_6_FSP_7_5	0.44	1.5	2.5	0.03	0.55	8	5	99.3
RH_6_FSP_8_1	0.45	1.5	2.5	0.02	0.53	8	5	99.1
RH_6_FSP_8_2	0.46	1.5	2.5	0.02	0.53	8	5	99.2
RH_6_FSP_8_3	0.44	1.5	2.5	0.03	0.55	8	5	99.0
RH_6_FSP_8_4	0.44	1.5	2.5	0.02	0.55	8	5	99.4
RH_6_FSP_9_1	0.42	1.5	2.5	0.02	0.57	8	5	99.8
RH_6_FSP_9_2	0.44	1.5	2.5	0.03	0.55	8	5	98.6
RH_6_FSP_9_3	0.44	1.5	2.5	0.03	0.52	8	4.99	98.3
RH_6_FSP_9_4	0.44	1.5	2.5	0.02	0.54	8	4.99	99.0
RH_6_FSP_10_1	0.49	1.5	2.5	0.04	0.51	8	5.01	100.9
RH_6_FSP_10_2	0.47	1.5	2.5	0.03	0.53	8	5	100.9
RH_6_FSP_10_3	0.45	1.5	2.5	0.03	0.53	8	4.99	100.7
RH_6_FSP_10_4	0.46	1.5	2.5	0.03	0.53	8	5	101.2
RH_6_FSP_10_5	0.47	1.5	2.5	0.03	0.51	8	5	102.0
RH_8_FSP_1_1	0.39	1.6	2.4	0.02	0.61	8	5	100.6
RH_8_FSP_1_2	0.42	1.5	2.5	0.02	0.58	8	5	100.9
RH_8_FSP_1_3	0.4	1.6	2.4	0.02	0.59	8	5	99.9
RH_8_FSP_1_4	0.41	1.6	2.4	0.03	0.59	8	5.01	98.9
RH_8_FSP_1_5	0.4	1.6	2.4	0.02	0.61	8	5.01	98.8
RH_8_FSP_1_6	0.4	1.6	2.4	0.02	0.6	8	5.01	97.9
RH_8_FSP_2_1	0.4	1.6	2.4	0.02	0.6	8	5.01	97.9
RH_8_FSP_2_2	0.39	1.6	2.4	0.02	0.6	8	4.99	98.9
RH_8_FSP_2_3	0.37	1.6	2.4	0.02	0.62	8	5	100.4
RH_8_FSP_2_4	0.39	1.6	2.4	0.02	0.62	8	5.01	100.5
RH_8_FSP_2_5	0.39	1.6	2.4	0.02	0.6	8	5	101.0
RH_8_FSP_2_6	0.38	1.6	2.4	0.02	0.61	8	5	100.8
RH_8_FSP_3_1	0.49	1.5	2.5	0.02	0.51	8	5.01	100.4
RH_8_FSP_3_2	0.42	1.6	2.4	0.02	0.59	8	5.02	99.3
RH_8_FSP_3_3	0.4	1.6	2.4	0.02	0.62	8	5.02	98.8
RH_8_FSP_3_4	0.39	1.6	2.4	0.02	0.59	8	4.99	98.8
RH_8_FSP_4_1	0.66	1.3	2.7	0.07	0.29	8	5.02	102.3
RH_8_FSP_4_2	0.39	1.6	2.4	0.02	0.59	8	5	100.9
RH_8_FSP_4_3	0.4	1.6	2.4	0.02	0.6	6	5.01	101.4
RH_8_FSP_4_4	0.4	1.6	2.4	0.02	0.6	6	5.01	101.7
RH_8_FSP_5_1	0.4	1.6	2.4	0.02	0.61	8	5	101.6
RH_8_FSP_5_2	0.38	1.6	2.4	0.02	0.61	8	5	101.0
RH_8_FSP_5_3	0.41	1.6	2.4	0.02	0.59	8	5.01	100.4
RH_8_FSP_5_4	0.4	1.6	2.4	0.02	0.6	8	5	101.0
RH_8_FSP_6_1	0.4	1.6	2.4	0.02	0.6	8	5.01	101.5
RH_8_FSP_6_2	0.38	1.6	2.4	0.02	0.63	8	5.01	101.2
RH_8_FSP_6_3	0.41	1.6	2.4	0.02	0.6	8	5.01	101.5
RH_8_FSP_6_4	0.39	1.6	2.4	0.02	0.61	8	5	101.4
RH_8 FSP_7_1	0.5	1.5	2.5	0.03	0.52	8	5.03	101.1
RH_8_FSP_7_2	0.41	1.6	2.4	0.02	0.61	8	5.01	100.2
RH_8_FSP_7_3	0.4	1.6	2.4	0.02	0.6	8	5.01	99.8
RH_8_FSP_7_4	0.39	1.6	2.4	0.02	0.63	8	5.02	100.4
RH_8_FSP_7_5	0.41	1.6	2.4	0.02	0.61	8	5.02	100.0
RH_8_FSP_8_1	0.47	1.5	2.5	0.02	0.53	8	5.02	101.6

	Na	Al	Si	K	Ca	O	Cation sum	Totals
RH_8_FSP_8_2	0.4	1.6	2.4	0.02	0.59	8	5.01	100.1
RH_8_FSP_8_3	0.39	1.6	2.4	0.02	0.61	8	5.01	99.4
RH_8_FSP_8_4	0.38	1.6	2.4	0.01	0.62	8	5	98.7
RH_8_FSP_8_5	0.4	1.6	2.4	0.02	0.62	8	5.01	99.3
RH_8_FSP_9_1	0.41	1.6	2.4	0.02	0.59	8	5.02	98.6
RH_8_FSP_9_2	0.38	1.6	2.4	0.02	0.63	8	5.01	98.6
RH_8_FSP_9_3	0.39	1.6	2.4	0.02	0.62	8	5.01	97.8
RH_8_FSP_9_4	0.38	1.6	2.4	0.02	0.61	8	5	97.7
RH_8_FSP_9_5	0.39	1.6	2.4	0.02	0.61	8	5	98.0
RH_8_FSP_10_1	0.41	1.6	2.4	0.02	0.6	8	5.02	101.0
RH_8_FSP_10_2	0.39	1.6	2.4	0.02	0.63	8	5.02	100.5
RH_8_FSP_10_3	0.38	1.6	2.4	0.02	0.62	8	5	100.2
RH_8_FSP_10_4	0.38	1.6	2.4	0.02	0.63	8	5.01	100.5
RH_8 FSP_11_1	0.51	1.5	2.5	0.02	0.49	8	5.01	100.7
RH_8_FSP_11_2	0.41	1.6	2.4	0.02	0.6	8	5.01	100.5
RH_8_FSP_11_3	0.39	1.6	2.4	0.02	0.61	8	5	99.5
RH_8_FSP_11_4	0.39	1.6	2.4	0.02	0.62	8	5.01	99.1
RH_8_FSP_11_5	0.39	1.6	2.4	0.02	0.61	8	5.01	99.6
RH_8_FSP_12_1	0.39	1.6	2.4	0.02	0.6	8	5.01	100.0
RH_8_FSP_12_2	0.4	1.6	2.4	0.01	0.68	8	5.01	100.0
RH_8_FSP_13_1	0.4	1.6	2.4	0.02	0.59	8	5	100.8
RH_8_FSP_13_2	0.4	1.6	2.4	0.02	0.61	8	5.02	101.4
RH_8_FSP_13_3	0.37	1.6	2.4	0.02	0.63	8	5.01	101.3
RH_8_FSP_13_4	0.38	1.6	2.4	0.02	0.61	8	5	101.0
RH_11_FSP_1_1	0.38	1.6	2.4	0.01	0.62	8	5.01	101.5
RH_11_FSP_1_2	0.37	1.6	2.4	0.01	0.66	8	5.02	101.5
RH_11_FSP_1_3	0.36	1.6	2.4	0.02	0.66	8	5.01	101.4
RH_11_FSP_1_4	0.36	1.6	2.4	0.02	0.67	8	5.02	101.7
RH_11_FSP_1_5	0.35	1.6	2.4	0.01	0.65	8	5	102.7
RH_11_FSP_1_6	0.37	1.6	2.4	0.01	0.65	8	5.01	102.0
RH_13_FSP_1_1	0.38	1.6	2.4	0.02	0.62	8	5	99.9
RH_13_FSP_1_2	0.39	1.6	2.4	0.02	0.62	8	5.01	99.7
RH_13_FSP_1_3	0.38	1.6	2.4	0.02	0.62	8	5	99.8
RH_13_FSP_1_4	0.36	1.6	2.4	0.02	0.65	8	5.01	98.9
RH_13_FSP_2_1	0.4	1.6	2.4	0.02	0.61	8	5	99.9
RH_13_FSP_2_2	0.37	1.6	2.4	0.02	0.64	8	5.01	100.6
RH_13_FSP_2_3	0.38	1.6	2.4	0.02	0.62	8	5	99.6
RH_13_FSP_2_4	0.38	1.6	2.4	0.02	0.63	8	5.01	99.3
RH_13_FSP_3_1	0.43	1.5	2.5	0.01	0.54	8	4.99	100.5
RH_13_FSP_3_2	0.41	1.5	2.5	0.02	0.57	8	5	100.7
RH_13_FSP_3_3	0.41	1.6	2.4	0.02	0.59	8	5.01	101.2
RH_13_FSP_3_4	0.43	1.5	2.5	0.02	0.57	8	5	101.1
RH_13_FSP_3_5	0.42	1.6	2.4	0.02	0.58	8	5.01	102.3
RH_13_FSP_4_1	0.33	1.7	2.3	0.01	0.67	8	5	99.9
RH_13_FSP_4_2	0.34	1.6	2.4	0.02	0.65	8	5	100.1
RH_13_FSP_4_3	0.38	1.6	2.4	0.02	0.63	8	5.01	100.4
RH_13_FSP_4_4	0.37	1.6	2.4	0.01	0.63	8	5.01	100.9
RH_13_FSP_5_1	0.42	1.6	2.4	0.01	0.59	8	5.01	101.7
RH_13_FSP_5_2	0.38	1.6	2.4	0.02	0.61	8	4.99	101.8
RH_13_FSP_5_3	0.37	1.6	2.4	0.02	0.64	8	5.02	100.8
RH_13_FSP_5_4	0.39	1.6	2.4	0.02	0.61	8	5.01	100.7
RH_13_FSP_5_5	0.37	1.6	2.4	0.02	0.62	8	5	100.3

Appendix 10 - Table of the chemical composition of ilmenite (number of ions calculated for 3 oxygen)

	Mg	Al	Ti	V	Mn	Fe	Co	O	Cation sum	Totals
6	0.03	0.01	0.97	0.01	0.01	0.98		3	2.01	99.0
7	0.03	0.01	0.97	0.01	0.01	0.98		3	2.01	98.4
8	0.02	0.01	0.96	0.02	0.02	0.99		3	2.01	97.3
9	0.04	0.01	0.93	0.01	0.01	1.03		3	2.04	99.8
10	0.03	0.02	0.95	0.01	0.02	1.01		3	2.03	99.3
11	0.04	0.01	0.95	0.01	0.01	1		3	2.03	99.0
12	0.04	0.01	0.95	0.01	0.01	1		3	2.02	99.8
13	0.04		0.97	0.02	0.01	0.98		3	2.01	101.6
14	0.05	0.01	0.96	0.01	0.01	0.97		3	2.02	100.3
15	0.06	0.01	0.93	0.01	0.01	1.03		3	2.05	97.5
16	0.04	0.01	0.94	0.02	0.01	1.01	0.01	3	2.03	98.0
17	0.04	0.01	0.94	0.01	0.01	1.01		3	2.03	97.7
22	0.03	0.01	0.94	0.01	0.01	1.02		3	2.03	99.2
23	0.02	0.01	0.95	0.01	0.01	1.03		3	2.03	98.3
24	0.02	0.01	0.94	0.01	0.01	1.04		3	2.04	99.3
36	0.12	0.02	0.93	0.01	0.01	0.97		3	2.05	98.6
37	0.14	0.02	0.93	0.01	0.01	0.94		3	2.05	97.6
38	0.14	0.02	0.93	0.01	0.01	0.93		3	2.04	98.0
39	0.14	0.02	0.93	0.01	0.01	0.94		3	2.04	98.6
40	0.12	0.02	0.94	0.01	0.01	0.95		3	2.04	99.1
41	0.15	0.02	0.93	0.01	0.01	0.93		3	2.05	98.7
43	0.19	0.02	0.92	0.01	0.01	0.89		3	2.05	97.7
44	0.18	0.02	0.91	0.02	0.01	0.89	0.01	3	2.05	98.0
45	0.2	0.02	0.92	0.01	0.01	0.89		3	2.05	98.2
46	0.2	0.02	0.92	0.01		0.9		3	2.06	97.0
47	0.2	0.02	0.91	0.02	0.01	0.89	0.01	3	2.05	98.1
48	0.17	0.02	0.92	0.01	0.01	0.92	0.01	3	2.05	97.4
58	0.18	0.01	0.92	0.01	0.01	0.91		3	2.05	98.2
59	0.17	0.02	0.92	0.01	0.01	0.91		3	2.05	97.9
64	0.15	0.01	0.96	0.01	0.02	0.97		3	2.02	99.3
65	0.14	0.01	0.95	0.01	0.02	0.9	0.01	3	2.03	98.3
66	0.15	0.01	0.96	0.01	0.02	0.89		3	2.03	98.0
67	0.14	0.01	0.95	0.01	0.01	0.91	0.01	3	2.04	97.2
72	0.07		0.94	0.02	0.02	0.98		3	2.03	99.5
73	0.06	0.01	0.94	0.01	0.02	1		3	2.04	97.2
74	0.07	0.01	0.93	0.01	0.02	1		3	2.04	97.5
75	0.06	0.02	0.91	0.02	0.01	1.03		3	2.05	100.8
76	0.05	0.01	0.94	0.01	0.01	1.02		3	2.04	97.6
77	0.06	0.01	0.95	0.01	0.02	0.99		3	2.03	100.1
78	0.05	0.01	0.95	0.02	0.01	0.99		3	2.02	99.4
79	0.04	0.01	0.96	0.01	0.02	0.98		3	2.02	99.2
80	0.06	0.01	0.95	0.01	0.01	0.98		3	2.03	98.6
81	0.07	0.02	0.93	0.02	0.01	1		3	2.04	101.6
82	0.06	0.02	0.93	0.01	0.01	1		3	2.04	101.9
83	0.05	0.01	0.96	0.01	0.01	1		3	2.03	100.9
84	0.06	0.01	0.94	0.01	0.01	1		3	2.04	100.7
85	0.16	0.01	0.94	0.01	0.01	0.92		3	2.04	101.0
86	0.17	0.01	0.92	0.02	0.01	0.91		3	2.04	101.2
87	0.16	0.02	0.92	0.02	0.01	0.92		3	2.05	101.9
88	0.16	0.02	0.93	0.01	0.01	0.92		3	2.04	100.2
89	0.15	0.01	0.93	0.01	0.01	0.94		3	2.05	97.6

	Mg	Al	Ti	V	Mn	Fe	Co	O	Cation sum	Totals
90	0.19	0.02	0.92	0.01	0.01	0.9		3	2.05	100.9
91	0.17	0.02	0.93	0.01	0.01	0.91		3	2.05	99.8
92	0.19	0.02	0.93	0.01	0.01	0.89		3	2.04	99.6
93	0.18	0.02	0.92	0.01	0.01	0.9		3	2.05	99.8
94	0.19	0.02	0.92	0.01	0.01	0.9		3	2.05	100.6
95	0.19	0.02	0.93	0.01	0.01	0.89		3	2.05	99.0
96	0.19	0.02	0.93	0.01	0.01	0.9		3	2.05	101.9
97	0.19	0.02	0.92	0.02	0.01	0.88		3	2.04	101.4
98	0.15	0.02	0.92	0.02	0.01	0.92		3	2.04	100.7
99	0.19	0.02	0.91	0.01	0.01	0.92		3	2.07	101.1
100	0.18	0.02	0.93	0.02	0.01	0.89		3	2.04	101.3
101	0.18	0.02	0.92	0.02	0.01	0.91		3	2.05	100.5
102	0.18	0.02	0.93	0.01	0.01	0.91		3	2.05	100.1
103	0.17	0.02	0.93	0.01	0.01	0.91		3	2.05	101.5
104	0.17	0.01	0.92	0.02	0.01	0.92		3	2.05	98.1
105	0.13	0.01	0.93	0.02	0.01	0.94		3	2.04	101.8
106	0.17	0.02	0.92	0.02	0.01	0.91		3	2.05	102.4
107	0.15	0.02	0.93	0.01	0.01	0.92		3	2.04	100.3
108	0.18	0.02	0.92	0.02		0.91		3	2.05	100.8
109	0.14	0.02	0.93	0.01	0.01	0.94		3	2.05	101.4
110	0.15	0.02	0.93	0.01	0.01	0.92		3	2.04	101.5
111	0.16	0.01	0.93	0.01	0.01	0.93		3	2.05	101.4
112	0.13	0.01	0.94	0.01		0.94		3	2.04	98.9
113	0.11	0.02	0.93	0.02	0.01	0.95		3	2.04	100.0
114	0.16	0.01	0.93	0.01	0.01	0.93		3	2.05	100.7
115	0.14	0.02	0.93	0.01	0.01	0.94		3	2.04	99.3
116	0.14	0.02	0.92	0.01	0.01	0.94		3	2.05	100.1
117	0.18	0.02	0.92	0.02	0.01	0.89		3	2.04	100.0
118	0.17	0.02	0.93	0.02		0.9		3	2.04	99.7
119	0.17	0.02	0.93	0.01	0.01	0.92		3	2.05	100.9
120	0.17	0.02	0.94	0.01		0.91		3	2.04	100.8
121	0.18	0.02	0.93	0.01	0.01	0.89		3	2.04	100.4
122	0.13	0.01	0.96	0.01	0.01	0.89		3	2.02	97.4
123	0.14	0.01	0.95	0.01	0.01	0.9		3	2.02	99.9
124	0.14	0.01	0.97		0.01	0.88		3	2.02	99.4
125	0.14	0.01	0.94	0.02	0.01	0.9		3	2.03	98.3

Appendix 11 - Table with chemical composition of the spinel phase (in atomic %)

	O	Mg	Al	Ti	V	Cr	Mn	Fe	Totals
RH_2_OPA_2_1	57.5	2.1	1.9	8.2	0.26	1.7	0.4	28.0	99.2
RH_10_OPA_1_1	54.7	4.1	6.3	1.3		17.3		16.2	99.6
RH_10_OPA_1_2	55.5	4.1	6.3	1.3		16.8		16.0	99.2
RH_10_OPA_1_3	54.7	5.2	6.3	1.2		17.3		15.3	98.4
RH_10_OPA_1_4	55.3	2.2	1.7	8.3	0.36	2.0	0.35	29.9	97.0
RH_10_OPA_1_5	55.6	3.6	4.9	2.2		15.6		18.1	99.1
RH_10_OPA_1_6	55.4	2.9	2.6	6.2	0.26	6.8	0.33	25.6	99.4
RH_10_OPA_1_7	54.6	2.4	1.7	8.2	0.3	2.0	0.32	30.5	97.2
RH_10_OPA_2_1	56.6	2.9	2.0	8.7		1.6		28.3	97.2
RH_10_OPA_2_2	57.3	2.7	1.8	9.1	0.3	1.3		27.7	99.0
RH_10_OPA_2_3	56.2	2.6	1.8	8.8		1.3	0.32	28.9	99.9
RH_10_OPA_2_4	57.1	2.8	1.6	9.3		1.0	0.29	27.9	99.0
RH_10_OPA_2_6	58.0	2.8	1.8	9.3		0.9		27.4	98.6
RH_10_OPA_2_7	57.5	2.5	1.6	9.2	0.33	0.9		28.0	100.1
RH_10_OPA_3_1	55.8	4.5	5.3	1.3		17.4		15.8	100.6
RH_10_OPA_3_2	56.1	5.5	5.3	1.3		16.9		14.8	100.4
RH_10_OPA_3_3	56.3	6.2	5.3	1.5		16.7		14.0	101.2
RH_10_OPA_3_4	56.0	5.2	5.4	1.2		17.2		15.0	100.5
RH_10_OPA_3_5	56.8	2.9	1.7	8.1	0.35	2.2		28.0	99.7
RH_10_OPA_3_6	57.3	2.9	1.5	8.8		1.5		28.2	98.5
RH_10_OPA_3_7	56.6	2.9	1.7	8.1		2.1		28.6	97.8
RH_10_OPA_3_8	56.2	3.1	2.8	5.1	0.29	8.7		23.8	98.5
RH_10_OPA_3_9	55.8	3.1	2.5	6.1		6.5	0.33	25.8	100.0
RH_10_OPA_3_10	56.4	3.1	2.4	6.0		6.9		25.3	99.2
RH_10_OPA_4_1	55.8	4.0	4.9	1.6		16.3		17.4	99.6
RH_10_OPA_4_2	56.0	3.8	4.8	1.7		16.1		17.7	99.8
RH_10_OPA_4_3	55.6	4.3	4.9	1.5		16.3		17.4	99.1
RH_10_OPA_4_4	55.9	3.5	4.6	1.8		16.0		18.2	98.2
RH_10_OPA_4_5	56.0	3.0	2.4	6.4		6.4		25.9	98.8
RH_10_OPA_4_6	55.8	3.0	2.4	6.4	0.31	5.7		26.5	98.7
RH_10_OPA_4_7	56.2	3.1	2.0	8.3		1.9		28.5	99.3
RH_10_OPA_5_1	56.8	3.5	6.0	1.4		15.8		16.5	102.6
RH_10_OPA_5_2	55.5	3.6	6.4	1.3		16.5		16.7	99.8
RH_10_OPA_5_3	56.2	3.5	6.3	1.4		16.1		16.6	101.0
RH_10_OPA_5_4	55.7	3.0	2.3	6.7		5.6	0.33	26.4	99.6
RH_10_OPA_5_5	56.1	2.7	2.4	6.4		6.3		26.2	98.0
RH_10_OPA_5_6	56.0	2.9	2.7	5.8		7.4		25.2	98.9
RH_10_OPA_5_7	56.5	3.0	2.2	6.8		5.3		26.3	99.0
RH_10_OPA_5_8	57.8	2.8	1.4	8.5	0.33	1.2	0.47	27.2	100.1
RH_10_OPA_5_9	58.0	3.0	1.7	8.8		1.5		27.0	97.9
RH_10_OPA_5_10	56.3	3.0	1.8	8.3		2.5		28.2	98.7
RH_10_OPA_7_1	55.9	2.9	3.5	4.0		11.5		22.3	99.0
RH_10_OPA_7_2	56.0	2.9	2.1	6.9		5.4		26.7	98.1
RH_10_OPA_7_3	56.3	2.8	2.9	4.8	0.38	8.9		23.8	98.4
RH_10_OPA_7_4	57.3	2.5	1.7	9.2	0.29	1.0		28.1	96.5
RH_10_OPA_7_5	56.6	2.8	1.6	8.6	0.4	1.5	0.32	27.9	98.0
RH_10_OPA_7_6	57.3	2.6	1.9	0.3	8.69	1.9		27.3	97.6
RH_11_OPA_2_5	57.0	3.7	3.7	0.8	0.22	1.7		32.8	99.5
RH_11_OPA_2_7	56.7	3.9	3.5	1.1	0.26	1.7		32.8	97.5
RH_11_OPA_3_3	56.3	4.1	3.4	7.2		0.6		28.4	95.5
RH_11_OPA_3_4	57.7	4.1	3.0	8.2	0.33	0.5		26.1	100.8
RH_11_OPA_3_5	57.0	3.7	3.3	6.0	0.3	0.5		29.1	100.4

	O	Mg	Al	Ti	V	Cr	Mn	Fe	Totals
RH_11_OPA_3_6	57.2	3.1	2.9	6.6	0.36	0.5		29.4	98.6
RH_11_OPA_4_1	55.1	4.6	3.8	7.5	0.29	0.9		27.9	97.9
RH_11_OPA_4_3	56.6	5.1	3.2	8.7	0.4	0.9		25.1	98.1
RH_11_OPA_4_5	57.1	4.5	3.0	7.2	0.28	0.8		27.2	100.0
RH_11_OPA_5_2	57.5	2.7	3.0	7.6		0.5		28.7	99.4
RH_11_OPA_5_3	57.0	2.7	2.5	7.8		0.5		29.6	98.7
RH_11_OPA_5_4	57.6	4.9	1.8	12.7		0.5	0.39	22.2	97.6
RH_11_OPA_5_5	56.5	2.1	2.9	6.0	0.31	0.6		31.7	98.4
RH_11_OPA_5_7	57.2	2.2	2.3	7.2		0.7		30.5	98.6
RH_11_OPA_6_1	57.1	3.4	4.5	1.5		16.7		16.9	102.6
RH_11_OPA_6_2	56.8	4.2	4.5	1.3		17.0		16.2	101.6
RH_11_OPA_6_3	56.2	5.4	4.4	1.3		17.1	0.39	15.1	102.3
RH_11_OPA_6_4	57.1	3.2	4.4	1.4		16.8		17.1	101.7
RH_11_OPA_6_5	56.6	3.1	4.3	0.5		17.0		17.7	102.5
RH_11_OPA_9_3	56.2	3.8	3.8	1.0		1.7	0.21	33.4	99.4
RH_11_OPA_9_5	57.7	3.6	3.7	3.4		1.7	0.19	29.7	100.7
RH_11_OPA_9_6	58.2	3.2	2.3	4.0		2.9	0.23	29.2	99.5
RH_13_OPA_1_2	54.9	3.9	3.2	8.5	0.32	0.6		28.7	99.7
RH_13_OPA_1_3	56.1	4.1	3.2	8.4		0.6		27.6	99.2
RH_13_OPA_1_4	54.8	4.0	3.2	8.4	0.34	0.5	0.25	28.6	100.4
RH_13_OPA_2_1	55.8	1.9	1.7	9.9	0.32	0.6	0.4	29.3	98.4
RH_13_OPA_2_2	55.7	2.4	1.4	9.8	0.31	0.6	0.33	29.4	98.7
RH_13_OPA_2_3	55.5	2.5	1.4	9.9		0.7	0.3	29.7	99.0
RH_13_OPA_2_4	55.9	2.4	1.6	9.9	0.28	0.4		29.6	98.8
RH_13_OPA_2_5	55.7	2.7	1.6	10.0	0.41	0.3	0.3	29.1	98.5
RH_13_OPA_2_6	56.0	2.1	1.5	9.9	0.27	0.4	0.37	29.5	98.8
RH_13_OPA_3_1	55.0	3.0	5.3	1.5		16.9		18.3	101.6
RH_13_OPA_3_2	54.6	3.2	5.1	1.5		17.2		18.4	99.6
RH_13_OPA_3_3	57.6	1.8	1.6	8.5		2.6	0.32	27.6	100.4
RH_13_OPA_3_4	56.6	2.5	1.6	9.4		1.0	0.36	28.6	99.9
RH_13_OPA_3_5	56.7	2.5	1.5	9.4		1.3	0.28	28.4	99.4
RH_13_OPA_3_6	57.4	1.8	1.4	8.9	0.3	0.7	0.46	28.9	100.1
RH_13_OPA_3_7	54.9	2.6	2.3	6.4		6.5	0.33	27.0	99.7
RH_13_OPA_3_8	57.1	2.3	1.4	9.6	0.39		0.34	28.8	100.2
RH_13_OPA_3_9	57.4	2.2	1.4	9.4			0.37	29.3	98.1
RH_13_OPA_3_10	58.1	1.3	1.4	9.7		0.2	0.52	28.9	98.3
RH_13_OPA_3_11	57.8	0.7	1.2	10.0			0.62	29.7	98.3
RH_13_OPA_4_1	57.1	2.9	2.0	9.2	0.32	0.3	0.36	27.8	97.8
RH_13_OPA_4_2	56.8	3.3	2.3	9.1		0.5		28.0	100.4
RH_13_OPA_4_3	57.5	3.1	2.4	9.2		0.4	0.26	27.1	99.7
RH_13_OPA_5_1	55.7	2.9	1.7	9.7	0.34	0.5	0.39	28.7	97.1
RH_13_OPA_5_2	55.2	2.7	1.7	9.8	0.29	0.3	0.43	29.5	100.6
RH_13_OPA_5_3	56.3	2.6	1.9	9.8		0.5	0.31	28.7	100.5
RH_13_OPA_5_4	56.3	2.7	1.8	9.7	0.36	0.3	0.27	28.6	100.0
RH_13_OPA_5_5	55.5	2.5	1.7	10.1	0.28	0.3		29.7	98.8
RH_13_OPA_6_1	57.0	3.5	2.8	8.7		0.7	0.34	27.1	102.2
RH_13_OPA_6_2	57.4	3.7	2.7	8.7		0.5		27.0	100.6
RH_13_OPA_6_4	56.8	3.8	3.0	8.5		0.7		27.3	99.0
RH_13_OPA_6_5	57.3	3.7	2.8	8.2	0.34	0.5	0.34	26.8	100.2
RH_13_OPA_6_6	56.7	3.8	2.7	8.4	0.3	0.7		27.5	99.3
RH_13_OPA_7_1	58.2	1.7	1.4	9.4	0.3		0.44	28.5	101.0
RH_13_OPA_7_2	57.3	2.3	1.3	9.6	0.31	0.3	0.27	28.7	100.3
RH_13_OPA_7_3	57.8	1.8	1.4	9.8		0.4	0.35	28.5	96.5
RH_13_OPA_7_4	58.0	1.2	1.6	9.4	0.27	0.3	0.46	28.8	98.3

	O	Mg	Al	Ti	V	Cr	Mn	Fe	Totals
RH_13_OPA_7_5	57.0	2.1	1.5	10.0		0.3	0.34	28.9	101.1
RH_13_OPA_7_6	57.2	2.0	1.2	9.8		0.3	0.34	29.1	101.0
RH_13_OPA_7_7	57.3	2.5	1.2	9.1	0.29		0.35	29.3	100.5
RH_13_OPA_7_8	57.3	1.9	0.9	9.9	0.28		0.29	29.4	101.1
RH_13_OPA_7_9	56.4	2.5	1.0	9.0	0.45		0.3	30.4	101.0
RH_13_OPA_7_10	57.3	1.6	1.0	9.9	0.38		0.39	29.5	100.3
RH_13_OPA_8_1	57.4	3.7	2.8	8.6		0.5	0.24	26.7	96.6
RH_13_OPA_8_2	57.8	3.7	2.6	8.7		0.5	0.21	26.6	97.5
RH_13_OPA_8_3	57.3	3.5	2.7	8.6		0.5	0.23	27.2	98.2
RH_13_OPA_8_4	57.1	3.5	2.8	8.8		0.6	0.26	27.0	96.5
RH_16_OPA_1_1	57.5	3.2	3.0	5.6		5.1		25.5	99.6
RH_16_OPA_1_2	57.6	3.1	2.6	6.5		3.4	0.26	26.6	99.7
RH_16_OPA_1_3	57.3	3.4	4.0	5.1		5.3		24.9	98.4
RH_16_OPA_1_4	57.7	3.2	3.0	5.8		4.4		25.8	98.2
RH_16_OPA_1_5	57.3	3.1	2.4	6.7		3.2		27.3	98.1
RH_16_OPA_1_6	57.3	3.2	3.1	5.7		4.7	0.28	25.8	98.3
RH_16_OPA_2_1	57.7	3.8	3.5	5.0		5.7		24.3	98.5
RH_16_OPA_2_2	57.7	3.9	4.4	4.3		6.5	0.28	23.0	101.3
RH_16_OPA_2_3	58.3	4.1	4.9	3.4	0.24	7.4		21.7	101.0
RH_16_OPA_2_4	57.7	4.5	4.8	3.7		6.8		22.5	100.5
RH_16_OPA_2_5	57.6	5.9	4.9	2.1		10.9		18.7	100.8
RH_16_OPA_2_6	57.3	5.0	5.0	2.7		9.0		21.0	99.0
RH_16_OPA_2_7	57.4	4.4	5.4	3.0		8.6		21.2	99.6
RH_16_OPA_2_8	57.9	3.8	3.4	5.1		5.4	0.28	24.2	99.4
RH_16_OPA_2_9	58.1	3.8	3.7	4.7	0.23	5.5		24.0	100.4
RH_16_OPA_2_10	57.4	5.3	5.0	2.3		10.0		19.9	100.3
RH_16_OPA_3_1	57.0	5.3	5.8	1.4		14.8		15.8	97.5
RH_16_OPA_3_2	57.0	5.2	5.5	1.5		14.7		16.0	100.4
RH_16_OPA_3_3	57.1	4.2	5.8	1.7		14.5		16.8	99.3
RH_16_OPA_3_4	56.8	5.0	5.8	1.4		14.8		16.2	99.0
RH_16_OPA_3_5	56.5	3.7	2.6	6.0		5.8		25.4	97.9
RH_16_OPA_3_6	56.8	3.8	2.1	6.7		4.7	0.27	25.7	101.7
RH_16_OPA_3_7	57.3	3.6	2.3	6.2	0.22	5.0		25.3	101.5
RH_16_OPA_3_8	56.9	3.7	2.3	6.4		5.0		25.8	98.8
RH_16_OPA_4_1	56.0	3.7	4.2	5.6		4.3		26.1	98.2
RH_16_OPA_4_2	56.0	3.6	3.8	5.6	0.25	4.3	0.31	26.1	100.1
RH_16_OPA_4_3	56.7	3.5	3.1	6.2	0.25	3.3		26.8	100.5
RH_16_OPA_4_4	56.4	3.5	3.0	6.4	0.25	3.0	0.31	27.3	100.4
RH_16_OPA_4_5	56.0	3.4	3.9	5.8		4.1		26.8	99.3
RH_16_OPA_4_6	56.2	3.7	4.2	5.7		4.1		26.1	97.9
RH_16_OPA_4_7	57.3	3.6	2.9	7.2		2.7	0.37	25.9	100.6
RH_16_OPA_5_1	57.0	5.4	5.1	1.3		15.7		15.6	101.9
RH_16_OPA_5_2	56.9	5.6	5.0	1.4		15.6		15.6	100.9
RH_16_OPA_5_3	57.2	4.8	5.0	1.4		15.4		16.2	99.2
RH_16_OPA_5_4	57.5	4.3	5.1	1.4		15.3		16.5	98.8
RH_16_OPA_5_5	56.9	7.2	4.8	1.2		16.4		13.5	99.9
RH_16_OPA_5_6	59.2	2.6	1.9	7.4	0.3	3.6	0.25	24.7	98.5
RH_16_OPA_5_9	58.0	2.5	1.4	5.8		2.9		29.7	98.7
RH_16_OPA_6_1	57.2	2.9	1.9	7.0	0.23	2.8		28.0	101.4
RH_16_OPA_6_2	57.3	3.1	1.9	6.6	0.26	3.9		26.9	101.4
RH_16_OPA_6_3	57.7	2.9	2.0	7.0		3.0		27.4	101.2
RH_16_OPA_6_4	57.6	3.1	2.0	5.9		6.0		25.5	98.5
RH_16_OPA_6_5	58.2	3.1	1.9	6.9		2.4	0.39	27.1	99.2
RH_16_OPA_6_6	58.0	2.8	2.0	6.4	0.35	4.1	0.31	26.0	99.3

	O	Mg	Al	Ti	V	Cr	Mn	Fe	Totals
RH_16_OPA_6_7	58.2	2.9	1.9	6.9	0.27	2.9	0.3	26.7	99.9
RH_16_OPA_6_8	59.0	2.7	1.9	6.9	0.23	3.2	0.49	25.6	99.1
RH_16_OPA_7_1	56.7	2.7	2.0	6.5		4.5	0.15	27.5	97.3
RH_16_OPA_7_2	56.9	2.7	1.9	6.8		4.0	0.26	27.5	97.2
RH_16_OPA_8_1	56.8	4.1	4.3	4.4		5.9	0.29	24.2	97.2
RH_16_OPA_8_2	57.6	3.8	4.3	4.5		6.4		23.5	99.1
RH_16_OPA_8_3	57.6	3.8	3.4	5.1	0.24	5.3		24.5	99.0
RH_16_OPA_8_4	57.6	3.5	4.1	4.6		6.0		23.9	98.8
RH_16_OPA_8_5	56.9	4.0	4.2	4.5		6.1	0.23	23.9	98.3
RH_16_OPA_8_6	57.3	5.2	5.1	2.4	0.17	9.9		20.0	98.2
RH_16_OPA_8_7	57.2	5.6	5.1	2.3		10.3		19.5	99.1
RH_16_OPA_8_8	57.4	5.2	5.2	2.3		10.4		19.5	99.1
RH_16_OPA_9_1	56.9	2.9	1.8	7.2		2.8	0.2	28.3	97.9
RH_16_OPA_9_2	56.5	3.2	1.9	6.5		4.1	0.24	27.6	99.6
RH_16_OPA_9_3	57.2	3.1	2.1	6.1		4.7	0.13	26.7	100.1
RH_16_OPA_9_4	56.7	3.1	2.0	6.4		4.4	0.17	27.2	100.0
RH_16_OPA_9_5	56.8	2.9	1.9	7.1		3.2	0.29	27.8	100.1
RH_16_OPA_9_6	57.1	3.1	2.3	5.1		6.6	0.18	25.6	99.6
RH_16_OPA_9_7	56.7	3.1	2.0	6.0		5.3	0.21	26.7	98.8
RH_16_OPA_9_8	57.2	3.0	2.0	6.5		4.0	0.2	27.1	98.3
RH_16_OPA_10_1	56.3	4.5	5.1	1.4		15.7	0.33	16.7	99.4
RH_16_OPA_10_2	56.5	5.5	4.9	1.5		15.7	0.33	15.6	101.4
RH_16_OPA_10_3	57.1	4.3	5.2	1.5		15.2		16.7	101.4
RH_16_OPA_10_4	56.4	3.5	5.4	1.7		14.8	0.05	18.2	99.7
RH_16_OPA_11_1	56.5	3.8	3.3	6.7		3.1		26.6	97.8
RH_16_OPA_11_2	56.4	3.5	3.0	6.5		3.3		27.3	97.1
RH_16_OPA_11_3	56.4	3.3	3.0	6.4		2.8		28.2	97.4
RH_18_OPA_1_1	53.7	6.2	5.2	1.8		15.4		17.7	102.4
RH_18_OPA_1_2	54.0	5.8	5.5	1.9		15.2		17.7	101.5
RH_18_OPA_1_3	54.3	4.9	5.3	1.9		14.8		18.8	100.4
RH_18_OPA_1_4	56.6	3.6	2.6	9.0		1.7	0.28	26.2	101.0
RH_18_OPA_1_5	57.0	4.1	2.7	8.2	0.25	2.1	0.33	25.3	99.3
RH_18_OPA_1_6	56.8	2.9	2.1	9.5	0.29	1.3	0.32	26.9	102.6
RH_18_OPA_2_1	54.2	6.9	5.9	1.5		16.4		15.2	102.1
RH_18_OPA_2_2	54.1	6.6	5.9	1.6		16.2		15.6	99.5
RH_18_OPA_2_3	54.1	6.5	6.1	1.5		16.2		15.6	98.5
RH_18_OPA_2_4	53.8	6.6	6.0	1.6		16.5		15.6	99.3
RH_18_OPA_2_5	56.3	2.7	2.2	9.0		2.5	0.34	27.1	100.5
RH_18_OPA_2_6	55.8	3.0	3.4	6.7		7.0		24.2	100.0
RH_18_OPA_2_7	56.1	3.4	2.9	8.1	0.33	3.1	0.31	25.9	101.2
RH_18_OPA_2_8	56.1	2.7	2.5	8.2	0.36	3.2	0.35	26.7	101.1
RH_18_OPA_3_1	54.0	7.0	6.5	1.4		16.9		14.2	100.7
RH_18_OPA_3_2	53.2	7.3	6.7	1.4		17.5		14.0	98.3
RH_18_OPA_3_3	53.6	6.9	6.5	1.4		17.2		14.4	97.9
RH_18_OPA_3_4	53.9	6.6	6.5	1.5		17.2		14.5	99.6
RH_18_OPA_3_5	54.6	3.5	2.6	8.1		4.8		26.4	98.0
RH_18_OPA_3_6	56.3	3.6	2.8	8.6		3.3		25.2	102.6
RH_18_OPA_3_7	54.8	4.0	4.0	5.7		6.7	0.31	24.5	101.6
RH_18_OPA_4_4	58.1	3.2	2.3	8.5	0.28	2.4		25.3	99.2
RH_18_OPA_4_5	55.4	3.8	3.8	4.9		8.2	0.31	23.7	98.8
RH_18_OPA_4_6	56.2	3.6	3.4	5.7		6.1		25.0	101.2
RH_18_OPA_4_8	56.6	5.9	5.7	1.7		14.4		15.7	99.9
RH_18_OPA_4_9	56.6	5.8	5.7	1.7		14.6		15.7	99.1
RH_18_OPA_4_10	55.8	6.1	5.8	1.7		14.7		16.0	98.8

	O	Mg	Al	Ti	V	Cr	Mn	Fe	Totals
RH_18_OPA_4_11	56.4	6.3	5.7	1.7		14.4		15.6	99.4
RH_18_OPA_5_1	55.1	4.8	5.7	1.6		15.1		17.7	97.7
RH_18_OPA_5_3	55.0	5.0	5.8	1.6		15.1		17.5	101.0
RH_18_OPA_5_4	55.9	4.5	5.6	1.7		14.6		17.7	100.8
RH_18_OPA_5_5	57.0	2.9	2.4	8.5		2.2	0.27	26.6	100.4
RH_18_OPA_5_6	56.7	2.6	2.6	8.7		3.0	0.33	26.1	101.7
RH_18_OPA_5_7	56.9	3.0	1.9	9.7	0.26	1.9		26.4	100.1
RH_18_OPA_5_8	57.0	2.4	1.9	9.0	0.28	1.3	0.29	27.8	101.0
RH_18_OPA_6_1	53.9	5.8	5.5	1.4		16.9		16.6	101.3
RH_18_OPA_6_2	53.5	6.5	5.9	1.6		16.7		15.8	102.2
RH_18_OPA_6_3	53.8	6.4	5.8	1.5		16.6		15.9	102.0
RH_18_OPA_6_4	53.2	6.7	6.0	1.6		16.6		15.9	102.1
RH_18_OPA_6_5	54.7	4.5	5.2	5.5		5.1		25.1	100.3
RH_18_OPA_6_6	54.5	4.0	4.9	6.5		5.4	0.36	25.4	100.5
RH_18_OPA_6_7	53.7	5.5	5.0	4.5	0.23	6.8		24.4	101.0
RH_18_OPA_7_1	55.5	6.6	5.8	1.5		16.4		14.3	98.7
RH_18_OPA_7_2	55.4	6.9	5.6	1.5		16.3		14.3	99.3
RH_18_OPA_7_3	55.2	7.1	5.5	1.4		16.5	0.28	14.1	99.6
RH_18_OPA_7_4	55.7	6.7	5.8	1.5		16.2		14.2	99.7
RH_18_OPA_7_5	58.0	3.4	3.0	7.4	0.25	3.9	0.28	23.8	99.5
RH_18_OPA_7_6	57.9	3.5	2.4	8.5	0.25	2.3	0.21	24.9	98.0
RH_20_OPA_1_2	56.4	3.4	2.1	6.7		1.5		29.8	99.0
RH_20_OPA_1_3	54.7	3.8	2.5	6.7		1.5	0.29	30.5	99.3
RH_20_OPA_1_4	56.4	3.6	2.4	6.6	0.31	1.4		29.3	99.2
RH_20_OPA_1_5	57.0	3.8	2.4	7.0		1.2		28.6	100.1
RH_20_OPA_1_6	55.6	3.7	2.4	6.6	0.31	1.5		29.9	101.1
RH_20_OPA_1_7	55.8	3.6	2.3	6.7		1.5		30.2	99.3
RH_20_OPA_1_8	57.9	3.6	2.3	7.0	0.32	1.0		27.9	98.6
RH_20_OPA_1_9	57.6	3.4	2.5	7.0	0.26	1.0		28.2	99.7
RH_20_OPA_2_1	54.8	5.8	4.8	3.9		6.0		24.7	102.3
RH_20_OPA_2_2	55.0	5.5	4.5	3.9		5.8		25.3	101.7
RH_20_OPA_2_3	55.3	4.9	4.2	4.0		6.4		25.2	102.1
RH_20_OPA_2_4	54.9	4.8	4.2	4.1		6.5		25.5	101.3
RH_20_OPA_2_5	54.7	5.2	4.5	3.9		6.2		25.1	100.9
RH_20_OPA_2_6	54.7	5.4	4.6	4.0		6.3		25.1	100.9
RH_20_OPA_2_7	55.2	5.2	4.8	3.9		5.9		25.0	100.5
RH_20_OPA_2_8	55.0	5.1	4.3	4.0		6.4		25.2	99.8
RH_20_OPA_3_1	55.8	3.9	2.9	6.4		1.9		29.0	100.5
RH_20_OPA_3_2	55.3	4.0	2.7	6.4		1.9		29.6	100.4
RH_20_OPA_3_3	56.3	3.9	2.9	6.2	0.25	1.9		28.6	100.6
RH_20_OPA_3_4	56.0	4.0	2.8	6.2		1.8		29.2	99.7
RH_20_OPA_3_5	55.8	3.7	2.8	6.3		2.0		29.5	99.9
RH_20_OPA_3_6	55.8	3.9	2.7	6.3	0.27	2.1		29.0	99.8
RH_20_OPA_3_7	56.0	3.8	2.7	6.5		2.1		29.0	99.5
RH_20_OPA_3_8	56.0	3.9	2.4	6.9		1.5		29.4	98.9
RH_20_OPA_3_9	56.4	4.1	2.4	7.1		1.8	0.32	27.9	99.2
RH_20_OPA_3_10	55.9	3.9	2.9	6.6		1.9		28.7	100.5
RH_20_OPA_3_11	56.9	3.7	2.3	7.3		1.6		28.4	99.9
RH_20_OPA_4_1	55.5	4.0	2.7	6.4		1.8		29.6	99.9
RH_20_OPA_4_2	55.8	3.7	2.8	6.6		1.7	0.29	29.2	100.0
RH_20_OPA_4_3	56.1	3.8	2.5	6.4	0.3	1.7		29.2	99.5
RH_20_OPA_4_4	55.3	3.9	2.7	6.5		1.8	0.33	29.5	98.8
RH_20_OPA_4_5	55.4	3.8	2.5	6.5		1.8	0.31	29.7	99.2
RH_20_OPA_4_6	56.0	3.3	2.5	6.7		1.8	0.32	29.3	100.4

	O	Mg	Al	Ti	V	Cr	Mn	Fe	Totals
RH_20_OPA_4_7	57.0	3.0	2.1	7.4		1.5	0.31	28.8	97.6
RH_20_OPA_4_8	58.3	3.7	2.5	6.7	0.3	1.4		27.1	97.6
RH_20_OPA_4_9	55.6	3.8	2.5	6.7		1.5		29.8	99.7
RH_20_OPA_5_1	56.3	4.4	3.0	5.9	0.25	1.6		28.5	101.3
RH_20_OPA_5_2	55.6	4.5	3.0	6.0		1.6	0.32	28.9	100.3
RH_20_OPA_5_3	56.1	4.2	3.0	6.2		1.7		28.9	101.8
RH_20_OPA_5_4	56.5	4.0	2.7	6.1	0.24	1.5		28.9	101.7
RH_20_OPA_5_5	56.3	4.2	2.8	6.2		1.7		28.8	100.6
RH_20_OPA_5_6	57.5	4.1	2.9	6.2		1.8		27.5	100.5
RH_20_OPA_5_7	57.0	4.7	3.7	5.8		1.9		26.9	102.2
RH_20_OPA_5_8	57.9	4.2	2.9	6.3		1.6	0.26	26.9	100.1
RH_20_OPA_6_1	55.9	5.4	5.6	2.0		14.2		17.0	102.7
RH_20_OPA_6_2	56.1	5.7	5.6	1.9		14.1		16.7	102.8
RH_20_OPA_6_3	55.6	5.6	5.5	1.8	0.21	14.1		17.1	102.4
RH_20_OPA_6_4	56.1	5.4	5.6	2.0		14.1		16.9	101.7
RH_20_OPA_6_5	56.1	5.3	5.7	1.9		14.0		17.0	102.3
RH_20_OPA_6_6	56.7	4.0	2.8	5.3		5.1		26.2	101.9
RH_20_OPA_6_7	56.0	3.8	2.4	6.4		3.2		28.3	102.2
RH_20_OPA_6_8	56.4	3.9	2.5	5.9		4.2		27.1	100.4
RH_20_OPA_6_9	56.3	3.7	2.4	5.6		4.3		27.7	100.8
RH_20_OPA_6_10	56.2	3.8	2.9	4.6	0.25	6.6		25.6	100.3
RH_20_OPA_6_11	56.6	4.2	2.9	5.0		5.7		25.7	100.7
RH_20_OPA_7_1	56.2	3.8	2.4	6.2		2.3		29.1	100.5
RH_20-OPA_7_2	55.7	3.6	2.6	6.2		2.2		29.8	99.4
RH_20-OPA_7_3	55.8	3.6	2.4	6.2	0.27	2.3		29.5	101.5
RH_20-OPA_7_4	55.9	3.8	2.4	6.1		2.4	0.36	29.1	100.0
RH_20-OPA_7_5	56.0	3.7	2.2	6.5		2.1	0.42	29.2	100.8
RH_20-OPA_7_6	56.6	3.6	2.3	6.6		2.0	0.27	28.7	100.5
RH_20-OPA_7_7	57.4	3.7	2.3	6.5		1.7	0.33	28.1	98.5
RH_20_OPA_7_8	56.1	3.8	2.0	6.6		1.8		29.6	99.8

Appendix 12 - Table of the calculated spinel components (in %)

	% Ulvöspinel	%Chromite	% Al-Mg-Spinel	%Magnesioferrite	%Magnetite
RH_2_OPA_2_1	38.5	7.8	8.9	5.6	39.3
RH_10_OPA_1_1	4.6	60.0	21.9	3.1	10.4
RH_10_OPA_1_2	4.5	59.3	22.1	3.5	10.6
RH_10_OPA_1_3	4.5	64.3	23.3	7.8	0.0
RH_10_OPA_1_4	35.8	8.8	7.4	5.6	42.4
RH_10_OPA_1_5	8.0	56.9	17.9	4.0	13.3
RH_10_OPA_1_6	26.1	28.5	10.8	6.7	27.8
RH_10_OPA_1_7	35.1	8.6	7.2	6.9	42.2
RH_10_OPA_2_1	42.1	7.7	9.6	9.2	31.3
RH_10_OPA_2_2	47.1	6.6	9.1	9.4	27.9
RH_10_OPA_2_3	42.6	6.4	8.5	8.2	34.3
RH_10_OPA_2_4	49.7	5.1	8.8	10.7	25.8
RH_10_OPA_2_6	50.1	4.8	9.5	10.3	25.3
RH_10_OPA_2_7	48.0	4.5	8.2	8.9	30.5
RH_10_OPA_3_1	4.7	65.1	19.9	6.7	3.6
RH_10_OPA_3_2	5.2	66.7	20.8	7.1	0.0
RH_10_OPA_3_3	5.9	67.2	21.2	5.6	0.0
RH_10_OPA_3_4	4.8	66.9	20.9	7.4	0.0
RH_10_OPA_3_5	39.2	10.4	8.4	9.7	32.4
RH_10_OPA_3_6	45.4	7.5	7.6	11.4	28.2
RH_10_OPA_3_7	38.3	9.9	7.9	9.9	33.9
RH_10_OPA_3_8	21.4	36.2	11.8	7.1	23.5
RH_10_OPA_3_9	26.0	27.5	10.5	8.1	27.9
RH_10_OPA_3_10	25.8	29.6	10.1	8.2	26.3
RH_10_OPA_4_1	6.0	60.1	18.0	5.9	10.0
RH_10_OPA_4_2	6.2	58.6	17.4	5.1	12.8
RH_10_OPA_4_3	5.7	60.3	18.1	7.0	8.9
RH_10_OPA_4_4	6.5	57.6	16.6	4.3	15.0
RH_10_OPA_4_5	27.3	27.3	10.1	7.7	27.6
RH_10_OPA_4_6	27.2	24.1	10.1	7.6	31.0
RH_10_OPA_4_7	39.5	9.1	9.6	10.0	31.7
RH_10_OPA_5_1	4.8	55.3	20.9	1.7	17.3
RH_10_OPA_5_2	4.3	55.7	21.6	1.3	17.1
RH_10_OPA_5_3	4.9	55.3	21.5	1.4	17.0
RH_10_OPA_5_4	29.3	24.3	10.0	7.8	28.6
RH_10_OPA_5_5	26.9	26.6	10.0	6.3	30.2
RH_10_OPA_5_6	23.7	30.6	11.0	6.6	28.1
RH_10_OPA_5_7	30.3	23.5	9.9	8.5	27.9
RH_10_OPA_5_8	45.3	6.6	7.6	11.3	29.2
RH_10_OPA_5_9	47.5	8.2	9.3	11.3	23.7
RH_10_OPA_5_10	39.8	11.9	8.6	10.1	29.6
RH_10_OPA_7_1	15.2	43.8	13.1	4.6	23.2
RH_10_OPA_7_2	30.3	23.5	9.3	7.9	29.1
RH_10_OPA_7_3	19.1	35.3	11.7	5.2	28.7
RH_10_OPA_7_4	48.1	4.9	8.6	8.9	29.4
RH_10_OPA_7_5	43.8	7.8	8.2	10.2	30.0
RH_10_OPA_7_6	0.9	6.6	6.8	5.6	80.1
RH_11_OPA_2_5	2.2	4.9	10.7	5.2	77.0
RH_11_OPA_2_7	3.1	4.9	10.4	6.2	75.5
RH_11_OPA_3_3	31.9	2.6	15.1	10.7	39.7
RH_11_OPA_3_4	44.2	2.8	16.1	14.0	22.8
RH_11_OPA_3_5	24.5	2.2	13.4	8.1	51.7

	% Ulvöspinel	%Chromite	% Al-Mg-Spinel	%Magnesioferrite	%Magnetite
RH_11_OPA_3_6	27.0	1.9	12.0	6.6	52.4
RH_11_OPA_4_1	33.9	4.1	17.4	12.3	32.2
RH_11_OPA_4_3	52.4	5.1	19.4	21.1	2.0
RH_11_OPA_4_5	35.3	4.1	14.6	14.7	31.2
RH_11_OPA_5_2	32.6	2.2	12.9	5.2	47.1
RH_11_OPA_5_3	33.6	1.9	10.7	6.5	47.3
RH_11_OPA_5_5	21.1	2.0	10.1	2.5	64.3
RH_11_OPA_5_7	29.0	2.6	9.1	4.4	54.9
RH_11_OPA_6_1	5.4	61.9	16.5	4.4	11.7
RH_11_OPA_6_2	5.2	65.6	17.3	7.3	4.6
RH_11_OPA_6_3	5.3	69.2	17.9	7.7	0.0
RH_11_OPA_6_4	5.2	61.2	16.1	3.6	13.8
RH_11_OPA_6_5	1.6	58.5	14.7	3.5	21.8
RH_11_OPA_9_3	2.9	4.7	10.8	5.4	76.2
RH_11_OPA_9_5	11.5	5.8	12.8	5.8	64.1
RH_11_OPA_9_6	14.8	10.6	8.6	7.4	58.6
RH_13_OPA_1_2	40.0	2.6	14.9	10.8	31.8
RH_13_OPA_1_3	41.2	3.0	15.9	12.3	27.7
RH_13_OPA_1_4	39.6	2.2	14.8	11.3	32.1
RH_13_OPA_2_1	48.4	3.1	8.3	4.9	35.3
RH_13_OPA_2_2	49.4	3.0	7.3	8.6	31.6
RH_13_OPA_2_3	50.6	3.6	7.2	9.2	29.4
RH_13_OPA_2_4	49.8	2.1	8.1	8.0	32.0
RH_13_OPA_2_5	52.8	1.5	8.2	10.1	27.5
RH_13_OPA_2_6	49.5	2.0	7.7	6.5	34.4
RH_13_OPA_3_1	5.1	56.4	17.5	1.3	19.6
RH_13_OPA_3_2	5.1	57.3	17.0	2.0	18.6
RH_13_OPA_3_3	40.1	12.5	7.7	4.7	35.0
RH_13_OPA_3_4	48.0	5.2	8.1	8.7	30.0
RH_13_OPA_3_5	48.2	6.4	7.5	9.3	28.5
RH_13_OPA_3_6	43.4	3.6	6.9	5.3	40.8
RH_13_OPA_3_7	26.1	26.5	9.1	6.1	32.2
RH_13_OPA_3_8	50.4	0.0	7.3	8.4	33.8
RH_13_OPA_3_9	47.6	0.0	6.9	7.6	38.0
RH_13_OPA_3_10	47.9	1.0	6.9	3.0	41.1
RH_13_OPA_3_11	48.3	0.0	5.5	0.5	45.7
RH_13_OPA_4_1	48.9	1.8	10.8	10.1	28.4
RH_13_OPA_4_2	47.7	2.6	11.8	11.5	26.5
RH_13_OPA_4_3	49.5	2.1	12.9	10.2	25.3
RH_13_OPA_5_1	51.2	2.5	9.1	10.5	26.6
RH_13_OPA_5_2	49.5	1.3	8.6	9.1	31.4
RH_13_OPA_5_3	50.9	2.5	9.6	8.8	28.2
RH_13_OPA_5_4	50.8	1.3	9.4	9.4	29.0
RH_13_OPA_5_5	50.4	1.5	8.5	8.0	31.6
RH_13_OPA_6_1	44.6	3.5	14.1	10.8	27.0
RH_13_OPA_6_2	45.7	2.7	14.3	12.1	25.2
RH_13_OPA_6_4	42.4	3.4	15.1	11.5	27.6
RH_13_OPA_6_5	42.4	2.5	14.4	11.9	28.9
RH_13_OPA_6_6	43.2	3.3	13.7	12.8	26.9
RH_13_OPA_7_1	47.8	0.0	7.3	5.1	39.8
RH_13_OPA_7_2	50.9	1.5	6.8	9.0	31.9
RH_13_OPA_7_3	50.8	2.0	7.3	5.7	34.2
RH_13_OPA_7_4	45.0	1.5	7.6	1.9	43.9
RH_13_OPA_7_5	52.0	1.4	7.6	7.3	31.7

	% Ulvöspinel	%Chromite	% Al-Mg-Spinel	%Magnesioferrite	%Magnetite
RH_13_OPA_7_6	51.3	1.6	6.4	7.3	33.5
RH_13_OPA_7_7	46.7	0.0	6.2	9.7	37.4
RH_13_OPA_7_8	52.4	0.0	4.6	7.9	35.0
RH_13_OPA_7_9	44.1	0.0	5.0	9.8	41.0
RH_13_OPA_7_10	50.4	0.0	5.0	5.6	39.1
RH_13_OPA_8_1	45.6	2.9	14.9	12.2	24.4
RH_13_OPA_8_2	47.4	2.6	14.0	13.1	23.0
RH_13_OPA_8_3	43.9	2.6	13.9	10.8	28.8
RH_13_OPA_8_4	25.0	1.7	7.9	6.0	59.4
RH_16_OPA_1_1	23.6	21.3	12.7	7.1	35.3
RH_16_OPA_1_2	28.6	15.0	11.3	8.0	37.1
RH_16_OPA_1_3	20.3	21.0	16.1	5.6	37.0
RH_16_OPA_1_4	24.9	18.7	13.0	7.2	36.2
RH_16_OPA_1_5	29.1	14.0	10.6	8.3	37.9
RH_16_OPA_1_6	23.5	19.4	12.9	6.7	37.5
RH_16_OPA_2_1	21.1	23.8	14.8	8.4	31.8
RH_16_OPA_2_2	17.4	26.2	17.7	6.9	31.8
RH_16_OPA_2_3	13.4	29.2	19.5	6.3	31.5
RH_16_OPA_2_4	14.9	27.3	19.2	8.4	30.2
RH_16_OPA_2_5	9.1	46.5	20.7	15.0	8.6
RH_16_OPA_2_6	10.7	35.4	19.8	9.9	24.2
RH_16_OPA_2_7	11.4	32.9	20.6	6.5	28.6
RH_16_OPA_2_8	22.2	23.4	14.6	9.1	30.7
RH_16_OPA_2_9	19.9	23.3	15.5	8.4	32.9
RH_16_OPA_2_10	9.3	40.2	20.2	11.3	19.1
RH_16_OPA_3_1	5.6	58.9	22.9	9.5	3.0
RH_16_OPA_3_2	6.1	59.0	22.1	9.6	3.2
RH_16_OPA_3_3	6.4	54.2	21.5	4.9	13.0
RH_16_OPA_3_4	5.5	57.1	22.5	8.1	6.8
RH_16_OPA_3_5	26.7	25.9	11.3	10.7	25.4
RH_16_OPA_3_6	32.2	22.5	10.3	13.0	22.0
RH_16_OPA_3_7	28.9	23.3	10.7	11.1	26.0
RH_16_OPA_3_8	29.9	23.4	10.6	12.1	24.0
RH_16_OPA_4_1	22.4	17.1	16.8	6.4	37.4
RH_16_OPA_4_2	22.5	17.2	15.5	6.8	38.0
RH_16_OPA_4_3	26.4	14.1	13.4	8.1	38.0
RH_16_OPA_4_4	27.2	12.7	12.8	8.5	38.8
RH_16_OPA_4_5	22.8	16.0	15.2	5.9	40.1
RH_16_OPA_4_6	22.5	16.5	16.8	6.4	37.8
RH_16_OPA_4_7	34.5	13.1	14.0	10.1	28.4
RH_16_OPA_5_1	5.4	63.6	20.5	10.5	0.0
RH_16_OPA_5_2	5.6	63.7	20.4	10.2	0.0
RH_16_OPA_5_3	5.5	61.3	19.9	9.1	4.2
RH_16_OPA_5_4	5.4	59.1	19.5	6.9	9.1
RH_16_OPA_5_5	5.2	68.8	20.2	5.9	0.0
RH_16_OPA_5_6	38.6	18.8	9.7	8.8	24.1
RH_16_OPA_5_9	23.1	11.7	5.6	7.2	52.4
RH_16_OPA_6_1	31.5	12.6	8.4	9.0	38.6
RH_16_OPA_6_2	30.1	17.9	8.6	10.0	33.4
RH_16_OPA_6_3	32.1	13.6	8.9	8.7	36.7
RH_16_OPA_6_4	26.0	26.6	8.7	9.3	29.4
RH_16_OPA_6_5	32.6	11.4	9.1	9.9	37.0
RH_16_OPA_6_6	29.2	18.6	9.2	8.2	34.7
RH_16_OPA_6_7	32.6	13.4	9.1	8.9	36.0

	% Ulvöspinel	%Chromite	% Al-Mg-Spinel	%Magnesioferrite	%Magnetite
RH_16_OPA_6_8	33.5	15.8	9.1	8.8	32.8
RH_16_OPA_7_1	27.9	19.3	8.4	7.3	37.1
RH_16_OPA_7_2	29.4	17.4	8.4	7.4	37.4
RH_16_OPA_8_1	17.5	23.5	17.1	7.5	34.3
RH_16_OPA_8_2	17.8	25.7	17.3	6.4	32.7
RH_16_OPA_8_3	21.8	22.9	14.5	9.0	31.7
RH_16_OPA_8_4	18.6	24.0	16.5	5.6	35.4
RH_16_OPA_8_5	18.1	24.8	17.1	7.7	32.3
RH_16_OPA_8_6	9.5	39.3	20.4	10.4	20.4
RH_16_OPA_8_7	9.5	42.1	20.8	12.7	14.9
RH_16_OPA_8_8	9.4	41.9	20.7	10.5	17.5
RH_16_OPA_9_1	32.2	12.4	7.9	9.0	38.6
RH_16_OPA_9_2	28.7	17.9	8.3	9.7	35.5
RH_16_OPA_9_3	26.9	20.4	9.1	9.2	34.4
RH_16_OPA_9_4	27.7	19.2	8.7	9.1	35.3
RH_16_OPA_9_5	31.7	14.2	8.6	8.5	36.9
RH_16_OPA_9_6	21.2	27.2	9.6	7.9	34.0
RH_16_OPA_9_7	26.0	22.7	8.6	9.1	33.6
RH_16_OPA_9_8	28.7	17.9	8.6	8.8	36.0
RH_16_OPA_10_1	5.3	59.4	19.5	7.2	8.6
RH_16_OPA_10_2	5.9	63.8	20.0	10.2	0.0
RH_16_OPA_10_3	5.6	57.7	19.9	6.5	10.3
RH_16_OPA_10_4	5.8	51.8	18.8	2.8	20.7
RH_16_OPA_11_1	29.9	13.6	14.6	9.8	32.1
RH_16_OPA_11_2	27.7	13.8	12.9	8.5	37.1
RH_16_OPA_11_3	26.0	11.6	12.4	7.4	42.7
RH_18_OPA_1_1	6.8	60.3	20.5	12.5	0.0
RH_18_OPA_1_2	7.1	58.8	21.2	11.6	1.3
RH_18_OPA_1_3	7.0	54.2	19.4	8.4	10.9
RH_18_OPA_1_4	49.2	9.4	14.2	12.6	14.7
RH_18_OPA_1_5	45.1	11.4	15.1	14.9	13.6
RH_18_OPA_1_6	52.4	7.2	11.4	10.5	18.5
RH_18_OPA_2_1	5.9	63.8	22.8	7.8	0.0
RH_18_OPA_2_2	6.0	62.5	22.9	8.5	0.0
RH_18_OPA_2_3	5.7	62.4	23.4	8.5	0.0
RH_18_OPA_2_4	6.0	63.0	22.9	8.0	0.0
RH_18_OPA_2_5	44.7	12.4	11.0	8.0	23.9
RH_18_OPA_2_6	29.3	30.3	14.6	5.7	20.1
RH_18_OPA_2_7	39.9	15.5	14.1	9.9	20.6
RH_18_OPA_2_8	38.4	14.9	11.9	6.6	28.1
RH_18_OPA_3_1	5.3	64.3	24.8	5.7	0.0
RH_18_OPA_3_2	5.2	65.4	25.0	4.5	0.0
RH_18_OPA_3_3	5.2	64.5	24.6	5.6	0.0
RH_18_OPA_3_4	5.7	64.8	24.4	5.3	0.0
RH_18_OPA_3_5	38.4	22.5	12.5	10.4	16.2
RH_18_OPA_3_6	46.0	17.7	14.7	11.8	9.9
RH_18_OPA_3_7	23.6	28.0	16.5	8.3	23.7
RH_18_OPA_4_4	46.4	13.1	12.6	10.9	17.0
RH_18_OPA_4_5	19.6	33.0	15.4	7.6	24.4
RH_18_OPA_4_6	24.0	25.7	14.4	8.0	28.0
RH_18_OPA_4_8	6.9	59.2	23.2	10.7	0.0
RH_18_OPA_4_9	6.8	59.6	23.5	10.2	0.0
RH_18_OPA_4_10	6.7	59.0	23.4	10.9	0.0
RH_18_OPA_4_11	7.0	59.2	23.5	10.3	0.0

	% Ulvöspinel	%Chromite	% Al-Mg-Spinel	%Magnesioferrite	%Magnetite
RH_18_OPA_5_1	5.8	55.1	20.8	7.3	11.0
RH_18_OPA_5_3	5.7	55.3	21.3	7.7	10.0
RH_18_OPA_5_4	6.3	53.6	20.7	6.3	13.1
RH_18_OPA_5_5	43.0	11.3	12.0	8.6	25.2
RH_18_OPA_5_6	43.2	14.9	12.9	6.5	22.6
RH_18_OPA_5_7	55.1	10.6	10.6	12.0	11.6
RH_18_OPA_5_8	44.6	6.4	9.5	7.0	32.5
RH_18_OPA_6_1	5.3	63.6	20.7	10.2	0.0
RH_18_OPA_6_2	6.1	63.3	22.3	8.3	0.0
RH_18_OPA_6_3	5.7	63.4	22.3	8.8	0.0
RH_18_OPA_6_4	5.9	62.7	22.7	8.7	0.0
RH_18_OPA_6_5	21.9	20.0	20.4	7.5	30.3
RH_18_OPA_6_6	26.1	21.7	19.6	6.4	26.2
RH_18_OPA_6_7	18.0	27.1	19.7	11.9	23.3
RH_18_OPA_7_1	5.7	65.0	23.0	6.3	0.0
RH_18_OPA_7_2	5.9	65.5	22.7	6.0	0.0
RH_18_OPA_7_3	5.6	66.3	22.2	6.0	0.0
RH_18_OPA_7_4	5.8	64.8	23.0	6.4	0.0
RH_18_OPA_7_5	38.1	20.2	15.3	9.8	16.6
RH_18_OPA_7_6	48.7	13.1	13.4	13.1	11.6
RH_20_OPA_1_2	28.6	6.5	9.0	9.8	46.2
RH_20_OPA_1_3	27.5	6.1	10.4	10.2	45.9
RH_20_OPA_1_4	28.5	5.8	10.3	10.3	45.1
RH_20_OPA_1_5	31.8	5.4	11.1	11.8	40.0
RH_20_OPA_1_6	27.6	6.1	10.1	10.4	45.8
RH_20_OPA_1_7	25.3	5.6	8.6	0.9	59.6
RH_20_OPA_1_8	32.8	4.7	10.8	11.3	40.4
RH_20_OPA_1_9	31.9	4.5	11.4	9.5	42.6
RH_20_OPA_2_1	15.5	23.9	19.1	13.5	28.0
RH_20_OPA_2_2	15.4	22.7	17.7	12.5	31.7
RH_20_OPA_2_3	15.7	24.9	16.3	10.9	32.2
RH_20_OPA_2_4	15.7	24.9	16.0	10.4	33.0
RH_20_OPA_2_5	15.1	24.2	17.3	11.7	31.7
RH_20_OPA_2_6	15.4	24.6	18.0	12.0	30.0
RH_20_OPA_2_7	14.8	22.8	18.2	10.7	33.5
RH_20_OPA_2_8	15.3	24.8	16.6	11.2	32.1
RH_20_OPA_3_1	26.8	8.0	12.2	10.0	43.0
RH_20_OPA_3_2	26.4	7.9	11.2	10.7	43.8
RH_20_OPA_3_3	25.9	8.0	12.0	10.5	43.5
RH_20_OPA_3_4	25.8	7.5	11.6	10.8	44.3
RH_20_OPA_3_5	25.4	8.0	11.2	9.3	46.0
RH_20_OPA_3_6	26.3	8.6	11.4	10.4	43.3
RH_20_OPA_3_7	27.4	8.9	11.3	10.6	41.9
RH_20_OPA_3_8	30.1	6.3	10.4	11.8	41.4
RH_20_OPA_3_9	33.2	8.6	11.1	13.6	33.4
RH_20_OPA_3_10	28.1	8.1	12.3	10.2	41.3
RH_20_OPA_3_11	33.6	7.5	10.5	12.1	36.4
RH_20_OPA_4_1	26.8	7.7	11.2	11.2	43.1
RH_20_OPA_4_2	27.7	7.1	11.6	9.6	43.9
RH_20_OPA_4_3	26.9	7.3	10.6	10.6	44.7
RH_20_OPA_4_4	27.0	7.6	11.2	10.8	43.3
RH_20_OPA_4_5	27.1	7.5	10.4	10.4	44.7
RH_20_OPA_4_6	27.9	7.5	10.5	8.3	45.8
RH_20_OPA_4_7	32.8	6.5	9.5	8.5	42.8

	% Ulvöspinel	%Chromite	% Al-Mg-Spinel	%Magnesioferrite	%Magnetite
RH_20_OPA_4_8	31.6	6.7	11.9	11.3	38.2
RH_20_OPA_4_9	28.1	6.3	10.6	10.5	44.6
RH_20_OPA_5_1	25.1	6.9	12.6	12.4	43.1
RH_20_OPA_5_2	25.0	6.9	12.7	12.6	42.8
RH_20_OPA_5_3	25.8	7.3	12.5	11.3	43.1
RH_20_OPA_5_4	25.8	6.4	11.4	11.0	45.4
RH_20_OPA_5_5	26.4	7.4	11.8	12.0	42.4
RH_20_OPA_5_6	27.7	8.0	12.7	12.1	39.5
RH_20_OPA_5_7	25.5	8.2	16.3	12.2	37.8
RH_20_OPA_5_8	29.2	7.6	13.4	13.0	36.7
RH_20_OPA_6_1	7.8	56.3	22.4	10.3	3.1
RH_20_OPA_6_2	7.6	57.7	22.7	11.8	0.2
RH_20_OPA_6_3	7.2	56.3	22.0	11.2	3.3
RH_20_OPA_6_4	7.9	56.6	22.4	10.4	2.7
RH_20_OPA_6_5	7.5	55.4	22.5	9.9	4.7
RH_20_OPA_6_6	22.1	21.4	11.8	10.9	33.7
RH_20_OPA_6_7	27.6	13.8	10.2	11.2	37.3
RH_20_OPA_6_8	25.6	18.1	10.6	11.7	33.9
RH_20_OPA_6_9	23.3	17.9	9.9	10.4	38.6
RH_20_OPA_6_10	18.6	26.6	11.6	9.7	33.5
RH_20_OPA_6_11	20.8	24.1	12.2	11.4	31.6
RH_20_OPA_7_1	25.9	9.4	10.2	10.9	43.7
RH_20-OPA_7_2	24.6	8.9	10.5	9.2	46.9
RH_20-OPA_7_3	25.4	9.4	9.9	9.9	45.4
RH_20-OPA_7_4	25.2	10.1	9.9	10.8	44.0
RH_20-OPA_7_5	28.2	9.0	9.3	11.2	42.4
RH_20-OPA_7_6	28.9	8.7	9.9	10.9	41.6
RH_20-OPA_7_7	29.4	7.5	10.4	11.3	41.5
RH_20_OPA_7_8	28.8	7.8	8.8	12.1	42.4

Appendix 13 - Table of the chemical composition of iddingsite (in wt%)

	Na	Mg	Al	Si	Ca	Ti	Fe	O	Totals
SoI 1_1905_2	0.12	6.4	1.0	10.6	0.4		29.0	27.7	75.2
SoI 1_1905_3	0.17	5.7	0.7	10.0	0.39		30.8	27.0	74.6
SoI 1_1905_4	0.11	7.1	0.3	10.7	0.39		28.9	27.7	75.3
SoI 1_1905_5	0.14	5.1	0.5	9.0	0.3		30.0	25.0	70.0
SoI 1_2105_1	0.71	3.2	0.3	4.7	0.08	0.02	46.4	24.7	80.1
SoI 1_2105_2	0.73	4.1	0.4	5.9	0.09	0.08	44.5	26.0	81.6
SoI 1_2105_3	0.74	4.4	0.4	6.4	0.09		43.3	26.3	81.7
SoI 7_2105_1	0.64	9.7	0.6	13.1	0.37		30.3	30.9	85.6
SoI 7_2105_2	0.68	7.6	0.5	12.2	0.37		31.6	28.8	81.8
SoI 7_2105_3	0.66	6.7	0.5	11.2	0.33		34.2	27.8	81.4
SoI 7_2105_4	0.61	4.2	0.4	6.6	0.09		42.0	22.9	76.9
SoI 7_2105_5	0.64	4.5	0.5	6.8	0.11		41.4	23.5	78.1
SoI 6_1506_1		2.6	0.5	7.9	0.31		46.6	27.9	85.8
SoI 6_1506_2	0.1	2.2	0.5	7.9	0.32		47.8	28.2	87.0
SoI 6_1506_3	0.12	5.1	0.7	12.4	0.47		35.2	31.0	85.0
SoI 6_1506_4	0.11	6.4	0.6	14.2	0.44		32.1	32.6	86.4
SoI 6_1506_5	0.03	3.0	0.6	8.7	0.37		42.2	27.6	82.5
SoI 6_1506_6	0.05	3.6	0.5	12.4	0.45		37.4	30.5	84.9
SoI 6_1506_7	0.14	2.3	0.4	7.7	0.3		47.8	27.9	86.5
SoI 7_1506_1	0.12	2.5	0.5	8.0	0.29		46.9	28.2	86.4
SoI 7_1506_2	0.14	2.7	0.4	8.0	0.3		46.0	27.9	85.4
SoI 7_1506_3	0.08	2.4	0.4	7.6	0.27		47.8	27.8	86.2
SoI 7_1506_4		3.7	0.6	11.8	0.47		38.2	30.4	85.2
SoI 7_1506_5	0.12	4.5	0.7	12.8	0.52		35.2	31.0	84.9
SoI 7_1506_6	0.02	4.2	0.6	12.9	0.53		37.4	31.6	87.2
SoI 7_1506_7	0.13	2.4	0.5	8.7	0.26		44.1	27.8	83.9
SoI 7_1506_8	0.09	1.9	0.3	6.5	0.24		47.1	25.9	82.1
SoI 15_1506_1	0.14	2.9	0.5	8.3	0.4	0.42	46.4	28.9	88.0
SoI 15_1506_2	0.04	3.1	0.6	9.1	0.43	0.47	43.6	29.0	86.3
SoI 15_1506_3		2.9	0.5	8.7	0.44	0.43	45.7	29.1	87.9
SoI 15_1506_4	0.05	4.1	0.6	13.8	0.43		36.6	32.2	87.8
SoI 15_1506_5	0.08	4.1	0.6	13.1	0.49	0.05	37.5	31.9	87.8
SoI 15_1506_6		4.7	0.6	13.0	0.46	0.04	36.7	31.7	87.1
SoI 15_1506_7	0.04	6.0	0.8	14.7	0.52	0.01	31.4	32.8	86.2
SoI 4_1806_1	0.12	3.9	0.7	11.2	0.45		36.1	29.0	81.4
SoI 4_1806_2	0.09	3.6	0.6	10.6	0.39		37.1	28.4	80.8
SoI 4_1806_3	0.11	3.8	0.7	10.9	0.45		36.9	28.9	81.7
SoI 4_1806_4	0.12	3.6	0.6	10.8	0.39		36.9	28.6	81.0
SoI 4_1806_5	0.06	2.1	0.5	7.2	0.31		45.3	26.4	81.8
SoI 4_1806_6		2.0	0.4	6.9	0.29		47.4	26.5	83.4
SoI 4_1806_7	0.15	1.9	0.4	7.0	0.31		48.1	27.0	84.8
SoI 4_1806_8	0.1	2.3	0.5	7.5	0.34		45.1	26.7	82.5
SoI 7_3006_1	0.14	3.5	2.1	8.4	0.47		37.8	27.6	80.0
SoI 7_3006_2	0.23	4.4	1.6	9.5	0.41		36.0	28.3	80.5
SoI 7_3006_3	0.07	4.8	1.8	9.5	0.49		35.8	28.6	81.0
SoI 9_3006_1	0.01	7.4	1.3	14.2	0.47	0.12	28.8	32.9	85.6
SoI 9_3006_2	0.11	4.5	1.6	9.6	0.38	0.05	37.2	28.9	82.5
SoI 9_3006_3	0.05	4.5	1.6	9.4	0.59	0.14	37.7	29.0	83.2
SoI 9_3006_4	0.13	2.6	2.1	3.7	0.2	5.54	39.9	25.9	80.1
SoI 11_3006_1	0.11	5.2	1.7	10.5	0.5		35.9	30.0	83.9
SoI 11_3006_2	0.07	5.0	1.5	10.3	0.48		36.2	29.7	83.5
SoI 11_3006_3	0.12	5.0	1.5	10.4	0.4		36.6	29.9	84.3

	Na	Mg	Al	Si	Ca	Ti	Fe	O	Totals
SoI 11_3006_4	0.14	7.5	2.1	14.8	0.51		27.7	33.8	86.7
SoI 11_3006_5	0.15	7.5	1.8	14.6	0.62		29.0	33.9	87.7
SoI 12_3006_1	0.14	5.3	1.6	10.8	0.42		35.9	30.4	85.0
SoI 12_3006_2	0.2	5.6	1.7	11.4	0.53		32.7	30.3	82.7
SoI 12_3006_3	0.06	3.6	2.5	8.5	0.5	0.25	37.7	28.2	81.4
SoI 12_3006_4	0.06	4.1	1.8	8.9	0.47		38.9	28.7	83.3
SoI 13_3006_1		4.2	1.7	8.7	0.39		38.6	28.2	82.1
SoI 13_3006_2	0.06	4.6	1.4	9.3	0.38		38.9	29.0	83.9
SoI 13_3006_3	0.1	5.6	1.4	10.8	0.43		34.7	29.9	83.1
SoI 13_3006_4	0.03	5.1	1.4	10.3	0.45		36.9	29.8	84.1
SoI 4_3006_1	0.19	2.8	2.2	8.9	0.75	0.81	38.9	28.8	83.5
SoI 4_3006_2	0.14	3.5	2.2	9.7	0.78	1.17	37.2	29.7	84.3
SoI 4_3006_3	0.13	2.7	2.4	9.0	0.66	0.47	38.4	28.6	82.4
SoI 5_3006_1	0.14	2.7	2.7	9.2	0.66	0.36	38.7	29.0	83.5
SoI 5_3006_2	0.02	3.2	2.4	9.4	0.59	0.6	38.8	29.4	84.4
SoI 5_3006_3	0.02	2.5	2.6	8.6	0.58	0.23	40.1	28.5	83.1
SoI 5_3006_4	0.09	2.7	2.6	8.9	0.69	0.46	39.6	29.1	84.1
SoI 5_3006_5	0.03	2.2	2.6	8.1	0.5	0.24	41.1	28.2	83.2
SoI 5_3006_6	0.12	2.5	2.9	8.5	0.6	0.14	40.9	28.8	84.4
SoI 6_3006_1	0.12	2.7	2.4	8.6	0.54	0.31	40.9	28.8	84.4
SoI 6_3006_2	0.28	3.4	2.8	9.9	0.61		39.4	30.6	87.5
SoI 6_3006_3	0.05	2.3	2.3	7.7	0.44		42.4	27.8	83.4
SoI 6_3006_4	0.16	4.8	2.4	14.6	0.94		31.8	33.9	89.2
SoI 6_3006_5	0.05	4.1	2.3	12.5	0.7		35.3	32.2	88.2
SoI 6_3006_6	0.22	4.0	2.4	12.0	0.63	0.23	35.9	32.0	88.3

Appendix 14 - Table of the chemical composition of altered olivine (in wt%)

	Na	Mg	Al	Si	K	Ca	Fe	O	Totals
SoI 3_1805_1	0.13	17.4	0.49	26.5	0.15	0.24	4.8	43.6	93.2
SoI 3_1805_2	0.09	18.8	0.48	27.9	0.06	0.21	4.5	45.9	97.8
SoI 3_1805_3	0.11	19.1	0.36	28.5	0.1	0.23	4.2	46.6	99.2
SoI 3_1805_4	0.09	18.0	0.2	27.2	0.16	0.15	3.7	44.2	93.8
SoI 9_1805_2	0.05	18.7	1.41	24.5	0.11	0.32	6.2	43.4	94.7
SoI 9_1805_3	0.15	16.5	0.36	25.5	0.21	0.21	5.9	42.1	91.0
SoI 2_1905_1	0.14	9.7	2.9	19.3	0.27	0.37	18.1	36.5	87.3
SoI 2_1905_2	0.21	12.9	2.2	22.5	0.23	0.69	8.8	38.9	86.3
SoI 2_1905_3	0.18	10.8	3.0	20.9	0.21	0.45	19.7	39.6	95.0
SoI 2_1905_4	0.24	12.3	2.3	22.1	0.08	0.69	11.6	39.0	88.3
SoI 2_1905_5	0.27	14.5	2.3	24.2	0.16	0.75	8.0	41.9	92.0
SoI 2_1905_6	0.26	13.4	2.5	23.6	0.2	0.66	12.0	41.8	94.3
SoI 4_2105_1	0.45	16.6	0.6	26.7	0.04	0.1	4.0	43.3	91.8
SoI 4_2105_2	0.45	16.4	0.53	26.6	0.07	0.11	4.0	42.9	91.0
SoI 4_2105_3	0.32	16.4	0.55	26.4	0.05	0.1	3.9	42.6	90.3
SoI 3_2205_1	0.33	13.2	1.9	24.4	0.18	0.67	4.2	39.8	84.7
SoI 3_2205_2	0.29	14.1	1.6	23.5	0.13	0.51	2.3	38.4	80.7
SoI 3_2205_3	0.29	13.9	1.4	23.0	0.07	0.4	2.3	37.5	78.9
SoI 3_2205_4	0.28	13.9	1.5	23.2	0.07	0.38	2.8	38.0	80.0
SoI 3_2205_5	0.31	13.3	2.0	24.3	0.24	0.55	4.2	39.8	84.8
SoI 4_2605_1	0.03	15.1	0.3	25.9	0.29	0.4	5.0	41.3	88.3
SoI 4_2605_2	0.04	14.0	0.25	24.2	0.19	0.25	4.3	38.4	81.7
SoI 4_2605_3	0.07	15.0	0.25	26.3	0.22	0.33	5.5	41.8	89.5
SoI 4_2605_4	0.07	13.9	0.28	24.3	0.19	0.2	4.4	38.5	81.9
SoI 5_2605_1	0.11	15.7	0.41	26.6	0.22	0.21	7.5	43.3	94.0
SoI 5_2605_2	0.08	15.0	0.28	25.6	0.16	0.24	4.8	40.8	86.9
SoI 5_2605_3	0.05	15.3	0.25	25.9	0.1	0.19	5.3	41.5	88.6
SoI 5_2605_4	0.01	15.0	0.19	25.3	0.11	0.24	5.2	40.5	86.5
SoI 3_2705_1	0.09	13.5	1.4	25.4	0.32	0.82	4.8	40.8	87.2
SoI 3_2705_2	0.1	16.2	1.0	26.5	0.13	0.47	3.5	43.0	90.9
SoI 3_2705_3	0.09	16.0	1.0	26.7	0.2	0.51	3.9	43.1	91.5
SoI 3_2705_4	0.04	16.6	1.0	26.9	0.17	0.44	2.8	43.5	91.4
SoI 3_2705_5	0.06	16.4	1.0	26.6	0.23	0.46	3.7	43.3	91.7
SoI 4_2705_1	0.07	14.9	0.28	26.1	0.34	0.28	6.7	42.0	90.7
SoI 4_2705_2	0.11	14.2	0.26	24.6	0.26	0.25	5.7	39.4	84.7
SoI 4_2705_3	0.01	14.6	0.19	24.6	0.18	0.28	4.4	39.2	83.4
SoI 4_2705_4	0.05	14.2	0.25	24.3	0.19	0.3	4.2	38.6	82.1
SoI 4_2705_5	0.05	14.0	0.18	23.9	0.19	0.28	5.4	38.3	82.3
SoI 4_2705_6	0.08	14.3	0.2	24.0	0.16	0.31	4.3	38.4	81.8
SoI 3_1506_1	0.1	13.8	1.4	25.0	0.27	0.71	4.2	40.4	85.9
SoI 3_1506_2	0.08	14.5	1.5	25.6	0.32	0.7	4.2	41.6	88.4
SoI 3_1506_3	0.08	15.1	1.1	24.9	0.19	0.49	3.1	40.4	85.2
SoI 3_1506_4	0.07	14.6	1.0	24.5	0.08	0.5	4.1	39.8	84.7
SoI 3_1506_5	0.04	14.4	1.1	24.4	0.17	0.6	4.1	39.7	84.5
SoI 3_1506_6	0.06	14.5	1.0	24.3	0.15	0.46	4.0	39.5	84.1
SoI 11_1506_1	0.05	11.8	1.2	23.8	0.3	0.91	7.0	38.4	83.4
SoI 11_1506_2	0.11	16.0	1.0	26.1	0.11	0.55	4.2	42.6	90.6
SoI 11_1506_3	0.04	16.3	0.9	26.5	0.2	0.47	3.9	43.1	91.4
SoI 11_1506_4	0.07	15.1	0.9	25.3	0.22	0.51	4.4	41.0	87.4
SoI 11_1506_5	0.02	16.6	1.0	26.7	0.29	0.54	3.1	43.3	91.5
SoI 12_1506_1	0.03	14.6	0.5	27.3	0.37	0.63	8.7	44.1	96.3
SoI 12_1506_2	0.04	15.0	0.42	26.9	0.35	0.48	7.8	43.4	94.5

	Na	Mg	Al	Si	K	Ca	Fe	O	Totals
SoI 12_1506_3	0.07	15.3	0.21	26.5	0.22	0.32	6.8	42.6	92.1
SoI 12_1506_4	0.03	15.3	0.2	26.1	0.27	0.3	4.9	41.5	88.6
SoI 12_1506_5	0.05	16.2	0.23	26.9	0.27	0.4	4.7	43.0	91.7
SoI 12_1506_6	0.04	15.0	0.15	25.6	0.21	0.29	4.4	40.6	86.2
SoI 12_1506_7	0.04	15.8	0.28	27.0	0.2	0.34	6.3	43.4	93.4
SoI 14_1506_1	0.06	16.5	0.24	27.5	0.34	0.25	6.6	44.5	96.0
SoI 14_1506_2	0	15.9	0.21	26.8	0.17	0.36	4.9	42.7	90.9
SoI 14_1506_3	0.07	14.0	0.35	26.7	0.37	0.53	7.8	42.6	92.5
SoI 14_1506_4	0.05	15.2	0.19	26.1	0.25	0.36	5.1	41.6	88.9
SoI 14_1506_5	0.06	15.6	0.21	26.6	0.32	0.4	5.2	42.5	90.9
SoI 14_1506_6	0	15.3	0.15	25.5	0.2	0.22	4.9	40.8	87.1
SoI 14_1506_7	0.06	15.6	0.24	26.6	0.22	0.31	5.8	42.6	91.3
SoI 14_1506_8	0.09	15.0	0.25	26.5	0.31	0.36	7.0	42.5	92.0
SoI 19_1506_1	0.08	10.8	1.4	24.2	0.27	1.22	7.7	38.7	84.3
SoI 19_1506_2	0.07	14.7	1.1	24.9	0.08	1.57	4.1	40.9	87.4
SoI 19_1506_3	0.04	14.8	1.2	25.3	0.11	0.62	4.5	41.2	87.8
SoI 19_1506_4	0.08	15.0	1.2	25.3	0.19	0.64	4.4	41.2	87.9
SoI 19_1506_5	0.12	15.1	1.2	25.3	0.2	0.71	4.1	41.4	88.1
SoI 20_1506_1	0.05	15.1	0.24	26.6	0.25	0.34	6.6	42.6	91.8
SoI 20_1506_2	0.06	15.5	0.24	26.8	0.16	0.38	6.0	42.9	92.0
SoI 20_1506_3	0.13	15.4	0.16	26.6	0.14	0.4	5.8	42.5	91.1
SoI 20_1506_4	0	15.5	0.13	26.4	0.27	0.27	5.2	42.0	89.8
SoI 20_1506_5	0.07	14.9	0.29	25.9	0.4	0.5	4.3	41.1	87.4
SoI 20_1506_6	0.01	14.8	0.17	25.2	0.13	0.25	5.1	40.1	85.7
SoI 20_1506_7	0.04	13.8	0.16	24.2	0.19	0.15	4.3	38.2	81.0
SoI 20_1506_8	0.06	15.3	0.21	26.2	0.32	0.38	4.8	41.7	88.9
SoI 5_1806_1	0.03	14.2	0.28	24.5	0.22	0.22	4.5	38.9	82.8
SoI 5_1806_2	0.04	13.1	0.19	23.0	0.15	0.14	4.2	36.4	77.2
SoI 5_1806_3	0.01	12.8	0.23	22.5	0.2	0.21	4.0	35.5	75.4
SoI 5_1806_4	0.06	15.2	0.2	26.2	0.21	0.34	4.7	41.6	88.5
SoI 5_1806_5	0.01	14.2	0.26	25.0	0.25	0.35	5.2	39.7	84.8
SoI 5_1806_6	0.11	13.8	0.32	23.2	0.17	0.31	4.0	37.1	79.0
SoI 11_1806_1	0.17	14.5	1.7	27.6	0.29	1.06	5.4	44.7	95.5
SoI 11_1806_2	0.04	14.0	1.6	27.2	0.29	1	5.9	43.8	93.9
SoI 11_1806_3	0.05	15.6	1.1	25.4	0.24	0.52	3.9	41.6	88.4
SoI 11_1806_4	0.08	15.3	1.1	25.4	0.32	0.63	4.5	41.6	88.8
SoI 11_1806_5	0.09	15.4	1.0	25.3	0.29	0.5	3.8	41.3	87.7
SoI 13_1806_1	0.02	15.7	0.27	26.6	0.14	0.3	5.7	42.7	91.5
SoI 13_1806_2	0.08	15.9	0.21	26.9	0.08	0.33	5.7	43.1	92.3
SoI 13_1806_3	0.07	15.1	0.28	26.3	0.15	0.35	5.5	41.9	89.7
SoI 13_1806_4	0.04	15.4	0.32	26.7	0.18	0.31	5.9	42.8	91.7
SoI 13_1806_5	0.02	15.4	0.24	26.1	0.2	0.31	5.2	41.8	89.2
SoI 13_1806_6	0.03	15.5	0.19	26.5	0.17	0.16	5.4	42.2	90.2
SoI 13_1806_7	0.06	15.4	0.33	26.6	0.22	0.36	5.1	42.4	90.5
SoI 15_1806_1	0.04	15.7	0.19	26.8	0.22	0.27	5.9	42.8	91.9
SoI 15_1806_2	0.03	15.2	0.23	26.5	0.21	0.31	5.8	42.2	90.5
SoI 15_1806_3	0.01	15.8	0.16	26.6	0.13	0.29	5.5	42.6	91.0
SoI 15_1806_4	0	15.7	0.17	26.4	0.06	0.3	5.4	42.2	90.2
SoI 10_2306_5	0.23	12.7	3.0	23.3	0.1	0.98	7.2	40.2	87.7
SoI 10_2306_6	0.18	12.8	3.3	23.3	0.09	1.06	7.2	40.5	88.6
SoI 10_2306_7	0.19	13.4	3.2	23.5	0.13	0.97	7.3	41.1	89.8
SoI 4_3006_1	0.2	5.6	2.17	24.2	0.35	1.4	15.6	38.4	87.8
SoI 4_3006_2	0.23	6.0	2.34	25.2	0.25	1.47	14.9	39.7	90.1
SoI 4_3006_3	0.3	5.2	2.1	24.5	0.56	1.36	15.4	38.4	87.9

	Na	Mg	Al	Si	K	Ca	Fe	O	Totals
SoI 2_0207_1	0.2	15.2	3.0	26.1	0.15	1.08	2.6	43.6	91.9
SoI 2_0207_2	0.24	15.5	3.0	27.2	0.14	1.09	2.3	45.0	94.5
SoI 2_0207_3	0.14	15.3	3.0	26.7	0.21	1	2.4	44.3	93.0
SoI 2_0207_4	0.15	15.5	3.0	26.6	0.12	1	1.9	44.2	92.5
SoI 2_0207_5	0.2	14.9	3.1	26.8	0.2	1.22	2.6	44.3	93.2
SoI 2_0207_6	0.13	15.7	3.1	27.7	0.07	1.06	1.9	45.6	95.1
SoI 9_0207_1	0.54	5.5	2.32	25.2	0.58	1.38	14.8	39.4	89.7
SoI 9_0207_2	0.33	4.5	2.36	24.1	1.83	1.04	19.1	38.8	92.0
SoI 9_0207_3	0.45	6.1	2.03	24.0	0.44	1.17	13.4	37.7	85.2
SoI 10_0207_1	0.32	6.5	2.26	24.3	0.4	1.22	15.1	39.0	89.1
SoI 10_0207_2	0.38	6.3	2.12	25.1	0.49	1.05	14.7	39.4	89.5
SoI 10_0207_3	0.39	6.1	2.31	24.8	0.42	1.15	14.3	39.1	88.6
SoI 12_0207_1	0.38	5.6	2.57	22.7	0.26	1.22	19.6	38.2	90.5
SoI 12_0207_2	0.22	5.0	2.34	19.8	0.37	1.08	24.4	35.5	88.8
SoI 23_0207_1	0.19	5.9	1.91	25.2	0.4	1.28	14.3	39.1	88.3
SoI 23_0207_2	0.23	5.2	1.76	24.5	0.6	1.22	15.2	37.9	86.6
SoI 23_0207_3	0.25	5.3	2	25.1	0.51	1.28	16.4	39.3	90.2
SoI 23_0207_4	0.43	5.5	1.86	25.0	0.53	1.23	15.0	38.8	88.3
SoI 23_0207_5	0.45	5.6	1.9	25.4	0.44	1.29	15.6	39.5	90.2
SoI 24_0207_1	0.24	6.5	1.97	26.2	0.41	1.39	14.2	40.7	91.6
SoI 24_0207_2	0.44	5.7	1.83	24.8	0.43	1.28	14.3	38.5	87.2
SoI 24_0207_3	0.25	5.7	2	24.9	0.52	1.23	14.4	38.7	87.8
SoI 24_0207_4	0.2	6.4	1.95	25.9	0.38	1.42	14.4	40.3	91.0
SoI 24_0207_5	0.21	6.0	1.84	25.8	0.51	1.34	15.1	40.0	90.8
SoI 24_0207_6	0.27	5.8	1.91	24.9	0.56	1.43	14.6	38.8	88.3
SoI 24_0207_7	0.4	6.8	2.36	23.7	0.43	1.24	16.3	39.0	90.3
SoI 24_0207_8	0.15	6.9	2.4	22.1	0.21	1.28	19.2	38.0	90.2
SoI 3_0407_1	0.14	15.2	2.2	24.0	0.17	0.87	2.5	40.5	85.7
SoI 3_0407_2	0.25	15.0	2.3	24.0	0.12	0.86	2.2	40.4	85.2
SoI 3_0407_3	0.3	16.1	2.2	25.1	0.17	0.74	2.8	42.4	89.8
SoI 3_0407_4	0.27	16.1	2.0	25.6	0.08	0.7	2.6	42.7	90.0
SoI 3_0407_5	0.12	16.5	2.1	25.3	0.17	0.9	3.0	42.8	90.9
SoI 3_0407_6	0.31	16.0	2.1	24.7	0.16	0.74	3.0	41.7	88.6
SoI 8_0407_1	0.24	16.3	2.3	25.7	0.18	0.86	2.6	43.3	91.5
SoI 8_0407_2	0.26	16.8	2.2	26.1	0.22	0.77	2.7	43.9	92.9
SoI 8_0407_3	0.3	15.1	2.0	25.0	0.07	0.8	5.0	42.1	90.5
SoI 8_0407_4	0.32	16.0	2.0	25.6	0.1	0.85	3.5	43.0	91.5
SoI 8_0407_5	0.26	16.0	2.0	25.1	0.22	0.72	2.7	42.1	89.2
SoI 8_0407_6	0.45	16.5	2.2	25.8	0.11	0.74	2.9	43.5	92.2
SoI 16_0407_1	0.16	9.5	3.65	21.6	0.03	1.23	16.4	39.3	91.9
SoI 16_0407_2	0.03	9.3	3.58	20.4	0.17	0.98	17.6	38.0	90.0
SoI 16_0407_3	0.04	8.2	4.04	20.8	0.05	1.29	17.5	38.3	90.2
SoI 17_0407_1	0.58	10.0	3.72	22.0	0.11	1.17	13.3	39.5	90.4
SoI 17_0407_2	0.62	8.1	3.92	21.8	0.19	1.2	16.8	39.2	91.8
SoI 18_0407_1	0.22	16.1	2.2	24.9	0.13	0.86	2.5	42.1	89.0
SoI 18_0407_2	0.21	14.8	1.9	24.6	0.05	0.77	4.7	41.3	88.4
SoI 18_0407_3	0.24	15.2	2.1	25.1	0.07	0.99	4.2	42.2	90.1
SoI 18_0407_4	0.26	16.2	2.2	25.1	0.08	0.94	2.4	42.4	89.6
SoI 18_0407_5	0.11	15.7	1.9	25.3	0.1	0.79	3.7	42.3	89.9
SoI 18_0407_6	0.18	15.5	2.0	25.0	0.13	0.73	3.4	41.8	88.7
SoI 20_0407_1	0.29	10.5	3.85	20.6	0.1	0.97	15.4	38.7	90.3
SoI 20_0407_2	0.27	9.8	3.86	20.6	0.11	0.99	14.6	38.1	88.4
SoI 20_0407_3	0.12	9.9	3.81	19.0	0.04	0.78	18.3	37.2	89.2
SoI 21_0407_1	0.32	9.7	3.51	21.4	0.18	1.17	16.0	39.1	91.4

	Na	Mg	Al	Si	K	Ca	Fe	O	Totals
SoI 21_0407_2	0.27	9.7	3.6	21.6	0.09	1.39	15.9	39.4	92.0
SoI 21_0407_3	0.42	10.0	3.56	22.0	0.12	1.32	14.8	39.7	91.9
SoI 21_0407_4	0.39	9.6	3.52	21.6	0.19	1.48	16.8	39.7	93.3
SoI 21_0407_5	0.31	9.6	3.59	21.6	0.22	1.26	16.5	39.5	92.7
SoI 22_0407_1	0.16	17.1	2.2	26.6	0.14	0.82	3.1	44.8	94.8
SoI 22_0407_2	0.09	17.2	2.2	26.8	0.11	0.88	2.6	44.9	94.7
SoI 22_0407_3	0.13	17.5	2.1	26.6	0.07	0.74	2.7	44.8	94.6
SoI 22_0407_4	0.19	16.6	2.2	26.1	0.18	0.86	2.6	43.7	92.4
SoI 22_0407_5	0.16	16.5	2.0	26.4	0.14	0.68	3.9	44.1	93.8
SoI 22_0407_6	0.03	16.6	2.1	25.6	0.08	0.83	2.3	42.9	90.4
SoI 22_0407_7	0.14	16.4	2.2	25.9	0.13	0.78	2.5	43.3	91.3
SoI 22_0407_8	0.04	15.3	1.9	25.5	0.11	0.68	5.1	42.5	91.2
SoI 22_0407_9	0.12	16.4	1.9	26.6	0.16	0.84	3.5	44.2	93.7
SoI 22_0407_10	0.26	16.5	2.1	25.9	0.07	0.91	2.6	43.4	91.6
SoI 23_0407_1	0.12	10.1	3.42	21.0	0.07	1.49	13.8	38.1	88.1
SoI 23_0407_2	0.32	10.3	3.47	21.1	0.12	1.38	12.4	38.1	87.3
SoI 23_0407_3	0.21	13.1	1.87	23.6	0.1	0.87	7.3	39.7	86.6
SoI 30_0407_1	0.05	13.8	1.69	23.8	0.11	0.53	6.7	39.9	86.6
SoI 30_0407_2	0.07	13.1	1.35	23.1	0.14	0.53	5.7	38.1	82.0
SoI 31_0407_1	0.14	15.5	2.4	24.5	0.12	0.79	2.3	41.6	87.7
SoI 31_0407_2	0.09	15.4	2.4	24.7	0.1	1	2.5	41.6	87.8
SoI 31_0407_3	0.51	11.0	3.8	22.5	0.12	1.14	11.7	40.2	90.9
SoI 31_0407_4	0.52	10.7	3.4	22.4	0.09	1.09	11.5	39.5	89.3
SoI 31_0407_5	0.7	8.1	3.9	21.6	0.24	1.35	16.3	38.9	91.2
SoI 33_0407_1	0.17	15.0	1.27	25.3	0.08	0.59	4.7	41.5	88.6
SoI 33_0407_2	0.07	9.9	1.75	18.2	0.05	6.42	6.3	33.2	75.9
SoI 33_0407_3	0.1	12.5	1.41	22.8	0.2	0.6	7.2	37.8	82.6
SoI 33_0407_4	0.18	15.5	1.4	25.4	0.13	0.7	4.6	42.1	90.0
SoI 33_0407_5	0.08	13.7	1.73	24.1	0.09	1.06	6.5	40.3	87.5
SoI 36_0407_1	0.3	13.2	1.4	23.6	0.23	0.77	6.5	39.1	85.0
SoI 36_0407_4	0.17	13.9	1.58	24.8	0.19	0.83	7.1	41.2	89.8
SoI 36_0407_5	0.12	13.1	1.51	24.4	0.11	0.61	7.9	40.4	88.2
SoI 39_0407_1	0.21	16.9	2.7	26.2	0.12	1.06	2.6	44.6	94.3
SoI 39_0407_2	0.25	16.3	2.1	25.7	0.22	0.8	2.6	43.1	91.1
SoI 39_0407_3	0.21	17.1	2.5	26.0	0.09	0.87	2.5	44.3	93.6
SoI 39_0407_4	0.14	16.0	2.1	25.7	0.14	0.69	4.2	43.2	92.0
SoI 39_0407_5	0.24	15.9	1.9	25.8	0.12	0.6	4.8	43.2	92.4
SoI 39_0407_6	0.21	15.8	1.9	25.5	0.14	0.81	4.4	42.7	91.4
SoI 39_0407_7	0.15	15.7	2.0	25.3	0.12	0.78	4.7	42.7	91.5
SoI 41_0407_1	0.03	16.1	2.6	25.0	0.15	1.02	2.2	42.6	89.8
SoI 41_0407_2	0.2	16.0	2.3	25.3	0.1	0.84	2.6	42.6	89.9
SoI 41_0407_3	0.14	16.0	2.0	25.7	0.06	1.07	3.0	43.0	91.0
SoI 41_0407_4	0.11	15.6	2.0	25.1	0.15	0.8	3.3	42.0	89.0
SoI 41_0407_5	0.31	13.9	2.2	24.1	0.12	0.84	6.9	41.0	89.2
SoI 41_0407_6	0.04	16.5	2.3	25.5	0.06	0.85	2.4	43.0	90.6
SoI 41_0407_7	0.2	16.1	2.0	25.3	0.11	0.69	3.3	42.6	90.3
SoI 44_0407_1	0.27	14.1	2.9	23.4	0.05	0.91	2.1	39.6	83.3
SoI 44_0407_2	0.03	14.9	2.4	23.4	0.13	0.8	2.1	39.6	83.3
SoI 44_0407_3	0.24	15.9	2.2	25.2	0.06	0.72	3.2	42.3	89.8
SoI 44_0407_4	0.4	15.9	2.2	25.4	0.16	0.7	3.8	42.9	91.6
SoI 44_0407_5	0.17	15.8	2.1	25.6	0.08	0.94	2.6	42.6	89.9
SoI 44_0407_6	0.17	15.6	2.1	24.9	0.12	0.7	3.7	41.9	89.2
SoI 44_0407_7	0.29	11.0	3.0	21.3	0.1	0.98	10.3	37.6	84.6
SoI 44_0407_8	0.24	11.4	3.2	21.5	0.1	1.12	10.4	38.4	86.4

	Na	Mg	Al	Si	K	Ca	Fe	O	Totals
SoI 44_0407_9	0.21	10.1	2.6	19.1	0.03	0.97	8.9	33.8	75.8
SoI 11_0507_1	1.11	14.8	4.6	24.5	0.11	0.48	1.2	42.7	89.5
SoI 11_0507_2	0.9	15.3	4.09	24.6	0.08	0.81	1.2	42.7	89.7
SoI 11_0507_3	0.61	15.1	3.74	24.5	0.07	0.63	1.1	42.0	87.8
SoI 11_0507_4	0.97	15.1	4.32	24.9	0.16	0.55	1.2	43.1	90.3
SoI 11_0507_5	0.44	15.3	3.87	24.2	0.23	1.07	1.4	42.1	88.5
SoI 22_0507_1	0.2	15.5	0.32	27.2	0.06	0.38	6.8	43.6	94.1
SoI 22_0507_2	0.23	15.1	1.04	26.4	0.13	0.55	5.6	42.9	92.0
SoI 22_0507_3	0.19	14.6	0.53	26.2	0.16	0.47	5.1	41.7	89.0
SoI 22_0507_4	0.17	14.5	0.35	25.8	0.17	0.38	4.8	40.8	86.9
SoI 22_0507_5	0.21	14.6	0.12	25.6	0.04	0.41	5.1	40.6	86.7
SoI 22_0507_6	0.16	15.1	0.13	26.7	0.14	0.5	6.0	42.5	91.2
SoI 22_0507_7	0.05	14.4	0.2	25.9	0.1	0.37	5.3	40.9	87.2
SoI 22_0507_8	0.18	14.3	0.12	26.1	0.03	0.41	5.9	41.1	88.1

Tidigare skrifter i serien ”Examensarbeten i Geologi vid Lunds Universitet”:

203. Jansson, Ida-Maria, 2006: An Early Jurassic conifer-dominated assemblage of the Clarence-Moreton Basin, eastern Australia.
204. Striberger, Johan, 2006: En lito- och biostratigrafisk studie av senglaciala sediment från Skuremåla, Blekinge.
205. Bergelin, Ingemar, 2006: $^{40}Ar/^{39}Ar$ geochronology of basalts in Scania, S Sweden: evidence for two pulses at 191-178 Ma and 110 Ma, and their relation to the break-up of Pangea.
206. Edvarssson, Johannes, 2006: Dendrokronologisk undersökning av tallbestånds etablering, tillväxtdynamik och degenerering orsakat av klimatrelaterade hydrologiska variationer på Viss mosse och Åbuamossen, Skåne, södra Sverige, 7300-3200 cal. BP.
207. Stenfeldt, Fredrik, 2006: Litostratigrafiska studier av en platåformad sand- och grusavlagring i Skuremåla, Blekinge.
208. Dahlenborg, Lars, 2007: A Rock Magnetic Study of the Åkerberg Gold Deposit, Northern Sweden.
209. Olsson, Johan, 2007: Två svekofenniska graniter i Bottniska bassängen; utbredning, U-Pb zirkondatering och test av olika abrasionstekniker.
210. Erlandsson, Maria, 2007: Den geologiska utvecklingen av västra Hamrångesynklinalens suprakrustalbergarter, centrala Sverige.
211. Nilsson, Pernilla, 2007: Kvidingedeltat – bildningsprocesser och arkitektonisk uppbyggnadsmodell av ett glacifluvialt Gilbertdelta.
212. Ellingsgaard, Óluva, 2007: Evaluation of wireline well logs from the borehole Kyrkheddinge-4 by comparsion to measured core data.
213. Åkerman, Jonas, 2007. Borrkärnekartering av en Zn-Ag-Pb-mineralisering vid Stenbrånet, Västerbotten.
214. Kurlovich, Dzmitry, 2007: The Polotsk-Kurzeme and the Småland-Blekinge Deformation Zones of the East European Craton: geomorphology, architecture of the sedimentary cover and the crystalline basement.
215. Mikkelsen, Angelica, 2007: Relationer mellan grundvattenmagasin och geologiska strukturer i samband med tunnelborrning genom Hallandsås, Skåne.
216. Trondman, Anna-Kari, 2007: Stratigraphic studies of a Holocene sequence from Taniente Palet bog, Isla de los Estados, South America.
217. Månsson, Carl-Henrik & Siikanen, Jonas, 2007: Measuring techniques of Induced Polarization regarding data quality with an application on a test-site in Aarhus, Denmark and the tunnel construction at the Hallandsås Horst, Sweden.
218. Ohlsson, Erika, 2007: Classification of stony meteorites from north-west Africa and the Dhofar desert region in Oman.
219. Åkesson, Maria, 2008: Mud volcanoes - a review. (15 hskp)
220. Randsalu, Linda, 2008: Holocene relative sea-level changes in the Tasiusaq area, southern Greenland, with focus on the Ta1 and Ta3 basins. (30 hskp)
221. Fredh, Daniel, 2008: Holocene relative sea-level changes in the Tasiusaq area, southern Greenland, with focus on the Ta4 basin. (30 hskp)
222. Anjar, Johanna, 2008: A sedimentological and stratigraphical study of Weichselian sediments in the Tvärkroken gravel pit, Idre, west-central Sweden. (30 hskp)
223. Stefanowicz, Sissa, 2008: Palynostratigraphy and palaeoclimatic analysis of the Lower - Middle Jurassic (Pliensbachian - Bathonian) of the Inner Hebrides, NW Scotland. (15 hskp)
224. Holm, Sanna, 2008: Variations in impactor flux to the Moon and Earth after 3.85 Ga. (15 hskp)
225. Bjärnborg, Karolina, 2008: Internal structures in detrital zircons from Hamrånge: a study of cathodoluminescence and back-scattered electron images. (15 hskp)
226. Noresten, Barbro, 2008: A reconstruction of subglacial processes based on a classification of erosional forms at Ramsvikslandet, SW Sweden. (30 hskp)
227. Mehlqvist, Kristina, 2008: En mellanjurassisk flora från Bagå-formationen, Bornholm. (15 hskp)
228. Lindvall, Hanna, 2008: Kortvariga effekter

av tefranedfall i lakustrin och terrestrisk miljö. (15 hskp)

229. Löfroth, Elin, 2008: Are solar activity and cosmic rays important factors behind climate change? (15 hskp)

230. Damberg, Lisa, 2008: Pyrit som källa för spårämnen – kalkstenar från övre och mellersta Danien, Skåne. (15 hskp)

331. Cegrell, Miriam & Mårtensson, Jimmy, 2008: Resistivity and IP measurements at the Bolmen Tunnel and Ådalsbanan, Sweden. (30 hskp)

232. Vang, Ina, 2008: Skarn minerals and geological structures at Kalkheia, Kristiansand, southern Norway. (15 hskp)

233. Arvidsson, Kristina, 2008: Vegetationen i Skandinavien under Eem och Weichsel samt fallstudie i submoräna organiska avlagringar från Nybygget, Småland. (15 hskp)

234. Persson, Jonas, 2008: An environmental magnetic study of a marine sediment core from Disko Bugt, West Greenland: implications for ocean current variability. (30 hskp)

235. Holm, Sanna, 2008: Titanium- and chromium-rich opaque minerals in condensed sediments: chondritic, lunar and terrestrial origins. (30 hskp)

236. Bohlin, Erik & Landen, Ludvig, 2008: Geofysiska mätmetoder för prospektering till ballastmaterial. (30 hskp)

237. Brodén, Olof, 2008: Primär och sekundär migration av hydrokarboner. (15 hskp)

238. Bergman, Bo, 2009: Geofysiska analyser (stångslingram, CVES och IP) av lagerföljd och lakvattenrörelser vid Albäcksdeponin, Trelleborg. (30 hskp)

239. Mehlqvist, Kristina, 2009: The spore record of early land plants from upper Silurian strata in Klinta 1 well, Skåne, Sweden. (45 hskp)

239. Mehlqvist, Kristina, 2009: The spore record of early land plants from upper Silurian strata in Klinta 1 well, Skåne, Sweden. (45 hskp)

240. Bjärnborg, Karolina, 2009: The copper sulphide mineralization of the Zinkgruvan deposit, Bergslagen, Sweden. (45 hskp)

241. Stenberg, Li, 2009: Historiska kartor som hjälp vid jordartsgeologisk kartering – en pilotstudie från Vångs by i Blekinge. (15 hskp)

242. Nilsson, Mimmi, 2009: Robust U-Pb baddeleyite ages of mafic dykes and intrusions in southern West Greenland: constraints on the coherency of crustal blocks of the North Atlantic Craton. (30 hskp)

243. Hult, Elin, 2009: Oligocene to middle Miocene sediments from ODP leg 159, site 959 offshore Ivory Coast, equatorial West Africa. (15 hskp)

244. Olsson, Håkan, 2009: Climate archives and the Late Ordovician Boda Event. (15 hskp)

245. Wollein Waldetoft, Kristofer, 2009: Svekofennisk granit från olika metamorfa miljöer. (15 hskp)

246. Månsby, Urban, 2009: Late Cretaceous coprolites from the Kristianstad Basin, southern Sweden. (15 hskp)

247. MacGimpsey, I., 2008: Petroleum Geology of the Barents Sea. (15 hskp)

248. Jäckel, O., 2009: Comparison between two sediment X-ray Fluorescence records of the Late Holocene from Disko Bugt, West Greenland; Paleoclimatic and methodological implications. (45 hskp)

249. Andersen, Christine, 2009: The mineral composition of the Burkland Cu-sulphide deposit at Zinkgruvan, Sweden – a supplementary study. (15 hskp)

250. Riebe, My, 2009: Spinel group minerals in carbonaceous and ordinary chondrites. (15 hskp)

251. Nilsson, Filip, 2009: Föroreningsspridning och geologi vid Filborna i Helsingborg. (30 hskp)

252. Peetz, Romina, 2009: A geochemical characterization of the lower part of the Miocene shield-building lavas on Gran Canaria. (45 hskp)

LUNDS UNIVERSITET

Geologiska institutionen
Centrum för GeoBiosfärsvetenskap
Sölvegatan 12, 223 62 Lund